Natural Resources Canada | Ressources naturelles Canada

GEOLOGICAL SURVEY OF CANADA
OPEN FILE 8373

Targeted Geoscience Initiative: 2017 report of activities, volume 2

N. Rogers (ed.)

2018

Celebrating 175 yrs

Canada

GEOLOGICAL SURVEY OF CANADA
OPEN FILE 8373

Targeted Geoscience Initiative: 2017 report of activities, volume 2

N. Rogers (ed.)

2018

© Her Majesty the Queen in Right of Canada, as represented by the Minister of Natural Resources, 2018

Information contained in this publication or product may be reproduced, in part or in whole, and by any means, for personal or public non-commercial purposes, without charge or further permission, unless otherwise specified.
You are asked to:
- exercise due diligence in ensuring the accuracy of the materials reproduced;
- indicate the complete title of the materials reproduced, and the name of the author organization; and
- indicate that the reproduction is a copy of an official work that is published by Natural Resources Canada (NRCan) and that the reproduction has not been produced in affiliation with, or with the endorsement of, NRCan.

Commercial reproduction and distribution is prohibited except with written permission from NRCan. For more information, contact NRCan at nrcan.copyrightdroitdauteur.rncan@canada.ca.

Permanent link: https://doi.org/10.4095/306586

This publication is available for free download through GEOSCAN (http://geoscan.nrcan.gc.ca/).

Recommended citation
Rogers, N. (ed.), 2018. Targeted Geoscience Initiative: 2017 report of activities, volume 2; Geological Survey of Canada, Open File 8373, 108 p. https://doi.org/10.4095/306586

Publications in this series have not been edited; they are released as submitted by the author.

Targeted Geoscience Initiative: 2017 report of activities, volume 2

Edited and compiled by
Neil Rogers

Extent, origin, and deposit-scale controls of the 1883 Ma Circum-Superior large igneous province, northern Manitoba, Ontario, Quebec, Nunavut and Labrador

W. Bleeker[1] and S.L. Kamo[2]

[1]*Geological Survey of Canada, 601 Booth Street, Ottawa, Ontario K1A 0E8*

[2]*Jack Satterly Geochronology Laboratory, University of Toronto, 22 Russell Street, Toronto, Ontario M5S 3B1*

Abstract

An update is presented on research in the setting and controls on Ni-Cu-PGE in the ca. 1883 Ma Circum-Superior belt, here with a specific focus on the Raglan belt of northern Quebec. A new stratigraphic interpretation indicates that the critical part of the stratigraphy is less imbricated by numerous thrusts than previously hypothesised and that the critical Povungnituk to Chukotat Group contact, i.e. the Raglan Horizon, is stratigraphic and not a regional thrust. This contact, along which hot komatiitic lavas flowed out over easily fusible graphitic mudstone of the Nuvilik Formation, is stitched together in a primary sense by thermo-mechanical erosion channels with some of the largest sulphide ore lenses hosted by the deepest lava channels that eroded down through Nuvilik sediments into footwall gabbro sills. Precise U-Pb ages on these gabbro sills, and on slightly younger gabbro sills that intruded above the lowermost komatiite flows and ore lenses, bracket the mineralization to ca. 1882 Ma, an age that is identical to those of the Thompson deposits in Manitoba. The bulk of the sulphide ore formed during peak effusion rates of komatiitic lava during the onset of the overall magmatic event. This major magmatic event has (coeval) expressions at the scale of the entire Superior craton and its margins, suggesting a geodynamic setting of hot mantle upwelling and continental break-up rather than perfectly synchronized arc processes.

Introduction

The initial focus of this activity has been on the Raglan belt, northern Quebec, and the structural-stratigraphic setting of its komatiite-hosted Ni-Cu-PGE deposits (Giovenazzo et al., 1989; Lesher, 2007; Bleeker and Ames, 2017). New U-Pb ages have been obtained on key elements in the stratigraphy. These new ages date the mineralization at 1882 Ma, an age that is identical to that of the Thompson Belt, Manitoba. Fieldwork and structural observations, in conjunction with an improved stratigraphic understanding, suggest considerably fewer thrusts than originally envisioned in the critical part of the tectono-stratigraphy, allowing for a more coherent interpretation of the original volcanic setting, and the formation and current setting of the Ni-Cu-PGE deposits. Preliminary results were reported by W. Bleeker (unpub. rept., 2013), Bleeker and Ames (2017) and Bleeker and Kamo (2017a, b), with key highlights summarised below.

Key Activity Highlights

Overall structure of the Raglan belt

A generalized north-to-south cross-section through the Cape Smith Belt is shown in Figure 1, highlighting first-order structures and tectono-stratigraphic domains. From north to south, these first-order structures and domains are:

1) A granitoid-dominated Paleoproterozoic (accreted?) terrane – the Narsajuaq arc (see St-Onge et al., 1992, 2006).
2) A major basement-cored domal antiform – the Kovik antiform, which we interpret as a relatively late metamorphic core complex (cf. Hoffman, 1985).
3) Stacked allochthons of higher metamorphic grade and deformational state in a tight synclinorium on the southern flank of the Kovik antiform.
4) A rather well-preserved, largely homoclinal, central part of the Cape Smith Belt, i.e. the Raglan belt proper, with only one significant thrust duplication of the main 'Raglan Horizon', and some south-vergent folding.
5) A footwall section to the Raglan Horizon consisting of Nuvilik Formation thinly bedded turbidites overlying volcanic rocks at the top of the Povungnituk Group.
6) An imbricated zone of parautochthonous lower Povungnituk Group strata, overlying Archean basement (see also Mungall, 2007).
7) Autochthonous Archean basement of the northern Superior craton.

In Figure 1, the critical Raglan Horizon, consisting of lowermost komatiite flows of the Chukotat Group that overlie and flowed over sulphide-bearing turbiditic mudstones and siltstones of the Nuvillik Formation, is shown as the bold purple line, at the base of the Chukotat Group. It is clearly offset and repeated by the south-verging Cross Lake fault (Lucas and St-

Corresponding author: Wouter Bleeker (wouter.bleeker@canada.ca)

Bleeker, W., and Kamo, S.L., 2018. Extent, origin, and deposit-scale controls of the 1883 Ma Circum-Superior large igneous province, northern Manitoba, Ontario, Quebec, Nunavut and Labrador; *in* Targeted Geoscience Initiative: 2017 report of activities, volume 2, (ed.) N. Rogers; Geological Survey of Canada, Open File 8373, p. 5–14. https://doi.org/10.4095/306592

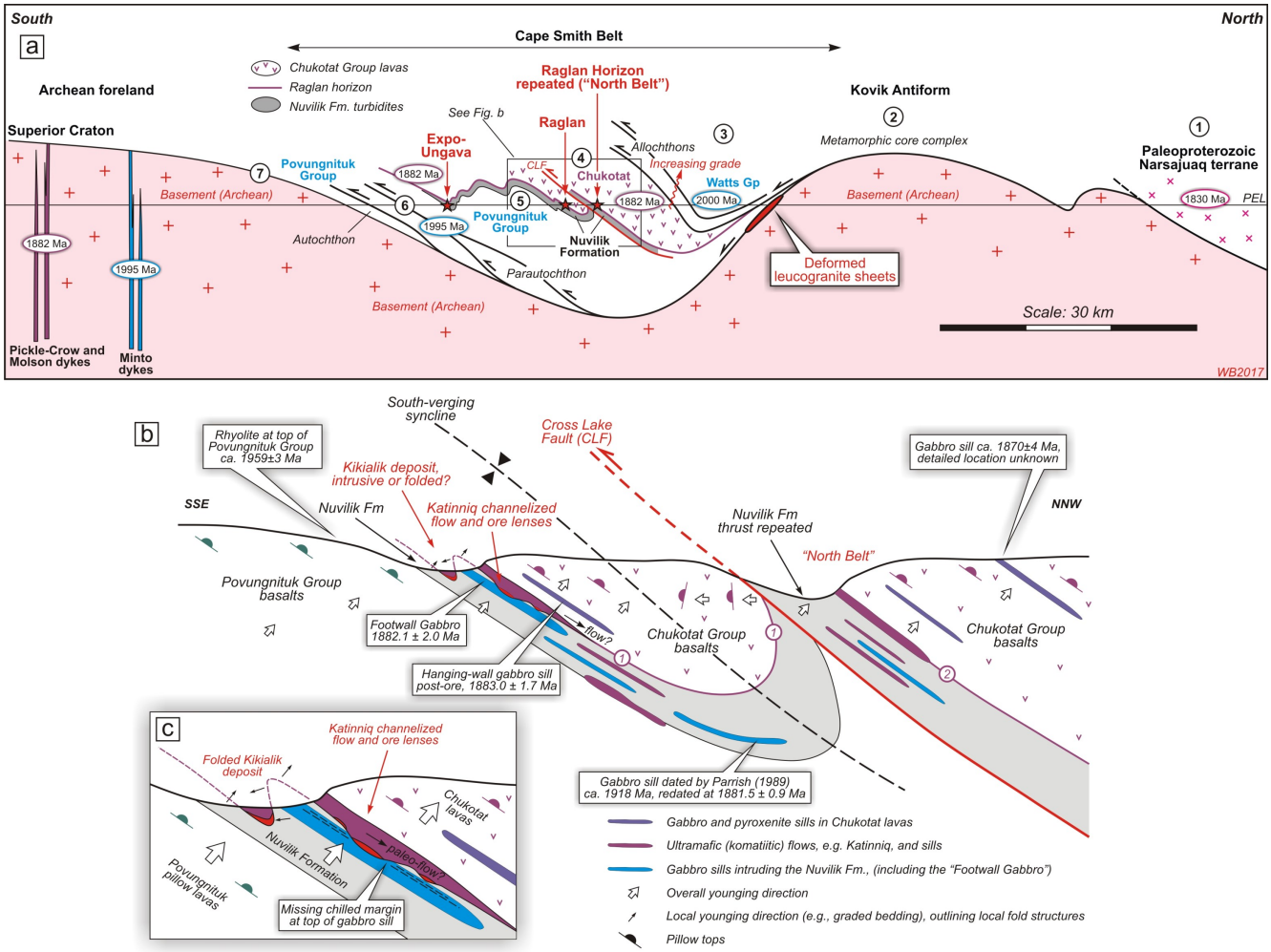

Figure 1. a) North-to-south regional-scale cross-section through the Cape Smith Belt, northern Quebec. Circled numbers (1 to 7) refer to tectono-stratigraphic domains and are discussed in the text. The mineralized Raglan Horizon, in the well-preserved north-dipping central part of the belt, is shown as a solid purple line, on the stratigraphic contact between turbiditic Nuvilik Formation mudstones and siltstones (in grey) and the overlying Chukotat Group lavas. Ni-Cu-PGE sulphide deposits and prospects are identified by red stars. See also Mungall (2007). b) Zoomed-in view of the central part of the Raglan belt, with the Katinniq ore bodies at the base of channelized basal komatiite flows. The Kikialik deposit, situated in a tight fold structure, is also shown. Some of the available high-precision ages are shown for reference. Note that the overall structure is that of a faulted syncline-anticline pair, the overturned limb of which has evolved into the Cross Lake Fault (CLF, in red), a fault of moderate displacement (reverse, north over south). The overall structure leads to repetition of the Raglan Horizon (1) across the fault into the North Belt (2). c) Inset that zooms in further to highlight the stratigraphic and structural relationships of the Raglan Horizon at the Katinniq and Kikialik deposits. Note the localization of some of the larger sulphide lenses (red) at Katinniq in channels that have eroded down into the Footwall Gabbro sill (gabbro sill in blue). Primary erosive contact indicated by missing chilled margin (see Bleeker and Ames, 2017).

Onge, 1992; St-Onge and Lucas, 1993), which is a thrust of moderate displacement merely representing the sheared overturned limb of what should be viewed as a south-verging syncline-anticline pair (Fig. 1b, c). Understanding this structure is important because, at some point, exploration that so far has largely focused on the southern main Raglan belt, will have to move to this structurally repeated 'North Belt'.

Stratigraphy

The overall stratigraphy of the Raglan belt, as we currently understand it, is summarized in Figure 2. This figure highlights that the main Raglan Horizon, the basal contact of Chukotat Group komatiites on Nuvillik mudstones and siltstones at the top of Povungnituk Group, is a stratigraphic contact, not a regional thrust (cf. St-Onge et al., 1992, 2006; Lucas and St-

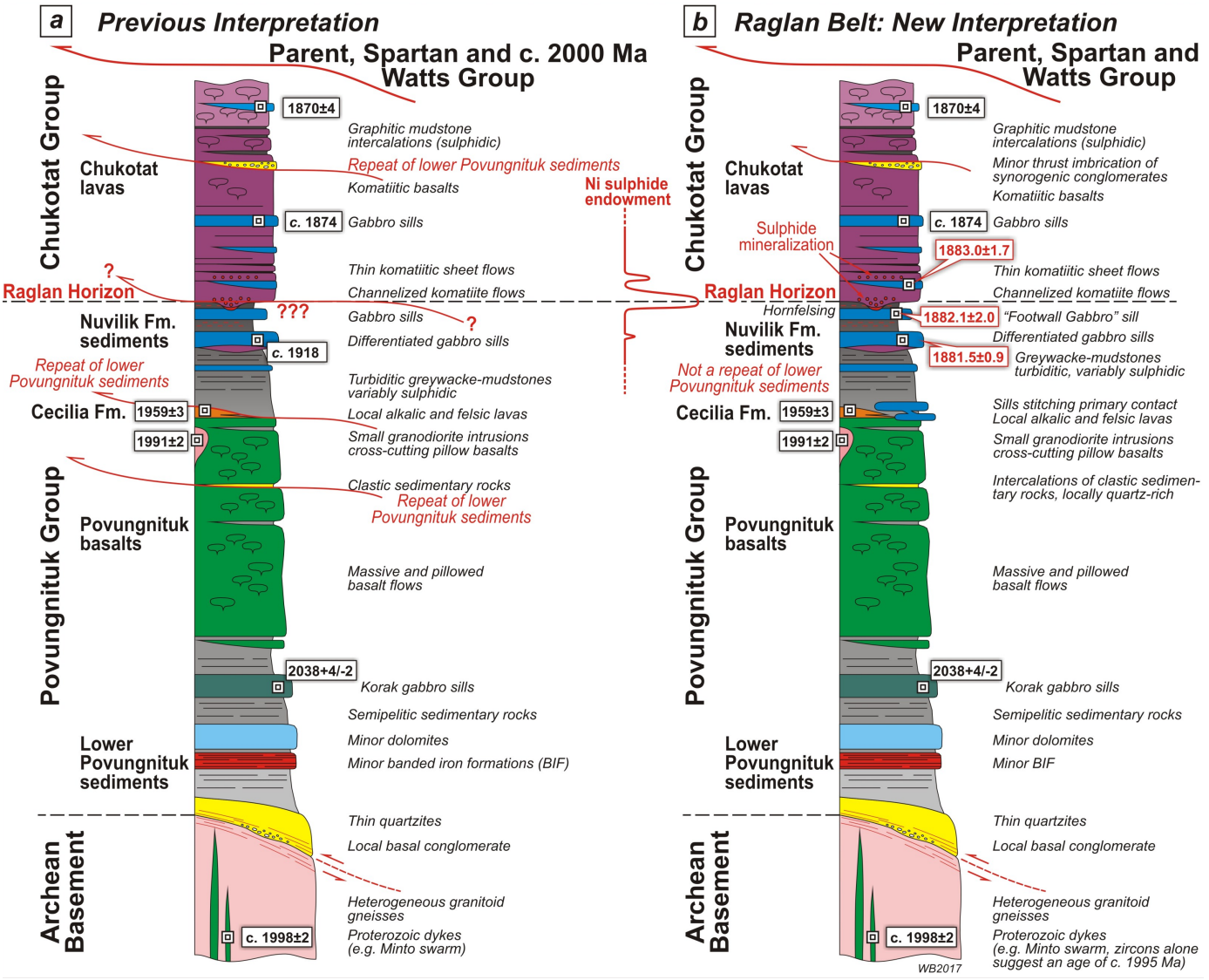

Figure 2. Lithostratigraphy of the Raglan belt. a) Previous interpretation with thrusts at the base of each sedimentary unit (based on a model of thrust imbrication and reappearance of lower Povingnituk sedimentary units). b) New interpretation based on this study, with far fewer thrust contacts. Most of the sedimentary members in the stratigraphy represent unique stratigraphic units rather than thrust repeats. Ages (in Ma) are highlighted, with new high-precision ages (this study) in red. For references, see Bleeker and Ames (2017).

Onge, 1992). This conclusion is supported by the following observations:

- Positive evidence for major thrusting on this contact, in terms of structural fabrics or out-of-sequence stacking, is lacking, although minor structural complexities cannot be ruled out.
- Multiple lines of evidence for thermal erosion channels of basal komatiites into underlying Nuvilik Formation sulphidic mudstones (e.g. Lesher, 2007).
- Conspicuous hornfelsing of Nuvilik mudstones immediately below hot komatiite flows, welding the two units together at the time of komatiite extrusion (Bleeker, unpub. rept., 2013).
- Sulphide contamination of the basal komatiite flows by assimilation of the Nuvilik Formation sulphidic mudstones and siltstones; the ultimate cause for sulphide ore formation.
- The empirical observation (Glencore plc, pers. comm., 2016) that some of the largest sulphide ore lenses are located on a local footwall of gabbro, where the deepest erosion channels have drilled through Nuvilik mudstones and into a large 'Footwall Gabbro' sill within the Nuvilik Formation (see Fig. 1c).

- The observation that at such localities, below the thermal erosion channels, the gabbro sill is missing its upper chilled margin (Bleeker and Ames, 2017).
- Similar U-Pb ages for gabbro sills in both footwall and hanging wall, again welding the Povungnituk and Chukotat Groups together in their original setting. A similar relationship also shows that the lower contact of the Nuvilik Formation is a stratigraphic contact rather than a thrust (Fig. 2b).

The conclusion that both the lower and upper contacts of the Nuvilik Formation, and thus the Povungnituk to Chukotat Group contact, are stratigraphic in nature greatly simplifies, if not unifies the overall understanding of the Raglan ore system. It also greatly simplifies strategies for future exploration. The background on why many of the contacts may have previously been interpreted as thrusts is discussed in Bleeker and Ames (2017), and Bleeker and Kamo (2017a, b).

Graded bedding in the turbiditic Nuvilik Formation allows determination of younging direction in essentially every outcrop and drill core where this unit is present or intersected. Unambiguous reversals of this younging direction clearly outline metre- to deposit-scale fold structures in the Raglan Horizon, such as in and around the Kikialik deposit (Fig. 1c). Not taking these younging reversals and structures into account may lead to the incorrect interpretation that the Kikialik deposit may sit below the Katinniq deposit, in an intrusive setting within the Nuvilik Formation. As shown schematically in Figure 1c, it is folding that controls the position of the Kikialik deposit and, seen from that perspective, its stratigraphic position is identical to that of the Katinniq deposit (Bleeker, unpub. rept., 2013).

New U-Pb geochronology

Also highlighted in Figure 2 are our new U-Pb zircon and baddeleyite dating results. For clarity, new results are indicated in red on the figure. We now have ages on differentiated gabbro sills in both the footwall to the Raglan horizon and on gabbro sills in the hanging wall, intruding above the basal komatiites. While some of the gabbro sills in the footwall are eroded into by the komatiite flows and ore channels, and therefore must be marginally older than the onset of komatiite volcanism (Lesher, 2007; Bleeker and Ames, 2017), those in the hanging wall intruded above the basal komatiite flows and major ore lenses, and therefore must be marginally younger than the onset of komatiite volcanism and ore formation. Yet, within the current resolution of the data (ca. 1–2 Ma), the ages overlap and indicate a sharp onset of the Chukotat komatiite event at 1882 Ma.

Our new data also clarify some older ages that have been questioned, particularly the age interpretation of 1918 +9/-7 Ma on a footwall gabbro sill (the Cross Lake sill) based on variably discordant baddeleyite and zircon data (Parrish, 1989; Bleeker, unpub. rept., 2013). After reinterpreting these data and predicting an age of ca. 1884 Ma to be more likely, we obtained new concordant data on chemically abraded zircons from the same sample. These results show this sill to be 1882 Ma, specifically 1881.5 ± 0.9 Ma (Fig. 3).

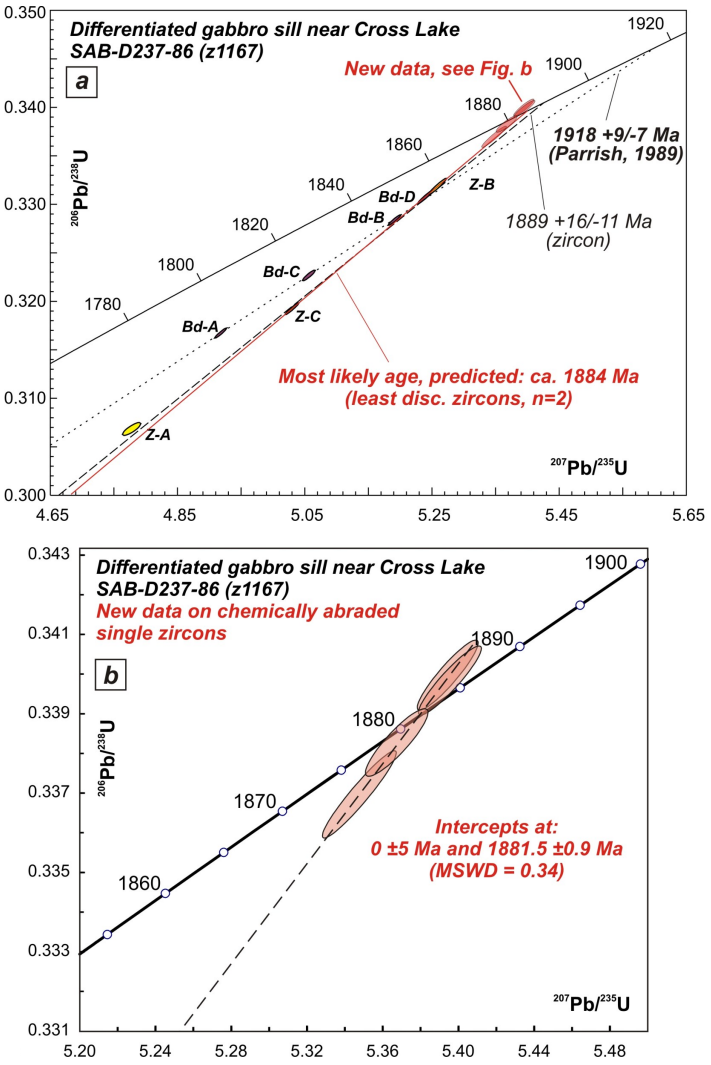

Figure 3. U-Pb age data for the differentiated mafic – ultramafic Cross Lake Sill at the western end of the Raglan belt. a) Original data of Parrish (1989), with variably discordant zircon fractions (Z, yellow) and baddeleyite fractions (Bd, purple ellipses). Original age interpretation based on a shallow-sloping regression line through the variably discordant baddeleyite data points (dotted line), with an upper intercept of 1918 +9/-7 Ma. Our alternative and preferred interpretation would be to ignore this shallow sloping array, affected by early Pb loss in partially altered baddeleyite crystals, and instead focus on the zircon data, particularly the two least discordant fractions, with a predicted age of ca. 1884 Ma (red line). See Bleeker (2014) for discussion. b) New data on chemically abraded single zircons from the same sample. The new data overlap the concordia curve and indicate an age of 1881.5 ± 0.9 Ma .

In Figure 4 we summarize a selection of current U-Pb age data, demonstrating the remarkable convergence of ages towards a single event at ca. 1882 to 1883 Ma, across much of the Superior craton and its margins. A similar convergence has often been demonstrated, in recent years, in modern U-Pb studies of young large igneous provinces (LIPs), for instance the Siberian Traps or Karoo LIP (Kamo et al., 2003; Burgess and Bowring, 2015; Svensen et al., 2012), indicating that the mantle instabilities and melting events that lead to typical LIPs, and their Ni-Cu-PGE ore systems, may be surprisingly short lived, on the order of ca. 1 Ma.

Also shown in Figure 4 is the original zircon age of a plagioclase-glomeroporphyritic gabbro sill in the 'Labrador Trough', part of the 'Montagnais sills' (Wardle, 1990; Findlay et al., 1995). Its quoted age was 1884.0 ± 1.6 Ma (Findlay et al., 1995), which now appears to be an older outlier in the overall dataset (Fig. 4). However, this apparently precise age was based on somewhat discordant zircon data (four fractions of multiple, air-abraded zircons), with a precise upper intercept, but a non-zero age lower intercept (ca. 465 Ma). Based on our experience with such datasets (Bleeker, 2014), and specifically the non-zero age lower intercept, we suspected that this date may be an overestimate of the true age. Again we have gone back to the original sample, archived at the Geological Survey of Canada, and repicked some of the high quality zircons. New chemical abrasion ID-TIMS data, on multiple single zircon grains, yield concordant and overlapping results, indicating an age of 1878.5 ± 0.8 Ma. This high-precision age now represents the young end of the event, post-dating ore formation along the Raglan Horizon and in the Cape Smith Belt. This

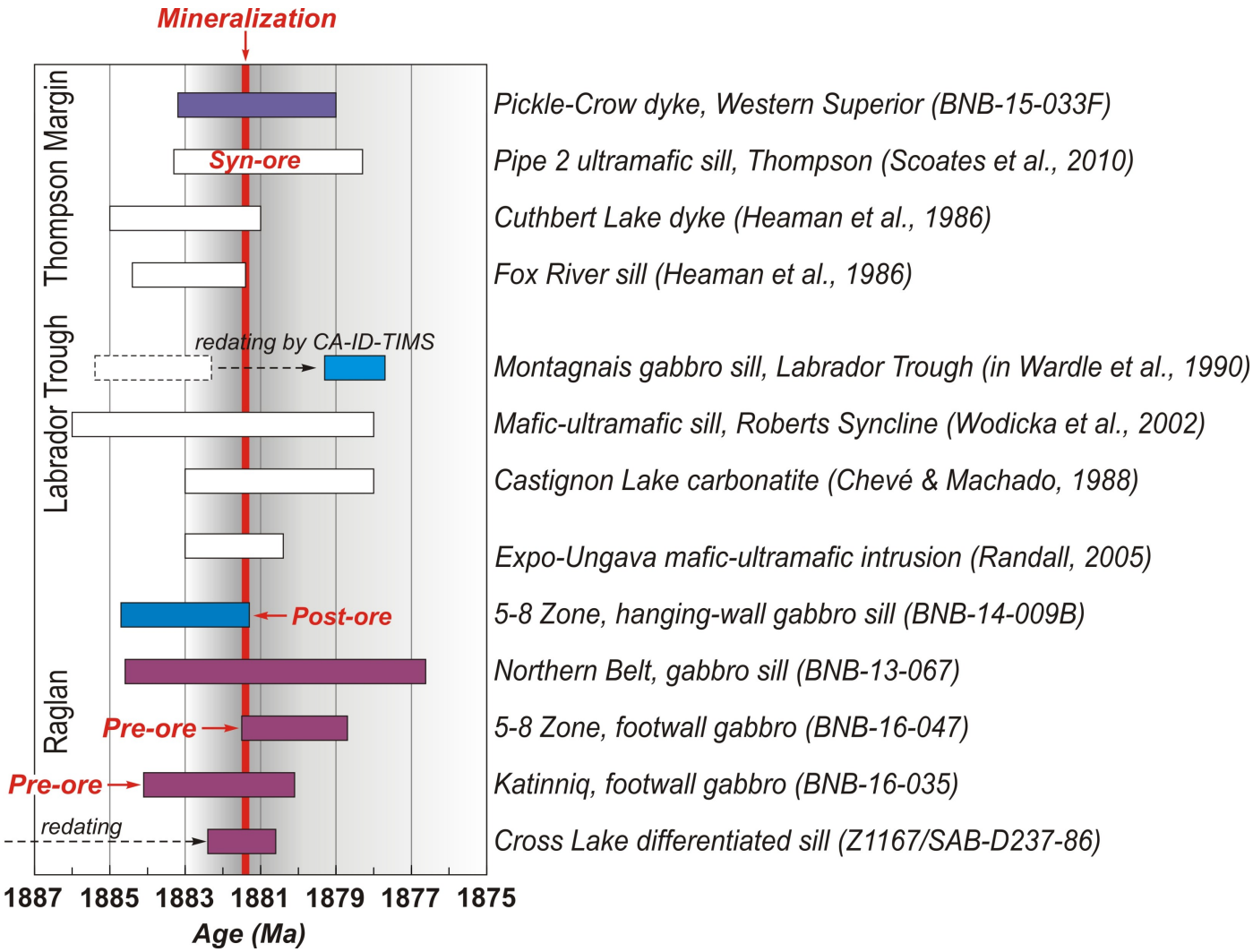

Figure 4. Summary of selected U-Pb zircon ages. New data by the authors are represented by the coloured age bars. Others are referenced to the original publication as indicated. Units specifically redated for this study are identified and discussed in the text. Dates that explicitly bracket ore formation are highlighted (pre-, syn- and post-ore). The LIP-scale event starts at 1883 Ma or shortly thereafter, and at Raglan peak komatiite outflow and ore formation (mineralization) occurs between 1882 and 1881 Ma.

may correlate with the plagioclase-glomeroporphyritic nature of this gabbro sill, suggesting significant residence time in deep - or sub-crustal underplated magma chambers.

Some regional correlations

The stratigraphy of the Cape Smith Belt, and specifically the Raglan belt in terms of mafic – ultramafic sills with an age of 1882 Ma, can be followed further east into the northern Labrador Trough, specifically the Roberts Syncline around the northern hamlet of Kangirsuk (Hardy, 1976; Madore and Larbi, 2001). There Wodicka et al. (2002) dated a differentiated mafic – ultramafic sill at 1882 ± 4 Ma. This same, or at least very similar sill, somewhat further north in the syncline, was drilled for low grade Ni-Cu sulphide mineralization. The entire Roberts Syncline with its basal sedimentary units and upper mafic flows, intruded by Raglan age sills, represents a continuation of the Cape Smith stratigraphy, not of the cyclic Labrador Trough stratigraphy (e.g. Rohon et al., 1993; Findlay et al., 1995; Clark and Wares, 2006; Henrique-Pinto et al., 2017) further south. Where and how the transition to more typical Labrador Trough stratigraphy occurs, somewhere south of Kangirsuk, remains to be resolved in detail.

Science Impact and Discussion

The conclusion that both the lower and upper contacts of the Nuvilik Formation, and specifically the Raglan Horizon, represent stratigraphic contacts greatly simplifies the overall Raglan ore system and future exploration strategies. Much of the Ni-Cu-(PGE) sulphide ore endowment of the Raglan belt occurs at or near the basal contact of the Chukotat Group lavas (as illustrated by the red curve in Figure 2b), and some of the larger ore lenses occur demonstrably in thermal erosion channels that have drilled down through the upper Nuvilik Formation sulphidic sediments into just marginally older footwall gabbro sills. This has been demonstrated in more than one location along the belt (Lesher, 2007; Glencore exploration staff, pers. comm., 2016; Bleeker and Ames, 2017). The onset of komatiitic volcanism is now precisely bracketed at ca. 1882 Ma, with most of the ore associated with peak komatiitic effusion rates early in this time interval, at the start of the Chukotat magmatic event. If the precisely dated Cross Lake sample, from a large differentiated mafic – ultramafic sill at Cross Lake, at the western end of the Raglan belt, represents a feeder sill to the lowermost komatiite flows, or possibly an 'invasive sill' (see Lesher, 2007), our age of 1881.5 ± 0.9 Ma directly dates the onset of komatiite volcanism.

Large, hot komatiite flow events will necessarily channelize, while flowing over a substrate of slightly older flows and/or sulphidic footwall sediments of the Nuvilik Formation (e.g. Lesher et al., 1984; Williams et al., 1998). Channelization and the consequent eroding into, and contamination with, sulphidic sediments is much less predictable for sill systems, hence the strong concentration (>90%) of ore endowment within the most Mg-rich komatiite flows along the base of the Chukotat Group. The evidence for thermal erosion, hornfelsing of the footwall, and the similarity of mafic – ultramafic sills below and above the Raglan Horizon, link the basal Chukotat lavas, and thus the whole group, stratigraphically to the underlying Nuvilik Formation. The key Povungnituk to Chukotat Group contact is thus a stratigraphic contact, not a regional thrust.

Sulphide-bearing mudstones of the uppermost Nuvilik Formation, the easily fusible stratigraphic substrate and ambient seafloor over which the Chukotat komatiite flows were emplaced, acted as a proximal sulphide source for the Raglan Ni-Cu-PGE sulphide ore bodies, as has long been surmised empirically, and from S isotopic data (Lesher, 2007). The numerous mafic – ultramafic differentiated sills, now dated to the same event, and spatially correlated with the komatiite flows on a regional scale, must be part of the feeder system. Dynamic parts of this feeder system could host economic mineralization, but the base of the lava pile is more prospective and predictable.

Most of the U-Pb data on units associated with the Raglan horizon (summarized in Figure 4) from the northern Labrador Trough to the western Cape Smith Belt, suggest a short-lived, LIP-scale magmatic event at about 1882 to 1883 Ma (see also Ernst and Bleeker, 2010). As far as can currently be resolved, this age is identical to that of komatiitic magmatism along the western margin of the Superior craton (Thompson, Manitoba: Bleeker, 1990 a, b, c; Scoates et al., 2017), and to the age of large intra-cratonic dykes that intruded the craton (Molson swarm: Heaman et al., 1986, 2009; Pickle-Crow dyke: Bleeker and Kamo, work in progress). The overall scale and volume of this magmatic event, its short-lived nature of ca. 1 to 2 Ma, and the involvement of initial high temperature magmas, compares well to modern LIP events.

Consequently, we interpret the overall geodynamic setting in terms of a hot mantle upwelling, possibly a deep-seated mantle plume, that impinged on the base of Superior craton's subcontinental lithosphere (Fig. 5). The initial ascent of this mantle upwelling may have been somewhat slower (tens of millions of years; see Davies, 1999: Fig. 5a), but accelerated in the uppermost mantle with overall lower viscosities. A flattening, buoyant plume head then rapidly spread (ca. 1–2 Ma) underneath thick cratonic lithosphere (Fig. 5b), flowing to 'thin spots' where high volume decompression melting led to the large-scale emplacement of mafic and ultramafic magmas, and ultimately ore formation. This overall model (see Sleep (1997) and Griffin et al. (2013) for more background) most easily explains the rich phenomenology at the scale of the Superior craton, in particular the nearly contemporaneous emplacement of mafic – ultramafic magmatic rocks along the entire length of the Circum-Superior Belt (Baragar and Scoates, 1981). The model also makes many predictions, a few of which are highlighted below:

- Alkaline complexes, possibly including early kimberlite clusters, were likely one of the first manifestations of the impingement of a hot mantle upwelling underneath Superi-

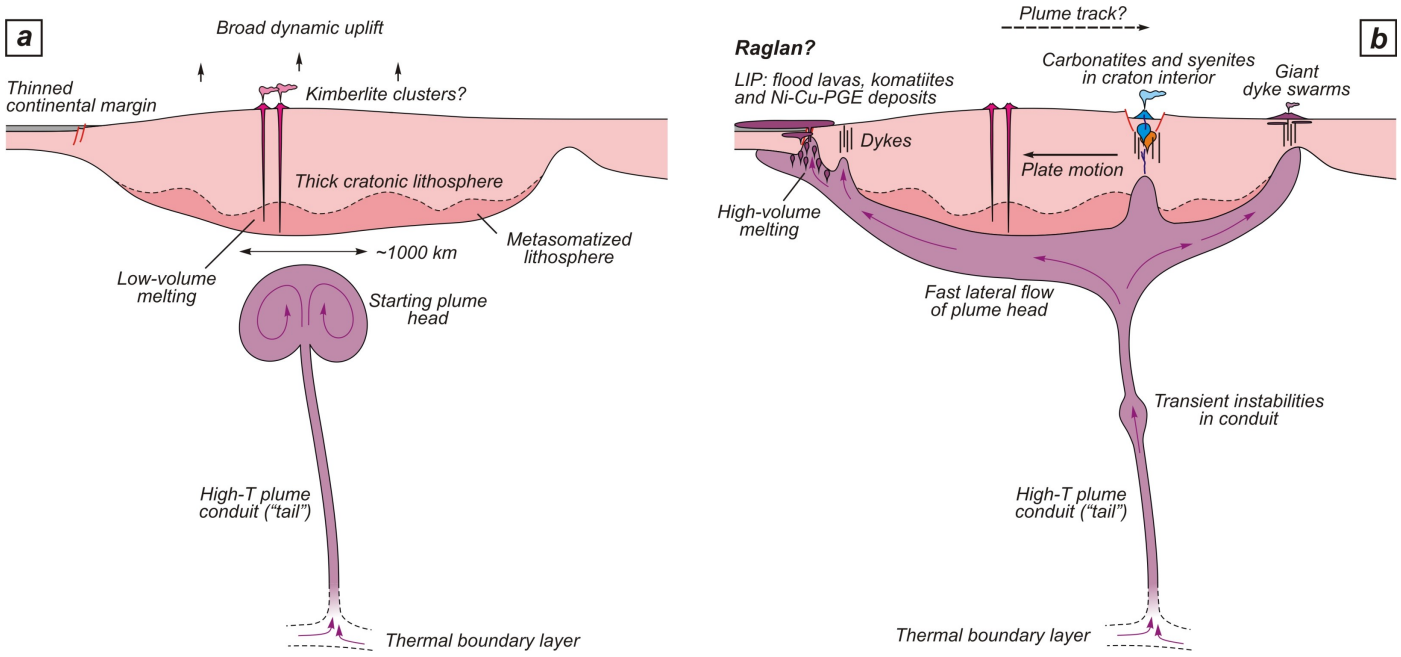

Figure 5. Interpreted geodynamic setting of the Raglan magmatic event and the broader Circum-Superior Belt magmatism. a) Initial slow rise of a hot mantle upwelling, possibly a mantle plume from a deep thermal boundary layer, below ancient continental lithosphere of the Superior craton, likely still part of a larger Superia plate at the time. Initial manifestations of the arrival of the hot upwelling or plume were broad uplift, possibly localized rifting, and low-volume melting of metasomatized lithosphere. b) Flattening and rapid spreading of the hot, buoyant, plume head below the subcontinental lithosphere and lateral flow to thin spots, where large-volume decompression melting led to LIP-scale volumes of ultramafic and mafic magmatic rocks. Elsewhere, carbonatite complexes intruded into local rift structures in the craton interior, and giant dyke swarms intruded into fracture patterns in the crust. Events can be essentially contemporaneous on the craton scale, over a ca. 1 to 2 Ma interval. Transient instabilities in the plume conduit may have led to new arrivals of hot ultramafic magmas in younger pulses (e.g. Waterton et al., 2017). Overall setting is suggestive of a continental breakup setting rather than a back-arc tectonic environment.

or craton subcontinental lithosphere (Fig. 5a). Indeed kimberlitic rocks of this age are known from the Castignon area (Chevé and Machado, 1988).

- Precise ages of such alkaline complexes (e.g. David et al., 2006; Rukhlov and Bell, 2010), at the scale of the craton, may provide information on the earliest interaction, and may potentially outline a plume track across the Superior craton as the Superior plate (i.e. supercraton Superia: see Bleeker, 2003; 2004) migrated over the mantle upwelling. This could be a rich avenue of further investigation.
- The overall geodynamic setting as portrayed in Figure 5 is more suggestive of a continental breakup setting than one of subduction-driven back-arc magmatism and associated upper mantle flow. Attempts to explain the ca. 1882 to 1883 Ma Circum-Superior Belt events in the latter context (i.e. back-arc) may be misguided (cf. Corrigan et al., 2007, 2009). Not only are there no arcs built on the circum-Superior margins, but arcs in general cannot explain the remarkable synchronicity of mafic – ultramafic magmas around the Superior.

Next Steps

To complete our reinterpretation of the Cape Smith and Raglan stratigraphy, we are investigating the detrital zircon populations of intercalated sedimentary units, specifically the Nuvilik Formation at the top of the Povungnituk Group, and the likely synorogenic conglomerates and sandstones captured within the Chukotat Group (Fig. 2b: see discussion in Bleeker and Ames, 2017). Other units that shed light on the overall structural/stratigraphic history will also be dated, for instance the leucogranite sheets at the contact of the Kovik antiform (Fig. 1a). From there we will extend our investigations and high-precision dating to other segments of the Circum-Superior Belt.

A relatively straightforward interpretation of the structure at Raglan (see Fig. 1b) will allow a more in-depth correlation between the main Raglan belt (e.g. Katinniq: horizon 1 in Fig. 1b), and the structurally repeated horizon in the North Belt (horizon 2 in Fig. 1b) and their relative prospectivities. If the paleoflow direction of the komatiite channels can be estab-

lished (e.g. Green and Dupras, 1999; see discussion in Lesher, 2007), for example, down-plunge to the northeast, the North Belt would represent a more distal position in the overall komatiitic flow field.

Acknowledgments

This report is a contribution to NRCan's Targeted Geoscience Initiative Program (TGI). Support for this study was provided through the Ni-Cu-PGE Systems Project's 'Activity NC-1.1: Extent, origin, and deposit-scale controls of the 1883 Ma Circum-Superior large igneous province, northern Manitoba, Ontario, Québec, Nunavut, and Labrador'.

The authors thank Glencore plc for their on-going logistical support for this project, without which we would not have been able to obtain some of the critical samples. Individual staff members at Raglan are sincerely thanked for their input, help with drill core sampling, and numerous discussions. Natasha Wodicka and Julie Peressini, both at GSC Ottawa, are thanked for their help and discussions on previously dated samples, and Mike Lesher, Laurentian University, for broad-ranging discussions on Raglan geology and the history of past research. This report benefited from the review of Neil Rogers.

References

Baragar, W.R.A. and Scoates, R.F.J., 1981. The circum-Superior belt: A Proterozoic plate margin?; *in* Developments in Precambrian Geology, v. 4, (ed.) A. Kröner; Elsevier, Amsterdam, p. 297–330.

Bleeker, W., 1990a. Evolution of the Thompson Nickel Belt and its nickel deposits, Manitoba, Canada; Ph.D. thesis, University of New Brunswick, Fredericton, New Brunswick, 400 p.

Bleeker, W., 1990b. New structural-metamorphic constraints on Early Proterozoic oblique collision along the Thompson Nickel Belt, Manitoba, Canada; *in* The Early Proterozoic Trans-Hudson Orogen of North America, (ed.) J.F. Lewry and M.R. Stauffer; Geological Association of Canada Special Paper 37, p. 57–73.

Bleeker, W., 1990c. Thompson Area — General geology and ore deposits; Geology and Mineral Deposits of the Flin Flon and Thompson Belts, Manitoba (Field Trip 10), Field Trip Guidebook 8th IAGOD Symposium, p. 93–125.

Bleeker, W., 2003. The late Archean record: A puzzle in ca. 35 pieces; Lithos, v. 71, p. 99–134.

Bleeker, W., 2004. Taking the pulse of planet Earth: A proposal for a new multi-disciplinary flagship project in Canadian solid earth sciences; Geoscience Canada, v. 31, p. 179–190.

Bleeker, W., 2014. The quest for better precision and more accuracy: Revisiting upper intercept ages; Geological Association Canada Annual Meeting, Fredericton, Abstract Volume 37, p. 31–32.

Bleeker, W. and Ames, D.E., 2017. System-scale and deposit-scale controls on Ni-Cu-PGE mineralisation in cratonic areas and their margins; *in* Targeted Geoscience Initiative, 2016 Report of Activities, (ed.) N. Rogers; Geological Survey of Canada, Open File 8199, p. 47–53.

Bleeker, W. and Kamo, S.L., 2017a. New precise U-Pb geochronological data and stratigraphic interpretation for the Raglan belt, northern Quebec; GAC-MAC Annual Conference, Kingston, Ontario, Abstract Volume 40, p. 32.

Bleeker, W. and Kamo, S.L., 2017b. New U-Pb geochronology and structural - stratigraphic interpretation for the Raglan Belt, northern Quebec; Proceedings of the 14th SGA Biennial Meeting, Québec, Quebec, v. 2, p. 419–422.

Burgess, S.D. and Bowring, S.A., 2015. High-precision geochronology confirms voluminous magmatism before, during, and after Earth's most severe extinction; Science Advances, v. 1, p.e1500470.

Chevé, S.R. and Machado, N., 1988. Reinvestigation of the Castignon Lake carbonatite complex, Labrador Trough, New Quebec; Geological Association of Canada - Mineralogical Association of Canada Annual Meeting, Program with Abstracts, v. 13, p. 20.

Clark, T. and Wares, R., 2006. Lithotectonic and metallogenic synthesis of the New Québec Orogen (Labrador Trough); Ministère des Ressources Naturelles, de la Faune et des Parcs, Quebec, MM2005-01, 180 p.

Corrigan, D., Galley, A.G., and Pehrsson, S., 2007. Tectonic evolution and metallogeny of the southwestern Trans-Hudson Orogen; *in* Mineral Deposits of Canada: A Synthesis of Major Deposit-Types, District Metallogeny, the Evolution of Geological Provinces, and Exploration Methods, (ed.) W.D. Goodfellow; Geological Association of Canada, Mineral Deposits Division, Special Publication No. 5, p. 881–902.

Corrigan, D., Pehrsson, S., Wodicka, N., and de Kemp, E., 2009. The Palaeoproterozoic Trans-Hudson Orogen: A prototype of modern accretionary processes; *in* Ancient Orogens and Modern Analogues, (ed.) J.B. Murphy, J.D. Keppie, and A.J. Hynes; Geological Society, London, Special Publications, v. 327, p. 457–479.

David, J., Dion, C., Goutier, J., Roy, P., Bandyayera, D., Legault, M., and Rhéaume, P., 2006. Datations U-Pb effectuées dans la Sous-province de l'Abitibi à la suite des travaux de 2004-2005; Ministère des Ressources naturelles et de la Faune, Québec; RP 2006-04, 22 p.

Davies, G.F., 1999. Dynamic Earth: Plates, Plumes and Mantle Convection; Cambridge University Press, Cambridge, United Kingdom, 458 p.

Ernst, R. and Bleeker, W., 2010. Large igneous provinces (LIPs), giant dyke swarms, and mantle plumes: Significance for breakup events within Canada and adjacent regions from 2.5 Ga to the Present; Canadian Journal of Earth Sciences, v. 47, p. 695–739.

Findlay, J.M., Parrish, R.R., Birkett, T.C., and Watanabe, D.H.,

1995. U–Pb ages from the Nimish Formation and Montagnais glomeroporphyritic gabbro of the central New Québec Orogen, Canada; Canadian Journal of Earth Sciences, v. 32, p. 1208–1220.

Giovenazzo, D., Picard, C., and Guha, J., 1989. Tectonic setting of Ni-Cu-PGE deposits in the central part of the Cape Smith Belt; Geoscience Canada, v. 16, p. 134–136.

Green, A.H. and Dupras, N., 1999. Exploration model for komatiitic peridotite-hosted Ni-Cu-(PGE) mineralization in the Raglan Belt; *in* Komatiitic Peridotite-Hosted Fe-Ni-Cu-(PGE) Sulphide Deposits in the Raglan Area, Cape Smith Belt, New Québec, (ed.) C.M. Lesher, C.M.; Laurentian University, Mineral Exploration Research Centre, Guidebook Series, v. 2, p. 191–199.

Griffin, W.L., Begg, G.C., and O'Reilly, S.Y., 2013. Continental-root control on the genesis of magmatic ore deposits; Nature Geoscience, v. 6, p. 905–910.

Hardy, R., 1976. Région des lacs Roberts, des Chefs (Roberts, des Chefs Lakes area); Ministère des richesses naturelles, Direction générale des mines, Service de l'exploration géologique, Rapport géologique 171, 99 p., 2 maps, scale 1: 63 360.

Heaman, L.M., Machado, N., Krogh, T.E., and Weber, W., 1986. Precise U-Pb zircon ages for the Molson dyke swarm and the Fox River sill: Constraints for Early Proterozoic crustal evolution in northeastern Manitoba, Canada; Contributions to Mineralogy and Petrology, v. 94, p. 82–89.

Heaman, L.M., Peck D., and Toope, K., 2009. Timing and geochemistry of 1.88 Ga Molson Igneous Events, Manitoba: Insights into the formation of a craton-scale magmatic and metallogenic province; Precambrian Research, v. 172, p. 143–162.

Henrique-Pinto, R., Guilmette, C., Bilodeau, C., and McNicoll, V., 2017. Evidence for transition from a continental forearc to a collisional pro-foreland basin in the eastern Trans-Hudson Orogen: Detrital zircon provenance analysis in the Labrador Trough, Canada; Precambrian Research, v. 296, p. 181–194.

Hoffman, P.F., 1985. Is the Cape Smith belt (northern Quebec) a klippe?; Canadian Journal of Earth Sciences, v. 22, p. 1361–1369.

Kamo, S.L., Czamanske, G.K., Amelin, Y., Fedorenko, V.A., Davis, D.W., and Trofimov, V.R., 2003. Rapid eruption of Siberian flood-volcanic rocks and evidence for coincidence with the Permian–Triassic boundary and mass extinction at 251 Ma; Earth and Planetary Science Letters, v. 214, p.75–91.

Lesher, C.M., Arndt, N.T., and Groves, D.I., 1984. Genesis of komatiite-associated nickel sulphide deposits at Kambalda, Western Australia: A distal volcanic model; *in* Sulphide Deposits in Mafic and Ultramafic Rocks, (ed.) D.L. Buchanan and M.J. Jones; Institute of Mining and Metallurgy, London, p. 70–80.

Lesher, C.M., 2007. Ni-Cu-(PGE) deposits in the Raglan area, Cape Smith Belt, New Québec; *in* Mineral Deposits of Canada: A Synthesis of Major Deposit-Types, District Metallogeny, the Evolution of Geological Provinces, and Exploration Methods, (ed.) W.D. Goodfellow; Special Publication No. 5, Mineral Deposits Division, Geological Association of Canada, p. 351–386.

Lucas, S.B. and St-Onge, M.R., 1992. Terrane accretion in the internal zone of the Ungava orogen, northern Quebec. Part 2: Structural and metamorphic history; Canadian Journal of Earth Sciences, v. 29, p. 765–782.

Madore, L. and Larbi, Y., 2001. Geology of the Riviere Arnaud area (25D) and adjacent coastal areas (25C, 25E and 25F); Géologie Quebec, Report RG 2001-06, 33 p.

Mungall, J.E., 2007. Crustal contamination of picritic magmas during transport through dikes: The Expo intrusive suite, Cape Smith Fold Belt, New Quebec; Journal of Petrology, v. 48, p. 1021–1039.

Parrish, R.R., 1989. U-Pb geochronology of the Cape Smith Belt and Sugluk block, northern Quebec; Geoscience Canada, v. 16, p. 126–130.

Randall, W., 2005. U-Pb geochronology of the Expo Intrusive Suite, Cape Smith Belt, and the Kyak Bay intrusion, New Quebec Orogen: Implications for the tectonic evolution of the northeastern Trans-Hudson Orogen; M.Sc. thesis, University of Toronto, Toronto, Ontario.

Rohon, M.L., Vialette, Y., Clark, T., Roger, G., Ohnenstetter, D., and Vidal, P., 1993. Aphebian mafic–ultramafic magmatism in the Labrador Trough (New Quebec): Its age and the nature of its mantle source; Canadian Journal of Earth Sciences, v. 30, p. 1582–1593.

Rukhlov, A.S. and Bell, K., 2010. Geochronology of carbonatites from the Canadian and Baltic Shields, and the Canadian Cordillera: Clues to mantle evolution; Mineralogy and Petrology, v. 98, p. 11–54.

Scoates, J.S., Scoates, R.J., Wall, C.J., Friedman, R.M., and Couëslan, C.G., 2017. Direct dating of ultramafic sills and mafic intrusions associated with Ni-sulphide mineralization in the Thompson Nickel Belt, Manitoba, Canada; Economic Geology, v. 112, p. 675–692.

Sleep, N.H., 1997. Lateral flow and ponding of starting plume material; Journal of Geophysical Research: Solid Earth, v. 102, p. 10 001–10 012.

St-Onge, M.R., Lucas, S.B., and Parrish, R.R., 1992. Terrane accretion in the internal zone of the Ungava orogen, northern Quebec. 1: Tectonostratigraphic assemblages and their tectonic implications; Canadian Journal of Earth Sciences, v. 29, p. 746–764.

St-Onge, M.R. and Lucas, S.B., 1993. Geology of the Eastern Cape Smith Belt: Parts of the Kangiqsujuaq, Cratere du nouveau-Quebec, and Lacs Nuvilik map areas, Quebec; Geological Survey of Canada, Memoir 438, 110 p.

St-Onge, M.R., Henderson, I., and Baragar, W.R.A., 2006. Geology, Cape Smith Belt and adjacent domains, Ungava Peninsula, Quebec-Nunavut; Geological Survey of Canada,

Open File 4930, 2 sheets, 1 CD-ROM.

Svensen, H., Corfu, F., Polteau, S., Hammer, Ø., and Planke, S., 2012. Rapid magma emplacement in the Karoo large igneous province; Earth and Planetary Science Letters, v. 325, p. 1–9.

Wardle, R.J., Ryan, B., Nunn, G.A.G., and Mengel, F.C., 1990. Labrador segment of the Trans-Hudson Orogen: Crustal development through oblique convergence and collision; *in* The Early Proterozoic Trans-Hudson Orogen of North America, (ed.) J.F. Lewry and M.R. Stauffer; Geological Association of Canada, Special Paper 37, p. 353–369.

Waterton, P., Pearson, D.G., Kjarsgaard, B., Hulbert, L., Locock, A., Parman, S., and Davis, B., 2017. Age, origin, and thermal evolution of the ultra-fresh ~1.9 Ga Winnipegosis Komatiites, Manitoba, Canada; Lithos, v. 268, p. 114–130.

Williams, D.A., Kerr, R.C., and Lesher, C.M., 1998. Emplacement and erosion by Archean komatiite lava flows: Revisited; Journal of Geophysical Research, v. 103, p. 27 533–27 549.

Wodicka, N., Madore, L., Larbi, Y., and Vicker, P., 2002. Geochronologie U-Pb de filons-couches mafiques de la Ceinture de Cape Smith et de la Fosse du Labrador; *in* L'exploration minerale au Quebec: notre savoir, vos découvertes, Seminaire d'information sur la recherche géologique, Programme et résumes 2002, Ministère des Ressources Naturelles, Quebec DV 2002-10, p. 48.

Controls on the localization and timing of mineralized intrusions in intra-continental rift systems, with a specific focus on the ca. 1.1 Ga Mid-continent Rift system

W. Bleeker[1], D.A. Liikane[2], J. Smith[1], M. Hamilton[3], S.L. Kamo[3], R. Cundari[4], M. Easton[5] and P. Hollings[6]

[1]*Geological Survey of Canada, 601 Booth Street, Ottawa, Ontario K1A 0E8*

[2]*Department of Earth Sciences, University of Toronto, Toronto, Ontario M5S 1A1*

[3]*Jack Satterly Geochronology Laboratory, University of Toronto, 22 Russell Street, Toronto, Ontario M5S 3B1*

[4]*Ontario Geological Survey, 435 James Street South, Thunder Bay, Ontario P7E 6S7*

[5]*Ontario Geological Survey, 933 Ramsey Lake Road, Sudbury, Ontario P3E 6B5*

[6]*Department of Geology, Lakehead University, 955 Oliver Road, Thunder Bay, Ontario P7B 5E1*

Abstract

A brief report is presented on the early stages of our study of the ca. 1.1 Ga Mid-continent Rift system, which hosts a diverse range of intrusions, many of which are mineralized and are being actively explored. Key questions to be addressed by this study are the localization of the mineralized intrusions, and whether we can resolve, through additional and more precise U-Pb geochronology, clear temporal, spatial, and tectonic patterns that link the various intrusions to the overall evolution of the rift system, and to specific stages of the flood basalt sequence. An initial compilation is presented of all known intrusions and their associated questions.

Introduction

North America's Mid-continent Rift (MCR) is one of the largest and best-preserved intra-continental rift systems of late Mesoproterozoic age (Wold and Hinze, 1982; Green, 1983; Van Schmus and Hinze, 1985; Hutchinson et al., 1990; Miller and Nicholson, 2013). This ca. 1.1 Ga failed rift (Fig. 1) hosts the second largest known layered intrusion, the Duluth Complex (e.g. Paces and Miller, 1993), with extensive low-grade Ni -Cu-Co-PGE resources, and possibly reef-type PGE mineralization (Hauck et al., 1997; Miller, 1998). The rift system also hosts a number of smaller, localized, conduit-type mafic – ultramafic intrusions ('chonoliths') that are mineralized with higher grade nickel-copper sulphides (e.g. Tamarack), one of which is being mined (Eagle: Ding et al., 2010, 2012; Ripley, 2014). These intrusions remain attractive but challenging targets for mineral exploration (Fig. 1; Table 1).

The broader rift system and its cratonic hinterland also host a wide variety of other mafic – ultramafic, carbonatitic, and alkaline intrusions (e.g. Weiblen, 1982; Sage, 1991; Wu et al., 2017), many of which have been or are being explored for a range of other commodities, from diamonds (Kyle Lake kimberlites) to rare metals (Nb: Nemegosenda) and copper and platinum group elements (e.g. Coldwell Complex: Good and Crockett, 1994; Ames et al., 2017). The overall age range of this compositionally diverse, intra-cratonic magmatic activity appears to span nearly 100 Ma, from ca. 1170 to 1070 Ma (Davis and Sutcliffe, 1985; Davis and Paces, 1990; Paces and Miller, 1993; Davis and Green, 1997; Heaman and Machado, 1992; Heaman et al., 2004, 2007; Fairchild et al., 2017; McCormick et al., 2017; Wu et al., 2017), with the early phases of magmatic activity generally seen as precursor events to the ca. 1115 to 1085 Ma main phase of the MCR (see Miller and Nicholson (2013) for a discussion of the evolutionary phases of the MCR).

The scope of this complex rift system could potentially reach as far away as northern Saskatchewan where diabase intrusions in the Athabasca sandstone basin are coeval to some of the key pulses of magmatic activity (ca. 1160 and 1108 Ma: French et al., 2002; Bleeker and Chamberlain, 2015). It remains to be determined whether these are separate events or the distant manifestations of the same overall tectono-magmatic system? Similarly, the southwestern arm of the MCR, extending far into the mid-continent, may be connected with the essentially contemporaneous Southwest USA Diabase Province (Hammond, 1990; Bright et al., 2014).

Finally, a significant number of discrete, regional to giant-scale mafic dyke swarms are associated with both the precursor and main phase of the MCR (Fig. 1; Green et al., 1987), with some of these dyke swarms having acted as the feeder systems to particular intrusions and specific units of the volcanic succession. However, in many cases a direct relationship between individual dykes and specific intrusions remains undocument-

Corresponding author: Wouter Bleeker (wouter.bleeker@canada.ca)

Bleeker, W., Liikane, D.A., Smith, J., Hamilton, M., Kamo, S.L., Cundari, R., Easton, M., and Hollings, P., 2018. Controls on the localization and timing of mineralized intrusions in intra-continental rift systems, with a specific focus on the ca. 1.1 Ga Mid-continent Rift system; *in* Targeted Geoscience Initiative: 2017 report of activities, volume 2, (ed.) N. Rogers; Geological Survey of Canada, Open File 8373, p. 15–27. https://doi.org/10.4095/306594

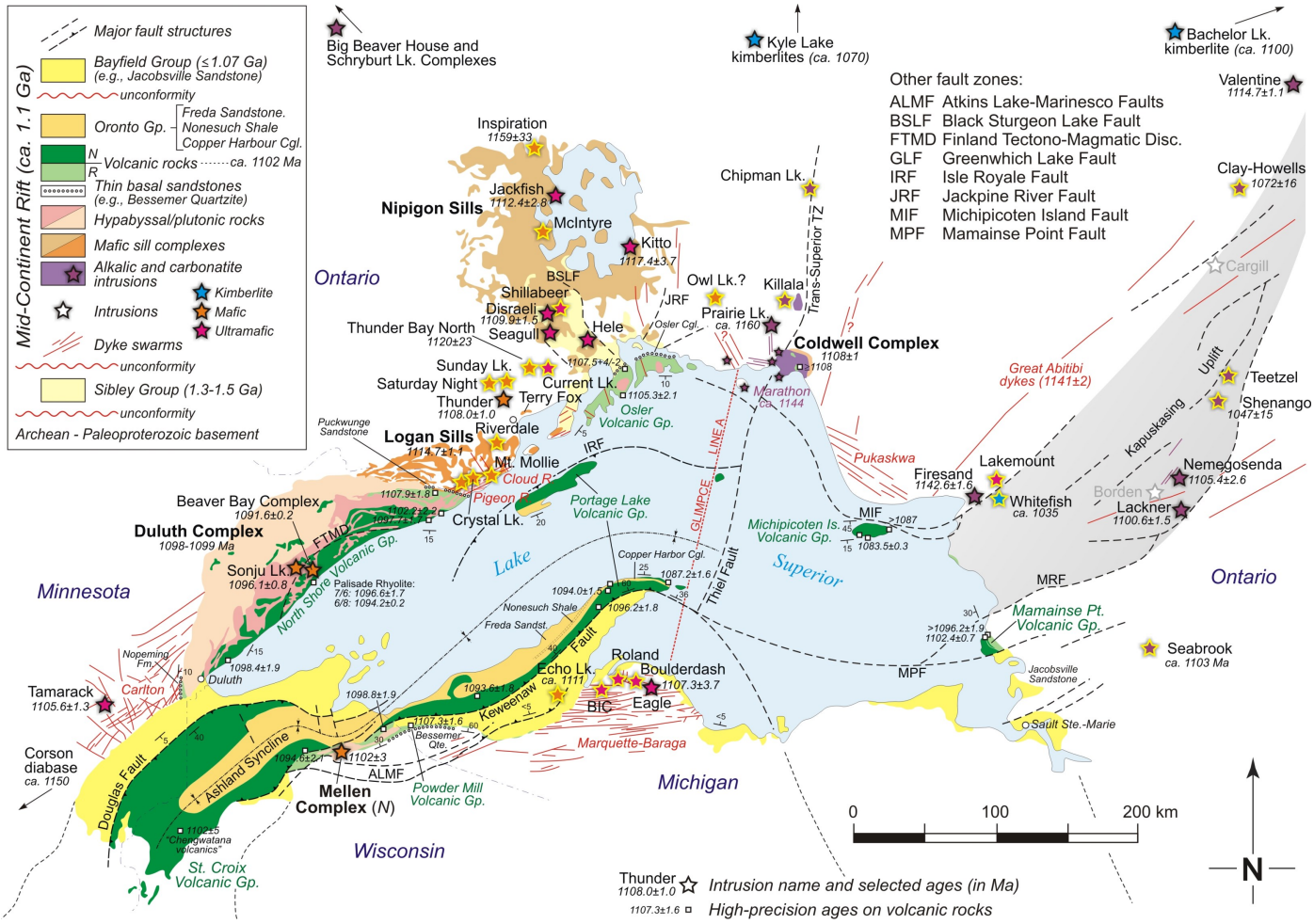

Figure 1. Summary map of the Mid-continent Rift, modified after Miller and Nicholson (2013) and references therein, highlighting all of the rift-related intrusions. Undated or inadequately dated intrusions, and (or) ages that are otherwise problematic, are shown by stars with yellow outline. Only a selection of ages are specifically shown, with the reader referred to Table 1 for additional age data and references. High-precision U-Pb ages on volcanic rocks are shown for reference (Davis and Sutcliffe, 1985; Davis and Paces, 1990; Davis and Green, 1997; Zartman et al., 1997; Schoene et al., 2006; Swanson-Hysell et al., 2014; Fairchild et al., 2017). The following intrusions were sampled during 2017 fieldwork: oldest marginal gabbro phase of the eastern Coldwell Complex; Sunday Lake and Saturday Night; the Inspiration and Riverdale sills, and various feeder dyke systems that are either undated or have problematic ages. We plan to tackle the different lobes of the Tamarack intrusion in the near future, as well as the Current Lake intrusion, and Crystal Lake intrusion and its potential feeder dyke.

ed. Precise ages on dyke swarms can thus test links to intrusions of interest and provide important insights into evolving stress patterns during rifting, as dykes propagate along the maximum principal stress direction (σ1) and open up against the minimum principal stress (σ3).

Key scientific questions and progress

The present study addresses a number of key scientific questions relevant to exploration: i) what localized the mineralized intrusions and was their ascent guided by deep-reaching fault structures?; ii) can we resolve any clear temporal, spatial, and tectonic patterns?; and iii) can specific styles of mineralization be related to specific primitive melt compositions and mantle source regions? In other words, how do the various intrusions relate in time and space to the overall evolution of the rift system, its various magmatic pulses and potentially distinct mantle sources? At the craton scale, can the long history of precursor events (ca. 50 Ma) be reconciled with a single mantle plume event, or mantle upwelling, requiring a long phase of 'plume incubation' (Kent et al., 1992; Saunders et al., 1992), or is a more complex model required, such as a mantle plume or upwelling impinging on an already rifted craton at ca. 1108 to 1109 Ma, at the time of onset of voluminous primitive tholeiitic volcanism (Davis and Green, 1997). See Hutchinson et al.

Table 1: Summary data on the different intrusions.

#	Intrusive Unit	Age (Ma)	Type of Age	Key References	Main Rock Types	Comments and Questions
MCR-related dyke swarms:						
1	Great Abitibi dykes	1141 ± 2	U-Pb, bd, wm7/6 age	Krogh et al., 1987	Olivine diabase, gabbro, monzodiorite	Giant swarm, only one dyke dated
	Ultramfic lamprophyres:					
2	Ultramafic "Marathon dykes" (e.g., McKellar Harbour dyke)	ca. 1144 1145 +15/-10	K-Ar U-Pb, prv	Platt and Mitchell., 1979, 1982; Platt et al., 1983 Queen et al., 1996	Ultramafic lamprophyre	Kimzeyite garnet in some dykes Age uncertainty allows link to Prairie Lake Complex
3	Lamprophyre dykes, Kapuskasing Uplift	ca. 1144	Ar-Ar	Queen et al., 1996	Ultramafic lamprophyre	Also age overlap with Abitibi dykes
	Various mafic dyke sets:					
4	NNE-trending dykes east of Coldwell	undated		OGS 1991a, Map 2543		Distinct from Marathon dykes?
5	NNW-trending dykes west of Coldwell	undated		OGS 1991a, Map 2543; this study	Diabase	Observed in road outcrops; reversely magnetized
6	Pukaskwa dykes (~315°)	undated		OGS 1991a, Map 2543; Weiblen, 1982; Green et al., 1987	Diabase	Could be confused with parallel Matachewans
7	NW- to N-trending dykes, Nipigon area	undated		OGS 1991b, Map 2542; this study	Diabase	Some have been shown to be Marathon swarm dykes
	Pigeon River swarm and parallel dykes:					
8	Pigeon River dyke (~070°), Crooks Twp.	1141 ± 20	U-Pb, zr and bd, disc.	Heaman et al., 2007	Diabase, gabbro	Higly discordant data, age interpretation likely too old
9	Arrow River dyke (~080°), Devon Twp.	1078 ± 3	U-Pb, bd, reverse disc., n=1	Heaman et al., 2007	Diabase	Arrow River, Devon Township
10	Mount Mollie dyke (080-090°)	1109.3 ± 6.3	U-Pb, bd, wm7/6 age, n=2	Hollings et al., 2010; Smyk and Hollings, 2009	Diabase, gabbro to leucogabbro, granophyre	Uncertainty on sample location; age contradicts feeder dyke hypothesis to Crystal Lake Intrusion
	NW-trending dykes:					
11	Cloud River dykes (~330°)	1109.2 ± 4.2	U-Pb, bd, wm6/8 age, n=2	Hollings et al., 2010; Cundari, 2012	Diabase	NW-trending Cloud R. dykes cut ENE-trending Pigeon R. dykes
	Other dyke swarms:					
12	Carlton dykes (~030°, multiple trends)	undated		Weiblen, 1982; Green et al., 1987; Miller and Nicholson, 2013	Diabase	Multiple trends, i.e. more than one swarm
13	Marquette-Baraga dykes (080°)	undated		Weiblen, 1982; Green et al., 1987; Miller and Nicholson, 2013	Diabase	Multiple trends, i.e. more than one swarm
14	Woodland dyke, Minnesota (~060°)	undated	Ar-Ar dating in progress	T. Boerboom, pers. comm., 2016	Lamprophyre	Large, approximately 8 m wide lamprophyre dyke, reversely magnetized
Various sills and sill complexes:						
	"Nipigon Sills", Nipigon area:					
15	Nipigon Sills	1109 +4/-2	U-Pb, zr (and bd)	Davis and Sutcliffe, 1985; see also Krogh et al., 1987	Diabase, pegmatitic gabbro, granophyre	These were referred to as "Logan Sills" by Davis and Sutcliffe, 1985
16	Havoc Lake diabase (HAV02-02)	1110.1 ± 2.5	U-Pb, bd, wm7/6, n=4	Heaman et al., 2007	Diabase	
17	Muskrat Lake diabase (ML01-01)	1112.7 ± 2.4	U-Pb, bd, wm7/6, n=2	Heaman et al., 2007	Diabase	
18	Grand Bay diabase (GB01-01)	1114.4 ± 8.3	U-Pb, bd, disc., scattered data	Heaman et al., 2007	Diabase	
19	North Bay diabase (LN08)	1110.1 ± 2.1	U-Pb, bd, wm7/6, n=2	Heaman et al., 2007	Diabase	
20	Gull River troctolite (GR01-01)	1111 ± 15	U-Pb, bd, wm7/6, n=2	Heaman et al., 2007	Troctolite	
21	South Bay diabase (LN139)	1106.8 ± 1.9	U-Pb, zr, reversly disc., wm7/6, n=2	Heaman et al., 2007	Diabase	
22	Kama Hill, upper sill (KH10)	1008 ± 29	U-Pb, zr, highly disc., n=2	Heaman et al., 2007	Diabase	Upper intercept through highly disc. zircon data
23	Inspiration (04RME-3210)	1059 ± 33	U-Pb, bd, disc., n=2, u. intercept	Heaman et al., 2007	Diabase, gabbro	Upper intercept from 2 disc. baddeleyite fractions, likely too old
24	McIntyre	1100.8 ± 4.4	U-Pb, bd, 7/6 age, n=1	Heaman et al., 2007	Diabase	More likely to be ca. 1110 Ma based on 6/8 age
	"Logan Sills", Thunder Bay area:					
25	Logan Sills	1114.7 ± 1.1	U-Pb, bd, 3.5-4.1% disc, wm7/6	Heaman et al., 2007	Diabase	Clustered discordant data, age interpretation likely too old
26	Terry Fox sill	undated			Diabase, plagioclase-phyric near roof contact	Interesting upper porphyry, with abundant xenoliths, melted roof rocks?
27	Riverdale	undated		Hollings et al., 2010; P. Hollings, pers. comm., 2017	Diabase, compositionally distinct	

Table 1: Cont.

#	Intrusive Unit	Age (Ma)	Type of Age	Key References	Main Rock Types	Comments and Questions
	Intrusions in northern Minnesota, likely related to Logan Sills:					
28	Nathan's Layered Series	1106.9 ± 0.6	U-Pb, zr, wm7/6, n=5	Paces and Miller, 1993, Weiblen et al., 1972	Olivine gabbro	Reversely magnetized, age suggest link with Logan Sills
29	Swamper Lake monzogabbro	1107.0 ± 1.1	U-Pb, zr, wm7/6, n=3	Davis and Green, 1997	Monzogabbro	Reversely magnetized, age suggest link with Logan Sills
30	Cucumber Lake granophyre	1106.8 ± 2.8	U-Pb, zr, u. intercept	Vervoort and Wirth, 2004; Vervoort et al., 2007	Granophyre	Reversely magnetized
31	Misquah Hills granophyre	1106.0 ± 4.8	U-Pb, zr, u. intercept	Vervoort and Wirth, 2004; Vervoort et al., 2007	Granophyre	
32	Whitefish Lake granophyre	1109.4 ± 5.1	U-Pb, zr, u. intercept	Vervoort and Wirth, 2004; Vervoort et al., 2007	Granophyre	
33	Mount Weber granophyre	1106.2 ± 3.6	U-Pb, zr, u. intercept	Vervoort and Wirth, 2004; Vervoort et al., 2007	Granophyre	
34	Greenwood Lake granophyre	1106 ± 3	U-Pb, zr, u. intercept	Vervoort and Wirth, 2004	Granophyre	
	Ultramafic intrusions:					
35	Kitto	1117.5 ± 3.7	U-Pb, bd, wm7/6, n=2	Heaman et al., 2007; Sutcliffe, 1986; Hart et al., 2002; Larmaan, 2007	Peridotite, olivine websterite and pyroxenite	Interstitial sulphides along basal contact and in websterite
36	Kitto diabase	1110.8 ± 4.3	U-Pb, bd, disc., u. intercept	Heaman et al., 2007	Diabase thought to intrude Kitto ultramafic body	
37	Seagull	1112.8 ± 1.4	U-Pb, bd, complex results	Heaman et al., 2007; Heggie, 2005; Hart and Macdonald, 2007	Dunite, peridotite to gabbro	Disseminated sulphides along basal contact, and reef-type PGE horizons
38	Jackfish	1112.4 ± 2.8	U-Pb, bd, wm6/8 age, n=2	Heaman et al., 2007; Hollings et al., 2007	Melagabbro to peridotite core surrounded by olivine gabbro	
39	Disraeli	1109.9 ± 1.4	U-Pb, bd, wm7/6, n=2	Heaman et al., 2007; Hart and Magyarosi, 2004; Hart and Macdonald, 2007	Peridotite to wehrlite core, with olivine gabbro marginal zone	Good baddeleyite age
40	Hele	1106.6 ± 1.5	U-Pb, bd, wm7/6, n=2	Heaman et al., 2007; Hollings et al., 2007	Peridotite and wehrlite, interlayered with olivine gabbro	Minor sulphides in peridotite
41	Shillabeer	undated		Hollings et al., 2007	Ultramafic rocks	
	Thunder Bay North Complex:					
42	Current Lake	1120 ± 23	U-Pb (unpubl.), no details	Smyk and Hollings, 2009; Chaffee, 2015	Feldspathic dunite to olivine melagabbro	Disseminated sulphides in peridotite, net-textured to massive sulphide in conduit
43	Steepledge Lake	undated		Thomas et al., 2011; D'Angelo, 2013	Peridotite to olivine gabbro	Basal peridotite hosts disseminated sulphides
44	Lone Island Lake	undated				
	Other intrusions:					
45	Thunder	1108.0 ± 1.0	U-Pb, zr (bd), CA-ID-TIMS, conc.	Trevisan, 2014; Trevisan et al., 2015	Feldspathic peridotite, melagabbro, and upper massive gabbro	Disseminated sulphides in basal ultramafic rocks
46	Sunday Lake	undated		Flank, 2017	Peridotite to monzogabbro (diorite)	Disseminated sulphides in basal ultramafic rocks
47	Saturday Night	undated			Peridotite to monzogabbro (diorite)	Disseminated sulphides in basal ultramafic rocks
48	Crystal Lake Intrusion	1099.6 ± 1.2	U-Pb, bd, wm7/6, n=2	Heaman et al., 2007; Cogulu, 1993a,b	Vari-textured gabbro, troctolite, chromite layers	Some controversy on what part of the complex was dated
49	Blake Gabbro	1091.0 ± 4.5	U-Pb, bd, wm6/8, 7/5 ages, n=2	Heaman et al., 2007	Gabbro	Blake Township
50	"Rainy River intrusion"	undated		W. Bleeker, unpublished observations on core	Peridotite-gabbro, metamorphosed, mineralized	Metamorphosed, cut by Fort Frances dyke, Archean; not MCR-related
	Younger gabbro intrusions in Osler Group:					
51	Moss Lake Gabbro	1094.7 ± 3.1	U-Pb, bd, wm6/8, 7/5 ages, n=2	Heaman et al., 2007	Gabbro	Black Bay Peninsula, intrusive units emplaced in Osler Group
52	St. Ignace Island Complex Gabbro	1089.2 ± 3.2	U-Pb, zr, unpubl.	Smyk et al., 2006	Gabbro	St. Ignace Island, intrusive units emplaced in Osler Group
	Duluth Complex and related intrusions, Minnesota:					
53	Duluth Complex	1099.0 ± 0.6	U-Pb, zr, wm7/6, n=5	Paces and Miller, 1993	Gabbroic anorthosite	
54	Duluth Complex	1099.1 ± 0.5	U-Pb, zr, wm7/6, n=6	Paces and Miller, 1993	Gabbroic anorthosite	
55	Duluth Complex	1098.6 ± 0.5	U-Pb, zr, wm7/6, n=8	Paces and Miller, 1993	Olivine gabbro	
56	Duluth Complex	1099.3 ± 0.3	U-Pb, zr, wm7/6, n=6	Paces and Miller, 1993	Olivine ferrogabbro	

Table 1: Cont.

#	Intrusive Unit	Age (Ma)	Type of Age	Key References	Main Rock Types	Comments and Questions
57	Kenwood Avenue granite	1098.2 ± 1.4	U-Pb, zr, wm7/6, n=4	Davis and Green, 1997	Granite	One of the youngest phases clearly associated with the Duluth Complex
58	Pine Mountain granophyre	1095.3 ± 3.8	U-Pb, zr, u. intercept	Vervoort and Wirth, 2004; Vervoort et al., 2007	Granophyre	
59	Eagle Mountain	1098.6 ± 3.8	U-Pb, zr, u. intercept	Vervoort and Wirth, 2004; Vervoort et al., 2008	Granophyre	
60	Finland granophyre	1098.2 ± 5.5	U-Pb, zr, u. intercept	Vervoort and Wirth, 2004; Vervoort et al., 2009	Granophyre	
61	Beaver Bay Complex (BBC), Silver Bay Intr.	1095.8 ± 1.2	U-Pb, zr and bd, wm7/6, n=6	Paces and Miller, 1993	Granophyric ferrogabbro	
62	Sonju Lake Intrusion (part of BBC)	1096.1 ± 0.8	U-Pb, bd, wm7/6, n=4	Paces and Miller, 1993	Ferrodiorite	
63	Intrusive aplites in Silver Bay Intr.	1091.6 ± 0.3	U-Pb, zr, CA-TIMS, wm6/8 age	Fairchild et al., 2017	Aplite within granophyre	$^{206}Pb/^{238}U$ ages on multiple chemically abraded zircons
Mafic-ultramafic intrusions south of Lake Superior:						
64	Tamarack	1105.6 ± 1.3	U-Pb, bd, slightly disc.	Goldner, 2011; Taranovic et al., 2015, 2016	Peridotite to gabbro	Net-textured to massive sulphide; disseminated sulphides thoughout
	Mellen Intrusive Complex:	1102.8 ± 2.8	U-Pb, zr, wm7/6 age, n=2	Zartman et al., 1997	Olivine gabbro, ferrogabbro, granophyre, and late granite	Basal mineralization confined to Mineral Lake Intrusion
65	Mineral Lake Intrusion	1102.1 ± 3.5	U-Pb, zr, upper intercept	Zartman et al., 1997	Granophyre	Wisconsin
66	Mellen Complex	1101.5 ± 2.9	U-Pb, zr, upper intercept	Zartman et al., 1997	Granite	Wisconsin
67	Echo Lake	1111	U-Pb, unpubl.	Cannon and Nicholson, 2001; Koerber and Thakurta, 2017	Peridotite, troctolite, gabbro	Localised PGE horizons associated with disseminated sulphides
68	Bovine Igneous Complex (BIC)	undated		Foley, 2011; Donoghue et al., 2014	Feldspathic wehrlite overlain by melatroctolite and olivine melagabbro	Basal, disseminated to locally massive sulphides, also reef-style PGE horizons
69	Roland Lake	undated		Dunlop, 2013	Feldspathic peridotite to pyroxenite	Minor sulphide mineralization, extent yet to be determined
70	Boulderdash	undated		Dunlop, 2013	Troctolite, melatroctolite	Minor sulphide mineralization, extent yet to be determined
71	Eagle	1107.3 ± 3.7	U-Pb, bd, wm7/6 age	Ding et al., 2010, 2012; see also Ripley, 2014; Clow et al., 2017	Feldspathic peridotite sheet, underlain by melatroctolite and olivine gabbro	Relationship to Eagle East?
72	Eagle East	undated		As for Eagle, see above	Melatroctolite	High-grade massive to semi-massive sulphides concentrated above keel
Coldwell Complex and nearby intrusions:						
73	Coldwell Complex	1108 ± 1	U-Pb, zr, u. intercept	Heaman and Machado, 1992; Mitchell et al., 1983, 1993; Good et al., 2015, 2017	Gabbro, ferroaugite syenite, nepheline syenite, quartz syenite	Disseminated Cu and PGE mineralization in vari-textured Two Duck Lake gabbro; remnants of pre-intrusive basalts, preserved as hornfelsed roof pendants (xenoliths)
	Eastern marginal gabbro, Centre 1 (CL7)	1107 +2/-1	U-Pb, bd and zr, u. intercept	Heaman and Machado, 1992	Gabbro	
	Two Duck Lake gabbro, Centre 1 (86CL1)	1108 ± 1	U-Pb, bd and zr, u. intercept	Heaman and Machado, 1992	Coarse vari-textured gabbro	
	Syenite, Centre 1	ca. 1108	U-Pb, zr, some scatter	Heaman and Machado, 1992	Syenite	
	Nepheline syenite, Centre 2 (CL22)	1109 +8/-4	U-Pb, zr and ti, disc.	Heaman and Machado, 1992	Nepheline syenite	
	Granite, Centre 3	≥1102	U-Pb, zr, disc.	Heaman and Machado, 1992	Granite	Centre 3 could be as young as 1102–1103 Ma
74	Prairie Lake	ca. 1163	U-Pb, bd and zr	Wu et al., 2017; Rukhlov and Bell, 2010	Pyroxenite, ijolite, carbonatite, syenite	Early precursor alkaline magmatism; plume incubation?
75	Killala	1050 ± 35 1185	Rb-Sr K-Ar	Bell and Blenkinsop, 1980; Sage, 1988d; Currie, 1976	Syenite, nepheline syenite, olivine gabbro, larvikite	Minor Nb and Ni-Cu sulphide mineralization
76	Owl Lake	undated				
77	Chipman Lake	1022 ± 31	K-Ar	Sage, 1985	Carbonatite and lamprophyre dykes	Emplaced along the Trans-Superior Tectonic Zone
	"Marathon dykes" (see under dykes)	ca. 1144				
Ultramafic intrusions near Wawa:						
78	Firesand	1142.6 ± 1.6 1019–1098	U-Pb, kmz K-Ar	Rukhlov and Bell, 2010; Sage, 1988e, 1991 Gittins et al., 1967	Carbonatite and related alkalic rocks	
79	Lakemount (a.k.a. Sunrise)	undated			Peridotite; basal Ni-Cu mineralization	Relation to MCR uncertain

Table 1: Cont.

#	Intrusive Unit	Age (Ma)	Type of Age	Key References	Main Rock Types	Comments and Questions
Alkaline and carbonatite intrusion east of Lake Superior:						
80	Seabrook Lake	1113 ± 36	K-Ar	Gittins et al., 1967; Sage, 1988a	Carbonatite, mafic breccias, ijolite, syenite	Minor Nb mineralizaton
81	Lackner Lake	1100.6 ± 1.5	U-Pb, bd, disc., n=3, intercept	Heaman et al., 2007	Carbonatite, ijolite and associated magnetite-apatite bodies, nepheline syenite	Minor Nb mineralizaton
82	Nemegosenda	1105.4 ± 2.6	U-Pb,	Heaman et al., 2007; Sage, 1987a	Carbonatite, ijolite, nepheline syenite, syenite, gabbro	Nb mineralization
83	Shenango	1047 ± 15	Rb-Sr	Bell and Blenkinsop, 1980; Sage, 1987b	Diorite, syenodiorite, monzonite and quartz monzonite	
84	Teetzel	1155 ± 45	K-Ar	Currie, 1976; Weiblen, 1982		
85	Clay-Howells	1075 ± 15	Rb-Sr	Bell et al., 1982; Sage, 1988b	Pyroxene syenite, intruded by magnetite-rich carbonatite dykes	REE, Nb and Fe (magnetite) mineralization
86	Valentine	1114.7 ± 1.1	U-Pb, bd, u. intercept	Rukhlov and Bell, 2010; Sage, 1988c	Carbonatite	Widespread but sub-economic Nb and P mineralization
Alkaline and carbonatite intrusion in NW Ontario:						
87	Big Beaver House	1093 ± 2 1109 ± 61	U-Pb, bd, disc., n=1 K-Ar, bi	Rukhlov and Bell, 2010; Sage, 1991 Sage, 1987c	Alkaline ultramafic rocks, carbonatite	Single 1.4% discordant bd fraction
88	Schryburt Lake	1084 ± 3	U-Pb, bd, disc., n=2, intercept	Rukhlov and Bell, 2010; Sage, 1988f, 1991	Ultramafic lamprophyre, carbonatite	Weighted mean of the 2 bd analyses is 1083.0 ± 1.2 Ma
Kimberlites:						
89	Kyle Lake kimberlites	ca. 1070	U-Pb, prv, single analysis	Heaman et al., 2004	Kimberlite, diamondiferous	Northern Ontario, underneath Paleozoic cover
90	Whitefish Lake	1035 ± 13 (1097 ± 7)	Rb-Sr, phl	Kaminsky et al., 2000	Kimberlite, micaceous, diamondiferous	Northeast of Wawa, four kimberlite pipes
91	Bachelor Lake	1104 ± 17	Rb-Sr, phl	Alibert and Albarede, 1988	Kimberlite	Western Quebec, underneath glacial till
Distal events:						
92	Corson diabase	ca. 1150	U-Pb, bd	McCormick et al., 2017	Olivine diabase	Near border of South Dakota and Minnesota
93	Texaco-Poersch core, Kansas	1097.5 ± 3.0	U-Pb, zr	Van Schmus, 1992	Gabbro	Kansas
94	Moore Lake gabbro	1109 ± 2	U-Pb, bd and zr	French et al., 2002	Gabbro, diabase	Gabbro sills intruding the Athabasca Basin, Saskatchewan
95	Douglas River diabase dyke	1165 ± 17	U-Pb, bd, in situ SIMS dating	Bleeker and Chamberlain, 2015	Diabase	Diabase dykes intruding the Athabasca Basin, Saskatchewan
96	SW USA Diabase Province	1115 to 1080	U-Pb, bd, various methods	Bright et al., 2014, and references therein	Diabase and gabbro sills, layered intrusion	Possibly a distal expression of the same MCR mantle upwelling?
97	Pahrump sills	1087 ± 3	U-Pb, bd	Heaman and Grotzinger, 1992	Diabase, gabbro	Diabase sills in Parump Group, southern California
98	Umkondo LIP, Kalahari craton	1112 to 1106	U-Pb, bd and zr	Hanson et al., 2004	Diabase, gabbro	Numerous diabase dykes and sills across Southern Africa

Notes: This is a compilation in progress, and some unpublished information is currently included.

Abbreviations: bd=baddeleyite, zr=zircon, ti=titanite, bi=biotite, phl=phlogopite, prv=perovskite, kmz=kimzeyite; conc.=concordant, disc.=discodant, wm7/6=weighted mean $^{207}Pb/^{206}Pb$ date, wm6/8=weighted mean $^{206}Pb/^{238}U$ date, u. intercept=upper intercept, n=number of analyses included.

(1990), Nicholson and Shirey (1990) and Shirey (1997) for arguments in favour of a mantle plume. Furthermore, some key aspects of the rift may be permissive of a passive rift model, as discussed by Hollings and Heggie (2014).

Although the MCR rift system has a rich legacy of past and on-going research, including a number of comprehensive dating studies (see Heaman et al. (2007) for a relatively recent compilation), most of these studies were carried out prior to the introduction of routine 'chemical abrasion' methods (Mattinson, 2005) in U-Pb single zircon geochronology. This advanced pre-treatment of zircon crystals greatly reduces discordance, thus minimizing interpretation of complex discordance patterns in U-Pb results, and therefore greatly improving overall accuracy. Other improvements, such as reduced laboratory blanks and mixed double-spike solutions, along with knowledge on subtle differences in isotopic systematics between zircon and baddeleyite (both of which are common accessory minerals in gabbroic and alkaline intrusions and may also occur in thick ponded basalt flows) allow for increased precision. Notably, a number of the earlier studies on MCR rocks have shown discrepancies between zircon and baddeleyite ages (e.g. Davis and Sutcliffe, 1985; see also Krogh et al., 1987; Davis and Paces, 1990; Trevisan et al., 2015).

Through these recent improvements in U-Pb geochronology, we now have the ability to resolve million-year, or even sub-million year-scale events in the complex magmatic evolution of well-preserved rift systems such as the MCR. By resolving and untangling some of the key processes we will gain insights into how the rift evolved, its various magmatic pulses and why mineralized intrusions occur where they do.

Figure 2. Examples of sampled intrusions in the field. a) Large gabbro sill (Logan?) cut by vertical NNW-trending diabase dyke (Cloud River?), southwest of Thunder Bay. b) Coarse pegmatitic gabbro segregations of the poorly dated Inspiration Sill near Armstrong, Ontario. c) Drill core across the upper contact of the Sunday Lake Intrusion (DDH SL-15-013). Upper rows show Quetico metasediments intruded by numerous granitoid dykelets, whereas lower rows show coarse-grained monzodiorite of the upper part of the Sunday Lake intrusion. The monzodiorite was sampled for U-Pb geochronology, where coarsest, and well below the contact zone to minimize possible wall rock contamination. d) Lowermost layered gabbro series of the eastern Coldwell Complex. e) Contact of earliest gabbro phase of eastern Coldwell Complex on partially melted rheomorphic breccias of Archean volcano-sedimentary rocks in the immediate footwall of the complex. f) Coarse, evolved, vari-textured pegmatitic gabbro (Two Duck Lake Gabbro) of the eastern Coldwell Complex, rich in PGE mineralization.

An initial sample suite was collected from Tamarack in the west to the Coldwell Complex in the east. Undated intrusive bodies sampled include the Sunday Lake and Saturday Night intrusions, as well as several feeder dyke systems and poorly dated (or undated) sills to help resolve existing age complexities. Examples of some of the sampled units are shown in Figure 2.

Next steps

High-precision age determinations are in progress or planned for currently undated intrusions and to resolve a number of the imprecise and/or problematic ages. From these initial results, age and tectonic patterns will emerge that will require further testing. Additionally, the 'multiple pulses' model for some of the mineralized intrusions will be tested. An example of such a body is Tamarack, a body that consists of three distinct lobes, where models for mineralization vary from three successive pulses with progressive reworking and upgrading of Cu-Ni sulphide mineralization with each pulse, to essentially a single pulse in a dynamic and complexly shaped conduit with constrictions and blow-outs. Zircon and baddeleyite mineral separates from dated intrusions are projected for further interrogation by combined U-Pb, Lu-Hf and trace element studies to shed light on mantle sources of the mineralized intrusions.

As the framework of precise ages improves and expands, we will be better able to link the various intrusions and their feeder systems (e.g. dyke swarms), to distinct phases of the evolution of the MCR, and to temporal, spatial, and tectonic patterns. Furthermore, accurate and precise ages for the intrusive events will also allow more detailed linking of specific dyke swarms and intrusions to the rapidly improving high-resolution age framework for the volcanic pile preserved along the centre of the rift, which comprises an important complementary and well-documented record of the geochemical evolution of the magmatism.

From existing data, it is obvious that high-volume tholeiitic volcanism was only initiated at 1108 ± 1 Ma, followed by younger pulses of effusive activity such as the North Shore Volcanic Group (and intrusive Duluth Complex) at ca. 1099 to 1095 Ma (e.g. Miller and Nicholson, 2013). Some of the well-dated intrusive tholeiitic units were clearly coeval with, or within error of, the onset of this main phase of magmatism (e.g. the original 'Logan Sill' ages of Davis and Sutcliffe (1985) in the Nipigon area), whereas many other mafic – ultramafic sills appear to be older (see Heaman et al., 2007). However, close inspection of these apparently older ages shows that some are based on more complex and/or significantly discordant data sets for which alternative interpretations are possible. With additional sampling, some of these older dates may resolve themselves into distinct, indeed older pulses (e.g. the Kitto intrusion?), while others may be shown to be a result of complex baddeleyite and zircon systematics (e.g. Bleeker, 2014). The Kitto ultramafic intrusion is currently an outlier in the overall data set, with a reported concordant baddeleyite age of 1117.5 ± 3.7 Ma (Heaman et al., 2007), and thus additional dating to confirm this is a priority. Another critical test will be to obtain a precise age of the Echo Lake intrusion south of Lake Superior, a large differentiated body with aspects of an early layered intrusion (Cannon and Nicholson, 2001; Koerber and Thakurti, 2017).

With reference to the more robust pre-1109 Ma ages, an interesting question is whether those intrusive systems fed any volcanic rocks and why there is so little preservation of such older volcanics? The answer may lie in a significant, transient phase of uplift immediately prior to the 1108 to 1109 Ma onset of the main flood basalt sequence. This phase of uplift, and immediately following subsidence, is clearly manifested by the unconformities and thin basal sandstone units (e.g. Bessemer Quartzite; see Figure 1) that occur at the base of the flood basalts (e.g. Hubbard, 1975; Ojakangas and Morey, 1982). This transient uplift likely marks the arrival of hot mantle material underneath the central rift area, and maximum dynamic support, estimated to have occurred at ca. 1110 to 1112 Ma. Most of the apparently older intrusion ages are within error of a ca. 1112 Ma initiation of magmatism, which would sharpen the overall 'Initiation Stage' of the MCR and decrease the age dispersion among apparently similar mafic – ultramafic intrusions early in the rift's evolution.

Acknowledgments

This report is a contribution to NRCan's Targeted Geoscience Initiative Program (TGI). Support for this study was provided through the Ni-Cu-PGE Systems Project's 'Activity NC-1.3: Controls on the localization and timing of mineralized intrusions in intra-continental rift systems, with a specific focus on the ca. 1.1 Ga Mid-continent Rift system'.

Dustin Liikane is conducting a TGI supported Ph.D. at University of Toronto, Toronto, Ontario. Jennifer Smith is conducting TGI supported post–doctoral research at GSC Ottawa. The authors thank our partners at Rio Tinto (Dean Rossell, Brian Goldner, Justin Laberge), North American Palladium (Dave Peck, Steve Flank), Transition Metals (Grant Moore, Scott McLean), Panoramic (Al McTavish), and Stillwater Canada (Dave Good, John McBride) for their help and constructive discussions. Rhian Evans and other members of the TGI-5 team are thanked for assistance in organizing the 2017 field season. This report benefited from the review by Neil Rogers.

References

Alibert, C. and Albarede, F., 1988. Relationships between mineralogical, chemical and isotopic properties of some North American kimberlites; Journal of Geophysical Research, v. 93, p. 7643–7671.

Ames, D.E., Kjarsgaard, I.M., McDonald, A.M., and Good, D.J., 2017. Insights into the extreme PGE enrichment of the W Horizon, Marathon Cu-Pd deposit, Coldwell Alkaline Complex, Canada: Platinum-group mineralogy, compositions and genetic implications; Ore Geology Reviews, v.

90, p. 723–747.

Bell, K. and Blenkinsop, J., 1980. Ages and initial $^{87}Sr/^{86}Sr$ ratios from alkali complexes of Ontario; *in* Geoscience Research Grant Program, Summary of Research 1979–1980, (ed.) E.G. Pye; Ontario Geological Survey, Miscellaneous Paper 93, p. 16–23.

Bell, K., Blenkinsop, J., Cole, T.J.S., and Menagh, D.P., 1982. Evidence from Sr isotopes for long-lived heterogeneities in the upper mantle; Nature, v. 298, p. 251–253.

Bleeker, W., 2014. The quest for better precision and more accuracy: Revisiting upper intercept ages; Geological Association of Canada Annual Meeting, Fredericton, Abstract Volume 37, p. 31–32.

Bleeker, W. and Chamberlain, K., 2015. Robust U-Pb age for the Douglas River dyke, Athabasca Basin – Further indications of a significant magmatic event in western Laurentia at 1165 Ma; *in* Reconstruction of supercontinents back to 2.7 Ga using the Large Igneous Province (LIP) Record: With implications for mineral deposit targeting, hydrocarbon exploration, and Earth system evolution – Year 5 Confidential Summary for Project Sponsors, (ed.) R.E. Ernst and W. Bleeker; Report A203, 9 p.

Bright, R.M., Amato, J.M., Denyszyn, S.W., and Ernst, R.E., 2014. U-Pb geochronology of 1.1 Ga diabase in the southwestern United States: Testing models for the origin of a post-Grenville large igneous province; Lithosphere, v. 6, p. 135–156.

Cannon, W.F. and Nicholson, S.W., 2001. Geology map of the Keweenaw Peninsula and adjacent area; US Geological Survey, Geological Investigations Series, Map I-2696, scale 1:100 000.

Chaffee, M.R., 2015. Petrographic and geochemical study of the hybrid rock unit associated with the Current Lake Intrusive Complex; M.Sc. thesis, University of Minnesota, Minneapolis, Minnesota, 139 p.

Clow, G.G., Normand L.L., Rennie, D.W., and Scholey, B.J.Y., 2017. Lundin Mining Corporation Technical Report on the Eagle Mine, Michigan, U.S.A; NI 43-101 Report, Lundin Mining Corporation.

Cogulu, E.H., 1993a. Factors controlling postcumulus compositional changes of chrome-spinels in the Crystal Lake Intrusion, Thunder Bay, Ontario; Geological Survey of Canada, Open File 2748, 77 p.

Cogulu, E.H., 1993b. Mineralogy and chemical variations of sulphides from the Crystal Lake Intrusion, Thunder Bay; Ontario. Geological Survey of Canada, Open File 2749. 52 p.

Cundari, R., 2012. Geology and geochemistry of Midcontinent Rift-related igneous rocks; M.Sc. thesis, Lakehead University, Thunder Bay, Ontario, 142 p.

Currie, K.L., 1976. The alkaline rocks of Canada; Geological Survey of Canada, Bulletin 239, 228 p., incl. "A" Series Map 1369A.

D'Angelo, M., 2013. Mineralogy, petrology and geochemistry of the Steepledge Intrusion; B.Sc. thesis, Lakehead University, Thunder Bay, Ontario, 83 p.

Davis, D.W. and Green, J.C., 1997. Geochronology of the North American Midcontinent rift in western Lake Superior and implications for its geodynamic evolution; Canadian Journal of Earth Sciences, v. 34, p. 476–488.

Davis, D.W. and Paces, J.B., 1990. Time resolution of geologic events on the Keweenaw Peninsula and implications for development of the Midcontinent Rift system; Earth and Planetary Science Letters, v. 97, p. 54–64.

Davis, D.W. and Sutcliffe, R.H., 1985. U-Pb ages from the Nipigon plate and northern Lake Superior; Geological Society of America Bulletin, v. 96, p. 1572–1579.

Ding, X., Li, C., Ripley, E.M., Rossell, D., and Kamo, S., 2010. The Eagle and East Eagle sulfide ore-bearing mafic-ultramafic intrusions in the Midcontinent Rift System, Upper Michigan: Geochronology and petrologic evolution; Geochemistry, Geophysics, Geosystems, v. 11, 22 p.

Ding, X., Ripley, E.M., and Li, C., 2012. PGE geochemistry of the Eagle Ni–Cu–(PGE) deposit, Upper Michigan: Constraints on ore genesis in a dynamic magma conduit; Mineralium Deposita, v. 47, p. 89–104.

Donoghue, K.A., Ripley, E.M., and Li, C., 2014. Sulfur isotope and mineralogical studies of Ni-Cu sulfide mineralization in the Bovine Igneous Complex intrusion, Baraga Basin, Northern Michigan; Economic Geology, v. 109, p. 325–341.

Dunlop, M., 2013. The Eagle Ni-Cu-PGE magmatic sulfide deposit and surrounding mafic dikes and intrusions in the Baraga Basin, Upper Michigan: Relationships, petrogenesis and implications for magmatic sulfide exploration; M.Sc. thesis, Indiana University, Bloomington, Indiana, 93 p.

Fairchild, L.M., Swanson-Hysell, N.L., Ramezani, J., Sprain, C.J., and Bowring, S.A., 2017. The end of Midcontinent Rift magmatism and the paleogeography of Laurentia; Lithosphere, v. 9, p. 117–133.

Flank, S., 2017. The petrography, geochemistry and stratigraphy of the Sunday Lake Intrusion, Jacques Township, Ontario; M.Sc. thesis, Laurentian University, Sudbury, Ontario, 71 p.

Foley, D.J., 2011. Petrology and Cu-Ni-PGE mineralization of the Bovine Igneous Complex, Baraga County, Northern Michigan; M.Sc. thesis, University of Minnesota, Minneapolis, Minnesota, 109 p.

French, J.E., Heaman, L.M., and Chacko, T., 2002. Feasibility of chemical U–Th–total Pb baddeleyite dating by electron microprobe; Chemical Geology, v. 188, p. 85–104.

Gittins, J., Macintyre, R.M., and York, D., 1967. The ages of carbonatite complexes in eastern Canada; Canadian Journal of Earth Sciences, v. 4, p. 651–655.

Goldner, B.D., 2011. Igneous petrology of the Ni-Cu-PGE mineralized Tamarack intrusion, Aitkin and Carlton Counties, Minnesota; M.Sc. thesis, University of Minnesota, Minneapolis, Minnesota, 156 p.

Good, D.J. and Crocket, J.H., 1994. Genesis of the Marathon Cu-platinum-group element deposit, Port Coldwell alkalic complex, Ontario; a Midcontinent rift-related magmatic sulfide deposit; Economic Geology, v. 89, p. 131–149.

Good, D.J., Epstein, R., McLean, K., Linnen, R.L., and Samson, I.M., 2015. Evolution of the Main Zone at the Marathon Cu-PGE sulfide deposit, Midcontinent Rift, Canada: Spatial relationships in a magma conduit setting; Economic Geology, v. 110, p. 983–1008.

Good, D.J., Cabri, L.J., and Ames, D.E., in press. PGM Facies variations for Cu-PGE deposits in the Coldwell Alkaline Complex, Ontario, Canada; Ore Geology Reviews.

Green, J.C., 1983. Geologic and geochemical evidence for the nature and development of the Middle Proterozoic (Keweenawan) Midcontinent Rift of North America; Tectonophysics, v. 94, p. 413–437.

Green, J.C., Bornhorst, T.J., Chandler, V.W., Mudrey, M.G., Jr., Myers, P.R., Pesonen, L.V., and Wilband, J.T., 1987. Keweenawan dykes of the Lake Superior region: Evidence for the evolution of the Middle Proterozoic Midcontinent Rift of North America; *in* Mafic Dyke Swarms, (ed.) H.C. Hall and W.F. Fahrig; Geological Association of Canada, Special Paper 34, p. 289–302.

Hammond, J.G., 1990. Middle Proterozoic diabase intrusions in the southwestern U.S.A. as indicators of limited extensional tectonism; *in* Mid-Proterozoic Laurentia-Baltica, (ed.) C.F. Gower, T. Rivers, and B. Ryan; Geological Association of Canada, Special Paper 38, p. 517–531.

Hanson, R.E., Crowley, J.L., Bowring, S.A., Ramezani, J., Gose, W.A., Dalziel, I.W., Pancake, J.A., Seidel, E.K., Blenkinsop, T.G., and Mukwakwami, J., 2004. Coeval large -scale magmatism in the Kalahari and Laurentian cratons during Rodinia assembly; Science, v. 304, p. 1126–1129.

Hart, T.R. and MacDonald, C.A., 2007. Geology and structure of the western margin of the Nipigon Embayment; Canadian Journal of Earth Sciences, v. 44, p. 1021–1040.

Hart, T.R, and Magyarosi, Z., 2004. Precambrian geology of the northern Black Sturgeon River and Disraeli Lake area, Nipigon Embayment, northwestern Ontario; Ontario Geological Survey, Open File 6138.

Hart, T.R., terMeer, M., and Jolette, C., 2002. Precambrian geology of Kitto, Eva, Summers, Dorothea and Sandra townships, northwestern Ontario; Phoenix Bedrock Mapping Project. Ontario Geological Survey, Open File 6095, 206 p.

Hauck, S.A., Severson, M.J., Zanko, L., Barnes, S.J., Morton, P., Alminas, H., Foord, E.E., and Dahlberg, E.H., 1997. An overview of the geology and oxide, sulfide, and platinum-group element mineralization along the western and northern contacts of the Duluth Complex; *in* Middle Proterzoic to Cambrian Rifting, Central North America, (ed.) R.W. Ojakangas, A.B. Dickas, and J.C. Green; Geological Society of America, Special Paper 312, p. 137–185.

Heaman, L.M. and Grotzinger, J.P., 1992. 1.08 Ga diabase sills in the Pahrump Group, California: Implications for development of the Cordilleran miogeocline; Geology, v. 20, p. 637–640.

Heaman, L.M. and Machado, N., 1992. Timing and origin of midcontinent rift alkaline magmatism, North America: evidence from the Coldwell Complex; Contributions to Mineralogy and Petrology, v. 110, p. 289–303.

Heaman, L.M., Kjarsgaard, B.A., and Creaser, R.A., 2004. The temporal evolution of North American kimberlites; Lithos, v. 76, p. 377–397.

Heaman, L.M., Easton, R.M., Hart, T.R., Hollings, P., MacDonald, C.A., and Smyk, M., 2007. Further refinement to the timing of Mesoproterozoic magmatism, Lake Nipigon region, Ontario; Canadian Journal of Earth Sciences, v. 44, p. 1055–1086.

Heggie, G.J., 2005. Whole rock geochemistry, mineral chemistry, petrology and Pt, Pd mineralization of the Seagull intrusion, Northwestern Ontario; M.Sc. thesis, Lakehead University, Thunder Bay, Ontario, 156 p.

Hollings, P. and Heggie, G., 2014. Rethinking the Midcontinent Rift – Puncturing the "plume paradigm"; *in* Proceedings and Abstracts, (ed.) J.D. Miller; Institute of Lake Superior Geology, 60th Annual Meeting, Hibbing, Minnesota, v. 60, p. 57–58.

Hollings, P., Smyk, M., Heaman, L.M., and Halls, H., 2010. The geochemistry, geochronology and paleomagnetism of dikes and sills associated with the Mesoproterozoic Midcontinent Rift near Thunder Bay, Ontario, Canada; Precambrian Research, v. 183, p. 553–571.

Hollings, P., Hart, T., Richardson, A., and MacDonald, C.A., 2007. Geochemistry of the Mesoproterozoic intrusive rocks of the Nipigon Embayment, northwestern Ontario: evaluating the earliest phases of rift development; Canadian Journal of Earth Sciences, v. 44, p. 1087–1110.

Hollings, P., Smyk, M., Heaman, L.M., and Halls, H., 2010. The geochemistry, geochronology, and paleomagnetism of dikes and sills associated with the Mesoproterozoic Midcontinent Rift near Thunder Bay, Ontario, Canada; Precambrian Research, v. 183, p. 553–571.

Hubbard, H.A., 1975. Lower Keweenawan volcanic rocks of Michigan and Wisconsin; U.S. Geological Survey, Journal of Research, v. 3, p. 529–541.

Hutchinson, D., White, R., Cannon, W., and Schulz, K., 1990. Keweenaw hot spot: Geophysical evidence for a 1.1 Ga mantle plume beneath the Midcontinent Rift system; Journal of Geophysical Research, v. 95, p. 10 869–10 884.

Kaminsky, F.V., Sablukov, S.M., Sablukova, L.I., and Shchukin, V.S., 2000. Petrology of kimberlites from the newly discovered Whitefish Lake field in Ontario; GeoCanada 2000, Abstract #1203.

Kent, R.W., Storey, M., and Saunders, A.D., 1992. Large igneous provinces: Sites of plume impact or plume incubation?; Geology, v. 20, p. 891–894.

Koerber, A. and Thakurta, J., 2017. Geochemical and petrological investigation of the prospective Ni-Cu-PGE mineralization at the Echo Lake intrusion in the upper peninsula of Michigan, USA; Geological Society of America Annual Meeting, Seattle, Abstracts with Programs, v. 49.

Krogh, T.E., Corfu, F., Davis, D.W., Dunning, G.R., Heaman, L.M., Kamo, S.L., Machado, N., Greenough, J.D., and Nakamura, E., 1987. Precise U-Pb isotopic ages of diabase dykes and mafic to ultramafic rocks using trace amounts of baddeleyite and zircon; *in* Mafic Dyke Swarms, (ed.) H.C. Halls and W.F. Fahrig; Geological Association of Canada, Special Paper 34, p. 147–152.

Laarman, J.E., 2007. Geochemistry and PGE mineralization of the Kitto intrusion: A product of Mesoproterozoic plume magmatism through fault bounded Archean crust, east Nipigon Embayment, northern Ontario; M.Sc. thesis, Lakehead University, Thunder Bay, Ontario, 276 p.

Mattinson, J.M., 2005. Zircon U/Pb chemical abrasion (CA-TIMS) method: Combined annealing and multi-step partial dissolution analysis for improved precision and accuracy of zircon ages; Chemical Geology, v. 220, p. 47–66.

McCormick, K.A., Chamberlain, K.R., and Paterson, C.J., 2017. U–Pb baddeleyite crystallization age for a Corson diabase intrusion: possible Midcontinent Rift magmatism in eastern South Dakota; Canadian Journal of Earth Sciences, v. 55, p. 111–117.

Miller, J.D., 1998. Potential for reef-type PGE mineralization in the Duluth Complex: Evidence from the Layered Series at Duluth; The Minnesota Prospector, Special Issue, p. 8–12.

Miller, J.D. and Nicholson, S.W., 2013. Geology and mineral deposits of the 1.1 Ga Midcontinent Rift in the Lake Superior region – An overview; *in* Field Guide to the Cu-Ni-PGE Deposits of the Lake Superior Region, (ed.) J.D. Miller; Precambrian Research Center Guidebook 13-1, p. 1–50.

Mitchell, R.H., Platt, R.G., and Cheadle, S.P., 1983. A gravity study of the Coldwell Complex, northwestern Ontario and its petrological significance; Canadian Journal of Earth Sciences, v. 20, p. 1631–1638.

Mitchell, R.H., Platt, R.G., Lukosius-Sanders, J., Artist-Downey, M., and Moogk-Pickard, S., 1993. Petrology of syenites from center III of the Coldwell alkaline complex, northwestern Ontario, Canada; Canadian Journal of Earth Sciences, v. 30, p. 145–158.

Nicholson, S.W. and Shirey, S.B., 1990. Midcontinent Rift volcanism in the Lake Superior region: Sr, Nd, and Pb isotopic evidence for a mantle plume origin; Journal of Geophysical Research, v. 95, p. 10 851–10 868.

Ojakangas, R.W. and Morey, G.B., 1982. 7A: Keweenawan prevolcanic quartz sandstones and related rocks of the Lake Superior region; *in* Geology and Tectonics of the Lake Superior Basin, (ed.) R.J. Wold and W.J. Hinze; Geological Society of America, Boulder, Colorado, Memoir 156, p. 85–96.

Ontario Geological Survey, 1991a. Bedrock map of Ontario, east-central sheet; Ontario Geological Survey, Map 2543, scale 1: 1 000 000.

Ontario Geological Survey, 1991b. Bedrock map of Ontario, west-central sheet; Ontario Geological Survey, Map 2542, scale 1: 1 000 000.

Paces, J.B. and Miller, J.D., 1993. Precise U-Pb ages of Duluth complex and related mafic intrusions, northeastern Minnesota: Geochronological insights to physical, petrogenetic, paleomagnetic, and tectonomagmatic processes associated with the 1.1 Ga midcontinent rift system; Journal of Geophysical Research: Solid Earth, v. 98, p. 13 997–14 013.

Platt, R.G. and Mitchell, R.H., 1979. The Marathon Dikes. I: Zirconium-rich titanian garnets and manganoan magnesian ulvoespinel-magnetite spinels; American Mineralogist, v. 64, p. 546–550.

Platt, R.G. and Mitchell, R.H., 1982. The Marathon Dikes: ultrabasic lamprophyres from the vicinity of McKellar Harbour, NW Ontario; American Mineralogist, v. 67, p. 907–916.

Platt, R.G., Mitchell, R.H., and Holm, P.M., 1983. Marathon dikes: Rb–Sr and K–Ar geochronology of ultrabasic lamprophyres from the vicinity of McKellar Harbour, northwestern Ontario, Canada; Canadian Journal of Earth Sciences, v. 20, p. 961–967.

Queen, M., Hanes, J.A., Archibald, D.A., Farrar, E., and Heaman, L.M., 1996. $^{40}Ar/^{39}Ar$ phlogopite and U–Pb perovskite dating of lamprophyre dykes from the eastern Lake Superior region: evidence for a 1.14 Ga magmatic precursor to Midcontinent Rift volcanism; Canadian Journal of Earth Sciences, v. 33, p. 958–965.

Ripley, E.M., 2014. Ni-Cu-PGE mineralization in the Partridge River, South Kawishiwi, and Eagle intrusions: A review of contrasting styles of sulfide-rich occurrences in the Midcontinent rift system; Economic Geology, v. 109, p. 309–324.

Rukhlov, A.S. and Bell, K., 2010. Geochronology of carbonatites from the Canadian and Baltic Shields, and the Canadian Cordillera: Clues to mantle evolution; Mineralogy and Petrology, v. 98, p. 11–54.

Sage, R.P., 1985. Geology of carbonatite-alkalic rock complexes of Ontario: Chipman Lake Area. Districts of Thunder Bay and Cochrane; Ontario Ministry of Northern Affairs and Mines, Ontario Geological Survey, Study 44.

Sage, R.P., 1987a. Geology of carbonatite-alkalic rock complexes in Ontario: Nemegosenda Lake Alkalic Rock Complex. District of Sudbury; Ontario Ministry of Northern Development and Mines, Ontario Geological Survey, Study 34.

Sage, R.P., 1987b. Geology of carbonatite-alkalic rock complexes in Ontario: Shenango Township Alkalic Rock Complex. District of Sudbury and Algoma; Ontario, Ministry of Northern Development and Mines, Ontario Geological Survey, Study 35.

Sage, R.P., 1987c. Geology of carbonatite-alkalic rock complexes in Ontario: Big Beaver House Carbonatite Complex.

District of Kenora; Ontario Ministry of Northern Development and Mines, Ontario Geological Survey, Study 51.

Sage, R.P., 1988a. Geology of carbonatite-alkalic rock complexes in Ontario: Seabrook Lake Carbonatite Complex. District of Algoma; Ontario Ministry of Northern Development and Mines, Ontario Geological Survey, Study 31.

Sage, R.P., 1988b. Geology of carbonatite-alkalic rock complexes in Ontario: Clay-Howells Alkalic Rock Complex. District of Sudbury and Algoma; Ontario Ministry of Northern Development and Mines, Ontario Geological Survey, Study 37.

Sage, R.P., 1988c. Geology of carbonatite-alkalic rock complexes in Ontario: Valentine Township Carbonatite Complex. District of Cochrane; Ontario Ministry of Northern Development and Mines, Ontario Geological Survey, Study 39.

Sage, R.P., 1988d. Geology of carbonatite-alkalic rock complexes of Ontario: Killala Lake Alkalic Rock Complex. District of Thunder Bay; Ministry of Northern Development and Mines, Ontario Geological Survey, Study 45.

Sage, R.P., 1988e. Geology of carbonatite-alkalic rock complexes in Ontario: Firesand River Carbonatite Complex. District of Algoma; Ontario Ministry of Northern Development and Mines, Ontario Geological Survey, Study 47.

Sage, R.P., 1988f. Geology of carbonatite-alkalic rock complexes in Ontario: Schryburt Lake Carbonatite Complex. District of Kenora; Ontario Ministry of Northern Development and Mines, Ontario Geological Survey, Study 50.

Sage, R.P., 1991. Alkaline rocks, carbonatite and kimberlite complexes of Ontario, Superior Province; *in* Geology of Ontario, Ontario Geological Survey, Special Volume 4, p. 683–709.

Saunders, A.D., Storey, M., Kent, R.W., and Norry, M.J., 1992. Consequences of plume-lithosphere interactions; Geological Society, London, Special Publications 68, p. 41–60.

Schoene, B., Crowley, J.L., Condon, D.J., Schmitz, M.D., and Bowring, S.A., 2006. Reassessing the uranium decay constants for geochronology using ID-TIMS U-Pb data; Geochimica et Cosmochimica Acta, v. 70, p. 426–445.

Shirey, S.B., 1997. Re-Os isotopic compositions of Midcontinent rift system picrites: implications for plume–lithosphere interaction and enriched mantle sources; Canadian Journal of Earth Sciences, v. 34, p. 489–503.

Smyk, M.C., Hollings, P., and Heaman, L.M., 2006. Preliminary investigations of the petrology, geochemistry and geochronology of the St. Ignace Island Complex, Midcontinent Rift, northern Lake Superior, Ontario; *in* Proceedings and Abstracts, (ed.) A.C. Wilson; Institute of Lake Superior Geology, 52nd Annual Meeting, Sault Ste. Marie, Ontario, v. 52, p. 61–62.

Smyk, M.C. and Hollings, P., 2009. Mesoproterozoic Midcontinent Rift-related mafic intrusions near Thunder Bay: Update; *in* Summary of Field Work and Other Activities 2009, Ontario Geological Survey, Open File Report 6240, p. 11–15.

Sutcliffe, R.H., 1986. The petrology, mineral chemistry and tectonics of Proterozoic rift-related igneous rocks at Lake Nipigon, Ontario; Ph.D. thesis, The University of Western Ontario, London, Ontario, 326 p.

Swanson-Hysell, N.L., Burgess, S.D., Maloof, A.C., and Bowring, S.A., 2014. Magmatic activity and plate motion during the latent stage of Midcontinent Rift development; Geology, v. 42, p. 475–478.

Taranovic, V., Ripley, E.M., Li, C., and Rossell, D., 2015. Petrogenesis of the Ni–Cu–PGE sulfide-bearing Tamarack Intrusive Complex, Midcontinent Rift System, Minnesota; Lithos, v. 212, p. 16–31.

Taranovic, V., Ripley, E.M., Li, C., and Rossell, D., 2016. Chalcophile element (Ni, Cu, PGE, and Au) variations in the Tamarack magmatic sulfide deposit in the Midcontinent Rift System: implications for dynamic ore-forming processes; Mineralium Deposita, v. 51, p. 937–951.

Thomas, D.G., Melnyk, J., Gormely, L., Searston, S., and Kulla, G., 2011. Thunder Bay North polymetallic project, Ontario, Canada; Magma Metals Ltd., NI 43-101 Technical Report on Preliminary Assessment, p. 10-14 – 10-18.

Trevisan, B.E., 2014. The petrology, mineralization and regional context of the Thunder mafic to ultramafic intrusion, Midcontinent Rift, Thunder Bay, Ontario; M.Sc. thesis, Lakehead University, Thunder Bay, Ontario, 285.

Trevisan, B.E., Hollings, P., Ames, D.E., and Rayner, N.M., 2015. The petrology, mineralization, and regional context of the Thunder mafic to ultramafic intrusion, Midcontinent Rift, Thunder Bay, Ontario; *in* Targeted Geoscience Initiative 4: Canadian nickel-copper-platinum group elements-chromium ore systems – fertility, pathfinders, new and revised models, (ed.) D.E. Ames and M.G. Houlé: Geological Survey of Canada, Open File 7856, p. 139–149.

Van Schmus, W.R. and Hinze, W.J., 1985. The midcontinent rift system; Annual Review of Earth and Planetary Sciences, v. 13, p. 345–383.

Vervoort, J., Wirth, K., Kennedy, B., Sandland, T., and Harpp, K., 2007. The magmatic evolution of the Midcontinent Rift: New geochronologic and geochemical evidence from felsic magmatism; Precambrian Research, v. 157, p. 235–268.

Weiblen, P.W., 1982. 6: Keweenawan intrusive igneous rocks; *in* Geology and Tectonics of the Lake Superior Basin, (ed.) R.J. Wold and W.J. Hinze; Geological Society of America, Boulder, Colorado, Memoir 156, p. 57–82.

Weiblen, P.W., Mathez, E.A., and Morey, G.B., 1972. Logan intrusions; *in* Geology of Minnesota: A Centennial Volume, (ed.) P.K. Sims and G.B. Morey; Minnesota Geological Survey, St. Paul, Minnesota, p. 394–410.

Wold, R.J. and Hinze, W.J., 1982. Geology and Tectonics of the Lake Superior Basin; Geological Society of America, Boulder, Colorado, Memoir 156, 280 p.

Wu, F.Y., Mitchell, R.H., Li, Q.L., Zhang, C., and Yang, Y.H., 2017. Emplacement age and isotopic composition of the

Prairie Lake carbonatite complex, Northwestern Ontario, Canada; Geological Magazine, v. 154, p. 217–236.

Zartman, R.E., Nicholson, S.W., Cannon, W.F., and Morey, G., 1997. U-Th-Pb zircon ages of some Keweenawan Supergroup rocks from the south shore of Lake Superior; Canadian Journal of Earth Science, v. 34, p. 549–561.

Sulphide textural variations and multiphase ore emplacement in the Eagle's Nest Ni-Cu-(PGE) deposit, McFaulds Lake greenstone belt, Ontario

N. Zuccarelli[1], C.M. Lesher[1], and M.G. Houlé[2,1]

[1]*Mineral Exploration Research Centre, Harquail School of Earth Sciences, Goodman School of Mines, Laurentian University, 935 Ramsey Lake Road, Sudbury, Ontario P3E 2C6*

[2]*Geological Survey of Canada, 490 rue de la Couronne, Québec, Quebec G1K 9A9*

Abstract

The McFaulds Lake greenstone belt, in addition to its world-class chromite endowment, also hosts significant magmatic Ni-Cu-(PGE) mineralization at the Eagle's Nest deposit. Mineralization at Eagle's Nest occurs in a dynamic system that contains multiple generations of sulphide textures, consistent with its interpretation as a magmatic feeder among a network of ultramafic intrusions. Massive sulphides and abundant leopard net-textured, oikocrystic net-textured, and inclusion net-textured sulphide mineralization formed first and were consolidated enough to be cross-cut by late-stage pyroxenite, creating disrupted net-textured sulphide and minor late-segregating massive/semi-massive sulphide melts. Resolving the fundamental characteristics and genesis of mineralization at Eagle's Nest will provide critical information about the evolution of large chromium and Ni-Cu-PGE ore systems associated with Archean komatiitic magmatism within the Superior Province.

Introduction

The multi-commodity mineral potential of the Ring of Fire (RoF) region of northern Ontario is demonstrated by the presence of six major chromite deposits, one major Ni-Cu-(PGE) deposit, four small volcanic massive sulphide (VMS) deposits, plus numerous other VMS, Fe-Ti-V, and gold occurrences (Fig. 1). The RoF region encompassed by the McFaulds Lake greenstone belt (MLGB), part of the Oxford-Stull domain of the Superior Province, records episodic volcanism, sedimentation, ultramafic to felsic intrusive activity, and tectonism spanning from at least 2.83 to 2.66 Ga (Metsaranta et al., 2015). This Archean basement is overlain by flat-lying Paleozoic carbonate-dominated strata and unconsolidated Quaternary deposits making exploration challenging.

The Double Eagle (DEIC) – Black Thor (BTIC) intrusive complexes, occurring within the central part of the MLGB, are distinct ultramafic-dominated intrusive complexes that constitute parts of a single multi-commodity komatiitic system (Fig. 2: Houlé et al., 2017). Composed of a thick lower ultramafic zone and a thinner upper mafic zone, these complexes host several major deposits (e.g. Blackbird 1-2, Black Horse, Big Daddy, Black Creek, Black Label and Black Thor chromite deposits and Eagle's Nest Ni-Cu-(PGE) deposit), along with many smaller occurrences.

The DEIC-hosted Eagle's Nest magmatic Ni-Cu-(PGE) sulphide deposit contains at least 20 Mt of ore grading 1.7% Ni, 0.98% Cu, and 4.4 g/t Pd+Pt (Burgess et al., 2012), making it one of the largest and richest Ni-Cu-(PGE) deposits discovered in Canada in the last 25 years. Mineralization is hosted by a subvertical (originally subhorizontal) ultramafic body dominated by komatiitic pyroxenite and peridotite that contains net-textured sulphide mineralization with only minor disseminated and massive sulphide mineralization (Mungall et al., 2010). This study aims to: i) establish the textural and mineralogical variations within and between each style of Ni-Cu-PGE sulphide mineralization; ii) characterize the geochemical signature of each of the textural styles; iii) define potential sulphur sources for the mineralization; and iv) constrain the genesis of the Fe-Ni-Cu sulphide mineralization.

Methodology

As the region under investigation contains almost no outcrops, most of the analysis is on drill core. Initial investigation was focused on identifying the various sulphide textures occurring within the deposit, as a prelude to characterizing the corresponding ore mineral assemblages. Subsequent investigations were directed towards determining the extent of the disrupted-net texture, identifying any additional sulphide textures present in the deposit, and characterizing texturally the barren ultramafic rock throughout the magmatic conduit, ahead of characterizing whole-rock geochemical variations.

Preliminary Results

Eagle's Nest mineralization mostly consists of an assemblage of pyrrhotite-pentlandite-chalcopyrite-(magnetite) that occurs predominantly as net-textured sulphides with minor

Corresponding author: Natascia Zuccarelli (nzuccarellipegoraro@laurentian.ca)

Zuccarelli, N., Lesher, C.M., and Houlé, M.G., 2018. Sulphide textural variations and multiphase ore emplacement in the Eagle's Nest Ni-Cu-(PGE) deposit, McFaulds Lake greenstone belt, Ontario; *in* Targeted Geoscience Initiative: 2017 report of activities, volume 2, (ed.) N. Rogers; Geological Survey of Canada, Open File 8373, p. 29–34. https://doi.org/10.4095/306598

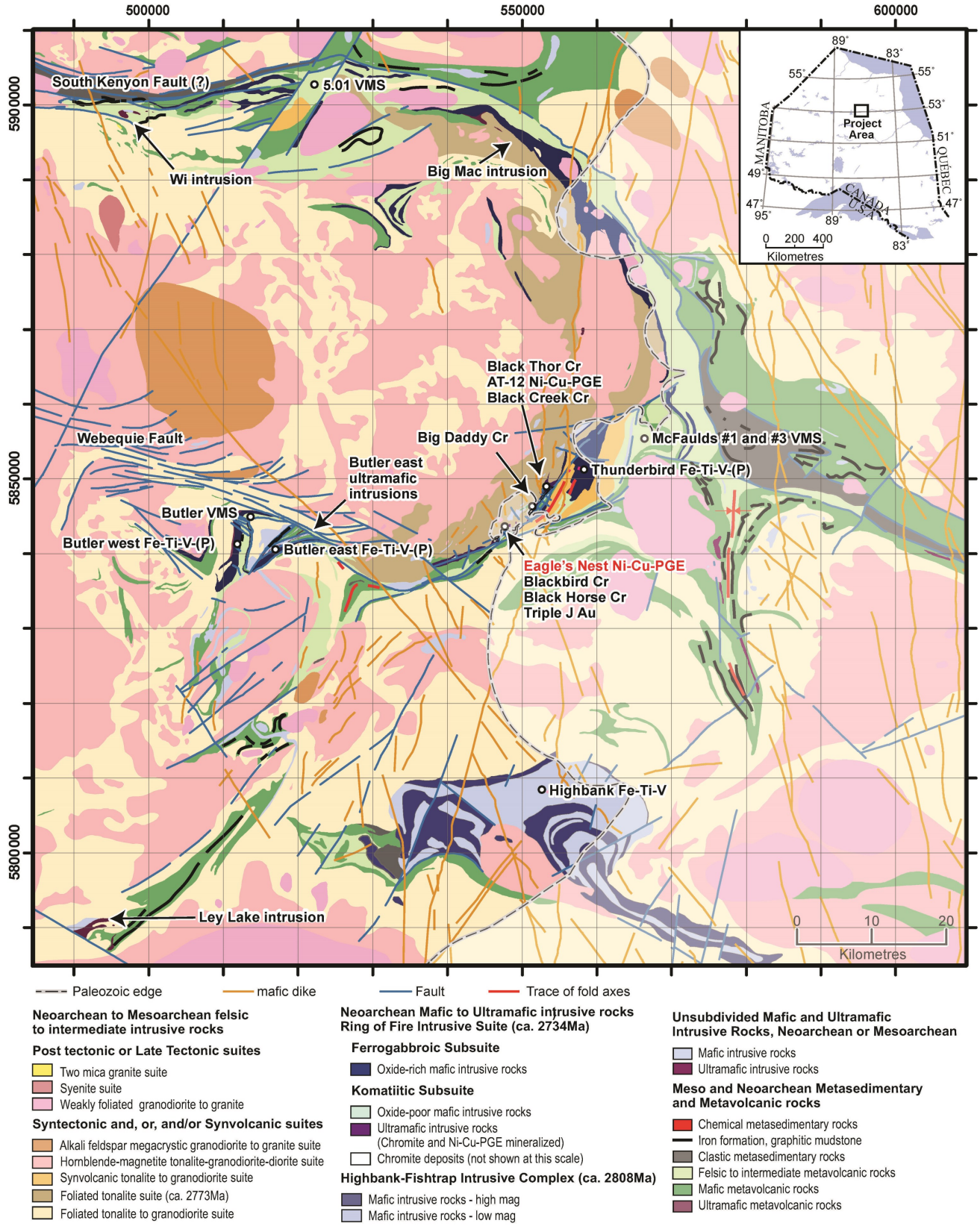

Figure 1. Simplified geological map of the McFaulds Lake greenstone belt showing the location of the main mineral deposits and occurrences in the "Ring of Fire" region (from Metsaranta and Houlé, 2017a–c). Paleozoic cover occurs on the west side of the Paleozoic edge line.

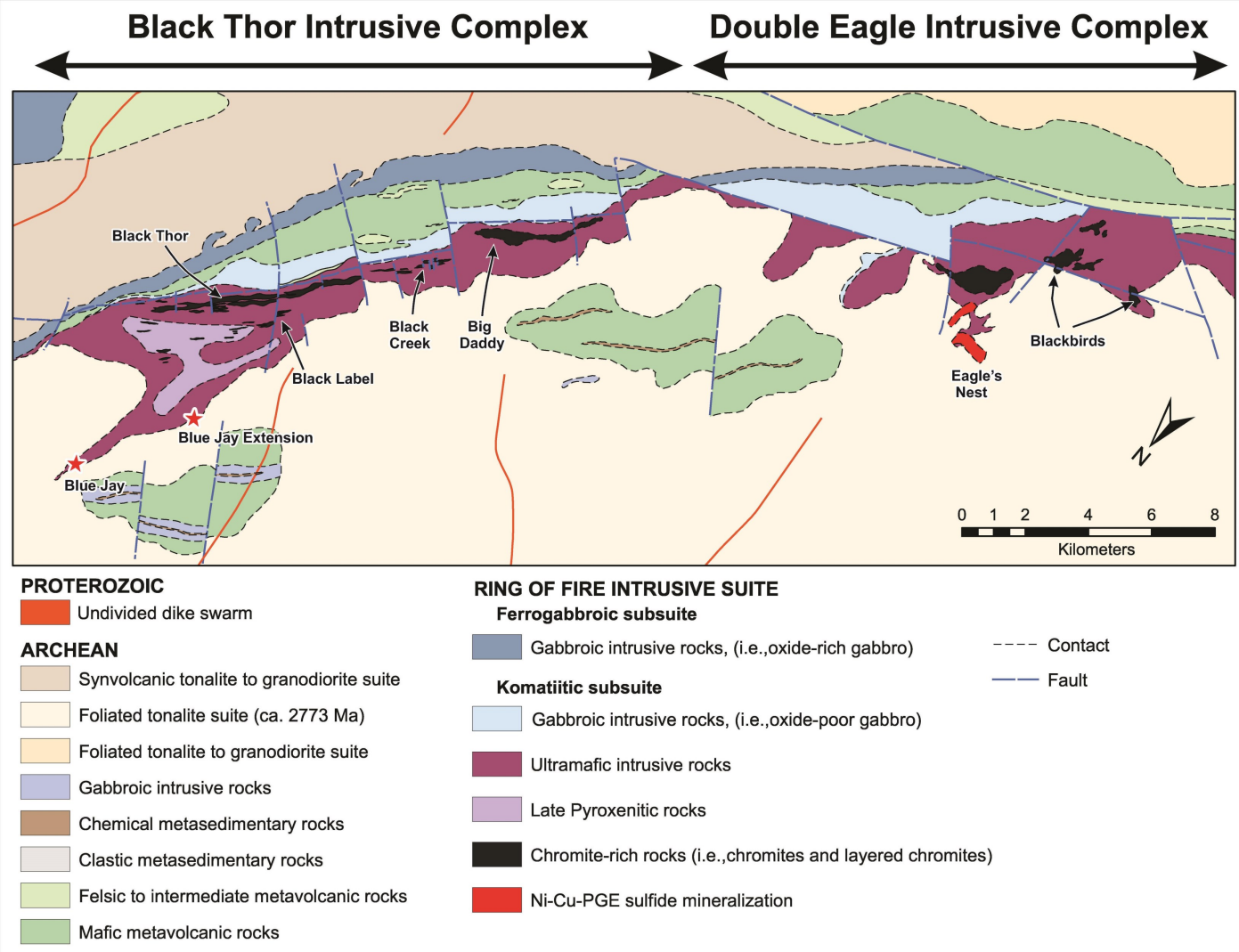

Figure 2. Geological map of the Black Thor (BTIC) and Double Eagle (DEIC) intrusive complexes in the McFaulds Lake greenstone belt showing the location of the main mineral deposits in the "Ring of Fire" region. The Eagle's Nest deposit occurs within the feeder system of the Double Eagle intrusive complex (Houlé et al., 2017).

disseminated sulphides, rare semi-massive sulphides, and minor massive sulphides (Table 1). The net-textured sulphide facies is divisible into six sub-facies: net, leopard-net, pinto-net, inclusion-net, disrupted-net, and patchy-net textures.

Table 1. Sulphide facies textures present at the Eagle's Nest deposit with various percentages of sulphur and sulphide abundances.

Texture	S (%)	Sulphide (%)
Massive	> 30	> 80
Semi-Massive	12-30	30-80
Net-Textured	5-12	15-30
Disseminated	2-5	5-15

Massive sulphides (Fig. 3a, b) occur as 5 to 60 m thick concordant/discordant lenses, 10 to 90 cm thick concordant/discordant veins, and 2 to 10 mm thick concordant/discordant veinlets. Some massive sulphide lenses/veins greater than 10 m contain a wide variety of clasts, including barren peridotite, pyroxenite, magnetite, net-textured sulphides, and rare felsic granofels (anhedral quartz-feldspar ± clinopyroxene). Most clasts are relatively homogeneous in composition and are typically 3 to 10 mm in diameter, but in some zones are more variable in size (10–300 mm). Some clasts appear to have 2 to 4 mm thick contact-metamorphosed and/or altered margins. Clasts are often associated with chalcopyrite, which is concentrated along contacts, alteration zones, veins or faults. Many massive sulphides contain 1 to 4 cm diameter pentlandite oikocrysts, whereas others contain more uniformly distributed exsolved pentlandite. Chalcopyrite is also commonly present

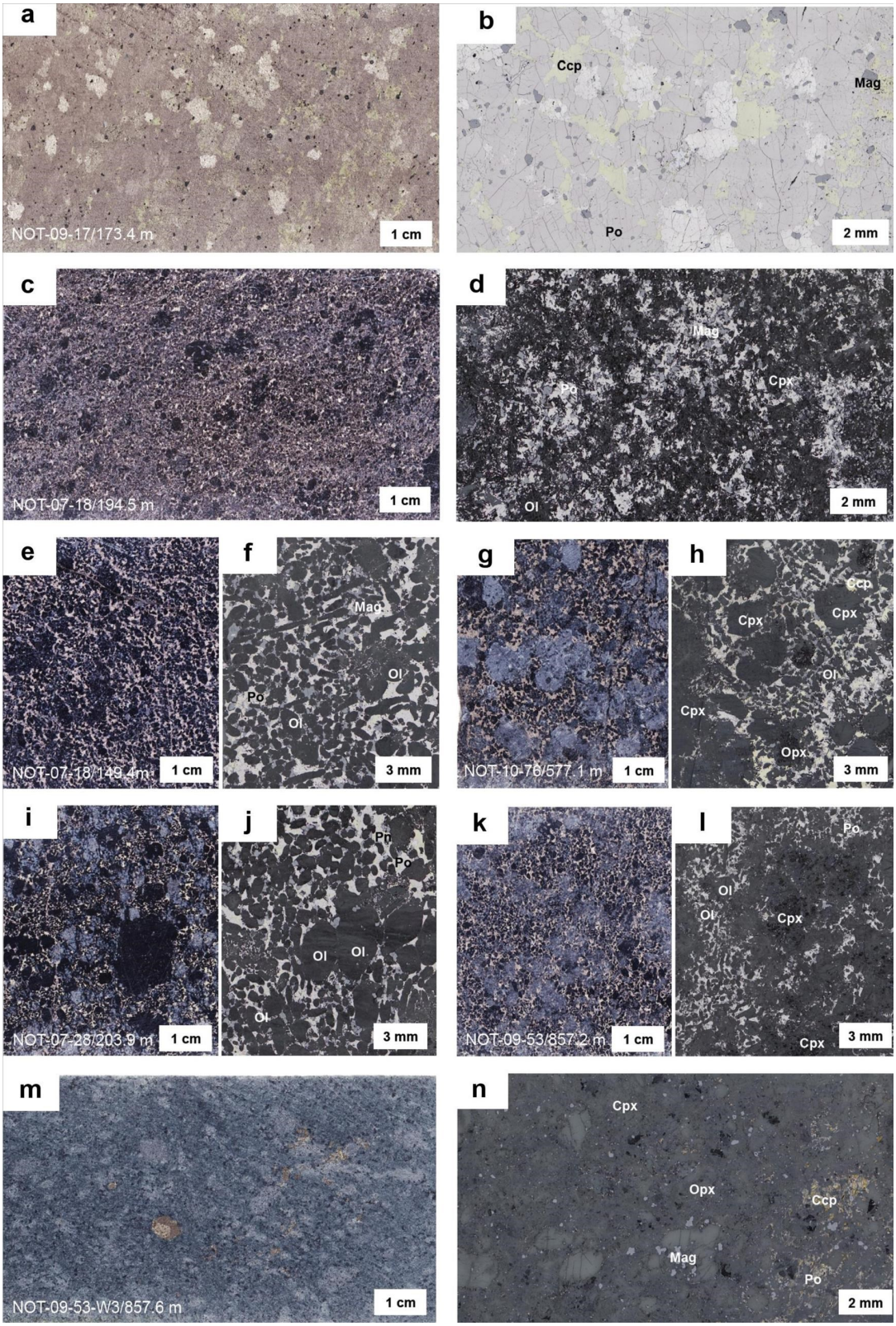

Figure 3. Major sulphide facies occurring within the Eagle's Nest deposit. Massive sulphide: a) in core; b) in thin section. Semi-massive sulphide: c) in core; d) in thin section. Net-texture, including leopard net: e) in core; f) in thin section. Pinto-net: g) in core; h) in thin section. Inclusion-net: i) in core; j) in thin section. Disrupted-net: k) in core; l) in thin section. Disseminated massive sulphide: m) in core; n) in thin section.

along contacts between massive sulphides and other textural facies, apparently infiltrating non-massive textures and creating zones of anomalously sulphide-rich net texture. Massive sulphides veinlets less than 1 cm contain only chalcopyrite and some pyrrhotite.

Semi-massive textures (Fig. 3c, d) are rare, but fine-grained semi-massive sulphides transgress net/leopard/pinto-textured sulphides, indicating that they have been mobilized. They are composed predominantly of pyrrhotite with very fine chalcopyrite and very fine pentlandite. The silicates include small olivine crystals (or serpentine after olivine) and a wide variety of alteration minerals.

Net textures *sensu stricto* are rare, but occur as thin films of sulphide surrounding serpentinized olivine. Most contain pyroxene oikocrysts that are divisible into five additional subfacies. Leopard-net textures (Fig. 3e, f) contain 5 mm dark pyroxene oikocrysts enclosing 1 to 2 mm cumulus olivine in a matrix of fine-grained pyrrhotite and coarse-grained (2–10 mm) chalcopyrite and pentlandite. Sulphide-olivine-sulphide interfacial angles are typically <60° (Fig. 3f), indicating that former sulphide melt 'wetted' olivine, implying a relatively high fO_2 (see Rose and Brenan, 2001). Pinto-net textures (Fig. 3g, h) contain 5 mm light talc-altered pyroxene with irregular margins enclosing 1 mm fresh olivine in a similar matrix (Fig. 3h). Inclusion-net textures (Fig. 3i, j) contain 30 to 300 mm inclusions of olivine/dunite, sometimes with visible sulphide located between individual olivine crystals with lesser magnetite and silicate-oxide facies iron formation. Disrupted-net textures (Fig. 3k, l) have been invaded by a later pyroxenite melt and are common in the centre of the mineralized zone, but also occur in the rest of the conduit within leopard-net mineralization as lenses less than 2 m thick. The contact between the invading pyroxenite melt and leopard-net mineralization is highly irregular, but fairly sharp. Patchy-net texture occurs as sulphides forming 3 to 7 cm discontinuous patches of net-texture in areas where olivine is more closely packed (see Bazilevskaya, 2009; Tonnelier, 2010).

Disseminated textures (Fig. 3m, n) occur as uniformly dispersed sulphides between fine-grained olivine and coarse-grained pyroxene, normally in close proximity to blebby and wispy sulphides in otherwise barren rock, commonly interlayered with net-textured/massive sulphides. The sulphides are largely pyrrhotite with pentlandite and minor chalcopyrite.

Contacts between late pyroxenite and leopard/pinto/inclusion net-textured sulphides are irregular, but relatively sharp, whereas contacts between massive and semi-massive/net-texture are irregular, with massive infiltrating net texture. These types of contacts occur adjacent to both thin veins (<1 m) and thicker (>1 m) lenses of massive sulphides (Zuccarelli et al., 2017).

The unmineralized ultramafic rocks near the mineralized zone consist predominantly of peridotite, with varying amounts of olivine, orthopyroxene, and clinopyroxene. However, many thin units of pyroxenite also occur proximal to mineralization, but generally in contact with the country rocks (e.g., granodiorite). These units are often highly altered with extensive biotite and talc replacement. It is not clear if they represent actual pyroxenitic units or contaminated and altered chill margins of the peridotitic units. A large zone (>100 m thick) of pyroxenite occasionally interrupted by minor peridotite, also occurs towards the paleo-top of the conduit away from basal mineralization. This pyroxenite is composed of variable amount of olivine, orthopyroxene and clinopyroxene, but commonly contains 20 to 30% olivine.

Discussion

The mechanics of the ore emplacement processes are still being studied, but the textures and crosscutting relationships indicate at least three phases of ore formation/modification:

1) Formation of initial massive, net/leopard-net/pinto-net/inclusion-net textured and disseminated ores in the subhorizontal magmatic conduit, most likely involving fluid dynamic segregation (Lesher, 2017) and sulphide percolation (Barnes et al., 2017) processes;
2) Local sulphide melt segregation and mobilization, forming sulphide schlieren and semi-massive and massive sulphide melts containing clasts derived from other parts of the system (barren peridotite, net-textured ores) and country rocks (massive magnetite, banded iron formation);
3) Emplacement of late pyroxenite melt towards the centre of the conduit, with 'fingers' of magma disrupting still-'mushy' leopard-net textured ore.

Pyroxenite crosscuts early net-textured facies relatively sharply without mobilizing sulphides, indicating that the olivine/pyroxene network behaved relatively rigidly, but does not cut semi-massive or massive sulphides, likely because they were still ductile at the time. The invasion of pyroxenite melt appears to have been in the form of small fingers, like on the margins of the Late Websterite Phase of the nearby Black Thor system (Spath et al., 2016), but at this stage it is not clear if a more massive phase of pyroxenite is present in the Eagle's Nest system. Crosscutting, infiltrating relationships between massive and net-textured mineralization suggest late-stage mobilization of massive sulphides, as sulphide melts crystallize at lower temperatures (<1100°C) than silicates (1200–1400°C; Naldrett, 2004) and thus remain mobile to lower temperatures.

The small size of the inclusions in net-textured mineralization indicates that the magmatic system was dynamic enough to carry small clasts, but not dynamic enough to carry large clasts (see Lesher, 2017). The clasts are sub-rounded to angular, with rounder clasts exhibiting more 'baking' along their margins. Consequently, it is likely that rounded clasts were incorporated earlier and/or carried farther than the angular clasts. Finally, because no 'exotic' xenoliths are present (all appear to be locally derived) this suggests ore formation and mobilization occurred close to the site of emplacement. The evidence for multiphase emplacement indicates a relatively long-lived ultramafic system, consistent with Eagle's Nest representing a feeder within the DEIC.

Future Work

Drill core data is currently being examined to characterize Ni-Cu-(PGE) mineralization and establish the genesis of the Eagle's Nest deposit. Additional thin section and whole-rock geochemical studies will include detailed reflected and transmitted light petrographic studies, to produce detailed textural and mineralogical analysis of the sulphide assemblages at Eagle's Nest deposit. Representative sulphide and platinum-group mineral assemblages will be investigated by electron probe microanalyzer and scanning electron microscope. Whole-rock geochemical data will be examined for commonalities amongst the various sulphide textures to identify possible geochemical fingerprints for the textures that can be broadly applied to establish the sulphide saturation history of the Eagle's Nest deposit.

Acknowledgments

This report is a contribution to NRCan's Targeted Geoscience Initiative Program (TGI). Support for this study was provided through the Ni-Cr-PGE Systems Project's 'Activity NC-2.1: Architecture of magmatic conduits in Cr-(PGE)/Ni-Cu-(PGE) ore systems'.

Natascia Zuccarelli is conducting a TGI-supported M.Sc. at Laurentian University, Sudbury, Ontario. The authors are grateful to Noront Resources Ltd. (Alan Coutts, Ryan Weston, Matt Downey, Stephen Flewelling, Matt Deller, Geoff Heggie, Cory Exell, Rob Lyght, Tristan Megan and Roydon Spence) for providing access to properties, geological information and very informative discussions throughout project development. This research activity would not have reached fruition without their knowledge and strong support. This report benefited from the review of Neil Rogers.

References

Barnes, S.J., Mungall, J.E., Le Vaillant, M., Godel, B., Lesher, C.M., Holwell, D., Lightfoot, P.C., Krivolutskaya, N., and Wei, B., 2017. Sulfide-silicate textures in magmatic Ni-Cu-PGE sulfide ore deposits; American Mineralogist, v. 102, p. 473–506.

Bazilevskaya, E., 2009. Primary and Secondary Textures of Fe-Ni-Cu sulfide mineralization in the Kattiniq member of the Raglan Formation, Cape Smith Belt, New Quebec; M.Sc. thesis, Laurentian University, Sudbury, 59 p.

Burgess, H., Gowans, R., Jacobs, C., Murahwi, C., and Damjanović, B., 2012. NI 43-101 Technical Report Feasibility Study McFaulds Lake Property Eagle's Nest project James Bay Lowlands Ontario, Canada; NI-43-101 Technical Report - Micon International Ltd., 113 p.

Houlé, M.G., Lesher, C.M., Schetselaar, E., Metsaranta, R.T., and McNicoll, V.J., 2017. Architecture of magmatic conduits in Cr-(PGE)/Ni-Cu-(PGE) ore systems; *in* Targeted Geoscience Initiative – 2016 Report of Activities, (ed.) N. Rogers; Geological Survey of Canada, Open File 8199, p. 55–58.

Lesher, C.M., 2017. Roles of residues/skarns, xenoliths, xenocrysts, xenomelts, and xenovolatiles in the genesis, transport, and localization of magmatic Fe-Ni-Cu-PGE sulfides and chromite; Ore Geology Reviews, v. 90, p. 465-484.

Metsaranta, R.T. and Houlé, M.G., 2017a. Precambrian Geology Winiskisis Channel area, "Ring of Fire Region", north sheet; Ontario Geological Survey, Preliminary Map P.3804; Geological Survey of Canada, Open File 8200, scale 1:100 000.

Metsaranta, R.T. and Houlé, M.G., 2017b. Precambrian Geology of the McFaulds Lake area, "Ring of Fire Region" - Central Sheet; Ontario Geological Survey, Preliminary Map P.3805; Geological Survey of Canada, Open File 8201, scale 1:100 000.

Metsaranta, R.T. and Houlé, M.G., 2017c. Precambrian Geology of the Highbank Lake Area - "Ring of Fire Region", Southern sheet; Ontario Geological Survey, Preliminary Map P.3806; Geological Survey of Canada, Open File 8202, scale 1:100 000.

Metsaranta, R.T., Houlé, M.G., McNicoll, V.J., and Kamo, S.L., 2015. Revised geological framework for the McFaulds Lake greenstone belt, Ontario; *in* Targeted Geoscience Initiative 4: Canadian Nickel-Copper-Platinum Group Elements-Chromium Ore Systems — Fertility, Pathfinders, New and Revised Models, (ed.) D.E. Ames and M.G. Houlé; Geological Survey of Canada, Open File 7856, p. 61–73.

Mungall, J.E., Harvey, J.D., Balch, S.J., Azar, B., Atkinson, J., and Hamilton, M.A., 2010. Eagle's Nest: A magmatic Ni-sulfide deposit in the James Bay Lowlands, Ontario, Canada; Society of Economic Geology Special Publication 15, p. 539–557.

Naldrett, A.J., 2004. Magmatic Sulfide Deposits: Geology, Geochemistry and Exploration; Springer-Verglag, Berlin, 727 p.

Rose, L.A. and Brenan, J.M., 2001. Wetting properties of Fe-Ni-Co-Cu-O-S melts against olivine: Implications for sulfide melt mobility; Economic Geology, v. 96, p. 145–157.

Spath, C.S., III, Farhangi, N., Lesher, C.M., Carson, H.J.E., Mehrmanesh, K., and Houlé, M.G., 2016. Geology and genesis of Fe-Ni-Cu-(PGE) mineralization in the Black Label Hybrid Zone of the 2.7 Ga Black Thor Intrusive Complex, McFaulds Lake greenstone Belt, Ontario, Canada; Geological Survey of Western Australia Record 2016/13:72

Tonnelier, N.J., 2010. Geology and genesis of the Jinchuan Ni-Cu-(PGE) deposit, China; Ph.D. thesis, Laurentian University, Sudbury, Ontario, 232 p.

Zuccarelli, N., Lesher, C.M., Houlé, M.G., and Weston, R.J., 2017. Sulfide textural variations and multiphase ore emplacement in the Eagle's Nest Ni-Cu-PGE deposit, McFauld's Lake greenstone belt, Ontario, Canada; Proceedings of Mineral Resources to Discover: 14th SGA Biennial Meeting, v. 2, p. 583–586.

3D geological modelling of the Double Eagle – Black Thor intrusive complexes, McFaulds Lake greenstone belt, Ontario

A.B. Laudadio[1], E. Schetselaar[2], M.G. Houlé[3] and C. Samson[1]

[1]*Department of Earth Sciences, Carleton University, 1125 Colonel By Drive, Ottawa, Ontario K1S 5B6*
[2]*Geological Survey of Canada, 601 Booth Street, Ottawa, Ontario K1A 0E8*
[3]*Geological Survey of Canada, 490 rue de la Couronne, Québec, Quebec G1K 9A9*

Abstract

A 3D geological model is in development of the subsurface architecture and structural disposition of the Double Eagle (DEIC) – Black Thor (BTIC) intrusive complexes of the 'Ring of Fire' intrusive suite in northwestern Ontario. The 3D geological model is constrained by drillhole data from exploration claims, geological maps and a revised structural interpretation based on high resolution magnetic data. Gridded total magnetic field intensity grid was used to outline linear to curvilinear magnetic lows, defining a system of anastomosing shear zones that had previously been outlined on medium resolution magnetic data. Structural fabrics in drill core confirm that these shear zones define the contacts between ultramafic and gabbroic units within the intrusions, as well as the contacts with their felsic intrusive and volcanic host rocks. The Frank shear zone, which follows the northern margin of the ultramafic rock units in both intrusive complexes, displaces the chromite- and Ni-Cu-(PGE)-bearing ore zones within the DEIC for 1 to 1.5 km in a dextral apparent sense. To the south, the McFaulds shear zone overprinted the intrusive contact between the ultramafic rocks of the DEIC and its mafic-dominated volcanic host rocks. The 3D geological model will be used in an attempt to restore the displacement of the DEIC and BTIC with respect to their magmatic conduits in 3D space. This will ultimately provide new insights into the plumbing system associated with the Ni-Cu-(PGE) and chromite mineralization.

Introduction

The Double Eagle (DEIC) – Black Thor (BTIC) intrusive complexes, that host major chromite and Ni-Cu-PGE deposits of the 'Ring of Fire' region, is located within the central part of the Oxford-Stull Domain of the Superior Province in northwestern Ontario (Fig. 1, 2). These 2.73 Ga ultramafic to mafic intrusive complexes occur within the McFaulds Lake greenstone belt (MLGB) that records episodic volcanism, sedimentation, ultramafic to felsic intrusive activity and tectonism spanning from at least 2.83 to 2.66 Ga (Fig. 1: Metsaranta et al., 2015). This Archean basement is overlain by flat-lying Paleozoic carbonate-dominated strata and unconsolidated Quaternary deposits making exploration challenging.

The DEIC and BTIC consist of elongate ultramafic-dominated intrusions constituting a single multi-commodity komatiitic system with an apparent thickness of up to 3 km along a strike length of 15 km (Houlé et al., 2017). Both complexes exhibit a komatiitic affinity with thick lower ultramafic sequences composed of dunite, lherzolite, and websterite host a number of world-class chromite deposits (Blackbirds, Black Horse, Big Daddy, Black Creek, Black Label and Black Thor), one major Ni-Cu-(PGE) deposit (Eagle's Nest), and numerous Ni-Cu-(PGE) occurrences (Fig. 1). The ultramafic sequences are overlain by a thinner mafic upper sequence composed mainly of melanogabbro, mesogabbro, and leucogabbro with lesser anorthosite (Fig. 2). Since the tectonic and structural influences on the plumbing systems of these Cr-(PGE) and Ni-Cu-(PGE) deposits are not well-constrained it remains to be determined whether the BTIC and DEIC formed as a single complex that has been tectonically dismembered or as two separate intrusions derived from the same magmatic source (Houlé et al., 2017).

This study aims to establish the architecture of the Black Thor (BTIC) and Double Eagle (DEIC) intrusive complexes in the McFaulds Lake greenstone belt. A 3D geological model is in development to examine the subsurface geometry and structural disposition of both intrusive complexes. Analyzing the spatial relationships between the main shear zones and the intrusive complexes, will help differentiate between the intact intrusive contacts and those transposed by post-ore deformation. This will provide new insights into the structural setting of the DEIC and BTIC, and thus the magmatic komatiitic plumbing system.

Methodology

The 3D geological model of both intrusive complexes is constrained by drillhole data, interpretations of high resolution aeromagnetic data and geological map compilations

Corresponding author: Alexandra Laudadio (AlexLaudadio@cmail.carleton.ca)

Laudadio, A.B., Schetselaar, E., Houlé, M.G,. and Samson, C., 2018. 3D geological modelling of the Double Eagle – Black Thor intrusive complexes, McFaulds Lake greenstone belt, Ontario; *in* Targeted Geoscience Initiative: 2017 report of activities, volume 2, (ed.) N. Rogers; Geological Survey of Canada, Open File 8373, p. 35–41. https://doi.org/10.4095/306599

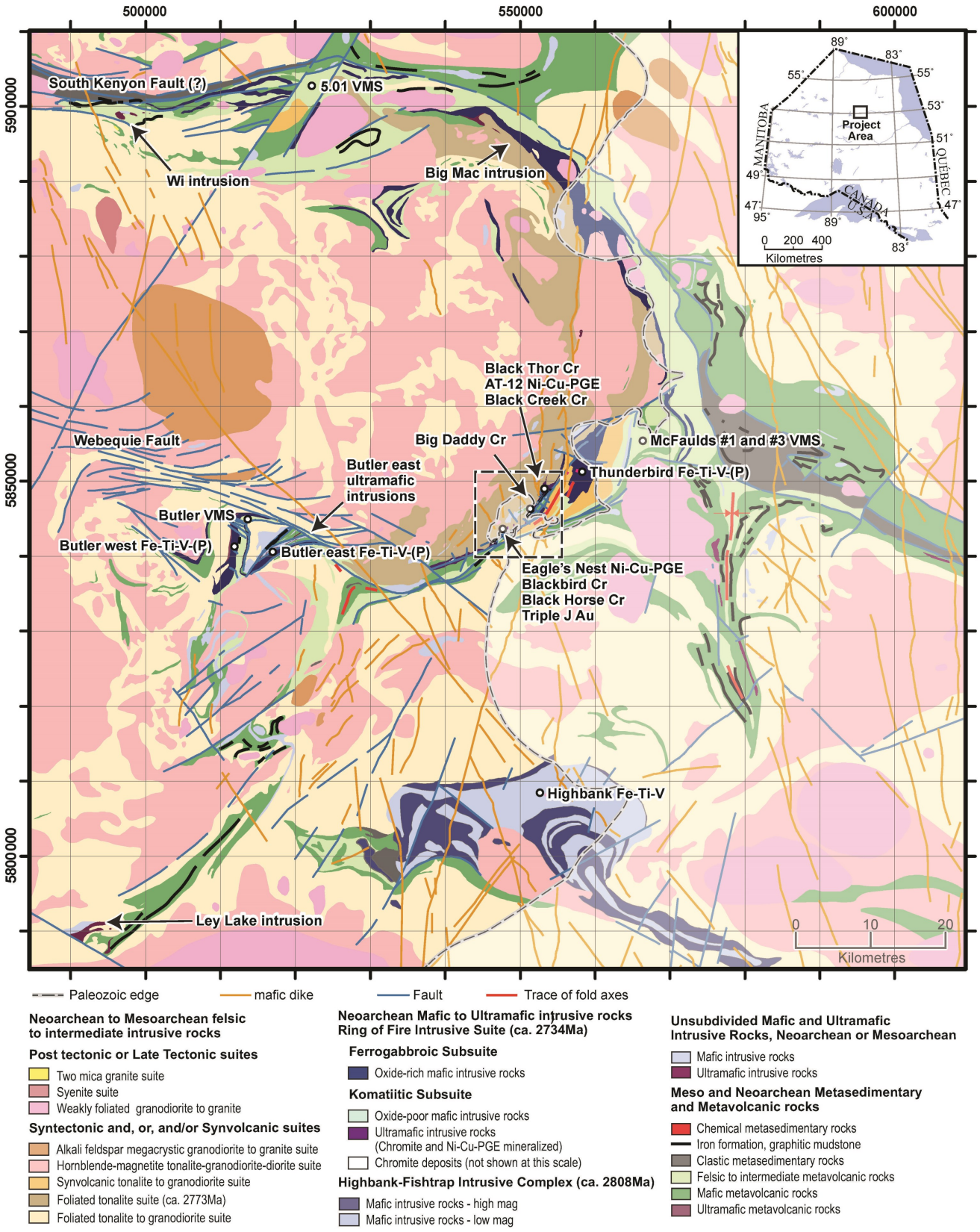

Figure 1. Simplified geological map of the McFaulds Lake greenstone belt showing the location of the main mineral deposits and occurrences in the 'Ring of Fire' region (from Metsaranta and Houlé, 2017a–c). Paleozoic cover rocks occur to the west of the Paleozoic edge line.

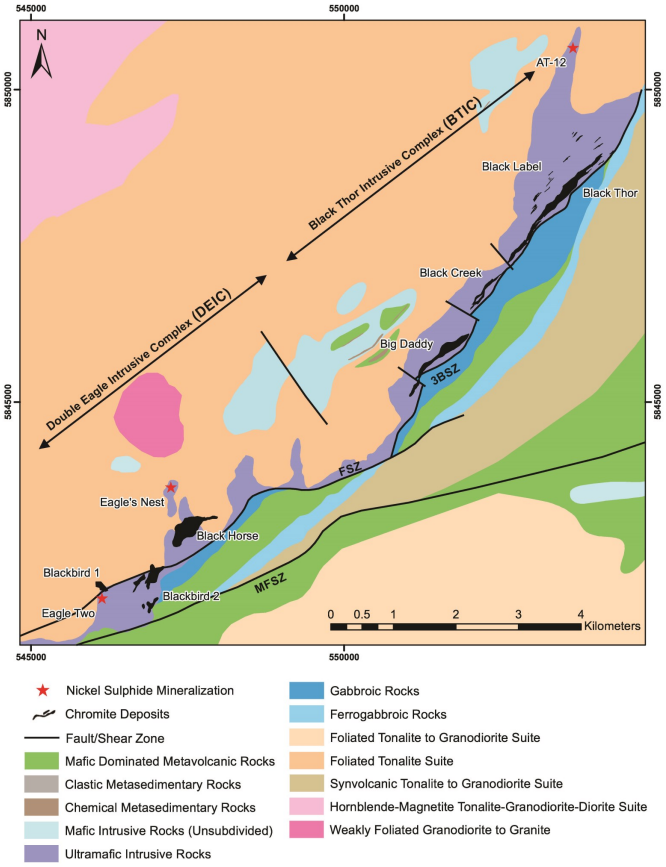

Figure 2. Geological map of the central part of the McFaulds Lake greenstone belt re-interpreted after Metsaranta and Houlé (2017b). The chromite deposits are the surficial representation of the respective ore zones lying at and below the surface. FSZ = Frank shear zone; 3BSZ = 3B splay of the FSZ; MFSZ = McFaulds Lake shear zone .

(Metsaranta and Houlé, 2017a, b, c). The first stage in model development consisted of building a thematic and systematically encoded drillhole database to harmonize available data from the various exploration claims in the area. Drill logs from approximately 1700 drillholes across the McFaulds Lake area have been compiled into a single database, with records organized into multiple thematic tables (lithostratigraphy, lithology, mineralization, alteration and structure). Drill log records belonging to these five themes were parsed out and systematically categorized into multiple levels of generalization (Fig. 3a; Laudadio et al., 2017). This thematic standardization of the drill log records facilitated establishing hole-to-hole correlations of laterally persistent unit contacts and key structures (e.g. faults and shear zones).

A preliminary 3D geological model was built (Fig. 3b) by fitting triangulated 3D surfaces to pre-selected drillhole markers and their corresponding 2D surface traces extracted from the regional geological map (Metsaranta and Houlé, 2017b). This 3D geological model was validated by re-logging 38 drillholes from across the McFaulds Lake area. The primary intention of this drillhole logging campaign was to establish contact relationships between specific units, validate the structural interpretation of the magnetic data and verify problematic intervals identified during the harmonization of the drillhole database.

Preliminary Results

The structural interpretation of high resolution magnetic data (Fig. 4a) and selected drill core intervals largely corroborates the structures presented on the previous geological map (Fig. 4b; Metsaranta and Houlé, 2017b). The northeast trending linear to curvilinear magnetic lows on the high resolution data (Fig. 4a), although more complex in shape, broadly correspond to linear magnetic lows on the medium resolution colour relief shaded grids (Fig. 4b). However, structural interpretation of the high resolution magnetic data indicates a connection between the Frank shear zone (FSZ) and the 3B shear zone (3BSZ) as a triple junction, which may suggest that they once formed a single structure that was dextrally offset along a newly developed splay at an angle to the overall regional strike.

Magnetic lows are spatially associated with shear fabrics observed in drill core, aligned over several kilometres along strike, which is in concordance with the linear magnetic lows corresponding to a series of anastomosing northeast trending shear zones (Fig. 4). Quartzo-feldspathic protomylonitic to mylonitic fabrics in granodiorite, felsic volcanic units and strongly foliated, intrusive ultramafic schist indicate that these regionally significant structures are predominantly ductile.

Dipping approximately 60° to the northwest, the FSZ (Fig. 2) developed preferentially in serpentinized and talc altered peridotitic, pyroxenitic and dunitic rocks. The FSZ is interpreted as one of the main tectonic structures accommodating displacement of lithological units and ore zones within the DEIC (M. Deller, pers. comm., 2017). The high strain zones of the FSZ and the 3BSZ predominantly overprint the contact between the ultramafic and mafic intrusive phases in both complexes (Fig. 2). The sigmoidal curvature and discontinuity of gabbro and mafic metavolcanic rocks units along the FSZ near this Y-shaped triple junction suggest a dextral sense of movement with a minimum offset of approximately 1 to 1.5 km (Fig. 2). This displacement is consistent with the relationship to the southwest where the DEIC sulphide-mineralized feeder (Eagle's Nest deposit) north of the FSZ is separated from the chromite deposits south of the FSZ (Eagle Two, Black Horse, Blackbird 1 and Blackbird 2: Fig. 2).

Variations in thickness and strain intensity of the sheared intervals suggest that the FSZ is heterogeneous in nature. Following this shear zone along strike, it transects the granodiorite (Fig. 5a) of the foliated tonalite suite in the southwest before it follows the contact between this unit and talcose peridotite of the DEIC (Fig. 5b). Drill core observations indicate that the high strain zone extends for several tens of metres into both units. After transecting the intrusive ultramafic rocks of the DEIC, the FSZ juxtaposes ‘lobe-shaped’ intrusive ultramafic

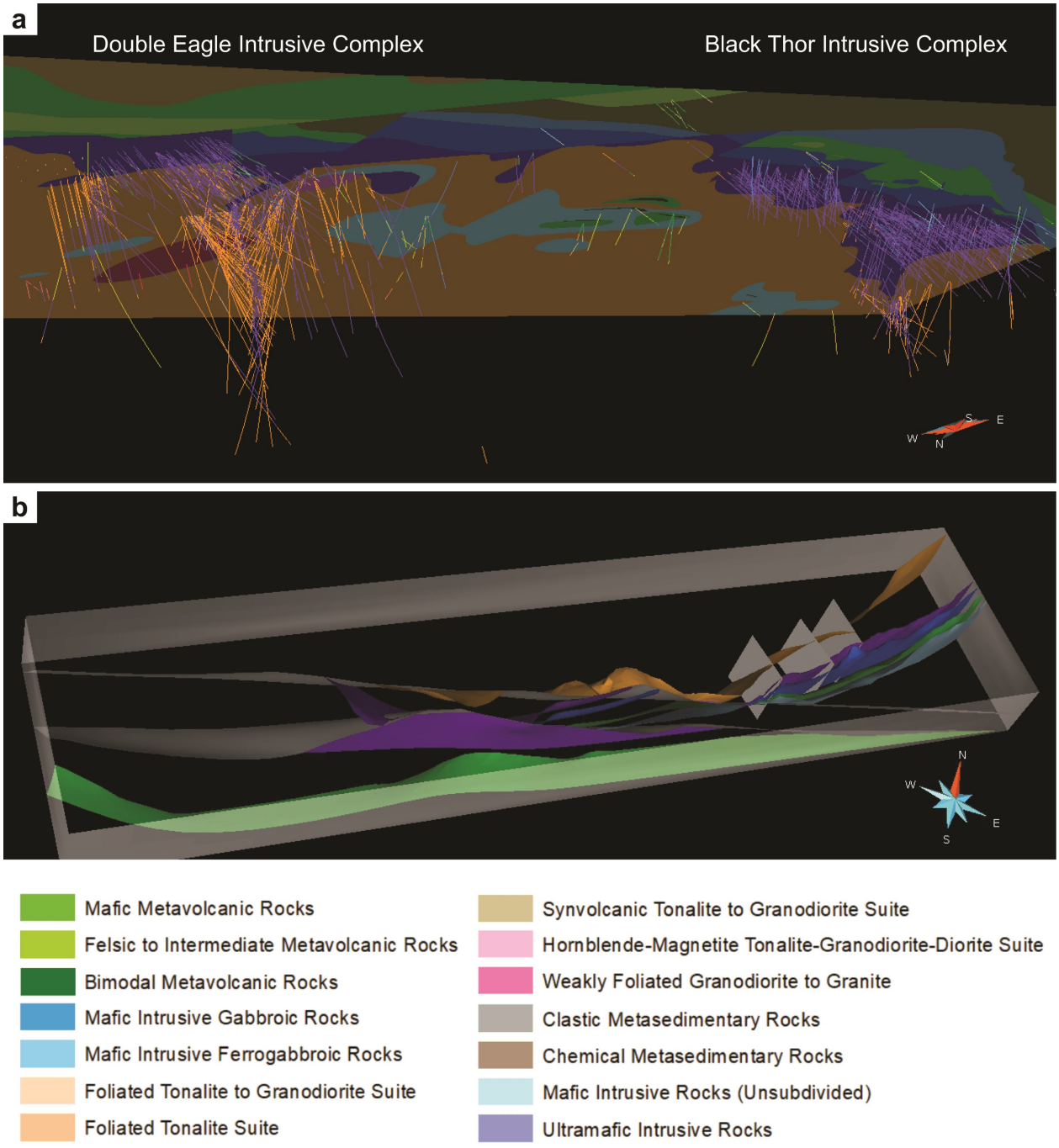

Figure 3. a) 3D scenes of the Double Eagle – Black Thor intrusive complexes illustrating the spatial correlation of generalized drillhole lithologies with their respective map units (after Metsaranta and Houlé, 2017b). b) Preliminary 3D geological model of the DEIC and BTIC, considering only the tectonic structures that transect the lithological contacts at a perpendicular angle producing significant displacement of the lithological units.

units in the hanging wall with the upper gabbroic sequence of the DEIC in the footwall. The lobe-shaped ultramafic unit in the hanging wall furthest to the southwest hosts the Eagle's Nest deposit and is interpreted as one of the feeders of the DEIC layered intrusion (Houlé et al., 2017). Further towards the northeast, the FSZ transects the gabbro, mafic-dominated volcanic host rocks and ferrogabbro intrusions. The preservation of sharp contacts between undeformed serpentinized peridotite and granodiorite in drill core (Fig. 5c) in combination with the irregular shape of the contact on the map compilation, suggests that the primary intrusive lower contacts of the DEIC and BTIC are relatively intact.

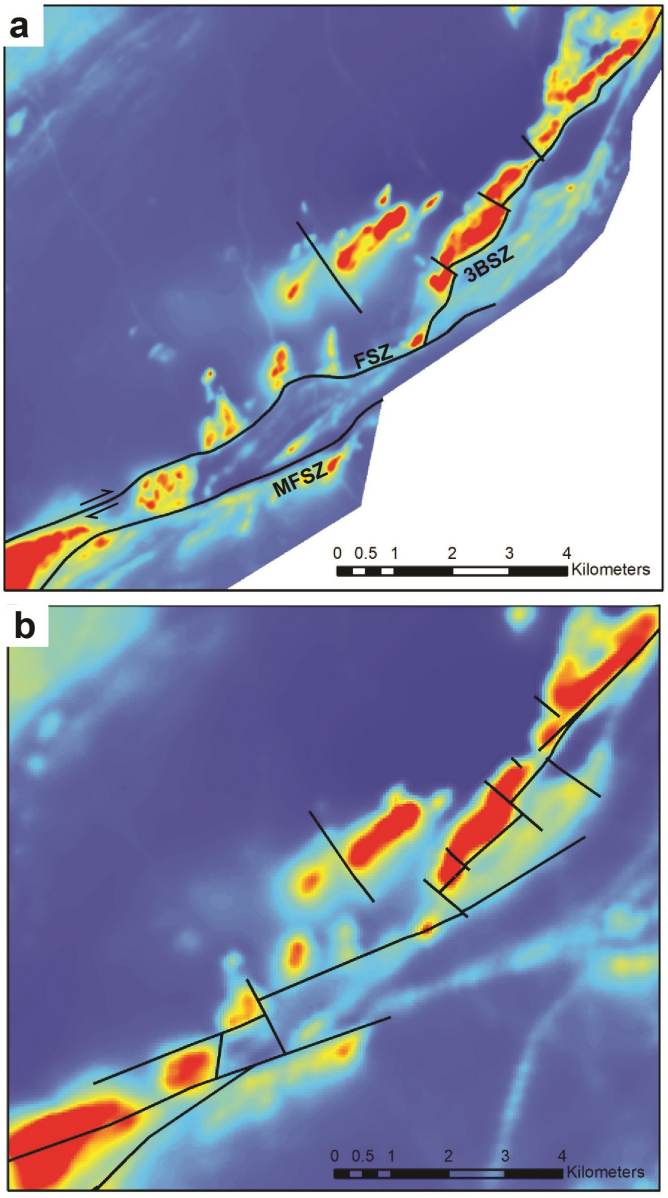

Figure 4. a) High resolution magnetic data (gridded from 75 m line spacing) with overlay of re-interpreted structures used to constrain the 3D geological model; b) Medium resolution magnetic data (gridded from 250 m line spacing) with overlay of structural elements interpreted by Metsaranta and Houlé (2017b). FSZ = Frank shear zone; 3BSZ = 3B splay of the FSZ; MFSZ = McFaulds Lake shear zone .

The MF shear zone (MFSZ), another regionally significant structure of the McFaulds Lake greenstone belt located to the south of the complexes (Metsaranta and Houlé, 2017b), follows the contact between the intrusive ultramafic rocks of the DEIC and the felsic and mafic volcanic rocks of the mafic-dominated volcanic unit (Fig. 5b, d–f) adjacent to the Blackbird 2 chromite deposit. Drill core observations show that the MFSZ steps away from the intrusive contact with strongly developed shear fabrics in felsic intervals of the mafic-dominated volcanic units (Fig. 5f). These felsic rocks likely acted as preferential zones of weakness during shear zone deformation. Towards the east-northeast, the MFSZ transects the mafic dominated volcanic rocks, ferrogabbro intrusion and synvolcanic tonalite (Fig. 2). A series of late-stage northwest striking brittle faults with minor offsets of 100 to 200 m displace sections of the BTIC (Fig. 2, 4b).

Future Work

Drill core data to characterize the 3D architecture and structural disposition of the DEIC and BTIC is currently being interpreted. Down-hole susceptibility data of the BTIC and DEIC will be examined in combination with petrographic analysis to investigate the effects of new growth and destruction of magnetite in shear zones, and corroborate geophysical responses of the various rock types present in the RoF region (Rainsford et al., 2017). Iterative improvements of the 3D geological model will be made by amending the drillhole database with the new observations, providing additional constraints for modelling the main lithological contacts and shear zones. Various 3D modelling approaches will be tested to select the optimal methodology for refining the geometry of the 3D surfaces, including the irregular lobe shaped contacts in the hanging wall of the FSZ. This next version of the 3D geological model will also be used to develop high resolution curvilinear grid models of the Black Thor, Black Label and Blackbird chromite horizons using assay data.

Acknowledgments

This report is a contribution to NRCan's Targeted Geoscience Initiative Program (TGI). Support for this study was provided through the Ni-Cr-PGE Systems Project's 'Activity NC-2.1: Architecture of magmatic conduits in Cr-(PGE)/Ni-Cu-(PGE) ore systems'.

Alexandra Laudadio is conducting a TGI supported M.Sc. at Carlton University, Ottawa. The authors are grateful to Noront Resources Ltd. (Alan Coutts, Ryan Weston, Matt Downey, Stephen Flewelling, Matt Deller, Geoff Heggie, Cory Exell, Rob Lyght, Tristan Megan and Roydon Spence) for providing access to properties, geological information and for very informative discussions throughout project development. This research activity would not have reached fruition without their knowledge and strong support. Moe Lavigne from KWG is also thanked for providing access to properties, diamond drill cores, geological information and for ongoing support and discussions. This report benefited from the review of Neil Rogers.

References

Houlé, M.G., Lesher, C.M., Schetselaar, E., Metsaranta, R.T., and McNicoll, V.J., 2017. Architecture of magmatic conduits in Cr-(PGE)/Ni-Cu-(PGE) ore systems; *in* Targeted Geoscience Initiative – 2016 Report of Activities, (ed.) N. Rogers; Geological Survey of Canada, Open File 8199, p. 55–58.

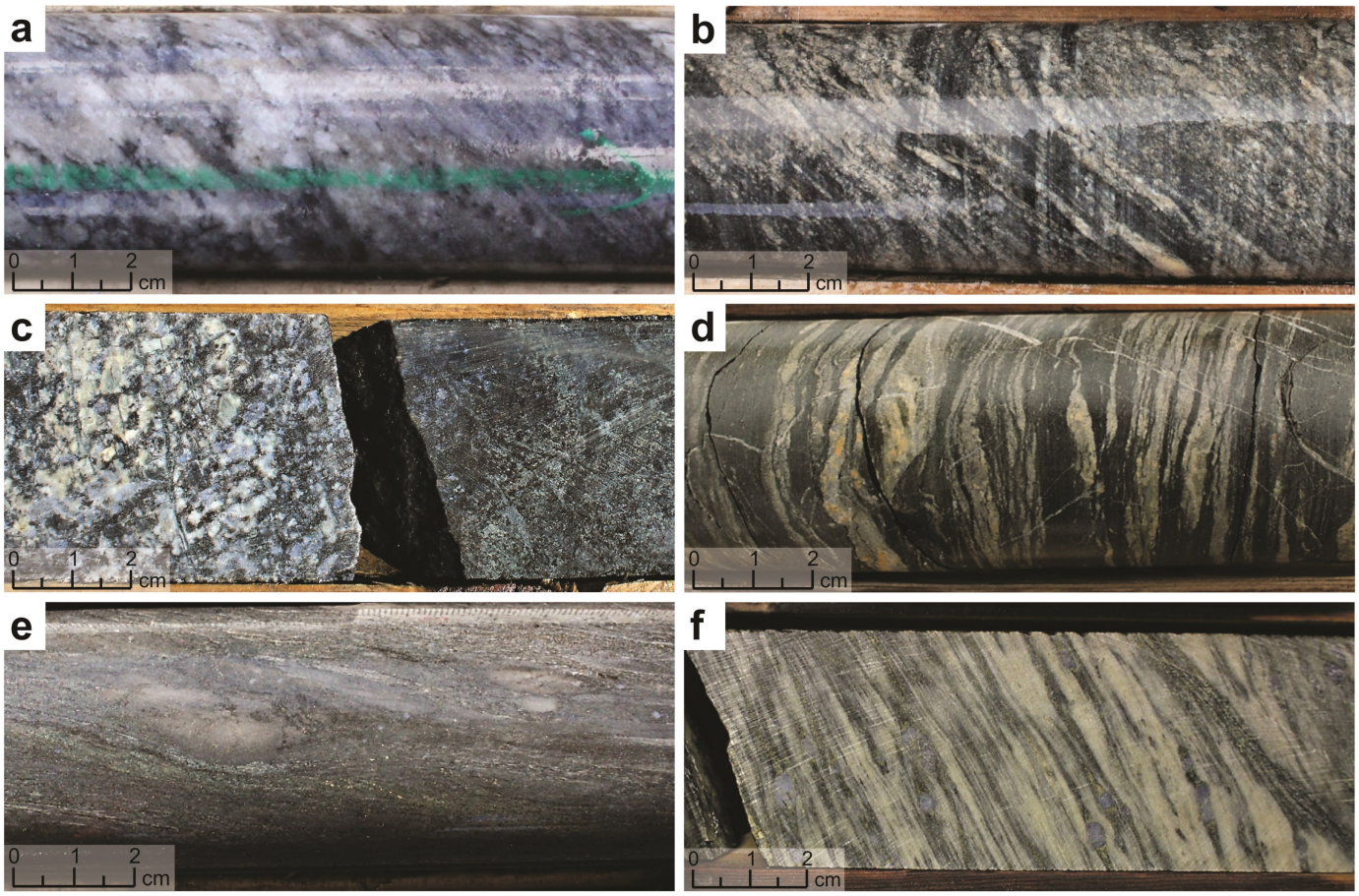

Figure 5. a) Sheared, medium-grained granodiorite of the Frank shear zone (FSZ) that exhibit a planar fabric composed primarily of biotite and ribbons of blue-grey quartz wrapping around plagioclase porphyroclasts. Drillhole NOT-10-1G194 at 538.23 m. b) Highly sheared, fine grained, talc-carbonate altered peridotite of the FSZ exhibiting strong foliation. Drillhole NOT-10-1G194 at 541.86 m. c) Sharp intrusive contact between granodiorite (left) and serpentinized peridotite (right) with preserved medium grained cumulate texture (pseudomorphic pyroxene and olivine). Drillhole FW-08-06 at 103.51 m. d) Sheared, fine-grained green chlorite/calcite altered mafic volcanics, within the mafic dominated volcanic unit, that exhibit a strong planar fabric. Drillhole NOT-08-1G078 at 386.5 m. e) Fine to medium grained felsic lapilli tuff with a fine grained matrix of quartz and biotite forming foliation. Rounded to angular lapilli composed of quartz and feldspar within the mafic dominated volcanic unit. Drillhole NOT-08-1G079 at 307 m. f) Mylonitized felsic volcanic rock interval within the mafic-dominated volcanic unit. The mylonitic foliation is defined by coarse blue-grey quartz porphyroclasts wrapped by fine grained light bands of carbonate and quartz and dark bands of chlorite and biotite. Drillhole NOT-08-1G079 at 423.8 m. Core diameter is 4.5 cm .

Laudadio, A.B., Schetselaar, E.M., Houlé, M.G., and Samson, C., 2017. 3D geological modelling of the Double Eagle – Black Thor intrusive complexes, McFaulds Lake greenstone belt, Ontario, Canada; Abstract, PDAC-SEG Student Minerals Colloquium, Prospectors and Developers Association of Canada, Toronto, Ontario <http://cmic-footprints.ca/smc/2017> [accessed February 11, 2018].

Metsaranta, R.T. and Houlé, M.G., 2017a. Precambrian Geology Winiskisis Channel area, "Ring of Fire Region", north sheet; Ontario Geological Survey, Preliminary Map P.3804; Geological Survey of Canada, Open File 8200, scale 1:100 000.

Metsaranta, R.T. and Houlé, M.G., 2017b. Precambrian Geology of the McFaulds Lake area, "Ring of Fire Region" - Central Sheet; Ontario Geological Survey, Preliminary Map P.3805; Geological Survey of Canada, Open File 8201, scale 1:100 000.

Metsaranta, R.T. and Houlé, M.G., 2017c. Precambrian Geology of the Highbank Lake Area - "Ring of Fire Region", Southern sheet; Ontario Geological Survey, Preliminary Map P.3806; Geological Survey of Canada, Open File 8202, scale 1:100 000.

Metsaranta, R.T., Houlé, M.G., McNicoll, V.J., and Kamo, S.L., 2015. Revised geological framework for the McFaulds Lake greenstone belt, Ontario; *in* Targeted Geoscience Ini-

tiative 4: Canadian Nickel-Copper-Platinum Group Elements-Chromium Ore Systems – Fertility, Pathfinders, New and Revised Models, (ed.) D.E. Ames and M.G. Houlé; Geological Survey of Canada, Open File 7856, p. 61–73.

Rainsford, D.R.B., Diorio, P.A., Hogg, R.L.S., and Metsaranta, R.T., 2017. The use of geophysics in the Ring of Fire, James Bay Lowlands – The chromite story; *in* Proceedings of Exploration 17: Sixth Decennial International Conference on Mineral Exploration, (ed.) V. Tschirhart and M.D. Thomas; p. 649–662.

New geochronological insights into the Taltson Domain of northern Alberta and Saskatchewan

J.W. Powell[1], D.I. Pană[2], C.D. Card[3], E.G. Potter[1], V. Tschirhart[1] and N. Joyce[1]

[1]*Geological Survey of Canada, 601 Booth Street, Ottawa, Ontario KIA 0E8*

[2]*Alberta Geological Survey, 4th Floor, Twin Atria Building, 4999-8th Avenue, Edmonton, Alberta T6B 2X3*

[3]*Saskatchewan Geological Survey, 2101 Scarth Street, Regina, Saskatchewan S4P 3V7*

Abstract

Recent discoveries of basement-hosted uranium deposits, such as those of the Patterson Lake corridor along the southwestern margin of the Athabasca Basin, have underscored the potential of high-strain corridors within the southwest Rae Province as major fluid conduits. Although these buried basement domains have often been defined using airborne geophysical data, the paucity of regional geochronological information makes it difficult to relate the geophysical signatures to the regional tectonothermal history. This report presents new zircon U-Pb Sensitive High-Resolution Ion Microprobe and biotite $^{40}Ar/^{39}Ar$ geochronological data for six samples that span the Taltson Domain of the southwest Rae Province. Three orthogneiss and one pegmatite sample from the Marguerite River area of northern Alberta crystallized at ca. 1.97 Ga and intruded 2.1 to 2.7 Ga crust, and biotite from a mylonitic shear zone yielded a ca. 1.82 Ga $^{40}Ar/^{39}Ar$ cooling age. Zircon cores from a sample of granitic gneiss sampled along the Clearwater River in northern Saskatchewan returned an imprecise crystallization age of 2422 ± 28 Ma (MSWD = 1.4), whereas recrystallized rims record granulite-facies metamorphism at 1923.0 ± 7.3 Ma.

Introduction

The Proterozoic Athabasca Basin and its surrounding basement rocks are the primary exploration target for uranium deposits in Canada (Fig. 1). Although exploration has historically focused on the unconformity between Paleo- to Mesoproterozoic fluvial sandstones of the Athabasca Basin and the underlying Paleoproterozoic basement, recent discoveries outside and along the southwestern margin of the Athabasca Basin challenge the standard unconformity-related deposit models. In particular, the known uranium deposits along the Patterson Lake corridor (PLC), northwestern Saskatchewan, are situated well below the unconformity and in altered orthogneisses and mafic to ultramafic rocks belonging to the Taltson Domain of the Rae Province. These host rocks are atypical when compared to the basement of unconformity-related uranium deposits east of the Snowbird Tectonic zone, where the Athabasca Basin unconformably overlies Archean to Paleoproterozoic felsic orthogneisses and metasedimentary rocks of the Hearne province (Card, 2017). Ore lenses in the PLC are located in reactivated basement structures that exhibit multiple episodes of deformation, silicification, alteration and mineralization that postdate metamorphism. Whereas resolving the protracted fluid flow through these fault zones is imperative to understanding the PLC uranium system, a first order problem exists in that the age of the basement protoliths, and their subsequent metamorphic history, remain poorly defined (Card and Noll, 2016). Accordingly, we report six new geochronological ages (Sensitive High-Resolution Ion Microprobe (SHRIMP) zircon U-Pb; biotite $^{40}Ar/^{39}Ar$) obtained for five samples from the Marguerite River area of northern Alberta, along with an outcrop from the Clearwater River in northern Saskatchewan. These dates provide initial constraints on the Taltson Domain along the southwestern margin of the Athabasca Basin and a basis for further geochronology studies in the mineralized corridor.

Geology of the southwest Rae Province in Saskatchewan and Alberta

The Taltson Domain, composed of 1.99 to 1.92 granitoid rocks of the Taltson magmatic zone (Pană et al., 2007) and the Mesoarchean to Paleoproterozoic Taltson basement complex (Bostock et al., 1991; McNicoll et al., 2000), delineates the western margin of the Rae Province in Alberta and Saskatchewan (Fig. 1). The Taltson Domain is best exposed in northeastern Alberta, where three narrow, north trending subduction and collision related plutonic belts of the Taltson magmatic zone (1.97−1.96 Ga; ca. 1.986 Ga; 1.94−1.92 Ga) form a composite batholith that intrudes and reworks the older Taltson basement complex (Hoffman, 1988; McDonough et al., 2000; McNicoll et al., 2000; Card et al., 2014). The U-Pb zircon and monazite ages in metamorphic tectonites of the Taltson basement complex suggest granulite facies metamorphic conditions between ca. 1.95 Ga and ca. 1.93 Ga, partly contemporaneous with the 'late' granitoid pulses (Bostock et al., 1987; Grover et al., 1997; McNicoll et al., 2000). Monazite ages of 1.93 to 1.91 Ga and titanite ages of 1.92 to 1.85 Ga from variably foliated granitoid

Corresponding author: Jeremy Powell (jeremy.powell@canada.ca)

Powell, J.W., Pană, D.I., Card, C.D., Potter, E.G., Tschirhart, V., and Joyce, N., 2018. New geochronological insights into the Taltson Domain of northern Alberta and Saskatchewan; *in* Targeted Geoscience Initiative: 2017 report of activities, volume 2, (ed.) N. Rogers; Geological Survey of Canada, Open File 8373, p. 43–56. https://doi.org/10.4095/306600

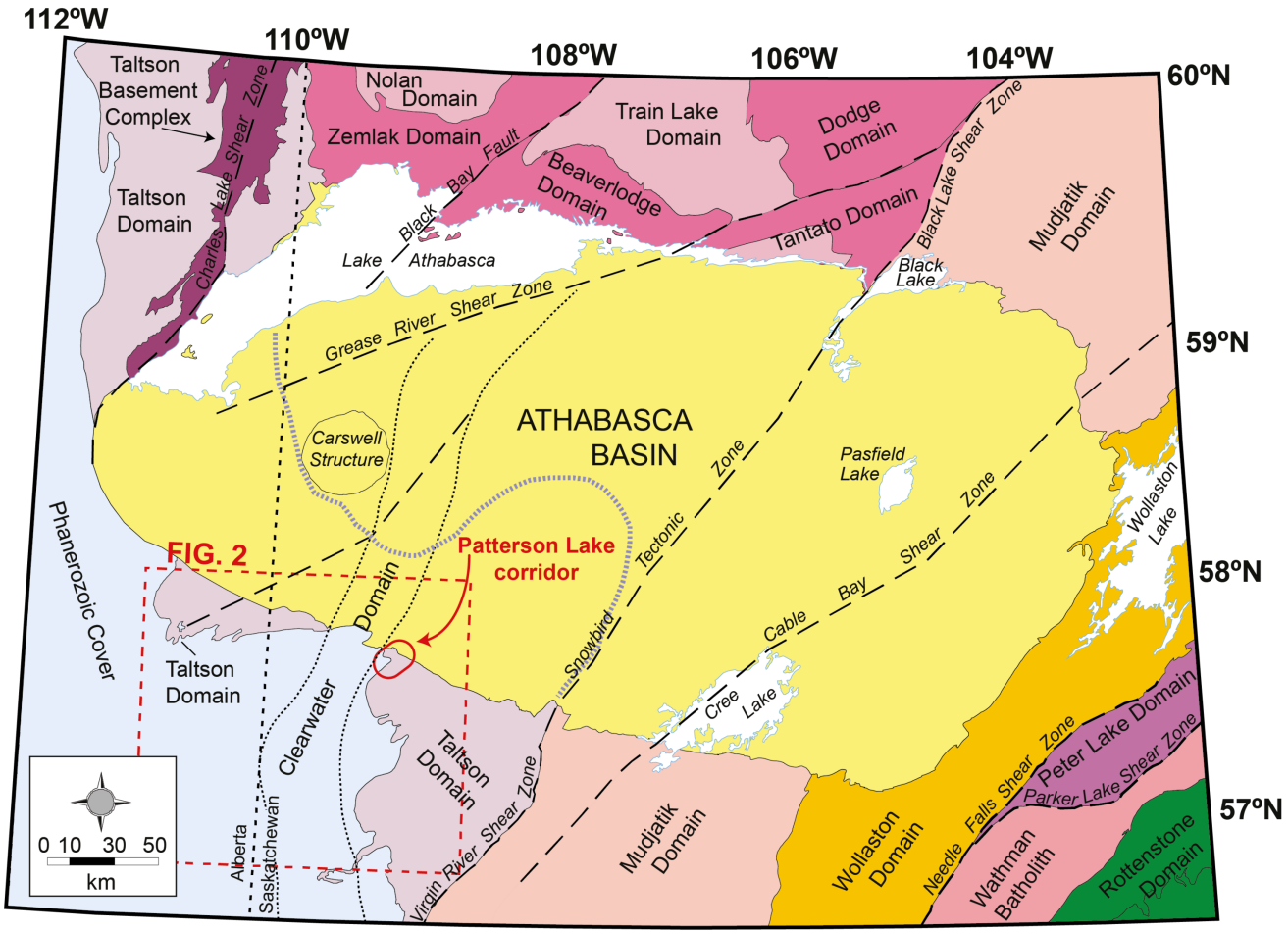

Figure 1. Geologic map highlighting basement domains of northern Saskatchewan and Alberta. Rocks discussed in this report, as well as host rocks for the Patterson Lake Corridor, lie within the Taltson Domain. The purple dotted line highlights the geophysical expression of the Taltson Domain underneath the Athabasca Basin. Black dotted lines denotes the surface projection of the Clearwater Domain. Modified after Card et al. (2007) and Jefferson et al. (2007).

rocks record syntectonic uplift during the passage from granulite to amphibolite-facies metamorphic conditions (McDonough et al., 2000; McNicoll et al., 2000; Pană et al., 2007). Aeromagnetic data suggests that the Taltson Domain extends further south, underlying the Proterozoic Athabasca Basin and Phanerozoic cover of the Western Canada Sedimentary Basin (Lyatsky and Pană, 2003; Pană et al., 2007). In Alberta, the only supporting evidence of this interpretation is a zircon U-Pb SHRIMP age of 1974 ± 5 Ma from the undeformed Maybelle granodiorite sampled from a drill hole proximal to erosional edge of the Athabasca Basin (Fig. 2; Stern et al., 2003). The Marguerite River area lies to the south of the Maybelle granodiorite and represents the only significant exposure of Precambrian bedrock in Alberta south of Lake Athabasca. Precambrian rocks of the Marguerite River area have not been dated prior to our study. However, many researchers (e.g. Ross 1991, 1992; Ross et al., 1993; Villeneuve et al., 1993) have suggested that the eastern half of the Marguerite River area, with a relatively low background magnetic field, is probably part of the Archean Rae Subprovince and the western half of the area, with a positive background magnetic field, is part of the Paleoproterozoic Taltson magmatic zone.

In Saskatchewan, rocks of the southwest Rae Province are predominantly granulite-facies orthogneisses and their retrogressed equivalents. Orthogneisses derived from dioritic and quartz dioritic protoliths are principle among these, with gneisses derived from granitoid precursors subordinate. Two diorite samples from the region have produced disparate U-Pb SHRIMP crystallization age determinations of 2459 ± 14 Ma (Card et al., 2014) and 1985 ± Ma (Stern et al., 2003). The older diorite is interpreted to be part of the Taltson basement complex, which forms part of a domain cored by Mesoarchean rocks that extends along the western part of the Rae Province from Saskatchewan to the Arctic Ocean (Davis et al., 2013). Gneissic granite that outcrops along the Clearwater River is also part of the Taltson basement complex, having returned an

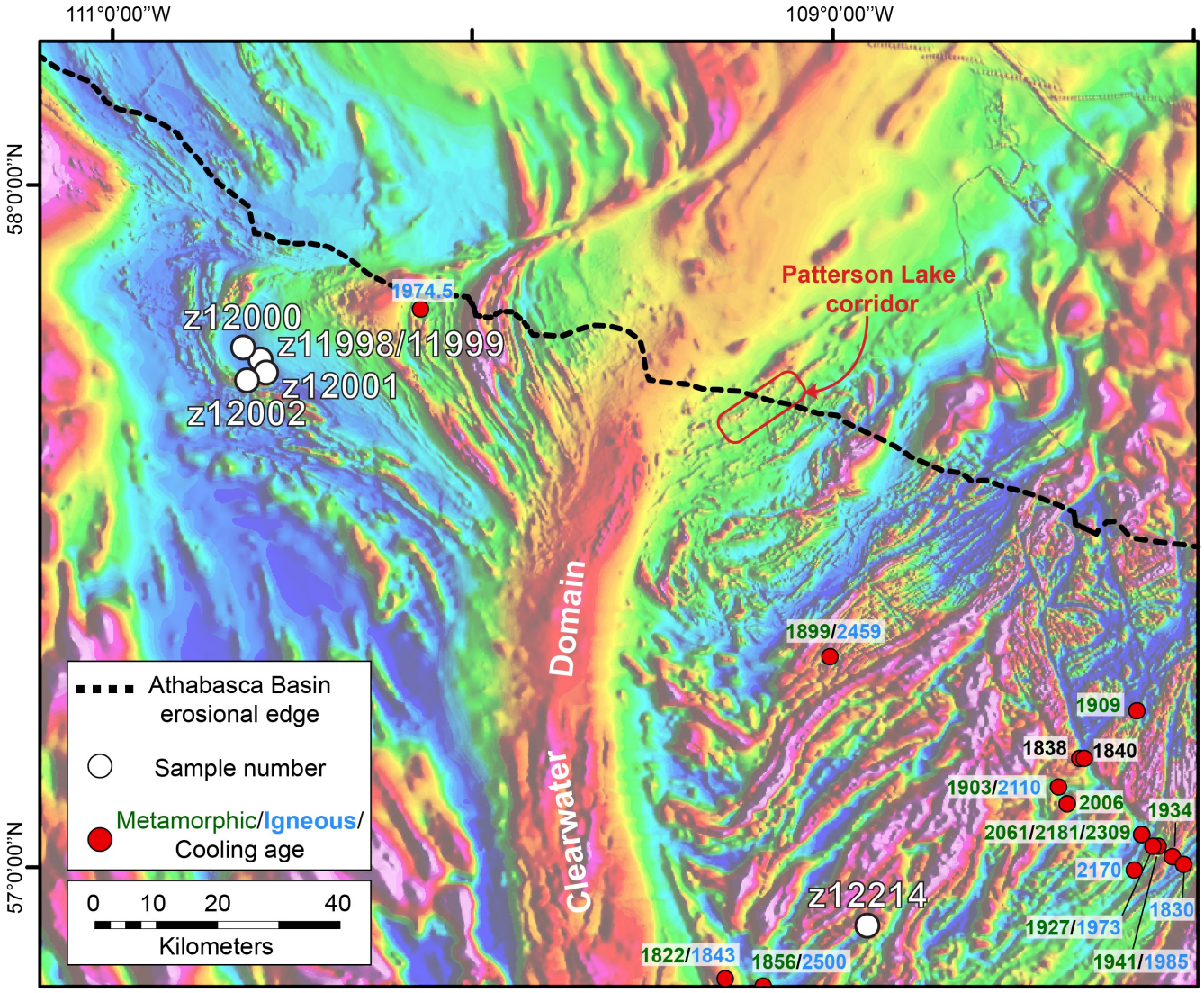

Figure 2. Aeromagnetic map (modified after Tschirhart, work in progress, 2017) of the study region showing sample locations and select zircon U-Pb and biotite $^{40}Ar/^{39}Ar$ ages from the southern Rae province (dates after Bickford et al., 1994; Halls and Hanes, 1999; Stern et al., 2003; Card et al., 2014).

imprecise U-Pb SHRIMP age determination of 2529 ± 16 Ma (Stern et al., 2003). Rocks of the Taltson basement complex were intruded by an extensive, 50 km long by 3 to 11 km wide, anorthosite complex that has returned a U-Pb SHRIMP crystallization age of 2110 ± 16 Ma (Card et al., 2014). The younger diorite, along with a leucotonalite that returned a crystallization age of 1975 ± 5 Ma (Stern et al., 2003), indicate an extension of the Taltson magmatic zone from Alberta into Saskatchewan. A regional metamorphic event between 1.94 and 1.93 Ga resulted in widespread, medium pressure, granulite facies mineral assemblages (Card et al., 2014). A second event at ca. 1.90 Ga, led to hydration and replacement of the older mineral assemblage with middle amphibolite facies minerals, particularly near major structural zones (Card et al., 2014). There is little to no evidence of a major metamorphic overprint during the 1.90 to 1.80 Ga Trans-Hudson orogeny, suggesting that the southwest Rae Province was rapidly exhumed after ca. 1.90 Ga (Mahan et al., 2006). Rather, the effects of the Trans-Hudson are manifested, in part, by post-metamorphic granite intrusions commonly emplaced in structural corridors between 1843 and 1819 Ma (Bickford et al., 1994; Stern et al., 2003).

Sample descriptions

The six samples investigated in this study were obtained from outcrops of Taltson Domain basement along the southwestern margin of the Athabasca Basin across Alberta and Saskatchewan (Fig. 2). Five of these samples span four localities across the Marguerite River area of northern Alberta. Samples z11998 to z12001 correspond to a broad aeromagnetic low that

is typified by fine- to medium-grained biotite orthogneiss with minor garnet, likely derived from microgranodiorite. Regionally, leucocratic and coarser grained varieties of biotite granodiorite are interlayered with quartz monzonite and granite forming kilometre long bands of white to grey gneiss. The igneous texture of the plutonic protoliths has been locally preserved, whereas most of the exposed rocks have acquired gneissic texture. In some cases, augen gneiss fabrics have developed in strained rocks with originally inequigranular igneous texture. In sample z11998 this augen gneiss texture developed in plagioclase grains (S2) overprints a northerly trending layering (S1) defined by biotite. In contrast, sample z11999 is a granitic pegmatite that was collected from the same outcrop as z11998 and is concordant with the S2 fabric (Fig. 3a). It is unclear from field relationships whether the pegmatite is pretectonic and emplaced at the same time as the quartz monzonite or syntectonic with the later deformation event. Sample z12000 (field # DP16-350) is a garnet, hornblende and biotite bearing quartz monzonite. The outcrop is weakly foliated, with an easterly subvertical foliation overprinting earlier subhorizontal layering (Fig. 3b). Shearing of the plutonic protoliths has produced mortar and mylonitic textures (Fig. 3c), as exemplified in sample z12001 where a massive, coarse-grained biotite-rich granodiorite is separated from an east trending medium grade-shear zone by a 25 cm thick ultramylonite layer (Fig. 3d). South of these localities, a narrow, linear aeromagnetic high coincides with a west-northwest kilometre wide shear zone that overprints all the rock types described in the Marguerite River area. Strain partitioning within the shear zone resulted in a series of proto- to ultramylonites with biotite-rich and leucocratic domains. A mylonitic gneiss (z12002) was sampled from this region for $^{40}Ar/^{39}Ar$ geochronology. The mylonite has alternating laminations characterized by polycrystalline quartz ribbons separated by a fine-grained, chloritic matrix (Fig. 3c). In the Taltson Domain of Saskatchewan, a sample of coarse-grained, garnet, biotite and pyroxene bearing granitic gneiss (z12214)

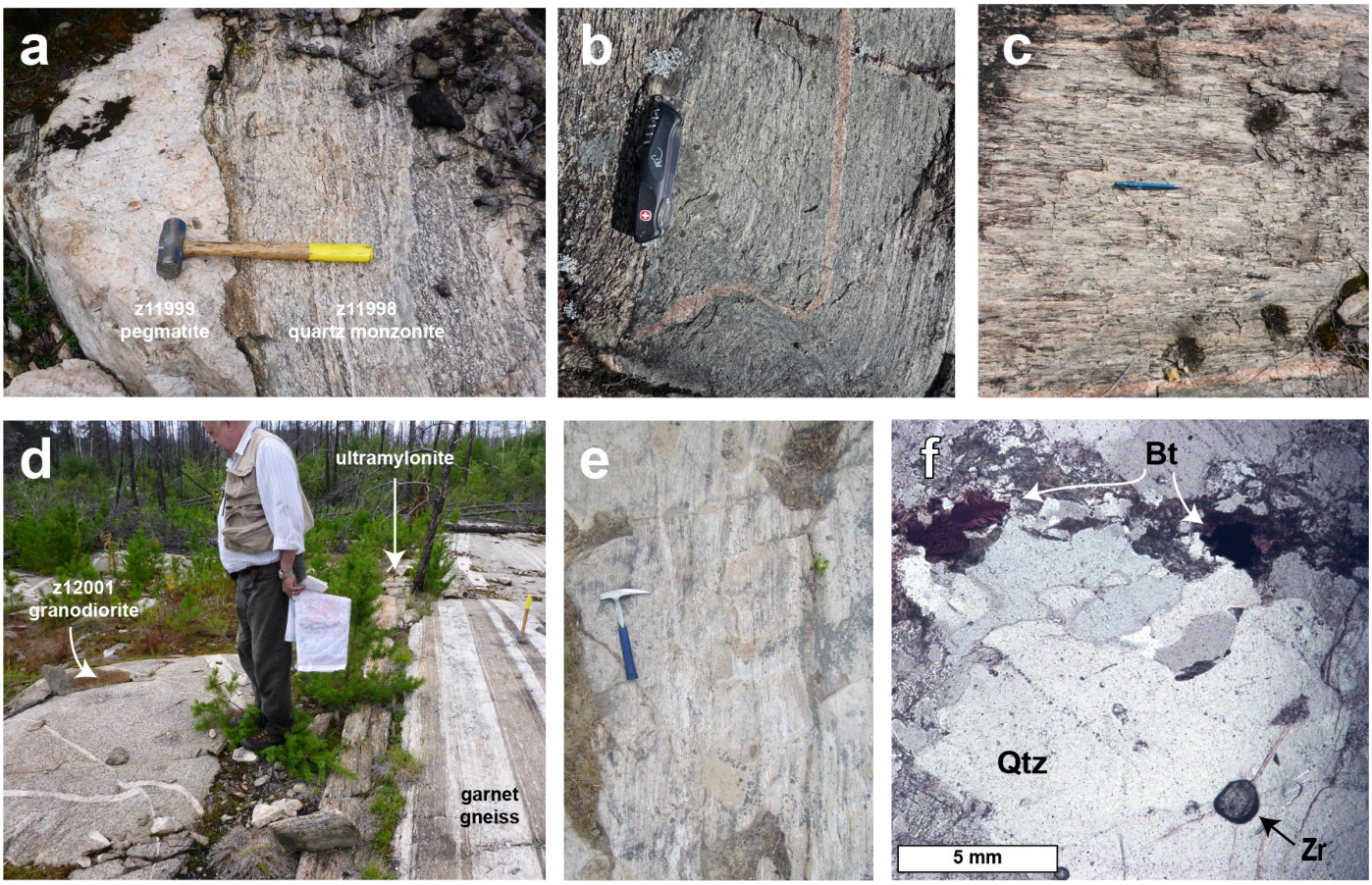

Figure 3. Representative images of Taltson Domain outcrops sampled for U-Pb and $^{40}Ar/^{39}Ar$ geochronology: a) Contact between quartz monzonite (sample z11998) and granitic pegmatite (sample z11999); b) Sample z12000 in outcrop; c) Mylonitic gneiss (z12002) sampled from aeromagnetic high in the Marguerite River area; d) Ultramylonitic contact between massive granodiorite (sample z12001) and garnet-gneiss; e) Granitic gneiss (sample z12214) outcrop along the Clearwater River in northern Saskatchewan; f) Photomicrograph of sample z12214 in plane polarized light, showing secondary quartz (qtz) surrounding a zircon (zr) crystal and embaying into and distorting biotite crystals (bt).

was collected for zircon U-Pb geochronology from an outcrop along the Clearwater River (Fig. 3e). In thin section, pyroxene is observed breaking down to biotite and the quartz appears to be secondary and reflective of pervasive silicification in the granitic gneiss (Fig. 3f).

Geochronologic methods and results

U-Pb geochronology

Following standard rock crushing and mineral separation, zircon grains of varying size and morphology (approximately 120 per sample) were mounted in two separate 2.5 cm epoxy pucks (IP864 and IP896) alongside primary and secondary laboratory standards (z6266, $^{206}Pb/^{238}U$ = 599 Ma; z1242, $^{207}Pb/^{206}Pb$ = 2679.7 Ma). Epoxy mounts were polished with diamond compound to reveal the mid-sections of zircon grains, and internal features such as zoning, cracks and alteration were imaged via backscatter electron (BSE), as well as cathodoluminescence (CL), using a Zeiss EVO50 scanning electron microprobe (SEM). SHRIMP (sensitive high-resolution ion microprobe) U-Pb zircon age determinations were conducted at the J.C. Roddick SHRIMP laboratory at the Geological Survey of Canada, in Ottawa. Analyses followed the procedures outlined in Stern (1997) and Stern and Amelin (2003). Briefly, analyses were conducted using an $^{16}O^-$ primary beam with spot sizes of 23 µm (z11998–z12002) and 15 µm (z12214) at a depth of approximately 1 µm. Data collection involved sets of six scans over 11 isotope masses of Zr, U, B, Th, Yb, Nd and Hf. Standards were analyzed every fourth analysis. Offline data processing was completed using SQUID2 (version 2.50.11.10.15, rev. 15 Oct 2011) and the common Pb correction utilized the Pb composition of the surface blank. Isoplot (v.4.15; Ludwig, 2009) was used to generate the Concordia diagrams and calculate weighted mean $^{207}Pb/^{206}Pb$ ages. Concordia error ellipses and weighted mean errors presented in the text are at the 95% confidence interval, whereas isotopic ratios and SHRIMP U-Pb zircon dates are reported at the 1σ level (Appendix 1).

Marguerite River U-Pb

Zircon grains recovered from sample Z11998 were 100 to 300 µm long, have euhedral, prismatic morphologies with well -developed oscillatory zoning visible in BSE images. In some cases, thick (20–50 µm) zoned rims surround diffusely zoned cores. Thirty-one analyses on 27 grains yield concordant (< 3% discordant) ages between 1924 and 2290 Ma (Fig. 4a). No systematic relationships were observed between uranium concentrations (182–1093 ppm U) and Th/U values (0.13–1.9) with respect to U-Pb data. The two oldest ages, 2225 and 2290 Ma, are considered inherited, as they were measured on structural cores and are distinctly older than the other analyses. Of the remaining 29 analyses, 25 form a concordant population with a weighted mean $^{207}Pb/^{206}Pb$ age of 1972.3 ± 4.3 Ma (MSWD = 2.2), which is interpreted as the crystallization age of the augen textured quartz monzonite. The youngest four analyses ($^{207}Pb/^{206}Pb$ ages of 1924 ± 12 to 1939 ± 7 Ma) are an enigmatic population with an uncertain interpretation. One of these analyses (z11998-10.2; 1927 ± 5 Ma; Appendix 1) is potentially attributable to a texturally recrystallized zone within a single zircon, whereas the others coincide with abnormal analytical conditions and were not subsequently reproducible.

Zircon recovery was poor in sample z11999, yielding only small (70−150 µm long) zircon grains with variable morphology, including euhedral, rounded and fragmentary grains. The majority of zircon grains display evidence of substantial lead loss, including extensive fractures and pitted zones that are dark in BSE images, and were not considered for U-Pb analysis. Twenty analyses from a smaller population of rounded to prismatic zircon grains with bright BSE intensities yielded U-Pb ages between 1787 ± 12 and 2690 ± 5 Ma (Fig. 4b). The vast majority of the data exhibit no relationship between U-Pb date and U concentration (180–816 ppm U) and Th/U (0.19–0.89). However, the youngest analysis ($^{207}Pb/^{206}Pb$ age = 1787 ± 18 Ma) corresponds to a zircon grain with a content of 1431 ppm U. We attribute this young age to partial lead loss related to metamictization and do not consider it any further. The two oldest analyses (2287 ± 13 Ma and 2690 ± 5 Ma) are distinctly older than the other ages and are interpreted as inherited cores. Thirteen analyses of oscillatory-zoned zircon grains and rims form a concordant population (< 4% discordant) with a mean $^{207}Pb/^{206}Pb$ age of 1968.3 ± 7.9 Ma (MSWD = 3.0). This age is within error of the quartz monzonite (sample z11998) through which it cuts, suggesting that the pegmatite was emplaced at the same time and deformed contemporaneously. Three younger analyses were excluded from this weighted mean date.

Zircon grains in sample z12000 are mostly prismatic and between 75 and 200 µm long. The CL images show well developed oscillatory zoning, as well as dark rims that encapsulate structural cores. Twenty-nine analyses from 25 zircon grains yield $^{207}Pb/^{206}Pb$ ages between 1933 ± 7 Ma and 2321 ± 8 Ma (Fig. 4c). Uranium concentrations for all analyses are distributed between 102 to 1024 ppm U, and Th/U values are between 0.03 and 1.15. A single zircon from which both core and rims were analyzed (z12000-122) exhibits a difference in Th/U value of 0.41 in the older core to 0.13 in the younger rim, despite similar uranium concentrations (729 ppm vs. 786 ppm U). The core ages are distinctly older than the remainder of the analyses and are interpreted to represent inheritance from Paleoproterozoic sources. A slightly discordant zircon analyses (2044 ± 6 Ma) is interpreted as a Paleoproterozoic zircon that has been subject to partial lead loss. Twenty-three ages form a concordant (< 4% discordant) population with a weighted mean $^{207}Pb/^{206}Pb$ age of 1977.5 ± 4.4 Ma (MSWD = 2.2) that is interpreted as the crystallization age of the quartz monzonite. A single younger analysis (1933 ± 7 Ma) was excluded from the weighted mean age calculation and will be discussed in detail later.

Zircon grains derived from sample z12001 are similar in size, morphology and CL response to those from z12000, being euhedral grains with pronounced oscillatory zoning. Thirty-six analyses were carried out on 30 zircon grains from sample

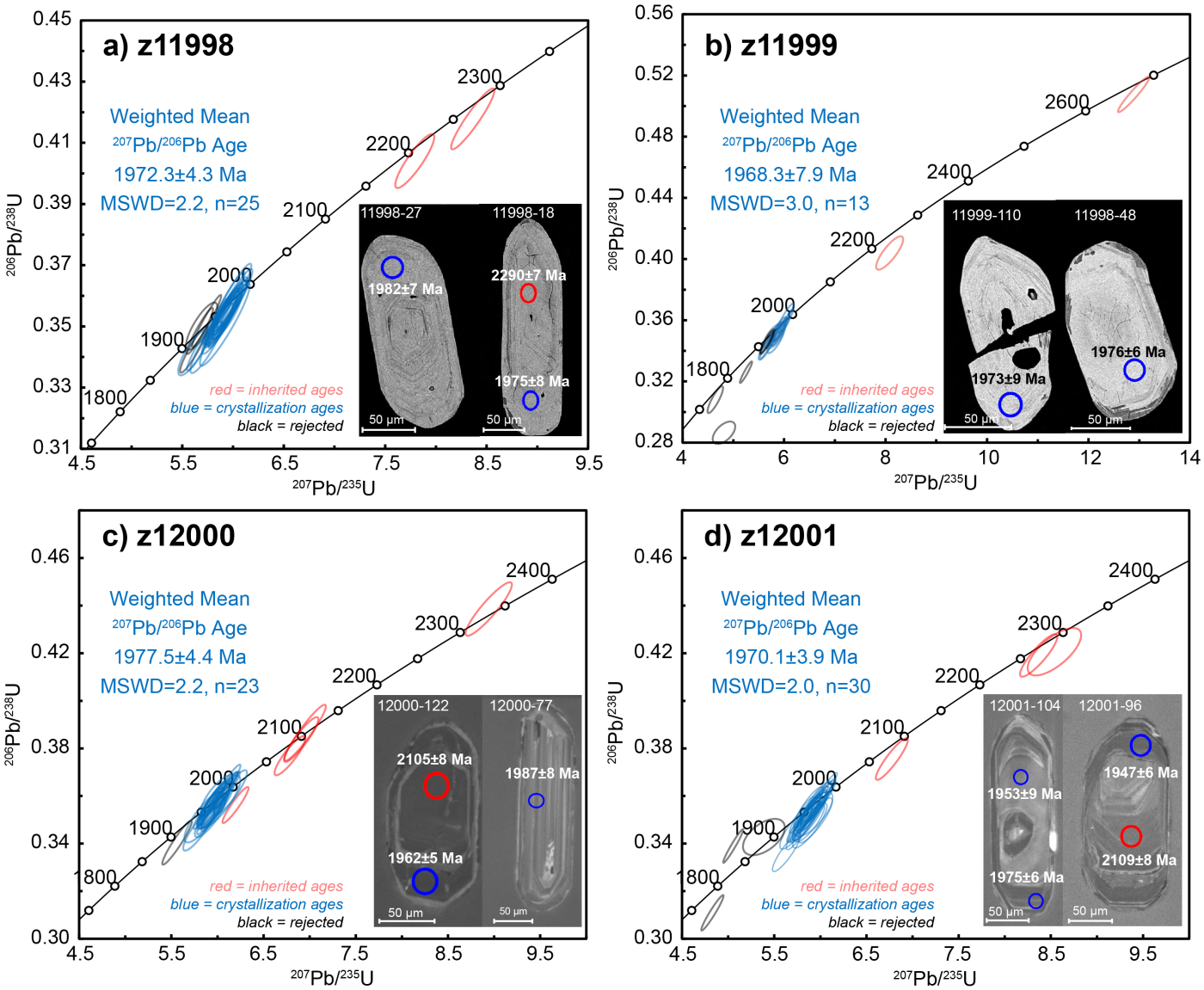

Figure 4. Concordia diagrams displaying U-Pb SHRIMP results for samples from the Marguerite River area of Alberta. Error ellipses are at the 95% confidence interval; data is provided in Appendix 1. Red, blue and black error ellipses reflect interpreted inherited, igneous crystallization and rejected analyses (discussed further in text). Inset images are of characteristic zircon grains (BSE, a–b; CL, c–d) with location of SHRIMP analyses and corresponding $^{207}Pb/^{206}Pb$ age. The colour of spot analyses in inset match error ellipses in the concordia diagram.

z12001. With the exception of the two youngest dates, which have high uranium contents ($^{207}Pb/^{206}Pb$ age = 1768 ± 4 and 1842 ± 5 Ma; U = 1487 and 1112 ppm) and are likely metamict, no relationships exist between variable uranium concentrations (177–1039 ppm U), Th/U values (0.13 to 0.91) and U-Pb ages of zircon cores and rims. Thirty analyses from oscillatory-zoned zircon grains and rims form a concordant population (< 4% discordant) with a weighted mean age of 1970.1 ± 3.9 Ma that is interpreted as the crystallization age of the granodiorite (Fig. 4d). The three older analyses from zircon cores ($^{207}Pb/^{206}Pb$ ages = 2109 ± 8 Ma to 2313 ± 17 Ma) are interpreted as inherited ages.

Whereas the ca. 1.97 Ga crystallization age is consistent for all four granitoids from the Marguerite River area, seven concordant dates of ca. 1.93 Ga were obtained from samples z11998, z11999 and z12000 (Fig. 4a–c). As stated previously, these analyses are not robust and lack a diagnostic textural or chemical pattern to distinguish them from the dominant population of crystallization ages. However, two analyses do correspond with apparent textural recrystallization (Fig. 5), in which irregular domains of homogeneous zircon grains cut across and disrupt the igneous growth zoning. In both zircon grains 11998 -10 (Fig. 5a) and 12000-106 (Fig. 5b) these textures have a more intense BSE response, higher uranium concentrations,

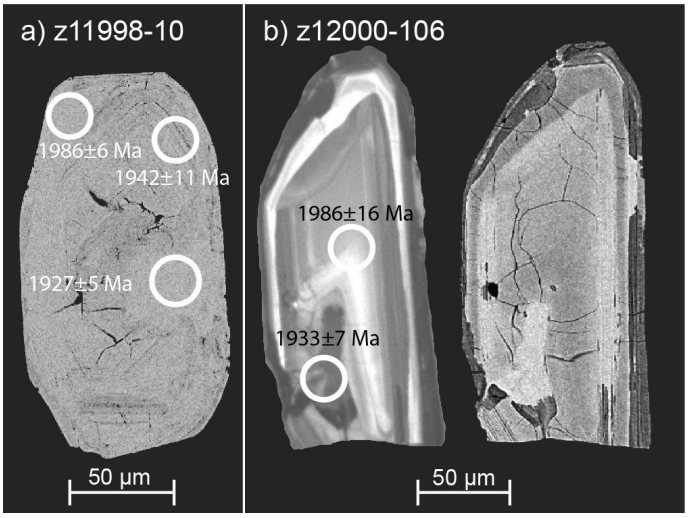

Figure 5. BSE and CL images of two zircon grains from the Marguerite River area that exhibit patches of local recrystallization that crosscut and convolute oscillatory growth zoning. SHRIMP U-Pb analyses indicate that these zones are younger than the surrounding igneous zircon and potentially date metamorphic or hydrothermal recrystallization.

lower Th/U ratios and yield younger $^{207}Pb/^{206}Pb$ ages than the surrounding igneous zircon. If these two analyses do correspond with local recrystallization at ca. 1.93 Ga, then the similar ages that lack obvious secondary textures may also be the product of subsolidus alteration.

Clearwater River granitic gneiss U-Pb

Zircon crystals recovered from sample z12214 form two discrete groups based on BSE imaging and morphology. The first is comprised of large (100–250 µm long), rounded to spherical grains, which are dark in BSE images and appear texturally homogeneous to faintly zoned. Some of these crystals contain obvious cores that have a brighter BSE response with better-defined zonation than the surrounding grain. The second group includes elongate (100–300 µm long) rounded to prismatic crystals that contain large cores with diffuse and oscillatory zoning. The surrounding rims are darker in BSE images and range in thickness from <10 µm to >50 µm. Twenty-nine analyses from 24 zircon grains yield $^{207}Pb/^{206}Pb$ ages between 1847 ± 53 Ma and 2565 ± 91 Ma (Fig. 6a). Structural cores are chemically distinct from rims with higher uranium contents (91–708 ppm versus 25–185 ppm U) and a more narrow range in Th/U values (0.18–0.70 vs. 0.14–2.8). Thirteen analyses from zircon cores have $^{207}Pb/^{206}Pb$ ages that span 2035 ± 20 Ma to 2565 ± 91 Ma. We attribute this dispersion to variable recrystallization during granulite facies metamorphism. This progression of $^{207}Pb/^{206}Pb$ ages in zircon cores becoming younger with increasing degree of recrystallization and resorption is observable in CL images (Fig. 6b–e). As a result, the crystallization age of z12214 is poorly defined and perhaps best approximated to the weighted mean $^{207}Pb/^{206}Pb$ age of 2422 ± 28 Ma (MSWD = 1.4) calculated from the five oldest, concordant zircon analyses. Comparatively, 16 concordant analyses from the zircon rims have a weighted mean $^{207}Pb/^{206}Pb$ age of 1923.0 ± 7.3 Ma (MSWD = 0.93), which is interpreted as the age of peak metamorphism.

$^{40}Ar/^{39}Ar$ geochronology

Laser $^{40}Ar/^{39}Ar$ step-heating analysis was carried out at the Geological Survey of Canada Noble Gas laboratory in Ottawa. Unaltered pieces of biotite (0.25–0.5 mm) were handpicked from samples z11998 and z12002 from the Marguerite River area of Alberta. Biotite separates were irradiated at the research reactor of McMaster University (GSC irradiation # 75a) for 960 MWh and irradiation flux was monitored with grains of PP -20 hornblende (Hb3gr equivalent: 1074 ± 5 Ma (1σ); Jourdan et al., 2006). Subsequent to irradiation, biotite grains were loaded into a copper planchet and placed into all-metal, ultra-high vacuum extraction line. Samples were step-heated using a Photon Machines 55W CO_2 laser, and released gas was analyzed isotopically using a Nu Instruments Noblesse noble gas spectrometer following the analytical methods and conditions of Kellett and Joyce (2014). Two single grain biotite aliquots for each sample were heated over 11 to 16 heating steps. Data collection and reduction calculations were performed using Mass Spec software version 7.93 (Deino, 2001).

Corrected argon isotopic data for samples z11998 and z12002 are reported in Appendix 2, however argon data from sample z11998 are highly disturbed and not discussed further. Results of step-heating experiments for both biotite aliquots from z12002 are displayed in Figure 7. We report pseudo-plateau ages for each aliquot, as the step-heating data do not meet the statistical rigours (three or more statistically equivalent consecutive heating steps that comprise greater than 50% of the total ^{39}Ar released) required for true plateau dates. However, the pseudo-plateau and integrated ages for both aliquots overlap (1820 ± 10 Ma to 1825 ± 7 Ma) suggesting a 1.82 Ga $^{40}Ar/^{39}Ar$ age for biotite from sample z12002.

Discussion and future work

New zircon U-Pb SHRIMP data presented in this study provide the first geochronological constraints for the age of the Precambrian basement in the Marguerite River area of northern Alberta. Previous interpretations have suggested that the basement in this area is part of the Archean Rae Province based on its low aeromagnetic signature relative to the high signatures expected for the Taltson magmatic zone (Villeneuve et al., 1993). However, crystallization ages between 1968 ± 7.9 Ma and 1977.5 ± 4.4 Ma reported in this study (Fig. 4a−d; Appendix 1) overlap with the 1974.5 ± 5 Ma Maybelle granodiorite to the northeast (Fig. 2; Stern et al., 2003) and 1.97–1.96 Ga 'I-type' granites of the Taltson magmatic zone north of the Athabasca Basin (McDonough and McNicoll, 1997; McDonough et al., 2000). These results confirm that the orthogneisses of the

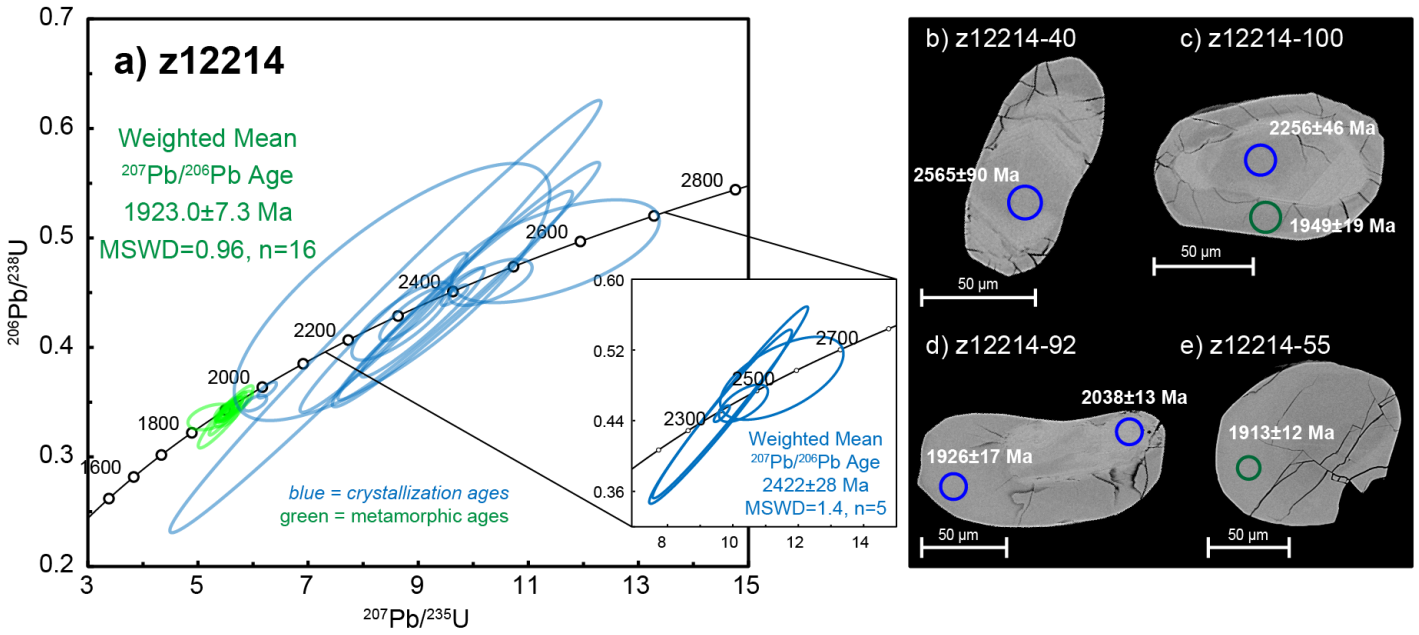

Figure 6. a) Concordia diagram displaying U-Pb SHRIMP results for a sample of granitic gneiss outcropping along the Clearwater River, Saskatchewan. Error ellipses are at the 95% confidence interval. Blue and green error ellipses reflect interpreted igneous crystallization and metamorphic analyses (discussed further in text). Inset plot shows the five analyses used to calculate the crystallization age; b–e) Cathodoluminescence images of zircon grains with location of SHRIMP analyses and corresponding $^{207}Pb/^{206}Pb$ age, highlighting increasing degree of zircon resorption and recrystallization due to metamorphism. The colour of spot analyses matches error ellipses in the concordia diagram.

Marguerite River area share a temporal, and likely genetic, connection with previously described subduction-related Taltson magmatic zone plutons. Neoarchean to Paleoproterozoic inherited zircon ages from the Marguerite River area correspond with dates previously reported for the western Rae Province, including the 2.5 to 2.3 Ga Arrowsmith orogeny (Berman et al., 2013) and the 2.13 to 2.09 Rutledge Basin that formed between the Rae Province to the east and Buffalo Head terrane to the west (Bostock and van Breemen, 1994). A small population of younger zircon ages (ca. 1.93 Ga) from three samples may record subsolidus recrystallization during peak Taltson metamorphic conditions (Fig. 4a–c, 5). However, these data are not robust and lack overarching diagnostic textural and chemical evidence. The ca. 1.82 Ga $^{40}Ar/^{39}Ar$ age for biotite from the mylonite sample z12002 (Fig. 7) is similar to ca. 1.86 to 1.80 Ga muscovite and biotite $^{40}Ar/^{39}Ar$ dates from shear zones in the Taltson magmatic zone in northeastern Alberta (Plint and McDonough, 1995; Pană, 2010). These data have previously been interpreted to represent protracted cooling following peak -metamorphism. However, it is likely that the shear zone in the Marguerite River area was reactivated during the emplacement of the Clearwater Domain granites at ca. 1.84 Ga (Stern et al., 2003). Such a process has been invoked for the Virgin River shear zone and the 1.82 Ga Junction granite (Bickford et al., 1994).

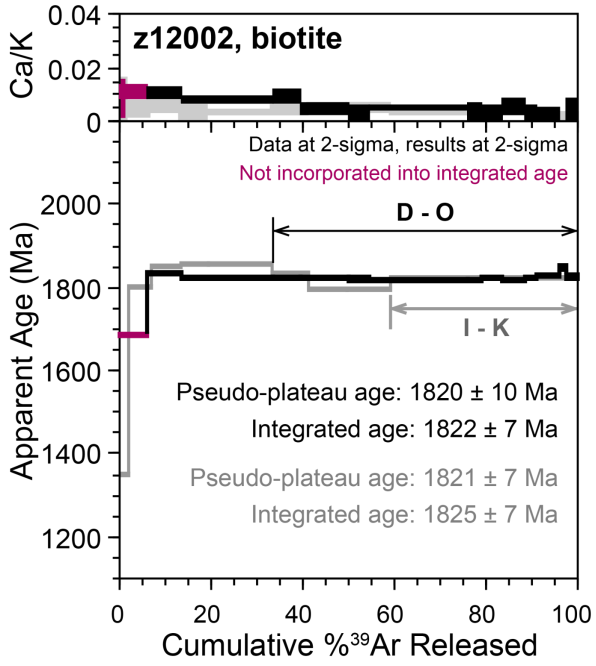

Figure 7. $^{40}Ar/^{39}Ar$ step-heating age spectra and Ca/K plots for biotite from sample z12002 from the Marguerite River area of Alberta. Grey plots and ages indicate results for the second aliquot. Corresponding data is provided in Appendix 2.

SHRIMP U-Pb analyses of zircon cores from the granitic gneiss sample z12214 from the Clearwater River, Saskatchewan, are concordant to discordant and give an imprecise crystallization age of 2422 ± 28 Ma (weighted mean $^{207}Pb/^{206}Pb$ age of the five oldest concordant analyses; Fig. 6a). This age is within error of the 2459 ± 14 Ma crystallization of the Lloyd Lake quartz diorite (Fig. 2; Card et al., 2014) and both ages are typical of the 2.5 to 2.14 Ga rocks that typify the Taltson basement complex in Alberta and the Northwest Territories (Bostock and Loveridge, 1988; McNicoll et al., 2000). Zircon rims from this sample yield a more robust metamorphic age of 1923.0 ± 7.3 Ma (Fig. 6a). Whereas this metamorphic age partially overlaps with the 1.94 to 1.93 Ga granulite-facies Taltson metamorphic event (e.g. Bostock and Loveridge, 1988; Bostock and van Breemen, 1994; McDonough et al., 2000; Stern et al., 2003), it also corresponds with ca. 1.92 to 1.90 metamorphic events recorded proximal to major regional structures (Stern et al., 2003), within the Lloyd Lake diorite (Card et al., 2014) and in U-Pb and $^{40}Ar/^{39}Ar$ dates from the Clearwater anorthosite (e.g. Halls and Hanes, 1999; Heaman et al., 1999; Card et al., 2014). Clearly, more work is required to understand the peak and post-peak metamorphic history of the Taltson Domain in northern Saskatchewan.

Although rocks outcropping in the region commonly retain evidence of >1.90 Ga events, major corridors of heterogeneous, ductile high strain better preserve the region's younger history. Uranium exploration drill samples show that rocks in high-strain corridors were flooded by blue quartz resulting in well-developed silicification fronts and strongly metasomatized country rocks, in which aluminium was concentrated (e.g. Card, 2017). These silicification textures were subsequently sheared suggesting that the quartz flooding occurred below the brittle – ductile transition (Card, 2017). Graphite and iron sulphides postdated quartz flooding and are commonly hosted by structural features that formed above the brittle – ductile transition (Pană et al., 2007; Card, 2017). Both mineral species are of hydrothermal origin and predate uranium mineralization (Card, 2017). Hydrothermal – metasomatic mineral assemblages preserved in the high-strain corridors demonstrate long term reuse of these major structural discontinuities. They are speculated to have precipitated after regional metamorphic events ceased at ca. 1.90 Ga, but before uranium mineralization began at ca. 1.60 Ga in the basin (Jefferson et al., 2007; Alexandre et al., 2009). Ongoing studies are incorporating geochronology, thermochronology and stable isotopes to understand the age of structural reactivation and fluid flow, and their relationship with alteration and uranium mineralization.

Acknowledgments

This report is a contribution to NRCan's Targeted Geoscience Initiative Program (TGI). Support for this study was provided through the Uranium-rich Mineralization Project's 'Activity U-1.3: Fault reactivation, fluid flow and geophysical quantification of fertile alteration in unconformity-related uranium systems'.

The authors would like to thank the collaboration of industry and the Alberta and Saskatchewan geological surveys in this study. Purepoint Uranium Group Ltd. and their Joint Venture partners AREVA Resources Canada and Cameco Corp., and Forum Uranium generously provided logistical support, and shared geological data and knowledge. Big Bear Contracting provided additional logistical support. Charlene Duffett ably assisted in field data collection. Robyn Vezina, Sean Hicks and Pamela Iraheta are thanked for their preparation of zircon grain mounts. We also thank Nicole Rayner, Tom Pestaj, Pat Hunt and Meghan Moher for their help on the SHRIMP and SEM, and Linda Cataldo for her assistance with the $^{40}Ar/^{39}Ar$ analyses. This manuscript benefited from insightful discussions with Bill Davis and Sally Pehrsson. This report benefited from the review of Neil Rogers.

References

Alexandre, P., Kyser, K., Thomas, D., Polito, P., and Marlat, J., 2009. Geochronology of unconformity-related uranium deposits in the Athabasca Basin, Saskatchewan, Canada and their integration in the evolution of the basin; Mineralium Deposita, v. 44, p. 41–59.

Bickford, M.E., Collerson, K.D. and Lewry, J.F., 1994. Crustal history of the Rae and Hearne provinces, southwestern Canadian Shield, Saskatchewan: constraints from geochronologic and isotopic data; Precambrian Research, v. 68, p. 1–21.

Berman, R.G., Pehrsson, S., Davis, W.J., Ryan, J.J., Qui, H., and Ashton, K.E., 2013. The Arrowsmith orogeny: Geochronological and thermobarometric constraints on its extent and tectonic setting in the Rae craton, with implications for the pre-Nuna supercontinent reconstruction; Precambrian Research, v. 232, p. 44–69.

Bostock, H.H., van Breemen, O., and Loveridge, W.D., 1987. Proterozoic geochronology in the Taltson Magmatic Zone; *in* Radiogenic Age and Isotopic Studies, Report 1, Geological Survey of Canada, Paper 87-2, p. 73–80.

Bostock, H.H. and Loveridge, W.D., 1988. Geochronology of the Taltson magmatic zone and its eastern cratonic margin, District of Mackenzie; *in* Radiogenic Age and Isotopic Studies, Report 2, Geological Survey of Canada, Paper 88-2, p. 59–65.

Bostock, H.H. and van Breemen, O., 1994. Ages of detrital and metamorphic zircons and monazites from a pre-Taltson magmatic zone basin at the western margin of the Rae Province; Canadian Journal of Earth Sciences, v. 31, p. 1353–1364.

Bostock, H.H., van Breemen, O., and Loveridge, W.D., 1991. Further Geochronology of plutonic rocks in northern Taltson Magmatic Zone, District of Mackenzie, N.W.T.; *in* Radiogenic Age and Isotopic Studies, Report 4, Geological

Survey of Canada, Paper 90-2, p. 67–78.

Card, C.D., 2017. Distribution and significance of crystalline rocks in the Patterson Lake uranium exploration corridor of northwest Saskatchewan; *in* Summary of Investigations 2017, Volume 2, Saskatchewan Geological Survey, Saskatchewan Ministry of the Economy, Miscellaneous Report 2017-4.2, Paper A-11, 19 p.

Card, C.D. and Noll, J., 2016. Host-rock protoliths, pre-ore metasomatic mineral assemblages and textures, and exotic rocks in the western Athabasca Basin: ore-system controls and implications for the unconformity-related uranium model; *in* Summary of Investigations 2016, Volume 2, Saskatchewan Geological Survey Saskatchewan Ministry of the Economy, Miscellaneous Report 2016-4-2, Paper A-8, 19 p.

Card, C.D., Pană, D., Portella, P., Thomas, D.J., and Annesley, I.R., 2007. Basement rocks to the Athabasca Basin, Saskatchewan and Alberta; *in* EXTECH IV: Geology and Uranium EXploration TECHnology of the Proterozoic Athabasca Basin, Saskatchewan and Alberta, (ed.) C.W. Jefferson and G. Delaney; Geological Survey of Canada, Bulletin v. 588, p. 69–87.

Card, C.D., Bethune, K.M., Davis, W.J., Rayner, N., and Ashton, K.E., 2014. The case for a distinct Taltson orogeny: Evidence from northwest Saskatchewan, Canada. Precambrian Research, v. 255, p. 245–265.

Davis, W.J., Berman, R.G., and MacKinnon, A., 2013. U-Pb geochronology of archival rock samples from the Queen Maud block, Thelon tectonic zone and Rae craton, Kitikmeot region, Nunavut, Canada; Geological Survey of Canada, Open File 7409, 40 p.

Deino, A.L., 2001. Users manual for Mass Spec v. 5.02; Berkeley Geochronology Center Special Publication 1a, 119 p.

Grover, T.W., Pattison, D.R.M., McDonough, M.R., and McNicoll, V., 1997. Tectonometamorphic evolution of the southern Taltson Magmatic zone and associated shear zones, northeastern Alberta; The Canadian Mineralogist, v. 35, p. 1051–1067.

Halls, H.C. and Hane, J.A., 1999. Paleomagnetism, anisotropy of magnetic susceptibility, and argon-argon geochronology of the Clearwater anorthosite, Saskatchewan, Canada; Tectonophysics, v. 312, p. 235–248.

Heaman, L.M., Ashton, K.E., Hartlaub, R.P., and Harper, C.T., 1999. Preliminary U-Pb age constraints on the timing of the Clearwater anorthosite complex, metamorphism in the Train Lake Domain, and age of the Ourom Lake Group; Summary of Investigations 1999, vol. 1., Saskatchewan Geological Survey, Saskatchewan Energy and Mines, Miscellaneous Report 99-4.1, p. 137–139.

Hoffman, P.F., 1988. United Plates of America, the birth of a craton: Early Proterozoic assembly and growth of North America; Annual Review of Earth and Planetary Science Letters, v. 16, p. 543–603.

Jefferson, C.W., Thomas, D.J., Gandhi, S.S., Ramaekers, P., Delaney, G., Brisbin, D., Cutts, C., Portella, P., and Olson, R.A., 2007. Unconformity-associated uranium deposits of the Athabasca Basin, Saskatchewan and Alberta; in EXTECH IV: Geology and Uranium EXploration TECHnology of the Proterozoic Athabasca Basin, Saskatchewan and Alberta, (ed.) C.W. Jefferson and G. Delaney; Geological Survey of Canada, Bulletin v. 588, p. 23–68.

Jourdan, F., Verati, C., and Feraud, G., 2006. Intercalibration of the Hb3gr $^{40}Ar/^{39}Ar$ dating standard; Chemical Geology, v. 231, p. 177–189.

Kellett, D. and Joyce, N., 2014. Analytical details of the single- and multicollection $^{40}Ar/^{39}Ar$ measurements for conventional step-heating and total-fusion age calculation using the Nu Noblesse at the Geological Survey of Canada; Geological Survey of Canada, Technical Note 8, 27 p.

Lee, J.Y., Marti, K., Severinghaus, J.P., Kawamura, K., Yoo, H.S., Lee, J.B., and Kim, J.S., 2006. A redetermination of the isotopic abundances of atmospheric Ar; Geochimica et Cosmochimica Acta, v. 70, p. 4507–4512.

Lyatsky, H. and Pană, D., 2003. Catalogue of selected gravity and magnetic maps of northern Alberta; Alberta Energy and Utilities Board, EUB/AGS Special Report 56, 37 p.

Ludwig, K.R., 2009. Isoplot 4.1, a geochronological toolkit for Microsoft excel; Berkeley Geochronology Center Special Publication 4, 76 p.

Mahan, K.H., Williams, M.L., Flowers, R.M., Jercinovic, M.J., Baldwin, J.A., and Bowring, S.A., 2006. Geological constraints on the Legs Lake shear zone with implications for regional exhumation of lower continental crust, western Churchill Province, Canadian Shield; Contributions to Mineralogy and Petrology, v. 152, p. 223–242.

McDonough, M.R. and McNicoll, V.J., 1997. U-Pb age constraints on the timing of deposition of the Waugh Lake and Burntwood (Athabasca) groups, southern Taltson magmatic zone, northeastern Alberta; *in* Radiogenic Age and Isotope Studies, Report 10, Geological Survey of Canada, Current Research 1997-F, p. 101–111.

McDonough, M.R., McNicoll, V.J., Schetselaar, E.M., and Grover, T.W., 2000. Geochronological and kinematic constraints on crustal shortening and escape in a two-sided oblique-slip collisional and magmatic orogeny, Paleoproterozoic Taltson magmatic zone, northeastern Alberta; Canadian Journal of Earth Sciences, v. 37, p. 1549–1573.

McNicoll, V.J., Theriault, R.J., and McDonough, M.R., 2000. Taltson basement gneissic rocks; U-Pb and Nd isotopic constraints on the basement of the Paleoproterozoic Taltson magmatic zone, northeastern Alberta; Canadian Journal of Earth Sciences, v. 37, p. 1575–1596.

Pană, D., 2010. Overview of the geological evolution of the Canadian Shield in the Andrew Lake area based on new field and isotope data, northeastern Alberta (NTS 74M/16); Energy Resources Conservation Board, ERCB/AGS Open File Report 2009-22, 76 p.

Pană, D., Creaser, R.A., Muehlenbachs, K., and Wheatley, K., 2007. Basement geology in the Alberta portion of the Athabasca Basin: context for the Maybelle River area; in EXTECH IV: Geology and Uranium EXploration TECHnology of the Proterozoic Athabasca Basin, Saskatchewan and Alberta, (ed.) C.W. Jefferson and G. Delaney; Geological Survey of Canada, Bulletin, v. 588, p. 135–153.

Plint, H.E. and McDonough, M.R., 1995. $^{40}Ar/^{39}Ar$ and K-Ar age constraints on shear zone evolution, southern Taltson magmatic zone, northeastern Alberta; Canadian Journal of Earth Sciences, v. 32, p. 281–291.

Ross, G.M., 1991. Precambrian basement in the Canadian Cordillera: An introduction; Canadian Journal of Earth Sciences, v. 28, p. 1133–1139.

Ross, G.M., 1992. Tectonic evolution of crystalline basement along the Central Transect; *in* LITHOPROBE Report #28, (ed.) G.M. Ross; Alberta Basement Transects Workshop, p. 120–138.

Ross, G.M., Villeneuve, M.E., Parrish, R.R., and Theriault, R.J., 1993. Tectonic assembly of crystalline basement, Alberta Basin: Implications for mantle evolution and ancestry of Canada's Pacific margin; *in* LITHOPROBE Report #31, (ed.) G.M. Ross; Alberta Basement Transects Workshop, p. 134–143.

Steiger, R.H. and Jäger, E., 1977. Subcommission on geochronology: Convention on the use of decay constants in geo- and cosmochronology; Earth and Planetary Science Letters, v. 36, p. 359–362.

Stern, R.A., 1997. The GSC Sensitive High Resolution Ion Microprobe (SHRIMP): Analytical techniques of zircon U-Th-Pb age determinations and performance evaluation; Geological Survey of Canada, Current Research 1997-F, p. 1–31.

Stern, R.A. and Amelin, Y., 2003. Assessment of errors in SIMS zircon U-Pb geochronology using a natural zircon standard and NIST SRM 610 glass; Chemical Geology, v. 197, p. 111–146.

Stern, R.A., Card C.D., Pană, D., and Rayner, N., 2003. SHRIMP U-Pb ages of granitoid basement rocks of the southwestern part of the Athabasca Basin, Saskatchewan and Alberta; *in* Radiogenic Age and Isotopic Studies, Report 16, Geological Survey of Canada, Current Research 2003-F, 20 p.

Villeneuve, M.E., Ross, G.M., Theriault, R.J., Miles, W., Parrish, R.R., and Broome, J., 1993. Tectonic subdivision and U-Pb geochronology of the crystalline basement of the Alberta basin, western Canada; Geological Survey of Canada, Bulletin 447, 93 p.

Appendix 1. U-Pb zircon SHRIMP analytical results for Taltson Domain samples from northern Alberta and Saskatchewan

Spot name	U (ppm)	Th (ppm)	$^{232}Th/^{238}U$	Yb (ppm)	abs. error (1σ)	Hf (ppm)	abs. err (1σ)	$^{204}Pb/^{206}Pb$	err (%)	$f(206)^{204}$ %	$^{206}Pb^*$ (ppm)	$^{208}Pb^*/^{206}Pb^*$	err (%)	$^{207}Pb^*/^{235}U$	err (%)	$^{206}Pb^*/^{238}U$	err (%)	Corr. Coeff	Apparent ages (Ma) $^{207}Pb^*/^{206}Pb^*$	err (%)	$^{206}Pb/^{238}U$	err (abs)	$^{207}Pb/^{206}Pb$	err (abs)	% Disc.
z11998, Marguerite River area, Alberta NAD83 UTM zone 12 542089E 6400240N, IP864																									
11998-003.1	441	149	0.35	229	4	11400	104	2.2E-5	41	0.04	134.4	0.102	2.0	5.940	1.0	0.3544	0.9	0.920	0.1216	0.4	1955	16	1980	7	+1
11998-009.1	592	441	0.77	378	6	11419	102	8.8E-6	58	0.02	181.4	0.231	1.2	5.952	1.0	0.3564	0.9	0.935	0.1211	0.3	1965	15	1973	6	+0
11998-010.1	692	290	0.43	332	5	11277	101	1.6E-5	39	0.03	203.1	0.131	1.4	5.607	1.1	0.3415	0.9	0.824	0.1191	0.6	1894	15	1942	11	+3
11998-010.2	809	108	0.14	207	3	12509	111	1.5E-5	38	0.03	242.3	0.041	2.4	5.673	0.9	0.3486	0.9	0.946	0.1180	0.3	1928	15	1927	5	-0
11998-010.3	752	143	0.20	226	10	13403	310	7.3E-6	58	0.01	226.5	0.055	2.2	5.898	0.9	0.3506	0.9	0.944	0.1220	0.3	1938	15	1986	6	+3
11998-011.1	695	315	0.47	274	4	11870	106	-2.5E-6	100	0.00	212.0	0.141	1.4	5.942	1.0	0.3551	0.9	0.943	0.1214	0.3	1959	15	1976	6	+1
11998-016.1	680	286	0.43	252	4	12054	107	1.9E-5	35	0.03	210.3	0.122	1.5	5.976	0.9	0.3600	0.9	0.942	0.1204	0.3	1982	15	1962	6	-1
11998-017.1	565	300	0.55	261	4	11314	102	1.5E-4	29	0.27	171.6	0.163	1.7	5.923	1.1	0.3536	0.9	0.834	0.1215	0.6	1952	15	1978	11	+2
11998-018.1	363	103	0.29	189	3	11779	105	2.3E-5	41	0.04	130.4	0.086	2.3	8.365	1.0	0.4179	1.0	0.932	0.1452	0.4	2251	18	2290	7	+2
11998-018.2	376	74	0.20	177	3	12654	113	5.3E-5	29	0.09	114.8	0.060	3.0	5.946	1.1	0.3556	1.0	0.904	0.1213	0.5	1961	16	1975	8	+1
11998-021.1	1029	352	0.35	275	4	12357	110	1.2E-5	38	0.02	310.5	0.106	1.3	5.852	0.9	0.3514	0.9	0.958	0.1208	0.3	1941	15	1968	5	+2
11998-027.1	672	325	0.50	271	8	11651	104	1.6E-4	14	0.27	204.1	0.148	1.5	5.935	1.0	0.3537	0.9	0.914	0.1217	0.4	1952	15	1982	7	+2
11998-036.1	421	81	0.20	227	4	12768	122	2.4E-5	41	0.04	128.3	0.054	2.9	5.911	1.0	0.3544	0.9	0.916	0.1210	0.4	1956	16	1970	7	+1
11998-041.1	703	322	0.47	561	8	10349	93	6.7E-5	20	0.12	243.9	0.141	1.3	7.793	1.0	0.4042	0.9	0.885	0.1398	0.5	2188	17	2225	8	+2
11998-043.1	1062	228	0.22	675	23	13879	126	1.1E-5	38	0.02	321.0	0.064	1.7	5.739	1.0	0.3519	1.0	0.966	0.1183	0.3	1943	17	1931	5	-1
11998-044.1	667	189	0.29	237	4	12699	113	1.5E-4	33	0.26	200.6	0.090	4.1	5.691	1.1	0.3502	0.9	0.812	0.1179	0.6	1935	15	1924	12	-1
11998-044.2	745	144	0.20	282	4	13690	123	3.8E-5	25	0.07	219.7	0.060	2.2	5.678	1.0	0.3431	0.9	0.939	0.1200	0.3	1902	15	1956	6	+3
11998-046.1	381	50	0.13	153	3	13703	123	5.1E-5	30	0.09	117.4	0.038	4.0	5.976	1.4	0.3590	1.3	0.943	0.1207	0.5	1978	22	1967	8	-1
11998-050.1	366	196	0.55	239	4	10995	98	4.8E-6	100	0.01	110.6	0.165	1.8	5.868	1.1	0.3515	1.0	0.910	0.1211	0.4	1942	16	1972	8	+2
11998-051.1	292	80	0.28	309	5	10836	97	3.4E-5	41	0.06	89.5	0.082	2.8	5.975	1.5	0.3567	1.4	0.942	0.1215	0.5	1967	24	1978	9	+1
11998-054.1	296	49	0.17	161	3	12642	114	6.2E-6	100	0.01	87.2	0.048	3.8	5.737	1.1	0.3433	1.0	0.893	0.1212	0.5	1902	17	1974	9	+4
11998-055.1	350	95	0.28	381	6	11148	106	4.3E-5	33	0.07	105.9	0.085	2.6	5.886	1.1	0.3520	1.0	0.902	0.1213	0.5	1944	16	1975	8	+2
11998-077.1	358	116	0.33	400	6	10568	94	1.4E-5	58	0.02	107.5	0.103	4.2	5.847	1.1	0.3494	1.0	0.908	0.1214	0.4	1932	16	1977	8	+3
11998-092.1	481	219	0.47	254	4	11729	105	2.2E-5	41	0.04	147.6	0.139	1.7	5.988	1.0	0.3570	0.9	0.923	0.1216	0.4	1968	16	1980	7	+1
11998-095.1	568	129	0.23	323	5	12190	245	3.4E-5	30	0.06	167.2	0.071	2.2	5.613	1.0	0.3426	0.9	0.926	0.1188	0.4	1899	15	1939	7	+2
11998-102.1	182	55	0.31	218	3	9560	85	9.5E-6	100	0.02	54.8	0.102	3.2	5.919	1.7	0.3507	1.6	0.931	0.1224	0.6	1938	26	1992	11	+3
11998-106.1	568	117	0.21	207	3	12408	110	2.4E-22	9999	0.00	172.5	0.064	2.2	5.895	1.1	0.3533	1.1	0.952	0.1210	0.3	1950	18	1971	6	+1
11998-110.1	680	719	1.09	467	7	10948	98	1.3E-5	45	0.02	209.0	0.321	0.9	6.019	1.0	0.3581	0.9	0.941	0.1219	0.3	1973	15	1984	6	+1
11998-111.1	1093	202	0.19	225	4	13507	121	6.8E-5	17	0.12	330.3	0.058	1.9	5.825	0.9	0.3518	0.9	0.952	0.1201	0.3	1943	15	1957	5	+1
11998-113.1	472	265	0.58	275	4	11351	102	4.5E-5	29	0.08	142.7	0.169	1.6	5.903	1.0	0.3517	0.9	0.916	0.1217	0.4	1943	16	1982	7	+2
11998-117.1	494	326	0.68	393	6	9249	83	-3.7E-6	100	-0.01	152.1	0.201	1.4	5.992	1.0	0.3580	0.9	0.925	0.1214	0.4	1973	16	1977	7	+0
z11999, Marguerite River area, Alberta NAD83 UTM zone 12 542089E 6400240N, IP864																									
11999-006.1	1431	173	0.13	251	12	15592	156	9.5E-5	13	0.17	378.8	0.040	6.2	4.641	1.3	0.3082	1.2	0.865	0.1092	0.7	1732	18	1787	12	+3
11999-009.1	293	72	0.25	354	5	11097	100	7.3E-5	29	0.13	86.3	0.077	3.2	5.654	1.1	0.3426	1.0	0.877	0.1197	0.5	1899	17	1951	10	+3
11999-014.1	809	262	0.33	487	7	11443	102	1.9E-4	12	0.33	240.4	0.105	3.1	5.826	1.1	0.3461	0.9	0.823	0.1221	0.6	1916	15	1987	11	+4
11999-020.1	496	274	0.57	297	9	11751	267	2.0E-4	15	0.35	150.9	0.177	1.7	5.880	1.1	0.3540	0.9	0.877	0.1205	0.5	1954	16	1963	9	+1
11999-022.1	816	316	0.40	355	5	15002	296	1.1E-5	45	0.02	228.7	0.121	1.4	5.247	0.9	0.3262	0.9	0.945	0.1167	0.3	1820	14	1906	5	+5
11999-026.1	533	97	0.19	297	5	12091	223	1.2E-4	17	0.21	158.6	0.061	4.8	5.666	1.0	0.3465	0.9	0.904	0.1186	0.4	1918	15	1935	8	+1
11999-039.1	445	313	0.73	298	9	9896	217	1.9E-5	38	0.03	194.0	0.219	1.2	12.889	1.0	0.5078	0.9	0.955	0.1841	0.3	2647	20	2690	5	+2
11999-041.1	547	312	0.59	237	4	11421	102	6.3E-5	23	0.11	170.6	0.185	1.4	6.038	1.0	0.3629	0.9	0.918	0.1207	0.4	1996	16	1966	7	-2
11999-048.1	577	147	0.26	363	6	14121	126	3.0E-6	100	0.01	175.5	0.086	2.0	5.923	1.0	0.3541	0.9	0.935	0.1213	0.3	1954	15	1976	6	+1
11999-055.1	180	61	0.35	170	3	10572	95	2.9E-4	20	0.51	62.5	0.118	3.5	8.079	1.3	0.4042	1.1	0.820	0.1450	0.8	2188	20	2287	13	+5
11999-056.1	458	102	0.23	482	16	11388	102	2.6E-5	38	0.05	139.4	0.081	2.3	5.955	1.0	0.3546	0.9	0.920	0.1218	0.4	1957	16	1983	7	+2
11999-057.1	740	449	0.63	487	7	9351	90	2.5E-5	30	0.04	228.5	0.212	1.1	6.035	0.9	0.3593	0.9	0.944	0.1218	0.3	1979	15	1983	6	+0
11999-062.1	534	458	0.89	212	3	11163	100	2.8E-5	33	0.05	157.2	0.276	1.1	5.655	1.0	0.3425	0.9	0.929	0.1197	0.4	1899	15	1952	6	+3
11999-063.1	372	74	0.21	123	2	12227	109	5.8E-4	9	1.01	111.7	0.074	4.0	5.809	1.4	0.3498	1.0	0.666	0.1204	1.1	1934	16	1963	19	+2
11999-072.1	259	69	0.28	259	4	10976	98	7.4E-4	18	1.28	63.7	0.096	8.4	4.813	1.9	0.2866	1.0	0.553	0.1218	1.6	1624	15	1983	28	+20
11999-083.1	481	151	0.32	468	7	11765	105	1.3E-4	18	0.23	145.2	0.114	2.0	5.825	1.0	0.3512	0.9	0.896	0.1203	0.5	1940	16	1961	8	+1
11999-088.1	792	351	0.46	300	5	12301	110	4.6E-5	21	0.08	237.7	0.150	1.3	5.769	0.9	0.3495	0.9	0.944	0.1197	0.3	1932	15	1952	6	+1
11999-101.1	716	187	0.27	291	5	12920	116	5.7E-5	20	0.10	212.5	0.082	1.8	5.655	1.0	0.3454	0.9	0.937	0.1188	0.3	1912	15	1938	6	+2
11999-103.1	357	83	0.24	160	3	13059	116	4.3E-5	33	0.07	107.8	0.073	2.8	5.893	1.1	0.3517	1.0	0.901	0.1215	0.5	1943	16	1978	8	+2
11999-110.1	514	173	0.35	376	6	11178	100	1.6E-4	17	0.27	155.1	0.116	2.0	5.868	1.0	0.3514	0.9	0.889	0.1211	0.5	1941	16	1973	9	+2
z12000, Marguerite River area, Alberta NAD83 UTM zone 12 521260E 6402244N, IP864																									
12000-003.1	716	317	0.46	602	9	11384	102	4.5E-5	24	0.08	223.7	0.147	1.4	6.076	1.2	0.3634	1.1	0.957	0.1213	0.3	1998	19	1975	6	-1
12000-004.1	445	270	0.63	455	7	11045	99	-1.5E-5	50	-0.03	136.1	0.188	1.5	5.961	1.0	0.3560	0.9	0.920	0.1215	0.4	1963	16	1978	7	+1
12000-012.1	352	263	0.77	497	8	9867	88	2.4E-5	45	0.04	107.6	0.234	1.5	5.974	1.1	0.3555	1.0	0.907	0.1219	0.4	1961	16	1984	8	+1
12000-014.1	137	86	0.65	297	5	9546	85	-1.3E-5	100	-0.02	42.0	0.215	2.5	5.975	1.4	0.3563	1.2	0.854	0.1216	0.7	1965	20	1980	13	+1
12000-018.1	811	32	0.04	767	20	14317	128	8.7E-6	50	0.02	248.9	0.012	4.7	5.993	1.1	0.3570	1.0	0.961	0.1217	0.3	1968	17	1982	5	+1
12000-020.1	635	43	0.07	448	12	16023	379	1.8E-5	41	0.03	192.0	0.022	4.1	5.920	1.0	0.3518	0.9	0.934	0.1220	0.3	1943	15	1986	6	+3
12000-022.1	699	42	0.06	536	8	14004	126	2.1E-5	35	0.04	212.6	0.017	4.6	5.877	1.0	0.3540	0.9	0.937	0.1204	0.3	1954	15	1962	6	+0
12000-030.1	322	123	0.39	218	3	10495	94	-1.5E-5	58	-0.03	106.9	0.120	2.2	6.950	1.3	0.3867	1.2	0.942	0.1303	0.4	2108	22	2103	8	-0
12000-035.1	373	156	0.43	373	11	10267	92	1.0E-4	20	0.18	115.6	0.127	2.0	5.995	1.2	0.3604	1.0	0.795	0.1207	0.7	1984	16	1966	13	-1
12000-044.1	631	704	1.15	636	10	9683	86	4.8E-5	24	0.08	194.0	0.394	1.8	5.954	1.0	0.3580	0.9	0.932	0.1206	0.4	1973	15	1965	6	-0
12000-049.1	694	248	0.37	427	7	11921	106	1.9E-5	35	0.03	216.1	0.113	1.5	6.100	0.9	0.3624	0.9	0.944	0.1221	0.3	1993	15	1987	6	-0
12000-050.1	693	609	0.91	598	18	10113	264	1.4E-5	41	0.02	215.8	0.293	1.0	6.077	0.9	0.3624	0.9	0.943	0.1216	0.3	1993	15	1980	6	-1
12000-053.1	278	107	0.40	223	4	9447	84	-5.7E-6	100	-0.01	91.6	0.135	2.2	6.907	1.1	0.3839	1.0	0.907	0.1305	0.5	2094	18	2105	8	+1
12000-055.1	566	307	0.56	421	19	11895	298	1.9E-5	41	0.03	171.7	0.164	1.5	5.968	1.0	0.3533	0.9	0.929	0.1225	0.4	1950	15	1993	6	+2
12000-069.1	1024	171	0.17	349	5	14478	130	1.7E-4	11	0.29	313.4	0.062	2.1	6.195	0.9	0.3563	0.9	0.937	0.1261	0.3	1965	15	2044	6	+5
12000-076.1	498	24	0.05	402	6	13546	122	3.7E-6	100	0.01	152.3	0.013	5.8	5.927	1.0	0.3558	0.9	0.910	0.1208	0.4	1962	16	1968	8	+0
12000-076.2	118	85	0.74	240	4	9492	85	4.6E-5	58	0.08	35.7	0.215	2.8	5.853	1.5	0.3511	1.2	0.828	0.1209	0.8	1940	21	1969	15	+2
12000-077.1	342	237	0.72	471	7	11000	98	1.5E-5	58	0.03	104.5	0.239	1.5	5.978	1.1	0.3552	1.0	0.907	0.1221	0.5	1959	16	1987	8	+2
12000-102.1	494	182	0.38	277	4	11560	103	1.9E-4	16	0.33	150.4	0.123	2.0	5.940	1.1	0.3545	0.9	0.880	0.1215	0.5	1956	16	1979	9	+1
12000-106.1	102	84	0.85	238	4	10258	92	6.8E-5	50	0.12	31.2	0.271	2.7	6.018	1.6	0.3576	1.3	0.817	0.1220	0.9	1971	22	1986	16	+1
12000-106.2	779	38	0.05	419	6	15375	139	1.5E-4	13	0.26	227.9	0.015	8.9	5.561	1.2	0.3405	1.1	0.947	0.1184	0.4	1889	18	1933	7	+3
12000-108.1	331	351	1.10	617	9	8637	77	1.8E-4	20	0.31	99.8	0.390	1.3	5.919	1.1	0.3512	1.0	0.851	0.1222	0.6	1940	16	1989	11	+3
12000-113.1	217	139	0.66	312	5	9902	90	2.3E-5	58	0.04	64.4	0.214	3.3	5.796	1.2	0.3460	1.0	0.878	0.1215	0.6	1915	17	1978	10	+4
12000-115.1	209	116	0.58	416	6	9015	81	3.2E-14	9999	0.00	64.8	0.185	2.2	6.139	1.2	0.3616	1.1	0.885	0.1231	0.6	1990	18	2002	10	+1
12000-118.2	974	27	0.03	725	11	13446	123	1.0E-5	41	0.02	303.2	0.009	5.0	6.084	0.9	0.3624	0.9	0.956	0.1218	0.3	1994	15	1982	5	-1
12000-121.1	214	82	0.40	238	4	9964	89	-1.8E-22	9999	0.00	80.7	0.129	2.4	8.941	1.1	0.4387	1.0	0.911	0.1478	0.5	2345	21	2321	8	-1
12000-122.1	729	291	0.41	444	7	10404	93	6.8E-5	18	0.12	235.9	0.139	2.1	6.785	1.0	0.3770	0.9	0.885	0.1305	0.5	2062	16	2105	8	+2
12000-122.2	786	96	0.13	435	14	13763	296	2.5E-5	29	0.04	242.2	0.038	2.6	5.957	0.9	0.3588	0.9	0.947	0.1204	0.3	1976	15	1962	5	-1
12000-134.1	995	26	0.03	886	13	14080	127	1.2E-5	38	0.02	304.1	0.009	5.2	5.924	0.9	0.3559	0.9	0.956	0.1207	0.3	1963	15	1967	5	+0
z12001, Marguerite River area, Alberta NAD83 UTM zone 12 524957E 6396856N, IP864																									
12001-007.1	721	388	0.56	452	16	12396	113	1.6E-3	6	2.73	212.4	0.178	3.5	5.386	1.7	0.3428	0.9	0.529	0.1139	1.5	1900	15	1863	26	-2
12001-010.1	902	379	0.43	460	7	11230	100	2.3E-5	29	0.04	280.6	0.142	1.2	6.046	0.9	0.3622	0.9	0.952	0.1211	0.3	1992	15	1972	5	-1
12001-011.1	706	436	0.64	459	7	10982	207	2.4E-5	33	0.04	216.9	0.210	1.2	5.993	1.2	0.3577	1.1	0.957	0.1215	0.3	1971	19	1979	6	+0
12001-019.1	323	123	0.39	205	3	11290	100	3.6E-5	38	0.06	98.1	0.126	2.2	5.904	1.1	0.3533	1.0	0.898	0.1212	0.5	1950	16	1974	9	+1
12001-019.2	331	138	0.43	197	3	10652	95	2.4E-5	50	0.04	95.6	0.125	2.4	5.633	1.1	0.3365	1.0	0.889	0.1214	0.5	1870	16	1977	9	+6

Appendix 1. Cont.

Spot name	U (ppm)	Th (ppm)	$^{232}Th/^{238}U$	Yb (ppm)	abs. error (1σ)	Hf (ppm)	abs. err (1σ)	$^{204}Pb/^{206}Pb$	err (%)	$f(206)^{204}$ %	$^{206}Pb^*$ (ppm)	$^{208}Pb^*/^{206}Pb^*$	err (%)	$^{207}Pb^*/^{235}U$	err (%)	$^{206}Pb^*/^{238}U$	err (%)	Corr. Coeff	Apparent ages (Ma) $^{207}Pb^*/^{206}Pb^*$	err (%)	$^{206}Pb/^{238}U$	err (abs)	$^{207}Pb/^{206}Pb$	err (abs)	% Disc.
z12001, Marguerite River area, Alberta NAD83 UTM zone 12 524957E 6396856N, IP864																									
12001-020.1	450	203	0.47	223	4	11600	104	3.2E-5	35	0.06	137.1	0.136	2.9	5.908	1.0	0.3545	0.9	0.914	0.1209	0.4	1956	16	1969	7	+1
12001-023.1	392	144	0.38	285	4	9679	87	3.7E-5	35	0.06	119.2	0.115	2.1	5.929	1.1	0.3537	1.0	0.906	0.1216	0.4	1952	16	1979	8	+2
12001-023.2	551	82	0.15	148	2	14077	125	2.8E-5	33	0.05	166.7	0.042	3.0	5.863	1.0	0.3524	0.9	0.928	0.1206	0.4	1946	15	1966	7	+1
12001-028.1	496	221	0.46	243	4	11111	239	2.2E-5	41	0.04	149.6	0.138	1.7	5.848	1.0	0.3511	0.9	0.922	0.1208	0.4	1940	16	1968	7	+2
12001-032.1	1487	289	0.20	811	22	16095	148	2.4E-5	20	0.04	433.0	0.055	2.5	5.054	0.9	0.3391	0.9	0.968	0.1081	0.2	1882	14	1768	4	-7
12001-035.1	177	156	0.91	189	3	10665	95	3.0E-5	58	0.05	52.9	0.281	2.0	5.885	1.3	0.3477	1.1	0.860	0.1228	0.7	1923	18	1997	12	+4
12001-037.1	404	166	0.42	245	8	11320	101	1.3E-5	58	0.02	121.0	0.123	2.0	5.825	1.0	0.3486	1.0	0.913	0.1212	0.4	1928	16	1974	8	+3
12001-039.1	588	73	0.13	133	2	13802	123	2.7E-5	33	0.05	181.1	0.039	3.0	6.023	1.0	0.3588	0.9	0.931	0.1217	0.4	1977	16	1982	6	+0
12001-039.2	1112	315	0.29	349	5	13041	118	2.4E-5	28	0.04	297.0	0.086	1.5	4.828	1.0	0.3110	1.0	0.959	0.1126	0.3	1746	15	1842	5	+6
12001-041.1	311	90	0.30	194	7	10348	92	3.8E-5	38	0.07	92.9	0.086	2.7	5.814	1.3	0.3478	1.2	0.926	0.1212	0.5	1924	20	1975	9	+3
12001-043.1	265	99	0.39	189	3	11452	111	1.3E-5	71	0.02	81.3	0.116	2.5	5.951	1.1	0.3569	1.0	0.888	0.1210	0.5	1967	17	1970	9	+0
12001-044.1	617	397	0.66	428	55	11162	100	2.5E-5	33	0.04	187.2	0.199	3.0	5.879	1.0	0.3533	0.9	0.930	0.1207	0.4	1950	15	1966	6	+1
12001-047.1	524	400	0.79	427	7	9803	88	4.1E-5	29	0.07	158.5	0.232	1.3	5.850	1.0	0.3519	0.9	0.921	0.1206	0.4	1943	15	1965	7	+1
12001-053.1	358	189	0.55	213	3	10879	98	2.1E-5	45	0.04	129.4	0.164	1.7	8.538	1.4	0.4207	1.0	0.697	0.1472	1.0	2264	18	2313	17	+3
12001-061.1	201	117	0.60	205	3	9422	85	9.0E-5	32	0.16	60.7	0.177	2.5	5.921	1.5	0.3525	1.1	0.742	0.1218	1.0	1946	18	1983	17	+2
12001-068.1	446	102	0.24	126	2	12670	113	2.3E-5	41	0.04	133.4	0.069	2.5	5.791	1.0	0.3485	0.9	0.917	0.1205	0.4	1927	16	1964	7	+2
12001-076.1	339	164	0.50	224	4	10762	96	5.2E-5	32	0.09	101.8	0.155	2.0	5.854	1.1	0.3495	1.0	0.895	0.1215	0.5	1932	16	1978	9	+3
12001-078.1	556	85	0.16	159	3	12235	109	2.5E-5	35	0.04	166.5	0.047	2.8	5.775	1.0	0.3484	0.9	0.928	0.1202	0.4	1927	15	1959	7	+2
12001-078.2	351	151	0.44	203	3	11465	102	1.3E-4	19	0.23	108.0	0.127	2.2	5.959	1.1	0.3579	1.0	0.879	0.1207	0.5	1972	16	1967	9	-0
12001-088.1	619	191	0.32	184	3	12426	111	1.2E-5	50	0.02	187.9	0.093	1.8	5.868	1.0	0.3533	0.9	0.935	0.1205	0.3	1950	15	1963	6	+1
12001-089.1	223	103	0.48	195	3	11053	100	3.5E-5	50	0.06	67.1	0.146	2.6	5.873	1.2	0.3507	1.1	0.868	0.1215	0.6	1938	18	1978	11	+2
12001-090.1	483	164	0.35	296	5	11849	107	2.7E-5	38	0.05	144.7	0.102	2.1	5.882	1.1	0.3489	0.9	0.836	0.1223	0.6	1929	16	1990	11	+4
12001-096.1	733	190	0.27	186	3	12753	114	2.3E-5	32	0.04	221.9	0.082	1.8	5.796	0.9	0.3521	0.9	0.943	0.1194	0.3	1945	15	1947	6	+0
12001-096.2	432	162	0.39	245	4	11412	103	8.5E-5	22	0.15	139.3	0.116	2.1	6.774	1.0	0.3756	1.0	0.910	0.1308	0.4	2056	17	2109	8	+3
12001-097.1	257	98	0.39	195	3	11432	111	1.3E-4	24	0.22	76.5	0.114	2.9	5.731	1.2	0.3465	1.0	0.848	0.1200	0.6	1918	17	1956	12	+2
12001-098.1	188	104	0.57	188	3	9918	89	2.0E-5	71	0.03	56.6	0.163	2.6	5.944	1.3	0.3498	1.1	0.865	0.1232	0.6	1934	18	2004	11	+4
12001-104.1	610	169	0.29	211	3	13201	118	5.6E-6	71	0.01	186.0	0.086	1.9	5.935	1.0	0.3549	0.9	0.937	0.1213	0.3	1958	15	1975	6	+1
12001-104.2	315	131	0.43	195	3	11432	221	5.4E-5	32	0.09	96.3	0.123	2.3	5.870	1.1	0.3554	1.0	0.890	0.1198	0.5	1960	17	1953	9	-0
12001-106.1	575	214	0.38	314	5	10937	98	4.0E-5	28	0.07	176.2	0.114	1.8	5.935	1.0	0.3564	0.9	0.925	0.1208	0.4	1965	16	1968	7	+0
12001-114.1	351	202	0.59	199	3	11273	101	3.5E-5	38	0.06	107.2	0.176	1.8	5.938	1.1	0.3557	1.0	0.900	0.1211	0.5	1962	16	1972	8	+1
12001-127.1	1039	412	0.41	260	4	12703	114	5.9E-6	50	0.01	374.1	0.118	1.2	8.368	1.0	0.4192	0.9	0.882	0.1448	0.5	2257	17	2285	8	+1
z12214, Clearwater river outcrop, Saskatchewan NAD83 UTM zone 12 623086E 6307905N, IP896																									
12214-003.1	75	112	1.56	84	3	11443	652	1.6E-4	41	0.27	21.5	0.455	2.9	5.523	1.5	0.3363	1.0	0.664	0.1191	1.2	1869	17	1943	21	+4
12214-004.1	51	83	1.67	89	4	11185	648	1.2E-4	58	0.21	14.8	0.513	3.0	5.508	3.7	0.3369	3.5	0.931	0.1186	1.3	1872	56	1935	24	+4
12214-005.1	25	67	2.80	45	2	12080	546	4.9E-4	41	0.85	7.1	0.864	3.4	5.242	3.3	0.3368	1.4	0.434	0.1129	3.0	1871	23	1847	53	-2
12214-012.1	138	48	0.36	100	4	12291	530	7.0E-5	45	0.12	40.4	0.117	3.8	5.492	1.2	0.3395	0.9	0.782	0.1173	0.7	1884	15	1916	13	+2
12214-013.1	73	31	0.45	54	2	11761	579	2.7E-5	100	0.05	21.5	0.119	5.1	5.623	1.4	0.3457	1.0	0.739	0.1180	0.9	1914	17	1925	17	+1
12214-013.2	136	57	0.43	79	3	12364	612	2.8E-5	71	0.05	39.7	0.130	3.5	5.485	1.2	0.3397	0.9	0.790	0.1171	0.7	1885	15	1912	13	+2
12214-014.1	99	92	0.95	84	3	11877	465	3.9E-5	71	0.07	29.1	0.291	2.8	5.571	1.3	0.3407	1.0	0.765	0.1186	0.8	1890	16	1935	15	+3
12214-029.1	258	102	0.41	233	16	10021	553	2.7E-5	45	0.05	102.3	0.117	2.5	9.922	9.8	0.4608	9.6	0.983	0.1561	1.8	2443	196	2414	30	-1
12214-032.1	134	164	1.27	96	4	11669	588	7.1E-5	45	0.12	39.0	0.374	2.1	5.541	2.5	0.3398	2.4	0.953	0.1183	0.7	1886	38	1930	13	+3
12214-033.1	485	144	0.31	325	13	11578	567	1.1E-5	58	0.02	145.5	0.092	3.3	6.043	1.4	0.3494	0.8	0.596	0.1254	1.1	1932	14	2035	20	+6
12214-039.1	262	69	0.27	201	8	12164	406	-1.2E-5	71	-0.02	95.5	0.085	3.0	8.698	4.2	0.4243	3.4	0.810	0.1487	2.5	2280	66	2331	42	+3
12214-040.1	198	40	0.21	150	6	12676	422	4.0E-5	41	0.07	83.0	0.062	3.6	11.496	6.7	0.4882	3.9	0.587	0.1708	5.4	2563	83	2565	91	+0
12214-055.1	142	50	0.36	74	3	12597	540	1.2E-13	9999	0.00	41.7	0.109	3.8	5.498	1.1	0.3405	0.9	0.822	0.1171	0.6	1889	15	1913	12	+1
12214-060.1	176	428	2.51	173	10	11640	510	5.4E-5	45	0.09	52.5	0.755	1.3	5.664	1.1	0.3475	0.9	0.816	0.1182	0.6	1923	15	1929	11	+0
12214-061.1	392	120	0.32	278	21	11562	629	2.7E-5	38	0.05	149.6	0.092	2.3	9.623	9.3	0.4446	9.1	0.977	0.1570	2.0	2371	180	2423	33	+3
12214-079.1	91	33	0.38	134	5	10844	452	3.3E-5	71	0.06	33.1	0.117	4.2	9.082	5.0	0.4232	4.8	0.955	0.1556	1.5	2275	92	2409	25	+7
12214-092.1	94	66	0.72	198	17	12154	518	8.1E-5	50	0.14	27.5	0.211	3.4	5.555	1.3	0.3414	1.0	0.728	0.1180	0.9	1893	16	1926	17	+2
12214-092.2	658	449	0.70	665	82	8800	378	2.6E-5	30	0.04	204.2	0.220	1.8	6.261	1.1	0.3615	0.8	0.751	0.1256	0.7	1989	14	2038	13	+3
12214-094.1	185	111	0.62	100	4	12622	421	1.0E-5	100	0.02	55.2	0.181	2.5	5.587	1.1	0.3468	0.9	0.845	0.1168	0.6	1919	15	1908	10	-1
12214-097.1	708	121	0.18	187	7	13655	598	7.9E-6	50	0.01	279.6	0.053	2.1	10.323	3.0	0.4599	1.9	0.633	0.1628	2.3	2439	38	2485	39	+2
12214-097.2	147	33	0.23	343	87	11790	713	1.1E-4	28	0.20	56.9	0.058	20.9	8.528	13.7	0.4510	10.6	0.775	0.1372	8.7	2399	213	2192	151	-11
12214-100.1	99	38	0.40	211	13	9015	300	-1.3E-5	100	-0.02	36.6	0.107	3.7	8.408	19.0	0.4285	18.8	0.990	0.1423	2.7	2299	364	2256	46	-2
12214-100.2	57	8	0.14	59	2	13015	434	3.2E-5	100	0.06	17.2	0.035	10.9	5.785	1.5	0.3511	1.1	0.715	0.1195	1.0	1940	18	1949	19	+1
12214-102.1	81	109	1.39	127	5	11407	530	-4.5E-5	71	-0.08	24.2	0.430	2.4	5.711	1.3	0.3470	1.0	0.745	0.1194	0.9	1920	17	1947	16	+2
12214-104.1	165	73	0.46	333	18	9516	415	2.8E-5	50	0.05	61.1	0.140	4.5	8.883	2.7	0.4304	2.3	0.854	0.1497	1.4	2307	44	2342	24	+2
12214-104.2	334	153	0.47	414	32	9621	388	1.2E-5	58	0.02	118.7	0.138	1.7	8.376	7.4	0.4137	7.2	0.969	0.1468	1.8	2232	135	2309	31	+4
12214-113.1	318	194	0.63	432	17	9026	301	2.7E-5	41	0.05	122.3	0.181	1.7	9.662	1.0	0.4481	0.9	0.827	0.1564	0.6	2387	17	2417	10	+1
12214-121.1	107	82	0.79	86	3	11734	505	8.8E-5	45	0.15	31.4	0.234	3.0	5.590	1.3	0.3431	1.0	0.742	0.1182	0.9	1902	16	1928	15	+2
12214-122.1	90	214	2.45	184	7	11993	656	1.0E-4	45	0.18	26.5	0.741	1.8	5.490	1.4	0.3422	1.0	0.718	0.1163	1.0	1897	16	1901	17	+0

Notes (see Stern, 1997):

Spot name follows the convention *x-y-z;* where x = sample number, y = grain number and z = spot number

Uncertainties reported at 1σ (absolute) and are calculated by numerical propagation of all known sources of error.

$f(206)^{204}$ refers to mole fraction of total ^{206}Pb that is due to common Pb, calculated using the ^{204}Pb-method; common Pb composition used is the surface blank

* Radiogenic Pb (corrected for common Pb)

Appendix 2. Biotite $^{40}Ar/^{39}Ar$ step heating results for samples from the Marguerite River area, Alberta

Heating Step[a]	Laser Power (W)	Isotopic Abundances (cps)[c] ^{40}Ar	±1σ	^{39}Ar	±1σ	^{38}Ar	±1σ	^{37}Ar	±1σ	^{36}Ar	±1σ	Background Isotopic Abundances (cps)[d] ^{40}Ar Bkgd	±1σ	^{39}Ar Bkgd	±1σ	^{38}Ar Bkgd	±1σ	^{37}Ar Bkgd	±1σ	^{36}Ar Bkgd	±1σ
Sample Z12002, NAD83 UTM zone 12 521907E 6396855N, biotite, J = 30.403 x 10^{-3} (± 9.7 x 10^{-2}, 1σ)[b]																					
1A	0.15	1385197	1354	27084	18.93	11.73	9.578	152.13	17.14	45.117	1.3708	8839	210	68.250	1.10	9.26	2.7	72.257	0.71	53.358	0.71
1B	0.20	1887354	1719	32486	30.26	-1.60	3.959	169.26	18.30	14.478	1.6010	8839	210	68.250	1.10	9.26	2.7	72.257	0.71	53.358	0.71
1C	0.25	5052692	4167	87731	30.26	3.05	3.445	346.50	20.27	38.293	2.0360	8839	210	68.250	1.10	9.26	2.7	72.257	0.71	53.358	0.71
1D*	0.30	1495226	1212	26069	17.66	4.96	3.569	120.81	18.27	5.960	1.1500	7446	210	70.939	0.88	9.33	1.9	72.754	0.83	51.826	0.76
1E*	0.35	2572583	2061	44732	36.55	16.63	4.683	97.62	19.94	19.126	1.8299	7446	210	70.939	0.88	9.33	1.9	72.754	0.83	51.826	0.76
1F*	0.40	1207663	1077	21088	27.74	-1.13	4.798	23.91	20.12	6.568	1.1631	7446	210	70.939	0.88	9.33	1.9	72.754	0.83	51.826	0.76
1G*	0.45	5290498	4612	92310	31.51	14.20	5.618	228.97	22.48	30.488	1.2611	7446	210	70.939	0.88	9.33	1.9	72.754	0.83	51.826	0.76
1H*	0.50	813470	850	14252	12.63	-1.64	2.796	10.19	18.85	2.994	1.1333	11114	200	95.611	0.87	8.62	1.8	70.249	0.73	49.697	0.64
1I*	0.55	1113926	968	19431	13.89	6.62	6.426	21.40	17.88	7.305	1.1139	11114	200	95.611	0.87	8.62	1.8	70.249	0.73	49.697	0.64
1J*	0.60	1245969	1026	21739	15.15	2.24	4.070	56.59	18.24	7.920	1.0469	11114	200	95.611	0.87	8.62	1.8	70.249	0.73	49.697	0.64
1K*	0.70	612515	557	10664	11.00	-6.82	3.517	-5.05	17.35	6.523	0.9991	11114	200	95.611	0.87	8.62	1.8	70.249	0.73	49.697	0.64
1L*	0.80	1203743	1100	20874	25.22	-14.31	3.604	10.59	18.25	6.337	1.5875	8823	220	78.254	0.98	16.85	2.9	70.486	0.82	51.277	0.71
1M*	1.20	366749	535	6219	7.87	-5.14	5.920	-37.02	18.06	8.220	1.5886	8823	220	78.254	0.98	16.85	2.9	70.486	0.82	51.277	0.71
1N*	1.60	68991	321	1177	4.03	-7.01	3.330	9.83	18.76	-0.668	1.0340	8823	220	78.254	0.98	16.85	2.9	70.486	0.82	51.277	0.71
1O*	2.00	627062	703	10865	17.67	-11.46	3.330	6.87	19.72	7.117	1.8010	8823	220	78.254	0.98	16.85	2.9	70.486	0.82	51.277	0.71
1P	6.00	101073	331	1490	4.12	-6.17	2.005	2.31	18.29	48.520	1.2922	8268	220	57.648	0.85	10.44	1.6	73.122	0.75	51.014	0.6
2A	0.15	376940	432	10184	9.98	8.76	2.934	41.85	19.97	14.450	1.2391	9734	220	48.677	0.69	0.96	1.7	69.505	0.87	50.170	0.67
2B	0.20	1590575	1350	28169	17.65	6.68	2.449	63.08	19.92	15.606	1.1425	9734	220	48.677	0.69	0.96	1.7	69.505	0.87	50.170	0.67
2C	0.23	2405711	2156	40844	20.17	4.76	4.958	109.49	20.46	9.952	1.1076	9734	220	48.677	0.69	0.96	1.7	69.505	0.87	50.170	0.67
2D	0.25	2019440	1975	34220	18.91	2.91	2.360	51.92	19.42	4.164	1.1168	9734	220	48.677	0.69	0.96	1.7	69.505	0.87	50.170	0.67
2E	0.30	4886847	4753	82633	30.25	4.42	2.824	128.58	20.96	7.380	1.1343	7693	220	53.839	0.75	6.17	2.1	68.828	0.76	50.328	0.69
2F	0.35	2667574	2399	46135	23.95	0.83	3.577	89.86	19.92	3.522	1.1260	7693	220	53.839	0.75	6.17	2.1	68.828	0.76	50.328	0.69
2G	0.45	2838699	2394	50568	40.33	13.60	3.577	135.18	18.55	7.258	1.1431	7693	220	53.839	0.75	6.17	2.1	68.828	0.76	50.328	0.69
2H	0.55	3181535	2480	56641	42.85	67.10	7.476	134.52	20.07	9.926	1.4678	7693	220	53.839	0.75	6.17	2.1	68.828	0.76	50.328	0.69
2I*	0.70	5002780	3587	87108	31.51	-1.77	1.659	141.73	18.63	15.129	1.1217	9397	200	54.730	0.78	5.11	1.2	68.610	0.69	48.600	0.64
2J*	0.90	5499940	3955	95839	35.29	1.65	2.676	133.80	17.89	17.174	1.1054	9397	200	54.730	0.78	5.11	1.2	68.610	0.69	48.600	0.64
2K*	6.00	3293321	2481	57155	40.33	0.64	2.345	53.38	19.83	38.697	1.8820	9397	200	54.730	0.78	5.11	1.2	68.610	0.69	48.600	0.64
Sample Z11998, NAD83 UTM zone 12 524089E 6400240N, biotite, J = 30.573 x 10^{-3} (± 7.0 x 10^{-2}, 1σ)[b]																					
1A	0.15	1110132	1072	29521	16.40	-10.49	2.983	2692.51	29.81	86.188	1.4030	8268	220	57.648	0.85	10.44	1.6	73.122	0.75	51.014	0.6
1B	0.20	2113092	1834	40336	21.44	8.79	2.672	1092.58	23.55	13.489	1.0783	8268	220	57.648	0.85	10.44	1.6	73.122	0.75	51.014	0.6
1C	0.25	3541021	2901	58180	26.47	25.47	6.616	1967.26	26.19	8.750	1.0091	8268	220	57.648	0.85	10.44	1.6	73.122	0.75	51.014	0.6
1D	0.30	1866493	1525	30430	18.93	-5.34	4.083	1358.55	25.12	2.372	1.0778	9627	230	74.770	1.00	13.16	3.0	74.272	0.74	53.919	0.67
1E	0.35	2612888	2181	43359	21.44	-5.04	5.754	4551.83	37.33	3.812	1.0899	9627	230	74.770	1.00	13.16	3.0	74.272	0.74	53.919	0.67
1F	0.40	918251	863	15794	12.64	-8.71	3.304	6524.39	46.32	1.775	1.1275	9627	230	74.770	1.00	13.16	3.0	74.272	0.74	53.919	0.67
1G	0.45	274096	425	4713	7.63	-14.97	4.258	1545.63	25.04	-1.637	1.1287	9627	230	74.770	1.00	13.16	3.0	74.272	0.74	53.919	0.67
1H	0.50	730616	789	12652	11.12	-0.09	3.868	6875.95	53.72	3.227	1.0262	9305	230	57.023	0.78	10.98	2.7	70.610	0.74	51.707	0.64
1I	0.55	39856	317	700	3.00	-2.97	3.779	144.24	18.65	-0.955	1.0263	9305	230	57.023	0.78	10.98	2.7	70.610	0.74	51.707	0.64
1J	0.60	194442	364	3390	5.85	-0.96	4.052	1823.54	26.36	-2.547	1.1304	9305	230	57.023	0.78	10.98	2.7	70.610	0.74	51.707	0.64
1K	0.70	59223	332	1050	3.37	-5.26	4.745	493.11	20.54	-2.078	1.0732	9305	230	57.023	0.78	10.98	2.7	70.610	0.74	51.707	0.64
1L	0.80	242028	367	4078	6.99	12.64	4.748	953.59	22.57	-0.328	1.0207	6172	230	57.462	0.91	4.9	2.3	69.752	0.84	50.581	0.72
1M	1.20	526140	527	8865	9.37	-0.84	2.685	2118.25	28.65	4.387	1.1406	6172	230	57.462	0.91	4.9	2.3	69.752	0.84	50.581	0.72
1N	1.60	193250	346	3248	5.99	1.57	2.564	505.73	21.45	1.084	1.0961	6172	230	57.462	0.91	4.9	2.3	69.752	0.84	50.581	0.72
1O	2.00	10693	301	114	1.66	2.01	2.752	66.18	18.95	0.961	1.0974	6172	230	57.462	0.91	4.9	2.3	69.752	0.84	50.581	0.72
1P	6.00	11559	314	17	1.43	-2.89	2.604	1.35	18.74	32.454	1.2152	6172	230	57.462	0.91	4.9	2.3	69.752	0.84	50.581	0.72
2A	0.15	1158223	993	41560	18.91	10.23	2.400	4771.87	38.68	93.555	1.5224	10222	220	50.036	0.70	2.43	0.8	71.511	0.79	50.509	0.68
2B	0.20	3298966	2536	65284	27.73	4.70	1.817	1779.82	27.20	34.392	1.1975	10222	220	50.036	0.70	2.43	0.8	71.511	0.79	50.509	0.68
2C	0.23	1469794	1128	25178	15.14	10.54	2.639	638.67	22.37	2.703	1.1578	10222	220	50.036	0.70	2.43	0.8	71.511	0.79	50.509	0.68
2D	0.25	2418097	1754	40889	20.20	5.05	5.169	1637.88	25.59	11.908	1.1462	9083	240	75.930	1.20	7.98	4.1	72.670	0.76	51.934	0.78
2E	0.30	3922613	2853	65101	25.23	15.33	5.326	3054.87	31.49	13.827	1.1229	9083	240	75.930	1.20	7.98	4.1	72.670	0.76	51.934	0.78
2F	0.33	1899105	1478	31832	20.20	-2.37	4.267	1659.27	24.98	4.233	1.1686	9083	240	75.930	1.20	7.98	4.1	72.670	0.76	51.934	0.78
2G	0.35	1777224	1465	29669	17.68	-1.88	4.948	2130.78	29.35	4.024	1.1699	9083	240	75.930	1.20	7.98	4.1	72.670	0.76	51.934	0.78
2H	0.45	4183186	3586	68894	26.49	-5.01	4.289	9380.86	67.73	9.344	1.2345	9083	240	75.930	1.20	7.98	4.1	72.670	0.76	51.934	0.78
2I	0.55	1487092	1329	25695	13.88	4.46	7.045	22112.29	134.94	8.630	1.0811	8928	210	60.928	0.81	9.37	1.3	69.076	0.76	50.814	0.66
2J	0.70	1356289	1144	24080	13.88	5.02	3.757	27315.55	149.64	11.185	1.1808	8928	210	60.928	0.81	9.37	1.3	69.076	0.76	50.814	0.66
2K	1.60	1228243	998	21827	13.88	6.94	7.788	12764.75	77.48	5.935	1.0334	8928	210	60.928	0.81	9.37	1.3	69.076	0.76	50.814	0.66
2L	6.00	656439	602	11366	10.99	26.69	10.654	4502.25	38.22	5.717	1.1044	8928	210	60.928	0.81	9.37	1.3	69.076	0.76	50.814	0.66

Heating Step[a]	^{39}Ar Mol ∞ 10^{-14}	^{39}Ar % of total	Derived Results $^{36}Ar/^{39}Ar$ (X 10^{-5})	±1s	%(^{36}Ar)$_{Ca}$	$^{37}Ar/^{39}Ar$	±1s	Ca/K	±1σ	Cl/K	±1σ	$^{38}Ar/^{39}Ar$	±1s	$^{40}Ar/^{39}Ar$	±1s	$^{40}Ar^*/^{39}Ar$	±1σ	%$^{40}Ar^*$	Age (Ma)	±1σ	w/±J ±1σ	Inverse Isochron Data $^{36}Ar/^{40}Ar$	±%1σ	$^{39}Ar/^{40}Ar$	±%1σ	$^{36}Ar/^{39}Ar$ Er. Corr.
Sample Z12002																										
1A	0.10	1.6	166.580	5.060	0.1	0.0056	0.0006	0.0110	0.00124	-0.0627	1E-07	0.0004	0.00035	51.1445	0.0615	50.6439	0.0631	99.0	1681.5	1.364	3.74	0.00003	3.04	0.01955	0.12	0.0262
1B	0.11	1.9	44.570	4.930	0.3	0.0052	0.0006	0.0102	0.00110	-0.0642	1E-07	0.0000	0.00012	58.0973	0.0757	57.9609	0.0771	99.8	1833.0	1.530	3.97	0.00001	11.01	0.01721	0.13	0.0058
1C	0.31	5.1	43.650	2.320	0.3	0.0039	0.0002	0.0077	0.00045	-0.0637	5E-08	0.0000	0.00004	57.5931	0.0515	57.4593	0.0520	99.8	1823.0	1.038	3.80	0.00001	5.29	0.01736	0.09	0.0144
1D*	0.09	1.5	22.860	4.410	0.6	0.0046	0.0007	0.0091	0.00137	-0.0626	1E-07	0.0002	0.00014	57.3556	0.0606	57.2839	0.0620	99.9	1819.5	1.241	3.85	0.00000	19.14	0.01744	0.11	0.0032
1E*	0.16	2.6	42.760	4.090	0.1	0.0022	0.0004	0.0043	0.00087	-0.0617	9E-08	0.0004	0.00010	57.5111	0.0658	57.3798	0.0669	99.8	1821.4	1.337	3.89	0.00001	9.51	0.01739	0.11	0.0059
1F*	0.07	1.2	31.140	5.520	0.1	0.0011	0.0010	0.0022	0.00187	-0.0641	2E-07	-0.0001	0.00023	57.2677	0.0910	57.1708	0.0924	99.8	1817.2	1.851	4.09	0.00001	17.54	0.01746	0.16	0.0029
1G*	0.33	5.3	33.030	1.370	0.2	0.0025	0.0002	0.0049	0.00048	-0.0629	5E-08	0.0002	0.00006	57.3126	0.0537	57.2103	0.0539	99.8	1818.0	1.078	3.80	0.00001	4.11	0.01745	0.09	0.0198
1H*	0.05	0.8	21.010	7.950	0.1	0.0007	0.0013	0.0014	0.00259	-0.0644	3E-07	-0.0001	0.00020	57.0789	0.0782	57.0123	0.0817	99.9	1814.0	1.640	3.99	0.00000	37.31	0.01752	0.14	0.0021
1I*	0.07	1.1	37.600	5.730	0.1	0.0011	0.0009	0.0022	0.00180	-0.0619	2E-07	0.0003	0.00033	57.3269	0.0645	57.2108	0.0667	99.8	1818.0	1.336	3.88	0.00001	15.13	0.01744	0.11	0.0044
1J*	0.08	1.3	36.430	4.820	0.2	0.0026	0.0008	0.0051	0.00164	-0.0633	2E-07	0.0001	0.00019	57.3145	0.0618	57.2021	0.0635	99.8	1817.9	1.271	3.86	0.00001	13.13	0.01745	0.11	0.0048
1K*	0.04	0.6	61.170	9.370	0.0	- 0.0005	0.0016	-0.0009	0.00319	-0.0679	3E-07	-0.0006	0.00033	57.4403	0.0790	57.2535	0.0837	99.7	1818.9	1.675	4.01	0.00001	15.23	0.01741	0.14	0.0039
1L*	0.07	1.2	30.360	7.610	0.0	0.0005	0.0009	0.0010	0.00171	-0.0679	2E-07	-0.0007	0.00017	57.6679	0.0874	57.5733	0.0902	99.8	1825.3	1.799	4.07	0.00001	24.78	0.01734	0.15	0.0022
1M*	0.02	0.4	132.170	25.540	- 0.1	- 0.0060	0.0029	-0.0117	0.00569	-0.0698	6E-07	-0.0008	0.00095	58.9703	0.1139	58.5709	0.1369	99.3	1845.1	2.700	4.56	0.00002	19.25	0.01696	0.19	0.0057
1N*	0.00	0.1	-56.760	87.840	- 0.4	0.0083	0.0159	0.0164	0.03123	-0.0981	3E-06	-0.0060	0.00283	58.6072	0.3385	58.7732	0.4285	100.3	1849.0	8.433	9.20	- 0.00001	-155.50	0.01706	0.58	0.0024
1O*	0.04	0.6	65.500	16.580	0.0	0.0006	0.0018	0.0012	0.00356	-0.0704	4E-07	-0.0011	0.00031	57.7133	0.1140	57.5138	0.1241	99.7	1824.1	2.476	4.41	0.00001	25.18	0.01733	0.20	0.0025
1P	0.01	0.1	3257.330	87.220	0.0	0.0015	0.0123	0.0030	0.02407	-0.1244	2E-06	-0.0041	0.00135	67.8547	0.2910	58.1249	0.3773	85.7	1836.2	7.480	8.33	0.00048	2.68	0.01474	0.43	0.0933
2A	0.04	0.6	141.900	12.170	0.1	0.0041	0.0020	0.0081	0.00384	-0.0599	4E-07	0.0009	0.00029	37.0139	0.0558	36.5868	0.0664	98.9	1349.1	1.724	3.48	0.00004	8.56	0.02702	0.15	0.0102
2B	0.10	1.6	55.400	4.060	0.1	0.0022	0.0007	0.0044	0.00139	-0.0627	1E-07	0.0002	0.00009	56.4649	0.0596	56.2958	0.0608	99.7	1799.6	1.230	3.83	0.00001	7.29	0.01771	0.11	0.0094
2C	0.14	2.4	24.370	2.710	0.3	0.0027	0.0005	0.0053	0.00098	-0.0630	1E-07	0.0001	0.00012	58.8999	0.0603	58.8235	0.0609	99.9	1850.0	1.197	3.87	0.00000	11.02	0.01698	0.10	0.0071
2D	0.12	2.0	12.170	3.260	0.3	0.0015	0.0006	0.0030	0.00111	-0.0631	1E-07	0.0001	0.00007	59.0134	0.0663	58.9732	0.0670	99.9	1853.0	1.317	3.91	0.00000	26.21	0.01695	0.11	0.0032
2E	0.29	4.8	8.930	1.370	0.5	0.0016	0.0003	0.0030	0.00050	-0.0632	5E-08	0.0001	0.00003	59.1389	0.0615	59.1084	0.0616	100.0	1855.6	1.209	3.88	0.00000	14.89	0.01691	0.10	0.0061
2F	0.16	2.7	7.630	2.440	0.7	0.0019	0.0004	0.0038	0.00085	-0.0634	9E-08	0.0000	0.00008	57.8206	0.0600	57.7941	0.0605	100.0	1829.7	1.204	3.85	0.00000	30.85	0.01730	0.10	0.0025
2G	0.18	2.9	14.350	2.260	0.5	0.0027	0.0004	0.0052	0.00072	-0.0620	7E-08	0.0003	0.00007	56.1366	0.0652	56.0902	0.0655	99.9	1795.4	1.329	3.86	0.00000	15.48	0.01781	0.12	0.0040
2H	0.20	3.3	17.520	2.590	0.4	0.0024	0.0004	0.0047	0.00069	-0.0566	7E-08	0.0012	0.00013	56.1703	0.0610	56.1144	0.0615	99.9	1795.9	1.247	3.83	0.00000	14.60	0.01780	0.11	0.0038
2I*	0.31	5.0	17.370	1.290	0.3	0.0016	0.0002	0.0032	0.00042	-0.0638	4E-08	0.0000	0.00002	57.4316	0.0461	57.3760	0.0463	99.9	1821.3	0.926	3.77	0.00000	7.29	0.01741	0.08	0.0088
2J*	0.34	5.5	17.920	1.150	0.2	0.0014	0.0002	0.0027	0.00037	-0.0636	4E-08	0.0000	0.00003	57.3873	0.0464	57.3300	0.0466	99.9	1820.4	0.931	3.77	0.00000	6.33	0.01743	0.08	0.0101
2K*	0.20	3.3	67.710	3.290	0.0	0.0009	0.0003	0.0018	0.00068	-0.0641	7E-08	0.0000	0.00004	57.6205	0.0595	57.4144	0.0602	99.6	1822.1	1.204	3.84	0.00001	4.84	0.01736	0.10	0.0114
Sample Z11998																										
1A	0.10	1.7	291.950	4.760	0.9	0.0912	0.0010	0.1788	0.00198	-0.0688	2E-07	-0.0004	0.00010	37.6044	0.0419	36.7386	0.0441	97.7	1358.3	1.146	2.46	0.00008	1.64	0.02659	0.11	0.0509
1B	0.14	2.3	33.440	2.670	2.3	0.0271	0.0006	0.0531	0.00114	-0.0625	1E-07	0.0002	0.00007	52.3879	0.0533	52.2873	0.0539	99.8	1722.8	1.145	2.78	0.00001	8.10	0.01909	0.10	0.0091
1C	0.21	3.4	15.040	1.730	6.3	0.0338	0.0005	0.0663	0.00088	-0.0610	9E-08	0.0004	0.00011	60.8634	0.0570	60.8188	0.0573	99.9	1895.4	1.106	2.90	0.00000	12.04	0.01643	0.09	0.0059
1D	0.11	1.8	7.800	3.540	16.0	0.0446	0.0008	0.0875	0.00162	-0.0646	2E-07	-0.0002	0.00013	61.3374	0.0630	61.3157	0.0639	100.0	1905.0	1.227	2.95	0.00000	51.48	0.01630	0.10	0.0013
1E	0.15	2.5	8.790	2.510	33.3	0.1050	0.0009	0.2058	0.00169	-0.0642	2E-07	-0.0001	0.00013	60.2621	0.0585	60.2449	0.0591	100.0	1884.3	1.146	2.90	0.00000	40.60	0.01659	0.10	0.0018
1F	0.06	0.9	11.240	7.140	102.6	0.4131	0.0030	0.8097	0.00578	-0.0668	6E-07	-0.0006	0.00021	58.1395	0.0718	58.1525	0.0756	100.0	1843.2	1.502	3.03	0.00000	13434.20	0.01720	0.12	0.0000
1G	0.02	0.3	-34.730	23.950	-26.3	0.3279	0.0053	0.6428	0.01047	-0.0818	1E-06	-0.0032	0.00090	58.1571	0.1304	58.2968	0.1491	100.2	1846.1	2.956	3.96	- 0.00001	-55.11	0.01719	0.22	0.0019
1H	0.04	0.7	25.500	8.110	59.5	0.5435	0.0043	1.0652	0.00837	-0.0637	9E-07	0.0000	0.00031	57.7471	0.0804	57.7335	0.0851	99.9	1834.9	1.697	3.13	0.00000	76.06	0.01731	0.14	0.0011
1I	0.00	0.0	-136.280	146.510	- 4.2	0.2059	0.0266	0.4036	0.05222	-0.0871	5E-06	-0.0042	0.00539	56.8964	0.5136	57.3241	0.6755	100.7	1826.7	13.535	13.79	- 0.00002	-103.50	0.01757	0.90	0.0068
1J	0.01	0.2	-75.120	33.340	-20.0	0.5379	0.0078	1.0542	0.01535	-0.0642	2E-06	-0.0003	0.00120	57.3516	0.1460	57.6377	0.1776	100.5	1833.0	3.546	4.41	- 0.00002	-37.13	0.01743	0.25	0.0037
1K	0.00	0.1	-197.830	102.170	- 6.6	0.4694	0.0196	0.9201	0.03844	-0.0909	4E-06	-0.0050	0.00452	56.3818	0.3638	57.0253	0.4759	101.1	1820.7	9.568	9.92	- 0.00004	-48.55	0.01773	0.65	0.0100
1L	0.01	0.2	-8.030	25.030	-81.2	0.2338	0.0055	0.4583	0.01088	-0.0450	1E-06	0.0031	0.00116	59.3467	0.1358	59.3959	0.1553	100.1	1867.7	3.041	4.04	0.00000	-174.73	0.01685	0.23	0.0006
1M	0.03	0.5	49.480	12.870	13.5	0.2389	0.0032	0.4683	0.00635	-0.0645	6E-07	-0.0001	0.00030	59.3496	0.0864	59.2274	0.0947	99.8	1864.4	1.858	3.24	0.00001	29.82	0.01685	0.15	0.0023
1N	0.01	0.2	33.360	33.740	13.0	0.1557	0.0066	0.3052	0.01296	-0.0609	1E-06	0.0005	0.00079	59.4922	0.1528	59.4079	0.1831	99.9	1868.0	3.585	4.46	0.00000	115.08	0.01681	0.26	0.0011
1O	0.00	0.0	842.610	962.130	1.9	0.5801	0.1664	1.1370	0.32608	0.0319	3E-05	0.0177	0.02412	93.7399	2.9694	91.3059	4.1216	97.4	2404.4	59.958	60.03	0.00009	116.48	0.01066	3.17	0.0215
1P	0.00	0.0	186640.000	16818.670	0.0	0.0775	1.0777	0.1518	2.11229	-3.1368	2E-04	-0.1664	0.15037	664.7425	57.3967	107.4713	28.9599	16.2	2625.5	372.707	372.72	0.00281	4.62	0.00150	8.64	0.1845
2A	0.15	2.4	225.110	3.660	1.4	0.1148	0.0009	0.2250	0.00183	-0.0645	2E-07	0.0002	0.00006	27.8687	0.0271	27.2043	0.0293	97.6	1091.9	0.882	2.07	0.00008	1.65	0.03588	0.10	0.0459
2B	0.23	3.8	52.680	1.830	1.4	0.0273	0.0004	0.0534	0.00082	-0.0636	8E-08	0.0001	0.00003	50.5324	0.0444	50.3744	0.0448	99.7	1681.8	0.972	2.68	0.00001	3.51	0.01979	0.09	0.0192
2C	0.09	1.5	10.730	4.600	6.6	0.0254	0.0009	0.0497	0.00174	-0.0611	2E-07	0.0004	0.00010	58.3768	0.0569	58.3439	0.0586	99.9	1847.0	1.161	2.88	0.00000	44.45	0.01713	0.10	0.0014
2D	0.14	2.4	29.120	2.800	3.8	0.0401	0.0006	0.0785	0.00123	-0.0630	1E-07	0.0001	0.00013	59.1375	0.0519	59.0515	0.0526	99.9	1861.0	1.035	2.84	0.00000	9.90	0.01691	0.09	0.0061
2E	0.23	3.8	21.240	1.720	6.2	0.0469	0.0005	0.0920	0.00095	-0.0623	1E-07	0.0002	0.00008	60.2538	0.0497	60.1923	0.0500	99.9	1883.3	0.971	2.84	0.00000	8.52	0.01660	0.08	0.0075
2F	0.11	1.8	13.300	3.670	10.9	0.0521	0.0008	0.1022	0.00154	-0.0640	2E-07	-0.0001	0.00013	59.6596	0.0599	59.6224	0.0610	99.9	1872.2	1.191	2.91	0.00000	30.15	0.01676	0.10	0.0020
2G	0.10	1.7	13.560	3.940	14.8	0.0718	0.0010	0.1408	0.00194	-0.0640	2E-07	-0.0001	0.00017	59.9027	0.0609	59.8670	0.0621	99.9	1876.9	1.211	2.92	0.00000	33.16	0.01669	0.10	0.0020
2H	0.24	4.0	13.560	1.790	28.0	0.1362	0.0010	0.2669	0.00193	-0.0640	2E-07	-0.0001	0.00006	60.7192	0.0570	60.6917	0.0575	100.0	1892.9	1.110	2.89	0.00000	17.75	0.01647	0.09	0.0044
2I	0.09	1.5	33.590	4.210	71.5	0.8606	0.0053	1.6867	0.01033	-0.0627	1E-06	0.0002	0.00027	57.8759	0.0605	57.8770	0.0655	99.9	1837.7	1.304	2.93	0.00000	42.52	0.01727	0.10	0.0018
2J	0.08	1.4	46.450	4.900	68.1	1.1344	0.0062	2.2234	0.01225	-0.0626	1E-06	0.0002	0.00016	56.3246	0.0575	56.3197	0.0659	99.9	1806.5	1.336	2.93	0.00000	32.44	0.01774	0.10	0.0021
2K	0.08	1.3	27.190	4.730	60.0	0.5848	0.0036	1.1463	0.00700	-0.0618	7E-07	0.0003	0.00036	56.2725	0.0581	56.2583	0.0616	99.9	1805.2	1.249	2.89	0.00000	42.31	0.01776	0.10	0.0015
2L	0.04	0.7	50.300	9.720	22.0	0.3961	0.0034	0.7764	0.00663	-0.0500	7E-07	0.0023	0.00094	57.7547	0.0769	57.6492	0.0828	99.8	1833.2	1.654	3.10	0.00001	24.60	0.01731	0.13	0.0026

Notes:

[a] Letters are used to name each heating step; *Denotes steps used in the plateau or pseudoplateau age calculations.

[b] Nominal J, from GSC Irradiation Batch #75, referenced to PP20 hornblende = 1074 ± 10 Ma (2σ, Jourdan et al., 2006).

[c] Isotopic abundances corrected for baseline, blank, and detector intercalibration. ^{39}Ar and ^{37}Ar are decay-corrected values. Isotopic abundances are not corrected for nuclear interference reactions.

[d] Background isotopic abundances are determined during blank analyses, which are run prior to every four unknowns. Blank values are then applied to the subsequent unknown analyses.

Atmospheric argon $^{40}Ar/^{36}Ar$ = 298.56 (Lee et al., 2006).

Nucleogenic interference correction factors for Cd-shielded irradiation (±2σ):

$(^{39}Ar/^{37}Ar)_{Ca}$ = 0.0007 ± 0.00005

$(^{36}Ar/^{37}Ar)_{Ca}$ = 0.00028 ± 0.00016

$(^{38}Ar/^{37}Ar)_{Ca}$ = 0.00003 ± 0.00003

$(^{40}Ar/^{39}Ar)_K$ = 0.003 ± 0.005

$(^{38}Ar/^{39}Ar)_K$ = 0.011 ± 0.01

$^{40}Ar^*$ = radiogenic argon

Decay Constant (^{40}K λ_{total}) = 5.543 x 10^{-10}/yr (Steiger and Jager, 1977)

Preliminary geochemical characterization of the Central Mineral Belt uranium geochemistry database

P. Acosta-Góngora and E.G. Potter

Abstract

Preliminary geochemical characterization of the U±Cu±Mo±V mineralization in the Central Mineral Belt (CMB) of Labrador is developed based on data compiled within the recently published Central Mineral Belt uranium geochemistry database. The highest uranium concentrations are found in the Jacques Lake (up to 11 weight % U) and Michelin (up to 2 weight % U) areas, whereas copper and molybdenum concentrations are the highest in the Moran Lake (up to 1.6 weight % Cu) and Jacques (up to 1 weight % Mo) and Anna Lake (up to 0.3 weight % Mo) areas, respectively. Sodic alteration is the most common alkali alteration type in the CMB, with the emplacement of iron oxides mainly decoupled from potassium. Uranium-rich samples also plot within the 'least altered' field in the alteration type discriminant diagram. However, this might be an artefact of distinct alteration type overlaps, which may shift the major element composition of the mineralized rocks towards the least altered field. The lack of association of uranium and other base metals with alkali elements is further recognized by principal component analysis. However, additional statistical evaluation focused on the individual alteration types and categorized by the geographical areas within the CMB is necessary to better understand the mobility of uranium and base metal elements, along with their association with alteration facies.

Introduction

The Central Mineral Belt (CMB) of Labrador is known to host multiple U±Cu±Mo±V prospects and advanced exploration projects. Most of the early exploration in the CMB took place during the 1950s and up to the mid-1980s when there was a significant drop in the world uranium markets. The renewed demand of this commodity triggered extensive exploration campaigns during the mid-2000s resulting in the generation of large amounts of industry geophysical and geochemical data.

The geology and metallogeny of the CMB is summarized in the recent work of Sparkes (2017), which builds upon previous studies (e.g. Gower et al., 1982; Ryan et al., 1983; Kerr, 1994; Wilton, 1996). This work coupled with the extensive geochemical and geophysical data generated during the latest exploration wave, provides an excellent framework to characterize the CMB uranium-rich systems within current ore genesis models.

Iron-Oxide-Copper-Gold (IOCG) deposits represent some of largest and most productive uranium, copper and gold deposits (e.g. Olympic Dam). Over the past decade, geochemical characterization of IOCG systems has developed a series geochemical tools useful to detect prospective areas (e.g. Montreuil et al., 2013). In some localities, the CMB uranium systems preserve certain geological and mineralogical characteristics analogous to those of IOCGs, which include pervasive regional alkali-rich alteration occurring prior to brecciation, followed by iron oxides emplacement and subsequent mineralization. Thus, it is worthwhile to explore potential links between IOCG and the CMB uranium mineralization as means to advance exploration models.

The Central Mineral Belt uranium geochemistry database (CMBUG; Acosta-Gongora et al., 2018) consists of over 40 000 data entries compiled from Geological Survey of Newfoundland and Labrador data files and drill core geochemistry recorded in mineral assessment reports comprising the period of 2002 to 2011. In this report, we provide a general characterization of the uranium, copper and molybdenum concentrations in the CMB, classification of the CMBUG data in terms of their alteration types and a preliminary principal component analysis done on a smaller data suite of the CMBUG.

Geology of the Central Mineral Belt

The regional geology of the CMB described herein is derived from Gower et al. (1982), Ermanovics (1993), Kerr, (1994), Kerr et al. (1996), Wilton (1996), Hinchey (2007), Hinchey and LaFlamme (2009) and Sparkes et al. (2016), Sparkes (2017). The oldest units in the CMB are the Archean Nain Province gneisses, which are intruded by variably deformed tonalite, granodiorite and granite intrusions of the Kanairiktok Intrusive Suite (KIS). The Archean gneisses and KIS intrusions are transected by the 2.23 Ga Kikkertavak dykes.

The Paleoproterozoic metavolcanic and metasedimentary packages of the Moran Lake and Post Hill groups unconformably overly the Archean gneisses and KIS intrusions, but are not cut by the Kikkertavak dykes, giving a maximum depositonal age of 2.2 Ga. The Post Hill Group (northeastern CMB) is overlaid by mixed sedimentary and bimodal volcanic rocks of the Aillik Group. The Moran Lake Group (southwestern CMB) is unconformably overlaid by the Bruce River Group, which consists of conglomeratic arkose and sandstone overlaid by a

Corresponding author: Pedro Acosta-Góngora (pedro.acostagongora@canada.ca)

Acosta-Góngora, P., and Potter, E.G., 2018. Preliminary geochemical characterization of the Central Mineral Belt uranium geochemistry database; *in* Targeted Geoscience Initiative: 2017 report of activities, volume 2, (ed.) N. Rogers; Geological Survey of Canada, Open File 8373, p. 57–63. https://doi.org/10.4095/306601

thick sequence of 1.7 Ga felsic volcanic rocks. The youngest supracrustal sequences in the CMB are the Letitia and Seal Lake groups. The ca. 1.3 Ga Letitia Lake Group is dominated by alkaline volcanic rocks that are overlaid by sedimentary and mafic volcanic rocks of the Seal Lake Group.

The Archean intrusions and Paleoproterozoic sequences were metamorphosed (greenschist to amphibolite facies) and variably deformed by at least three orogenic episodes (Makkovikian: ca. 1.8–1.7Ga; Labradorian: 1.7–1.6 Ga; Grenvillian: ca. 1.0 Ga).

The CMB U±Th±Cu±Pb±Zn mineralization occurs within all the Archean to Paleo- to Mesoproterozoic intrusive (e.g. Two Time prospect), volcanic (e.g. Moran Lake Upper C and Michelin deposits) and sedimentary (e.g. Anna Lake prospect) rocks. Mineralization styles include breccia- (e.g. Two Time and Moran lake Upper C zone), fracture-hosted (e.g. Anomaly No. 17 prospect and Two Time deposit) and disseminated (e.g. Anna Lake prospect), although in most cases ore-bearing events are preceded by moderate to pervasive alkali metasomatism (e.g. Michelin deposit) and iron oxides replacements or breccia infill (mainly hematite).

Analytical methods

The major and trace element analyses compiled in the CMBUG were obtained from various laboratories mainly using 'partial digestion' (PD) and 'total digestion' (TD) methods. The most common PD procedure employed use Aqua Regia followed by inductively-coupled plasma atomic emission spectroscopy analysis. The TD techniques rely on a combination of three to four different acids to attempt to fully dissolve samples followed by inductively couple mass spectrometry analysis to provide relatively complete geochemical signatures. Although TD techniques are typically effective, incomplete digestion of the sample is still possible due to the presence of highly resistive minerals. Thus, the TD is best considered a 'near-total' digestion. In addition, elements that may volatilize during TD (e.g. As, Se, Te and U) may be under-represented in the analyses.

Less commonly, samples in the CMBUG were analyzed by a mixture of lithium metaborate/tetraborate fusion, instrumental neutron activation analysis and X-ray fluorescence techniques. The combination of these techniques allow a better quantification of major and trace elements contained in resistive minerals (e.g. magnetite).

Data distribution

The CMBUG encompasses over 40 000 data points from multiple locations within the CMB (Fig. 1). However, over 95% of the data are from six main areas: Moran, Jacques Lake, Snegamook, Michelin, Anna Lake, Kitts-Post Hill and Kanairiktok (Acosta-Góngora et al. 2018: Fig. 1, 2). These areas may represent one or many prospects and/or deposits. For example, the Moran dataset includes the Moran Lake Upper C Zone deposit and Moran Lake B and Armstrong prospects. On the other hand, the Jacques Lake dataset only comprises samples from the Jacques Lake deposit. In this report, data characterization is restricted to the aforementioned main locations and no further geographical distinction was considered.

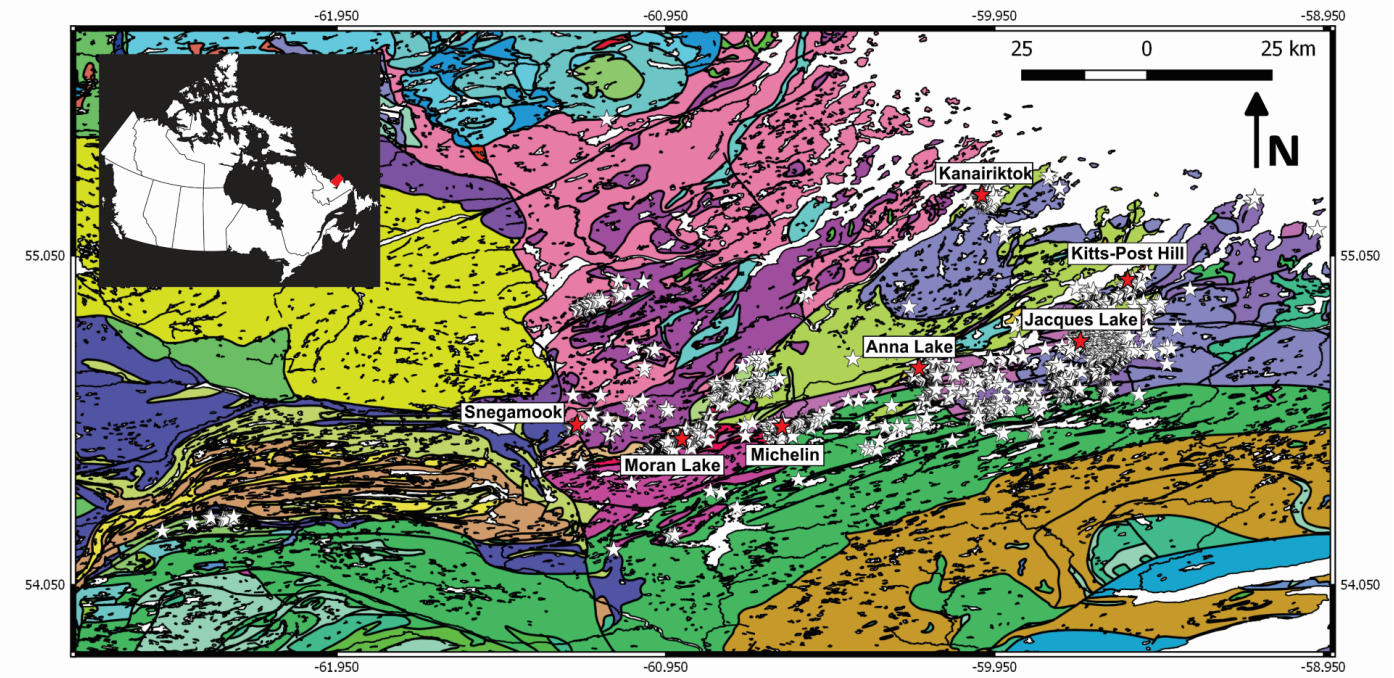

Figure 1. Central Mineral Belt geology after (Wardle et al., 1997) and locations of the geochemistry samples and/or locations of the drillholes from which samples were obtained for subsequent analysis.

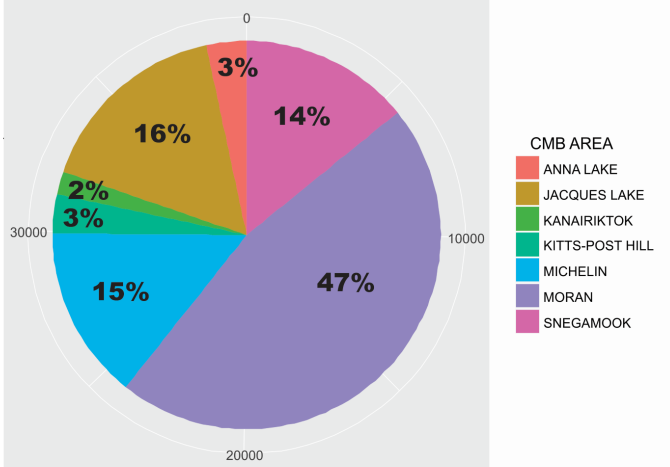

Figure 2. Pie chart represents the relative proportions of the data from the Moran, Jacques Lake, Snegamook, Michelin, Anna Lake, Kitts-Post Hill and Kanairiktok areas characterized in this report. The numbers displayed on the circumference of the chart correspond to number of samples (over 37 000 samples).

Distribution of uranium, copper and molybdenum in the Central Mineral Belt

The variability of the CMBUG dataset in terms of the element suite analyzed and the analytical techniques used to obtain such concentrations (PD versus TD) is significant. In some areas, uranium is the only element analyzed and it is reported as UO_3 weight %, whereas in other ones, a full major and trace element geochemical profile was acquired. Most data from the Kitts-Post Hill area is restricted to UO_3 weight % and thus excluded from the description below.

As few samples were analyzed by PD and TD, direct comparison between results for individual samples is difficult for most elements, except uranium, and to a lesser extent copper. Figure 3 shows that except for a less statistically significant set of outlier values, the covariations of uranium and copper concentrations between both digestion techniques follow well defined positive trends. In principle, this shows that at least in terms of uranium, copper and possibly other base metals (i.e. molybdenum, lead, zinc), the TD and PD results are effectively equivalent. However, since the CMBUG has different data sets for PD and TD, in the description below, the technique type is indicated unless both data sets maximum, mean and median values differ by a 30% or less. In cases were the difference is >30%, the TD results are the ones reported. The data description is done in terms of the maximum values, mean, median and of the CMB areas. The mean and median are commonly used to measure the 'centre' of a data population. The mean is more susceptible to distortion by extremely low or high values, whereas the median (50th percentile) is not, and therefore, the latter is considered a better measurement of the data population centre when extreme values are present.

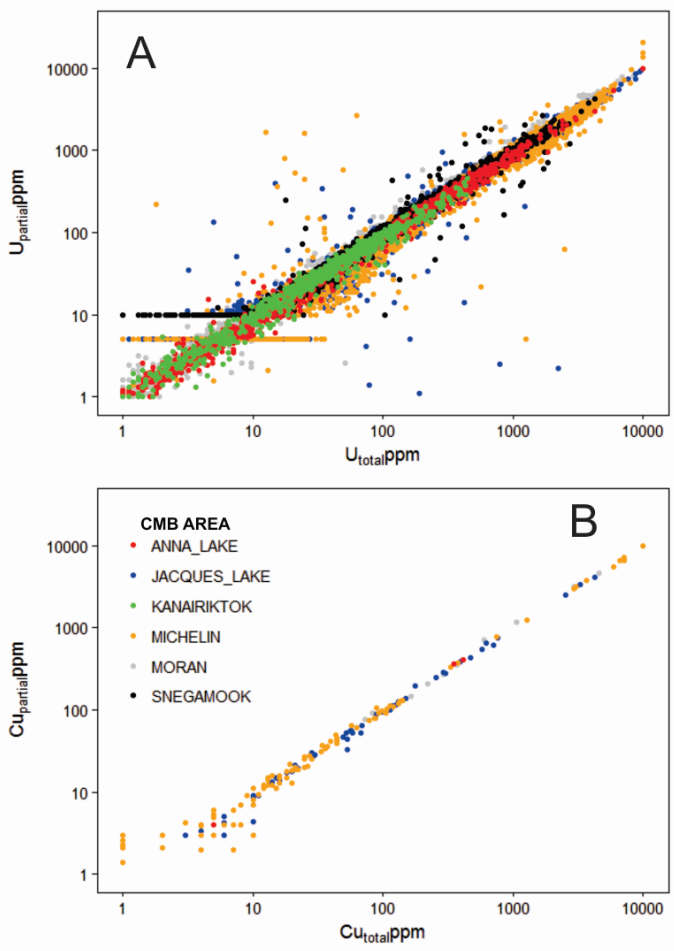

Figure 3. Binary plot of uranium and copper concentration obtained via total and partial digestions.

The Jacques Lake area has the highest uranium concentrations, reaching values of up to 11 weight % and with mean and median values of 383 ppm and 104 ppm, respectively (Fig. 4a, b). In the Michelin area the highest uranium concentrations are up to 2 weight % (PD), but compared to Jacques Lake, the former has the highest mean (549 ppm) and median (115 ppm) values of the entire data set (Fig. 4a, b). On the other hand, the Kanairiktok (up to 447 ppm) and Anna Lake (up to 1 weight %) areas have lower uranium contents with mean and median values of 50 and 23 ppm, and 185 and 17 ppm, respectively. The mean values of the Moran Lake area for TD (151 ppm) and PD (259 ppm) are higher than those of the Kanairiktok and Anna Lake areas, but the Moran's median values are the lowest of the entire dataset (15 and 17 ppm; Fig. 4a, b).

Partial digestion analyses for copper and molybdenum are not available for the Kanairiktok area, and in the Moran and Anna lake areas the PD dataset is much lower than that of the TD. Thus, the following description only refers to the TD concentrations. In terms of copper, the Moran Lake area records the highest maximum concentration value (up to 1.6 weight

%), and has mean and median values of 177 ppm and 91 ppm, respectively (Fig. 4c, d). The highest maximum concentration value for molybdenum is recorded in the Jacques Lake area (1 weight %: Fig. 4e, f). Here, the mean and median values correspond to 117 and 1 ppm, respectively. The Anna Lake area contains the second greatest mean (70 ppm) and the highest median (5 ppm) values for molybdenum in the CMB. In contrast, the lowest copper and molybdenum mean (Cu = 30 ppm and Mo = 3 ppm) and median (Cu= 8 ppm and Mo= 0.3 ppm) values were obtained in the Snegamook area, where maximum concentrations of those elements register up to 0.4 weight % (Cu) and 0.1 weight % (Mo).

Alteration characterization in the Central Mineral Belt

The alteration facies hosting uranium mineralization in the CMB is evaluated through the Montreuil et al. (2013) discrimination plot. For this purpose, only samples having non-zero Al, Na, K, Ca, Mg and Fe concentrations are selected.

Silicon concentrations are not given in the CMBUG, so those were calculated only for samples analyzed by TD. The calculation of Si content relies on an assumption that dissolution of the other major elements was nearly total and that the sum of trace elements contents is approximately 1 weight %. Therefore, the concentration of Si is estimated as 100-(other major elements + trace elements + loss on ignition). It is acknowledged though, that the estimation of Si in exceptionally U-rich (> 1 weight %) samples is less accurate.

In general, the CMBUG samples present significant scatter were most samples plot within the least altered and Na and Fe-(Mg) alteration fields (Fig. 5). In the Snegamook and Jacques Lake areas, most samples are Na-altered and a lower portion of those data plot mainly within the unaltered and K alteration fields (Fig. 5). In the Anna Lake, Kanairiktok, and Michelin areas, most samples plot within the least altered and Na alteration fields, with less significant clusters consistent with K, Ca-

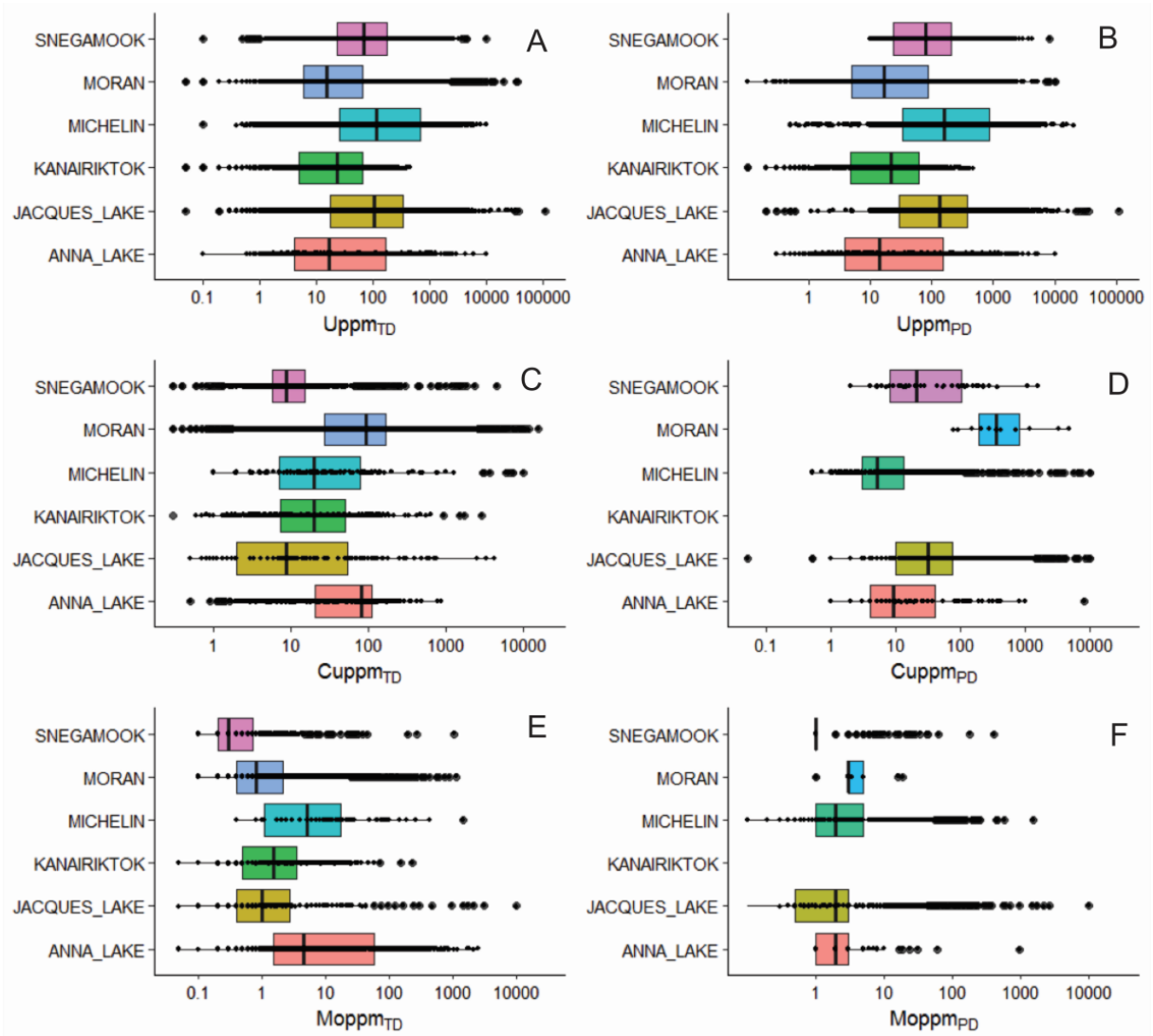

Figure 4. Distribution of partial (PD) and total digestion (TD) analyses of uranium, copper and molybdenum concentrations.

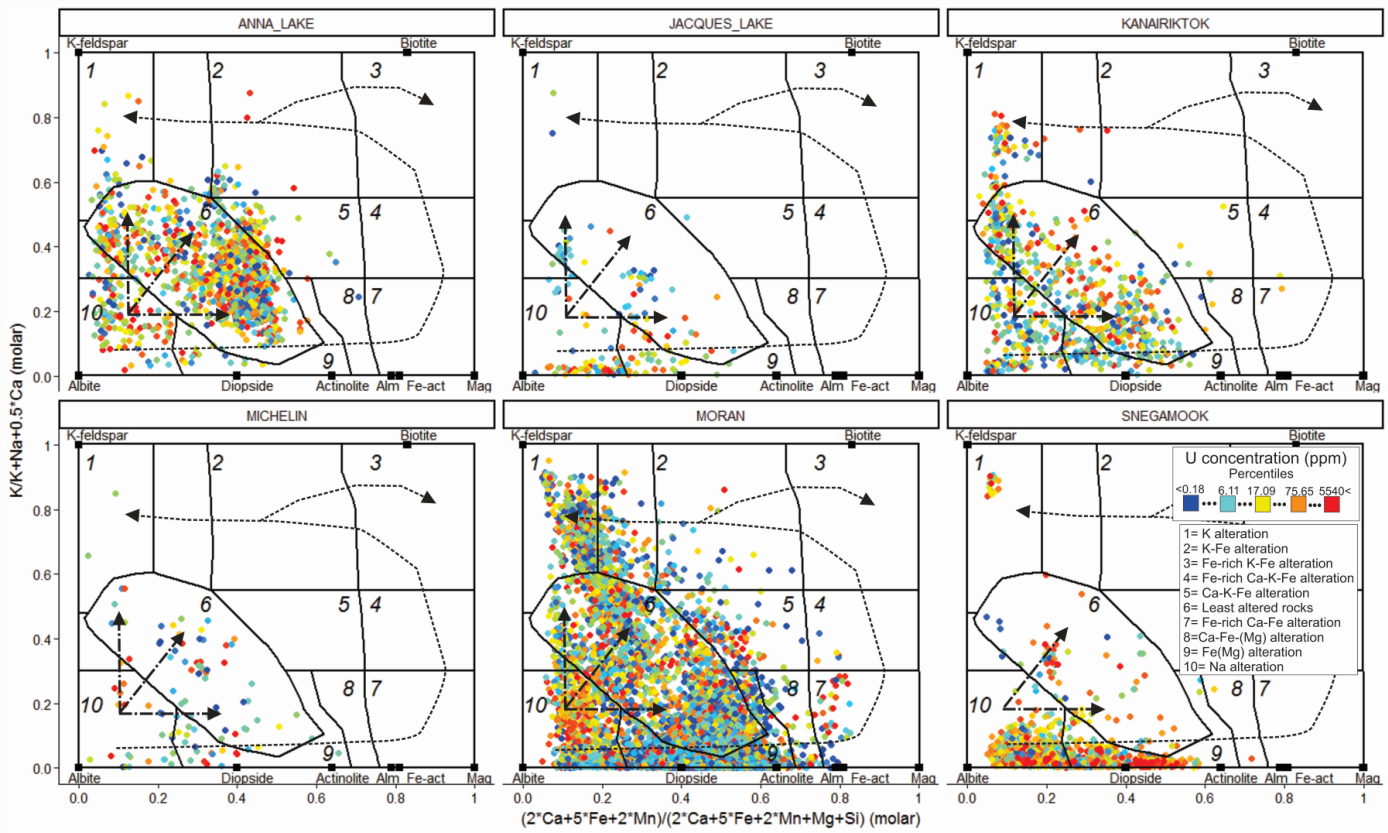

Figure 5. Montreuil et al. (2013) alteration discriminant plots of CMBUG data. The dashed arrow shows the evolutionary trend(s) recognized for IOCG systems (Corriveau, 2017; Corriveau et al. 2017). The three arrows radiating from the Na alteration field indicate possible trends of alteration overlaps responsible for shifting major element compositions to the least altered field.

K-Fe and K-Fe altered rocks (Fig. 5). The Moran Lake data accounts for the greatest portion of the CMBUG database and shows the largest scatter (Fig. 2, 5). Similar to other CMB locations, most samples are contained in the least altered, Na and Fe-(Mg) alteration fields, with a relatively minor portion plotting within the K, Ca-K-Fe, K-Fe, Fe-rich Ca-K-Fe and Ca-Fe alteration fields. Notably, it is observed that high uranium concentration distribution is not associated to a particular type of alteration type, instead uranium mineralization is found in almost all fields on the alteration plot, including that representing least altered rocks.

In IOCG deposits, sodic alteration is commonly associated with deeper and higher temperature parts of the hydrothermal system that evolve in time to Ca-Fe and K-Fe alteration assemblages (e.g. Corriveau et al. 2010; Fig. 5). Generally, rocks contained in the K-Fe field are considered as geochemically 'mature' and economically fertile. In the CMB, the data suite as a whole do not seem to follow the expected IOCG evolution path (Fig. 5), rather it either evolves from the Na to Fe-(Mg) alteration or from the Na to K alteration (Fig. 5). Both evolution paths may result in a shift of major elements contents into the least altered field (Fig. 5). However, it is possible that mineralization hosted in microveins and/or disseminated in relatively unaltered rocks could also account for the high uranium rocks in the least altered field.

In summary, the preliminary interpretations of the data distribution in the alteration plot are that: i) Na alteration is the most common alkali alteration in the CMB; ii) emplacement of iron oxides is generally decoupled from potassium (few samples located in the K-Fe alteration field); and iii) the mineralization is not necessarily associated to alkali or iron oxides altered rocks. However, the latter may result from alteration overlaps that shift the major element composition of mineralized rocks to the least altered field (Fig. 5).

Principal component analysis

The statistical characterization of whole-rock geochemistry requires previous methods for data treatment. The centre log-ratio transformation overcomes the closure constraint inherent to geochemical data, which allows the use of multivariate statistical tools (e.g. principal component analysis) for geochemical process identification. The data suite used to perform the principal component analysis (PCA) comprises around 5000

samples analyzed by TD and that contain a full geochemical profile including major and trace elements. To these data was applied the centre log-ratio transformation.

As a whole, it is noted that base metals tend to co-variate roughly together where cobalt, vanadium and iron form a subgroup distinct from that of cadmium, chromium, zinc, copper and nickel (Fig. 6). The association of the iron, cobalt and vanadium is likely related to the incorporation of the latter two elements in iron oxides such as magnetite and hematite. From the PCA it is also remarkable that alkali alteration related elements (e.g. potassium and sodium) do not correlate directly with uranium, as is also suggested by the alteration plot (Fig. 6). However, this lack of association, especially with sodium, might be masked by the fact that proportionally, the sodium alteration in the CMB is more common and regionally widespread in comparison to the local occurrences of uranium mineralization.

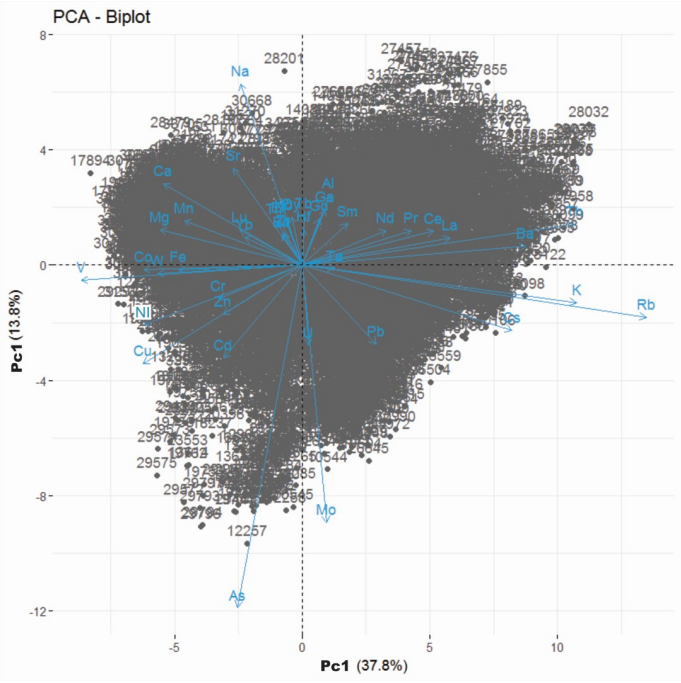

Figure 6. PCA analysis. Principal component 1(Pc1) plotted against Principal component 2 (Pc2) showing distinct covariation of elements.

Conclusions

Geochemical data from the CMBUG shows that the greatest uranium concentrations are found in the Jacques Lake (up to 11 weight % U) and Michelin (up to 2 weight % U) areas, whereas copper and molybdenum concentrations are the highest in the Moran Lake (up to 1.6 weight % Cu) and Jacques (up to 1 weight % Mo) and Anna lake (up to 0.3 weight % Mo) areas, respectively.

Evaluation of the data in the Montreuil et al. (2013) alteration plot indicates that: i) sodic alteration is the most common alkali alteration in the CMB; ii) the emplacement of iron oxides is generally decoupled from potassium; and iii) uranium mineralization is not necessarily associated to alkali or iron oxides altered rocks. Nevertheless, alteration type overlaps may shift the major element composition of mineralized rocks to the least altered field. The absence of association of uranium and other base metals with alkali elements is also recorded by PCA. However, further statistical analysis based on the individual alteration types and by geographical location of the CMBUG is necessary to fully characterize the mobility of uranium and base metal elements and their association with alteration facies.

Acknowledgments

This report is a contribution to NRCan's Targeted Geoscience Initiative Program (TGI). Support for this study was provided through the Uranium-rich Mineralization Project's 'Activity U-2.1: Metal pathways and traps in polymetallic (U +/- Fe, Cu, Au, REE) metasomatic ore systems project'.

References

Acosta-Góngora, P., Duffett, C., Sparkes, G., and Potter, E., 2018. The Central Mineral Belt uranium geochemistry database; Geological Survey of Canada, Open File 8352, 9 p.

Corriveau, L., Williams, P.J., and Mumin, A.H., 2010. Alteration vectors to IOCG mineralization from uncharted terranes to deposits; *in* Exploring for iron oxide copper-gold deposits: Canada and global analogues; Geological Association of Canada, Short Course Notes, 20, p. 89–110.

Corriveau, L., Potter, E.G., Acosta-Gongora, P., Blein, O., Montreuil, J.-F., De Toni, A.F., Day, W., Slack, J.F., Ayuso, R.A., and Hanes, R., 2017. Petrological mapping and chemical discrimination of alteration facies as vectors to IOA, IOCG, and affiliated deposits within Laurentia and beyond: Proceedings of the 14th SGA Biennial Meeting, Québec, p. 851–855.

Corriveau, L., 2017. Iron-oxide and alkali-calcic alteration ore systems and their polymetallic IOA, IOCG, skarn, albitite-hosted U±Au±Co, and affiliated deposits: A short course series. Part 1: Introduction; Geological Survey of Canada, Scientific Presentation 56, 80 p.

Ermanovics, I., 1993. Geology of Hopedale Block, southern Nain Province, and the adjacent Proterozoic terranes, Labrador, Newfoundland; Geological Survey of Canada, Memoir No. 431, 161 p.,

Gower, C.F., Flanagan, M.J., Kerr, A., and Bailey, D.G., 1982. Geology of the Kaipokok Bay–Big River area, Central Mineral Belt, Labrador; Government of Newfoundland and Labrador, Department of Mines and Energy, Mineral Development Division, Report 82-7, 77 p.

Hinchey, A.M., 2007. The Paleoproterozoic metavolcanic, metasedimentary and igneous rocks of the Aillik Domain, Makkovik Province, Labrador (NTS map area 13O/03); *in* Current Research, Government of Newfoundland and Lab-

rador, Department of Natural Resources, Geological Survey, Report 07-1, p. 25–44.

Hinchey, A.M. and LaFlamme, C., 2009. The Paleoproterozoic volcano-sedimentary rocks of the Aillik Group and associated plutonic suites of the Aillik domain, Makkovik Province, Labrador [NTS map area 13J/14]; *in* Current Research, Government of Newfoundland and Labrador, Department of Natural Resources, Geological Survey, Report 09-1, p. 159–182.

Kerr, A., 1994. Early Proterozoic magmatic suites of the eastern Central Mineral Belt (Makkovik Province), Labrador: Geology, geochemistry and mineral potential; Government of Newfoundland and Labrador, Department of Mines and Energy, Geological Survey Branch, Report 94-03, 167 p.

Kerr, A., Ryan, B., Gower, C.F., and Wardle, R.J., 1996. The Makkovik Province: Extension of the Ketilidian Mobile Belt in mainland North America; *in* Precambrian Crustal Evolution in the North Atlantic Region, (ed.) T.S. Brewer; Geological Society of London, Special Publication 1112, p. 155–177.

Montreuil, J.-F, Corriveau, L., and Grunsky, E.C., 2013. Compositional data analysis of hydrothermal alteration in IOCG systems, Great Bear magmatic zone, Canada: To each alteration type its own geochemical signature; Geochemistry: Exploration, Environment, Analysis, v. 13, p. 229–247.

Ryan, A.B., Kay, A., and Ermanovics, I., 1983. The geology of the Makkovik Subprovince between Kaipokok Bay and Bay of Islands, Labrador; Government of Newfoundland and Labrador, Department of Mines and Energy, Mineral Development Division, Maps 83-38 to 83-41, scale 1:50 000, 22 p.

Sparkes, G., 2017. Uranium mineralization within the central mineral belt of Labrador: A summary of the diverse styles, settings and timing of mineralization; Newfound Land and Labrador Geological Survey, Open file LAB/1684, 198 p.

Sparkes, G.W., Dunning, G.R., Fonkew, M., and Langille, A., 2016. Age constraints on the formation of iron oxide-rich hydrothermal breccias of the Moran Lake area: Evidence for potential IOCG-style mineralization within the Central Mineral Belt of Labrador; *in* Current Research, Government of Newfoundland and Labrador, Department of Natural Resources, Geological Survey, Report 16-1, p. 71–90.

Wilton, D.H.C., 1996. Metallogeny of the Central Mineral Belt and adjacent Archean basement, Labrador; Government of Newfoundland and Labrador, Department of Mines and Energy, Geological Survey, Mineral Resources Report 8, 178 p.

.

.

Orogenic comparison of structurally controlled gold systems of the Abitibi greenstone belt and central Newfoundland Appalachians: Implications for Newfoundland gold potential and recurring tectonic drivers of gold mineralization

I. Honsberger and W. Bleeker

Abstract

The Abitibi greenstone belt and the emerging Paleozoic gold district across the central Newfoundland Appalachians both extend over similarly sized areas and are characterized by crustal-scale faults associated with remnants of synorogenic clastic basins. The aim of this study to investigate whether the orogenic model for structurally controlled Archean lode gold deposits developed for the Abitibi belt is applicable to Newfoundland and, by extension, other regions. Although the Abitibi belt has a substantially greater gold endowment than the Newfoundland belt, this research is focused on a compare and contrast exercise with respect to lithology, stratigraphy, structure, magmatism and tectonic setting. Identifying similarities between Archean and Paleozoic gold districts may identify recurring orogenic processes and key ingredients that are fundamental to the development of structurally controlled gold systems.

Introduction

World-class (>100 tonnes of gold) Archean lode gold systems in granite-greenstone terranes of the Canadian Shield (e.g. Abitibi, Yellowknife) are characterized by structurally controlled quartz±carbonate vein systems within and surrounding major fault zones (Poulsen et al., 2000; Bleeker and Hall, 2007; Dubé and Gosselin, 2007; Bleeker, 2015). These systems are Canada's dominant economic gold deposit type with respect to number of deposits and historical production (Hodgson, 1993). Key lithotectonic markers of the gold-bearing fault corridors are preserved panels of clastic synorogenic sedimentary basins (±volcanics) and associated alkaline magmatic rocks that formed during a transient phase of crustal-scale extension (Bleeker, 2012, 2015). The predictive lithologic relationships and structural asymmetry of these Archean systems reflect a sequential chain of tectonic processes critical to the formation of economic gold deposits (Hodgson, 1993; Poulsen et al., 2000; Bleeker, 2012, 2015); thus, can be applied as a gold exploration tool. Long-term preservation of prolific gold deposits in the Timmins – Kirkland Lake area of the Abitibi greenstone belt is attributed to thermally-driven gold transport along major extensional faults, with subsequent inversion of these faults into thick-skinned thrusts serving to bury mineralized zones in footwall blocks containing synorogenic sedimentary rocks (Bleeker, 2015).

The predictive model established for formation and preservation of lode gold deposits in the Abitibi has been validated in other Archean gold systems, such as the Yellowknife belt, Northwest Territories, and the Agnew-Wiluna belt, Western Australia, but its applicability to younger structurally controlled gold systems is largely untested (Bleeker, 2015). The central Newfoundland Appalachians is a developing gold belt in Canada that preserves lithologic similarities to and a comparable spatial distribution of deposits over the same scale as the central and southern Abitibi belt (Fig. 1). Current prospecting in Newfoundland between Cape Ray and the northernmost extension of the Dog Bay Line is revealing a pattern of gold showings along major fault corridors associated with synorogenic sedimentation and magmatism.

This study tests if the Paleozoic central Newfoundland gold district developed via a comparable set of sequential orogenic processes at approximately the same rate as the Archean Abitibi system. Research involves comparing and contrasting the lithologies, stratigraphy, structure, magmatism and tectonic settings of both gold belts. As these attributes are thoroughly documented for the Abitibi (e.g. Bleeker, 2015), the central Newfoundland gold district will be the primary focus of new research. This study will serve to highlight predictable age-independent orogenic processes responsible for the development of structurally controlled economic gold deposits. This work will help to establish the gold potential of central Newfoundland and aid in future exploration.

Geological and structural settings

Central and southern Abitibi gold district

The Abitibi Subprovince is the southernmost Archean granite-greenstone terrane within the Superior Province (Goodwin, 1977; Wheeler et al., 1996). It consists primarily of supracrustal and granitoid rocks that formed between ca. 2750 and ca. 2665 Ma (Jackson and Fyon, 1991). Gneissic and granulitic Abitibi equivalents of the north-northeast trending Paleoprote-

Corresponding author: Ian Honsberger (ian.honsberger@canada.ca)

Honsberger, I., and Bleeker, W., 2018. Orogenic comparison of structurally controlled gold systems of the Abitibi greenstone belt and central Newfoundland Appalachians: Implications for Newfoundland gold potential and recurring tectonic drivers of gold mineralization; *in* Targeted Geoscience Initiative: 2017 report of activities, volume 2, (ed.) N. Rogers; Geological Survey of Canada, Open File 8373, p. 65–70. https://doi.org/10.4095/306602

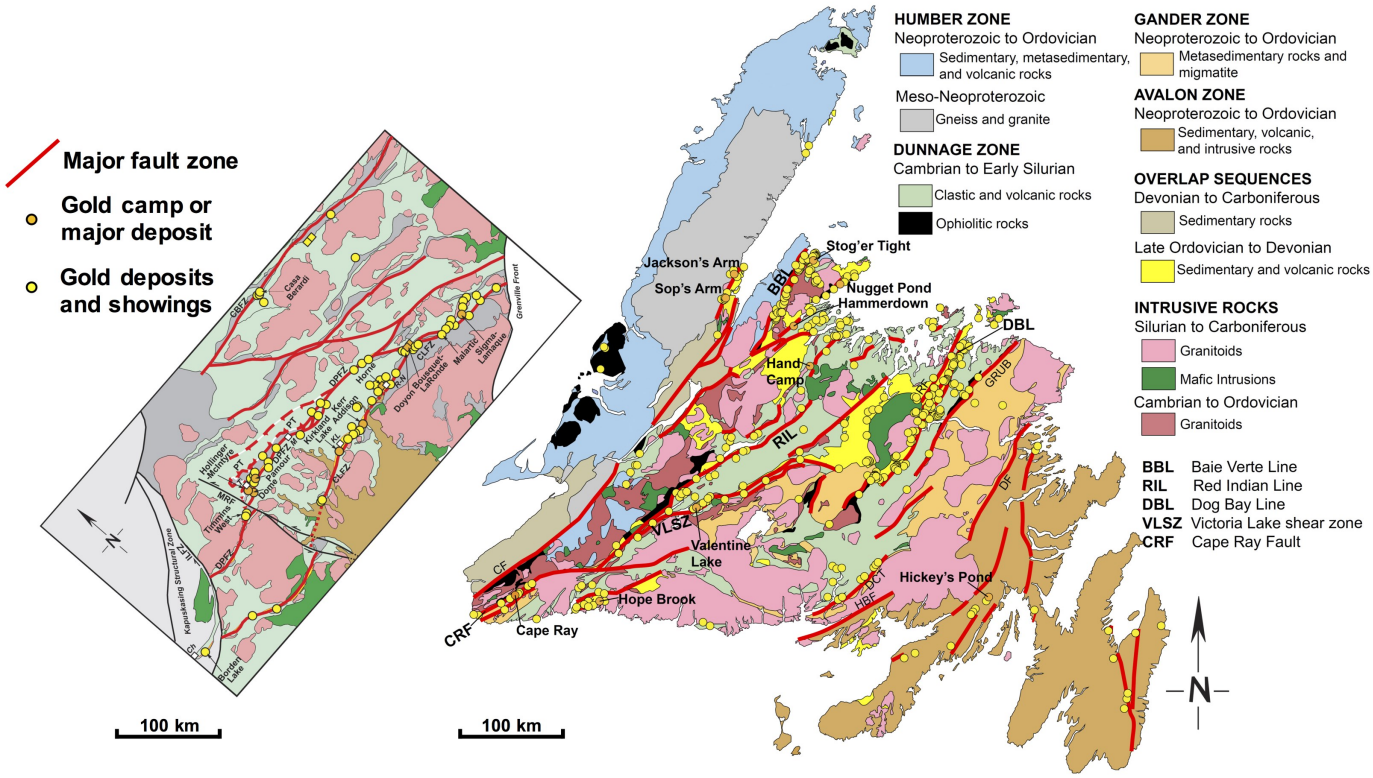

Figure 1. Comparison of Abitibi (left) and Newfoundland (right) structurally controlled gold systems at the same regional scale. Both are characterized by major fault networks associated with synorogenic clastic basins (coloured yellow) and gold mineralization. Synorogenic basins occur along the DBL, VLSZ, and CRF in central Newfoundland, and along the DPFZ and CLFZ in the Abitibi. Many of the locations marked yellow along the DBL are gold showings . Late Ordovician to Early Devonian synorogenic clastic basins (coloured yellow) occur along the DBL, VLSZ, and CRF. Abitibi map is from Bleeker (2015). Newfoundland map is modified from Colman-Sadd et al. (1990), with gold deposits and showings from Evans (1996), O'Driscoll and Wilton (2005) and Sandeman et al. (2017). Newfoundland: CF, Cabot Fault; DF, Dover Fault; GRUB, Gander River Ultrabasic Belt; HBF, Hermitage Bay Fault; RF, Reach Fault. Abitibi: CBFZ, Casa Beradi Fault Zone; Ch, Chapleau; CLFZ, Cadillac-Larder Fault Zone DPFZ; Destor-Porcupine Fault Zone; ILFZ, Ivanhoe Lake Fault Zone; KL = Kirkland Lake; M, Matheson; MRF, Paleoproterozoic Matagami River Fault; PT, Pipestone Thrust; R-N, Rouyn-Noranda.

rozoic Kapuskasing Structural Zone (Percival and West, 1994) truncate the western margin of the central and southern Abitibi gold district proper, whereas Mesoproterozoic gneiss complexes and supracrustal rocks of the Grenville Province (Rivers et al., 2012) truncate the southeastern edge of the subprovince (Wheeler et al., 1996; Ayer et al., 2005). The Abitibi Subprovince is bordered to the north and south, respectively, by sedimentary rocks of the Opatica and Pontiac subprovinces (Ayer et al., 2005; Ayer and Chartrand, 2011).

The largest concentration of Archean gold deposits and most prolific gold camps occur in the central and southern Abitibi greenstone belt (Poulsen et al., 2000: Fig. 1). Structurally controlled gold deposits in the Abitibi belt are associated with a tectono-stratigraphy comprised of the following elements (Poulsen et al., 2000; Bleeker, 2015): 1) deformed mafic and ultramafic volcanics and associated sedimentary rocks and magmatic intrusions, all of which are truncated by a ca. 2686 to 2680 Ma syntectonic unconformity; 2) tectonically buried clastic rocks (breccias, conglomerates, siltstones, and turbidites) and associated alkalic magmatic and volcanic rocks of synorogenic basins (Timiskaming assemblage), recording extension-related deepening between ca. 2680 Ma to ca. 2672 and subsequent basin filling during thrust inversion between ca. 2672 Ma and ca. 2665 Ma; 3) thick-skinned thrust blocks composed of older deformed volcanic rocks that were displaced along major terrane-scale fault planes ('breaks'). The Destor-Porcupine Fault Zone (DPFZ) and Cadillac-Larder Lake Fault Zone (CLFZ) in Timmins and Kirkland Lake, respectively, are the major fault breaks in the central and southern Abitibi (Fig. 1). Major gold deposits are preserved within structural footwalls comprised of geologic elements (1) and (2), whereas structural hanging walls, (3), have low gold potential due to lack of preservation from uplift and erosion (Bleeker, 2015).

At least three distinct phases of regional deformation are recorded in these rocks (Card, 1990; Poulsen et al., 2000; Bleeker, 2012, 2015). The oldest phase of deformation (D_A1) is

associated with the development of a fold and thrust belt that deformed and imbricated the underlying volcano-sedimentary terrane. The second phase (D_A2) post-dates synorogenic clastic deposition and extension-related magmatism, and correlates with regional deformation associated with thick-skinned thrust inversion. The third phase (D_A3) involved complex, late-stage, strike-slip deformation that accommodated about 10 to 100 km of net lateral displacement.

Central Newfoundland gold district

Newfoundland occupies the northeastern-most portion of the North American Appalachian orogen (Fig. 2), which formed by Paleozoic accretion and magmatism along the Laurentian margin (Williams et al., 1988; van Staal et al., 1998). Newfoundland preserves an exceptional record of the early to mid-Paleozoic tectonic evolution of the orogen in rocks within the Humber, Dunnage, Gander and Avalon zones (Williams, 1978). The Humber Zone underlies western Newfoundland and consists of basement and associated deformed cover rocks of the Early Paleozoic Laurentian margin. The Dunnage Zone spans central Newfoundland and contains peri-Laurentian (Notre Dame Subzone) and peri-Gondwanan (Exploits Subzone) accreted terranes, which are juxtaposed along faults defining the Red Indian Line (RIL) that constitutes the Iapetan suture (Williams et al., 1988; van Staal et al., 1998). The Notre Dame Subzone to the west of the RIL is underlain primarily by magmatic arc rocks that intruded the paleogeographically low-latitude microcontinent of Dashwoods (Waldron and van Staal, 2001), upon which peri-Laurentian supra-subduction zone ophiolites were obducted (van Staal and Barr, 2012). The Exploits Subzone to the east is comprised of Cambrian to Ordovician Ganderian continental and oceanic arc – back-arc complexes that formed on the opposing side of the Iapetus Ocean from Dashwoods (Williams et al., 1988; van Staal et al., 1998; Zagorevski et al., 2007). The Gander and Avalon Zones represent peri-Gondwanan continental fragments that were accreted to composite Laurentia during the Silurian to Early Devonian Salinic orogeny and Early Devonian Acadian orogeny, respectively (van Staal and Barr, 2012; van Staal et al., 2014).

Gold mineralization in central Newfoundland is concentrated along major faults within and along the Dunnage Zone (Fig. 1, 2). The major faults include, from west to east, the Baie Verte Line (BBL) and Cape Ray fault (CRF), RIL and Victoria Lake shear zone (VLSZ), Dog Bay Line (DBL) and Gander River Ultrabasic Belt (Fig. 1), with the largest known deposits associated with the VLSZ. The present research is focused on the emerging gold district that trends northeast to north-northeast across central Newfoundland along the CRF, VLSZ, and DBL (Fig. 1). The CRF separates the Dashwoods Subzone from the Exploits Subzone, whereas the VLSZ and DBL both occur within the Exploits Subzone (Fig. 1, 2). Despite some specific genetic variations along strike, a general stratigraphy containing the following elements (Zagorevski et al., 2007; van Staal et al., 2014) can be extrapolated along the gold-bearing corridor: 1) Neoproterozoic to Lower Ordovician arc and non-arc(?) basement rocks, truncated either by a fault (Notre Dame Subzone) or unconformity (Exploits Subzone); 2) Lower Ordovician to Upper Ordovician volcanic arc – back-arc terranes; 3) synorogenic sedimentary rocks, ranging from Late Ordovician to Early Silurian marine clastic rocks (Badger Group, Exploits Subzone only) to unconformably overlying Late Ordovician to Silurian (Windsor Point Group along CRF) and Middle to Late Silurian terrestrial clastic rocks and associated plutonic and volcanic rocks (Fogo Suite along VLSZ and DBL).

Three regional deformation phases are thought to have controlled primarily the regional geometry of structures in the vicinity of the VLSZ and RIL (Zagorevski et al., 2007); local deformation phases (Zagorevski et al., 2006) are not considered here. The oldest phase of deformation (D_N1, ca. 455 Ma) is

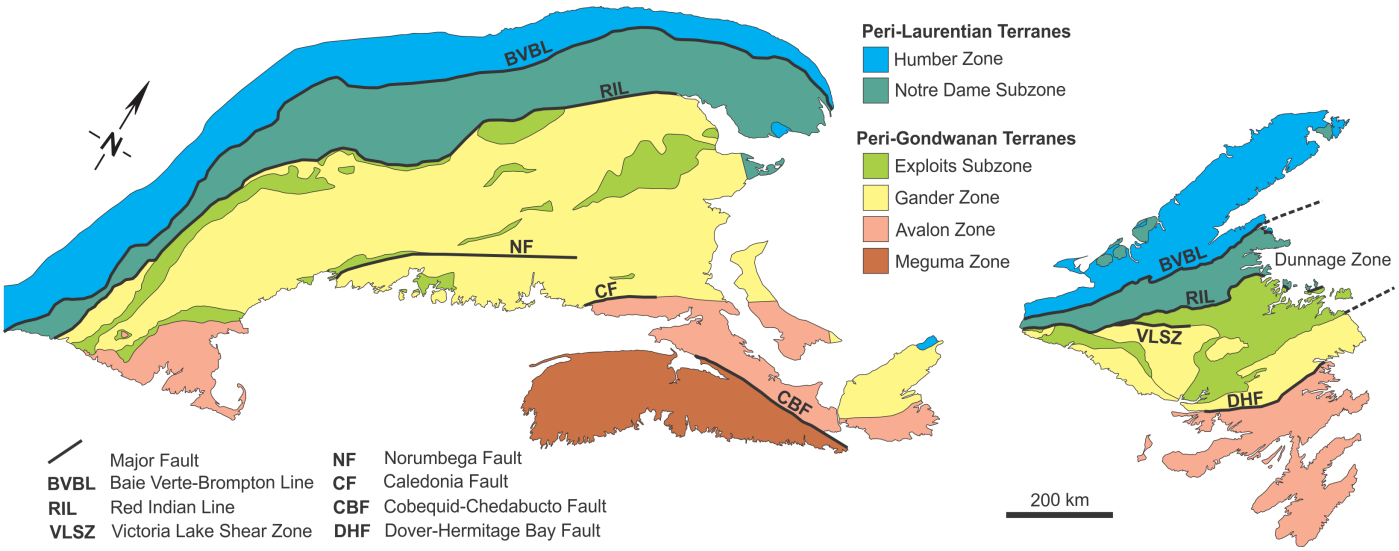

Figure 2. Generalized geologic map of the northern Appalachian orogen, adapted from Hibbard et al. (2006).

marked by thrust-induced shear zones formed during collision of the Red Indian Lake arc (peri-Laurentian) and Victoria arc (peri-Gondwanan). Subsequent deformation (D_N2, ca. 435–426 Ma; Zagorevski et al., 2006) folds D_N1 shear zones, transposes S_N1 foliation, and coincides with closure of the Tetagouche – Exploits back-arc basin, the suture of which is marked by the DBL (Williams et al., 1993; van Staal and Barr, 2012; van Staal et al., 2014). The last major phase of regional deformation (D_N4) is marked by mylonite zones associated with Early Devonian thrusting that juxtaposed low and high grade metamorphic rocks; the VLSZ and CRF are examples of such D_N4 structures (Lin et al., 1994; Dubé et al., 1996; Valverde-Vaquero et al., 2006).

Key first-order similarities

The central and southern Abitibi and central Newfoundland gold districts are structurally controlled by major fault zones of comparable scale (Fig. 1). Three main phases of regional deformation involving components of thrust burial and strike-slip are pervasive and associated with gold mineralization in both regions. The structural footwalls of the gold-bearing fault zones are marked by inverted synorogenic clastic sedimentary basins (±volcanics) that occur above deformed and imbricated volcano-magmatic-sedimentary sequences. These basins formed and were tectonically buried over a similar timespans; 20 Ma for the Abitibi (Bleeker, 2015) and ca. 30 Ma for Newfoundland (van Staal et al., 2014). Synorogenic clastic rocks are mylonitized locally along the major fault breaks. Lode gold deposits occur within and/or in proximity to granitoid rocks that are spatially, and often temporally, related to synorogenic basins. Strike-slip deformation is superimposed on the major fault breaks (e.g. DPFZ and CLFZ: Bleeker, 2015), and/or was associated with oblique thrusting (e.g. DBL: Williams et al., 1993; CRF: Dubé et al., 1996).

Key first-order differences

The Archean Abitibi gold district is considerably more prolific than central Newfoundland with respect to number of major deposits and production (Poulsen et al., 2000). More than 95% of gold produced in the central and southern Abitibi has come from the structural footwalls of the DPFZ and CLFZ (Bleeker, 1995, 2015). In Newfoundland, gold mineralization at Cape Ray is preserved within the structural footwall of the CRF, whereas deposits at Valentine Lake occur in the structural hanging wall of the Valentine Lake thrust (Colman-Sadd et al., 1990; van Staal et al., 2005). The DPFZ and CLFZ are thick-skinned thrust faults that reactivated older crustal-scale extensional faults associated with lithospheric delamination (Bleeker, 2015). The CRF, VLSZ and DBL in central Newfoundland are thrust sutures that formed as a result of accretionary tectonics involving subduction, tectonic underplating and slab break-off (Zagorevski et al., 2007; van Staal and Barr, 2012). Crustal-scale extension in central Newfoundland was primarily operative in supra-subduction zone back-arc basins that were subsequently consumed and closed during terrane accretion (Zagorevski et al., 2007; van Staal and Barr, 2012). The DBL is an example of a transpressional thrust suture that marks the closure site of such a basin (Williams et al., 1993; van Staal and Barr, 2012).

Mantle-derived magmatic rocks associated with formation of synorogenic basins in the Abitibi are thought to be products of lithospheric extension, magmatic underplating, and potentially delamination (Bleeker, 2015). Magmatic rocks associated with synorogenic basin development in central Newfoundland are interpreted as mantle melts formed during subduction of the Tetagouche – Exploits back-arc basin and Ganderia, which is associated with slab steepening, break-off and eventual eduction (reversed subduction) (Whalen et al., 2006; van Staal et al., 2014).

Research goals

The overarching goal of this study is to determine if the orogenic model for gold mineralization in the central and southern Abitibi greenstone belt is applicable to the emerging gold district of central Newfoundland. This research involves comparing and contrasting key orogenic ingredients related to the development and preservation of each gold system, and determining which common ingredients are critical to both systems and which may be spurious. Did a transient phase of crustal-scale extension stimulate and facilitate gold-bearing fluid transport in the Newfoundland system, as it did in the Abitibi? Is there asymmetry in the spatial extent of gold mineralization in Newfoundland (e.g. hanging wall vs. footwall), and what does this imply regarding a long term preservation mechanism? What is the reactivation history of the central Newfoundland fault system and how does it affect present fault geometries? What are critical recurring orogenic processes associated with structurally controlled gold mineralization? These types of questions will be addressed through careful stratigraphic and structural field observations of rocks associated with and along the major faults in Newfoundland. Details regarding the evolution of synorogenic basins will be particularly important for a thorough system comparison. Zircon geochronology of plutonic and volcanic rocks associated with synorogenic clastic basins will help to constrain local temporal relationships between magmatism, basin development and gold mineralization in Newfoundland.

Acknowledgments

This report is a contribution to NRCan's Targeted Geoscience Initiative Program (TGI). Support for this study was provided through the Gold Project's 'Activity G-2.1: Deep faults, synorogenic clastic sequences, alkaline magmatism and gold deposits: testing and refining the Timmins-Kirkland Lake model in areas with high gold potential'.

Ian Honsberger is conducting TGI supported post–doctoral research at GSC Ottawa. Collaboration with the Geological

Survey of Newfoundland and Labrador is gratefully acknowledged. This report benefited from the review of Neil Rogers.

References

Ayer, J.A. and Chartrand, J.E., 2011. Geological compilation of the Abitibi greenstone belt; Ontario Geological Survey, Miscellaneous Release Data 282.

Ayer, J.A., Thurston, P.C., Bateman, R., Dubé, B., Gibson, H.L., Hamilton, M.A., Hathway, B., Hocker, S.M., Houlé, M.G., Hudac, G., Ispolatov, V.O., Lafrance, B., Lesher, C.M., MacDonald, P.J., Péloquin, A.S., Piercey, S.J., Reed, L.E., and Thompson, P.H., 2005. Overview of results of the Greenstone Architecture Project: Discover Abitibi Initiative; Ontario Geological Survey, Open File Report 6154, 146 p.

Bleeker, W., 1995. Day 1: Surface geology of the Porcupine camp; *in* Tectonics and metallogeny of Archean crust in the Abitibi–Kapuskasing–Wawa region, field trip guidebook, (ed.) W. Bleeker; Geological Survey of Canada, Open File 3141, p. 13–37.

Bleeker, W., 2012. Targeted Geoscience Initiative (TGI-4) lode gold deposits in ancient deformed and metamorphosed terranes: The role of extension in the formation of Timiskaming basins and large gold deposits, Abitibi greenstone belt — A discussion; *in* Summary of Field Work and Other Activities, 2012; Ontario Geological Survey, Open File Report 6280, p. 47-1–47-12.

Bleeker, W., 2015. Synorogenic gold mineralization in granite-greenstone terranes: The deep connection between extension, major faults, synorogenic clastic basins, magmatism, thrust inversion, and long-term preservation; *in* Targeted Geoscience Initiative 4: Contributions to the Understanding of Precambrian Lode Gold Deposits and Implications for Exploration, (ed.) B. Dubé and P. Mercier-Langevin; Geological Survey of Canada, Open File 7852, p. 25–47.

Bleeker, W. and Hall, B., 2007. The Slave Craton: geology and metallogenic evolution; *in* Mineral Deposits of Canada: A Synthesis of Major Deposit Types, District Metallogeny, the Evolution of Geological Provinces, and Exploration Methods, (ed.) W.D. Goodfellow; Geological Association of Canada, Mineral Deposits Division, Special Publication No. 5, p.849–879.

Card, K.D., 1990. A review of Superior Province of the Canadian shield, a product of Archean accretion; Precambrian Research, v. 48, p. 99–156.

Colman-Sadd, S., Hayes, J., and Knight, I., 1990. The geology of the Island of Newfoundland; map 90-01; Government of Newfoundland and Labrador, Department of Mines and Energy, Geological Survey Branch, GS# NFLD/2192, scale: 1:1 000 000.

Dubé, B., Dunning, G.R., Lauziere, K., and Roddick, J.C., 1996. New insights into the Appalachian Orogen from geology and geochronology along the Cape Ray fault zone, southwest Newfoundland; Geological Society of America, Bulletin, v. 108, p. 101–116.

Dubé, B., and Gosselin, 2007. Greenstone-hosted quartz-carbonate vein deposits; *in* Mineral Resources of Canada: A Synthesis of Major Deposit-types, District Metallogeny, the Evolution of Geological Provinces, and Exploration Methods, (ed.) W.D. Goodfellow; Geological Association of Canada, Mineral Deposits Division, Special Publication 5, p. 49–73.

Evans, D.T.W., 1996. Epigenetic gold occurrences, eastern and central Dunnage Zone, Newfoundland; Government of Newfoundland and Labrador, Department of Mines and Energy, Geological Survey, Mineral Resources Report 9, 135 p.

Goodwin, A.M., 1977. Archean basin-craton complexes and the growth of Precambrian shields; Canadian Journal of Earth Sciences, v. 14, p. 2737–2759.

Hibbard, J.P., van Staal, C.R., Rankin, D.W., and Williams, H., 2006. Lithotectonic map of the Appalachian Orogen; Geological Survey of Canada Map 2096A, scale 1:1 500 000.

Hodgson, C.J., 1993. Mesothermal lode-gold deposits; *in* Mineral Deposit Modelling, (ed.) R.V. Kirkham, W.D. Sinclair., R.I. Thorpe and J.M. Duke; Geological Association of Canada, Special Paper 40, p. 635–678.

Jackson, S.L. and Fyon, J.A., 1991. The western Abitibi subprovince in Ontario; *in* Geology of Ontario, (ed.) P.C. Thurston, H.R. Williams, R.H. Sutcliffe and G.M. Stott; Ontario Geological Survey, Special Volume 4, p. 404–484.

Lin, S., van Staal, C.R., and Dubé, B., 1994. Promontory – promontory collision in the Canadian Appalachians; Geology, v. 22, p. 897–900.

O'Driscoll, J.M. and Wilton, D.H.C., 2005. Preliminary geochronological, geochemical and isotopic studies of auriferous systems in the Botwood Basin and environs, central Newfoundland; *in* Current Research, Government of Newfoundland and Labrador, Department of Natural Resources, Geological Survey, Report 05-1, p. 207–222.

Percival, J.A. and West, G.F., 1994. The Kapuskasing Uplift: A geological and geophysical synthesis; Canadian Journal of Earth Sciences, v. 31, p. 1256–1286.

Poulsen, K.H., Robert, F., and Dubé, B., 2000. Geological classification of Canadian gold deposits; Geological Survey of Canada, Bulletin 540, 106 p.

Rivers, T., Culshaw, N., Hynes, A., Indares, A., Jamieson, R., and Martignole, J., 2012. The Grenville Orogen – A post-Lihtoprobe perspective. Chapter 3; *in* Tectonic Styles in Canada: The LITHOPROBE Perspective, (ed.) J.A. Percival, F.A. Cook and R.M. Clowes; Geological Association of Canada, Special Paper 49, p. 97–236.

Sandeman, H.A.I., Dunning, G.R., McCullough, C.K., and Peddle, C., 2017. U-Pb geochronology, petrogenetic relationships and intrusion-related precious-metal mineralization in the northern Mount Peyton Intrusive Suite: Implications for the origin of the Mount Peyton trend, central Newfoundland (NTS 2D/04); *in* Current Research. Government of Newfoundland and Labrador, Department of Natural

Resources, Geological Survey, Report 17-1, p. 189–217.

Waldron, J.W.F. and van Staal, C.R., 2001. Taconian Orogeny and the accretion of the Dashwoods Block; a peri-Laurentian microcontinent in the Iapetus Ocean; Geology, v. 29, p. 811–814.

Williams, H., 1978. Tectonic lithofacies map of the Appalachian Orogen; Memorial University of Newfoundland, St John's, Newfoundland and Labrador, scale 1:1 000 000.

Williams, H., Colman-Sadd, S.P., and Swinden, H.S., 1988. Tectonic-stratigraphic subdivisions of central Newfoundland; Geological Survey of Canada Paper 88-1B, p. 91–98.

Williams, H., Currie, K.L., and Piasecki, M.A.J., 1993. The Dog Bay Line: A major Silurian tectonic boundary in northeast Newfoundland; Canadian Journal of Earth Sciences, v. 30, p. 2481–2494.

Valverde-Vaquero, P., van Staal, C.R., McNicoll, V., and Dunning, G.R., 2006. Mid – Late Ordovician magmatism and metamorphism along the Gander margin in central Newfoundland; Journal of the Geological Society of London, v. 163, p. 347–362.

van Staal, C.R. and Barr, S.M., 2012. Lithospheric architecture and tectonic evolution of the Canadian Appalachians and associated Atlantic margin; *in* Tectonic Styles in Canada: The LITHOPROBE Perspective, (ed.) J.A. Percival, F.A. Cook and R.M. Clowes; Geological Association of Canada, Special Paper 49, p. 41–95.

van Staal, C.R., Dewey, J.F., Mac Niocaill, C., and McKerrow, W.S., 1998. The Cambrian-Silurian tectonic evolution of the northern Appalachians and British Caledonides: History of a complex, southwest Pacific-type segment of Iapetus; *in* Lyell: the Past is the Key to the Present, (ed.) D.J. Blundell and A.C. Scott; Geological Society Special Publications, v. 143, p. 199–242.

van Staal, C.R., Valverde-Vaquero, P., Zagorevski, A., Rogers, N., Lissenberg, C.J., and McNicoll, V.J., 2005. Geology, Victoria Lake, Newfoundland and Labrador; Geological Survey of Canada, Open File 1667, scale 1:50 000.

van Staal, C.R., Zagorevski, A., McNicoll, V.J., and Rogers, N., 2014. Time-transgressive Salinic and Acadian orogenesis, magmatism, and Old Red Sandstone sedimentation in Newfoundland; Geoscience Canada, v. 41, p. 138–164.

Whalen, J.B., McNicoll, V.J., van Staal, C.R., Lissenberg, C.J., Longstaffe, F.J., Jenner, G.A., and van Breemen, O., 2006. Spatial, temporal and geochemical characteristics of Silurian collision zone magmatism, Newfoundland Appalachians: An example of a rapidly evolving magmatic system related to slab break-off; Lithos, v. 89, p. 377–404.

Wheeler, J.O., Hoffman, P.F., Card, K.D., Davidson, A., Sanford, B.V., Okulitch, A.V., and Roest, W.R. (comp.), 1996. Geological Map of Canada; Geological Survey of Canada, Map 1860A, scale 1:5 000 000.

Zagorevski, A., Rogers, N., McNicoll, V., Lissenberg, C.J., van Staal, C.R., and Valverde-Vaquero, P., 2006. Lower to Middle Ordovician evolution of peri-Laurentian arc and back-arc complexes in the Iapetus: Constraints from the Annieopsquotch Accretionary Tract, central Newfoundland; Geological Society of America, Bulletin, v. 118, p. 324–342.

Zagorevski, A., van Staal, C.R., McNicoll, V., Rogers, N., and Valverde-Vaquero, P., 2007. Tectonic architecture of an arc -arc collision zone, Newfoundland Appalachians; *in* Formation and Applications of the Sedimentary Record in Arc Collision Zones, (ed.) A. Draut, P.D. Clift and D.W. School; Geological Society of America Special Paper 436, p. 309–333.

Selwyn Basin magmatism and relationship to sediment-hosted Zn-Pb deposits

M.I. Leybourne[1], N. Van Wagoner[2], S. Paradis[3], D. Layton-Matthews[1] and J.A. Moertle[4]

[1]*Department of Geological Sciences and Geological Engineering, Queen's University, 36 Union Street, Kingston, Ontario K7L 3N6*

[2]*Department of Physical Sciences, Thompson Rivers University, 900 McGill Rd, Kamloops, British Columbia V2C 0C8*

[3]*Geological Survey of Canada, 9860 West Saanich Road, Sidney, British Columbia V8L 4B2*

[4]*12350 Del Amo Blvd Apt 410, Lakewood, California 90715*

Abstract

Paleozoic volcanic and intrusive rocks from the Selwyn Basin are being investigated to establish if there is genetic relationship between volcanism and sediment-hosted massive sulphide (SEDEX) mineralization with the aim of improving mineral exploration models. The spatial and temporal distribution of dominantly highly alkalic magmatism and SEDEX deposits in the Selwyn Basin are similar, but traditional models for SEDEX deposit formation have excluded any role of magmatism in their genesis. This study is testing whether magmatic systems supply heat and possibly metals and/or volatiles to the ore system. Herein we report preliminary petrological and geochemical data for samples from the Keno Hill, Anvil and MacMillan Pass districts, and Misty Creek Embayment.

Most of the volcanic rocks in the Anvil and MacMillan Pass districts are alkalic and mafic, although Paleozoic volcanic rocks and later dykes in the Keno Hill district are subalkalic. Significantly, most volcanic rocks in all districts are enriched to highly enriched in Ba, Cs, Nb and Th, and show a positive relationship between barium and thallium, similar to the Howards Pass SEDEX deposit, suggesting either the volcanic rocks have been altered by similar hydrothermal fluids as those that generated SEDEX mineralization or that the volcanic rocks formed from magmas that may have contributed metals and metalloids (e.g. Ba, Tl) to ore-forming magmatic-hydrothermal fluids. Thallium, strontium, carbon and oxygen isotopic analysis, combined with U-Pb dating are planned to constrain the connections between alkalic volcanism and SEDEX formation in the Selwyn Basin.

Introduction

Development of accurate ore deposit models is fundamental to the generation of improved mineral exploration models. Base metal deposits have long been recognized as falling on a spectrum from magmatic (i.e. where the metals and fluids are derived directly from a crystalizing magma body such as Ni-Cu -PGE deposits) to magmatic-hydrothermal (e.g. porphyry Cu, epithermal deposits) to strictly hydrothermal deposits (e.g. Mississippi Valley-type) deposits (Eckstrand and Hulbert, 2007; Sinclair, 2007; Richards, 2009; Potra and Moyers, 2017). Volcanogenic massive sulphide (VMS) deposits form as exhalative deposits on the seafloor or near the seafloor. Early models of VMS formation indicated that magmatism at ocean ridges provided the heat required to drive the hydrothermal systems that formed the deposits, but with little or no direct contributions from the magmas (e.g. Lydon, 1988). However, there is now an increasing recognition of the direct contribution of volatiles and metals from sub-seafloor intrusions in their formation (Yang and Scott, 1996; Beaudoin et al., 2007; Simonov et al., 2010; de Ronde et al., 2011; Leybourne et al., 2012). Similarly, deposit models for sediment-hosted massive sulphide (SEDEX) deposits have traditionally not included a role for magmatism in driving the hydrothermal systems or contributing volatiles or metals (Sangster, 1990; Magnall et al., 2016). Nevertheless, there are known spatial associations between SEDEX deposits and rift-related magmatism in the Selwyn Basin (Goodfellow et al., 1995) and at the Sullivan deposit in the Belt-Purcell basin of British Columbia (Anderson and Goodfellow, 2000). Goodfellow et al. (1995) noted that in addition to the spatial association in the Selwyn Basin there is, within the limitations of a lack of good age control, a temporal association, alluding to the possibility of a more fundamental genetic link between the two.

The continental margin of the northern Canadian Cordilleran developed and rifted intermittently during the early Palaeozoic, with concomitant emplacement of alkalic (and ultrapotassic) volcanic and intrusive rocks along the continental margin. During the Paleozoic in the Selwyn Basin, many of the large

Corresponding author: Matthew Leybourne (ml164@queensu.ca)

Leybourne, M.I., Van Wagoner, N., Paradis, S., Layton-Matthews, D., and Moertle, J.A., 2018. Selwyn Basin magmatism and relationship to sediment-hosted Zn-Pb deposits; *in* Targeted Geoscience Initiative: 2017 report of activities, volume 2, (ed.) N. Rogers; Geological Survey of Canada, Open File 8373, p. 71–92. https://doi.org/10.4095/306603

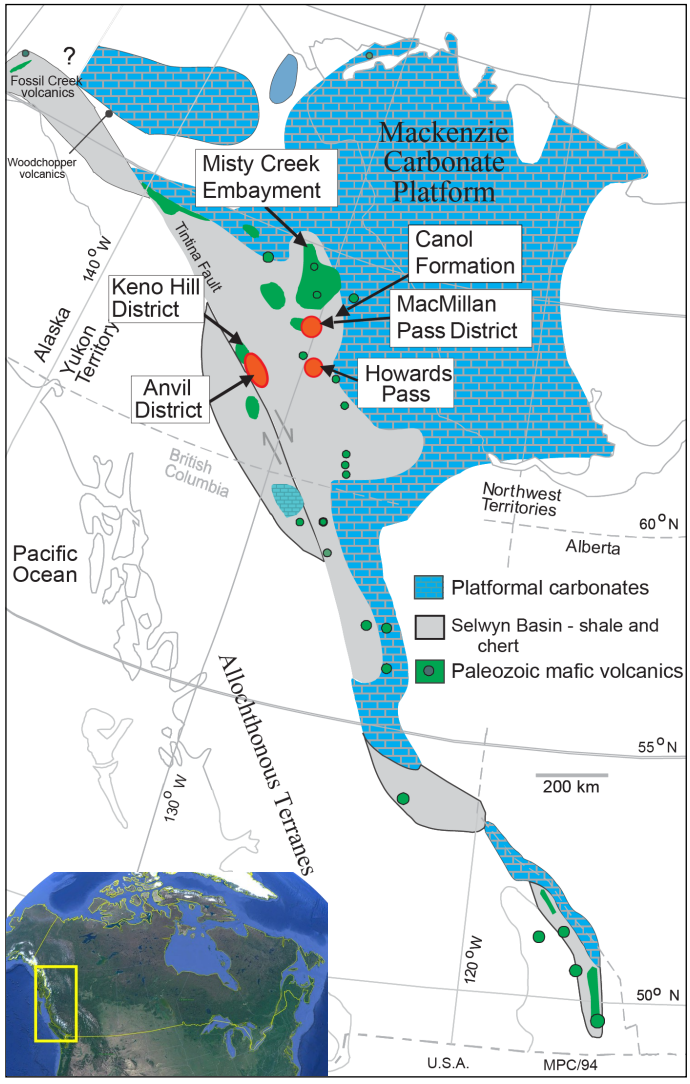

Figure 1. Location map of localities with volcanic rocks sampled for the current study (modified from Goodfellow et al., 1995). Also shown is the location of the Howards Pass SEDEX deposit (J.M. Peter, pers. comm., 2018) and the Canol Formation (Fernandes et al., 2017), for which some (non-volcanic) rock data are presented here.

clastic sediment-hosted Zn-Pb (±Ag, ±Ba) deposits and other deposit types (e.g. VMS and Ag-Pb-Zn veins) formed (Goodfellow et al., 1995). Although there is a spatial correlation between magmatism and SEDEX mineralization, temporal and genetic relationships have yet to be proven or disproven. Precise ages of the magmatic occurrences have yet to be determined. Primary textures, structures, mineralogy, and geochemistry need to be documented to reconstruct paleotectonic settings and constrain the role in the formation of syngenetic ore deposits.

Consequently, there is a need to resolve the field and geochemical (elemental, isotopic and age) relationships between these volcanic rock occurrences using modern analytical techniques to provide the context to develop of more effective mineral exploration strategies. Understanding the characteristics of the volcanic settings may allow for the identification of discrete volcanic centres and indirectly to structural corridors that were sites of rifting and hydrothermal activity. By better constraining the geochemistry, timing of volcanism and intrusive activity in the Selwyn Basin, we hope to be able to identify the chemical signatures of magmatic-hydrothermal input to the deposits. Isotopic analyses (i.e. whole-rock Nd-Sm isotopes, zircon U-Th-Pb dating) will be conducted on samples from SEDEX mineralization and results will be compared to the magmatic rocks to test possible genetic relationships.

The objectives of our work on the volcanic rocks of the Selwyn Basin are to: i) determine the nature of the relationship (beyond spatial) between SEDEX mineralization and magmatism (i.e. is the relationship temporal and/or genetic, or purely causal); ii) determine precise ages and geochemical signatures of the magmatic rocks associated with sediment- and volcanic-hosted Zn-Pb mineralization, with a particular emphasis on U-Pb zircon dating and analysis of magmatic metals and metalloids; iii) refine our understanding of the tectonic processes associated with the magmatic rocks; iv) determine if the magmatic rocks reflect specific structural and heat corridors and the extent to which long-lived lithospheric structures control magma emplacement and hydrothermal activity; v) better document temporal and spatial variations in the physical and chemical volcanology and how these may relate to mineralization; and vi) refine the exploration model for base metal deposits in sedimentary basins, if our data allow it.

Fieldwork for this study took place in the Keno Hill (105M/13, M/14), Anvil (105K/3, K/6), and MacMillan Pass (105O/1, O/2) districts of the Selwyn Basin, central Yukon (Fig. 1). These three districts are host to Zn-Pb (±Ag, ±Ba) deposits (SEDEX, Ag-Pb-Zn vein-type, and rare VMS).

Geology

The geological history of the Selwyn Basin is presented in Goodfellow (2007) and Nelson and Colpron (2007). Briefly, the Paleozoic Selwyn Basin is dominated by marine sedimentary units ranging from deep marine (black shales) to shallow marine (sandstones) to carbonate platformal rocks. The Selwyn Basin underwent protracted extensional tectonics from the Late Proterozoic to the Mississippian, resulting in an epicontinental margin, characterized by a basin and arch morphology (Goodfellow et al., 1993). The rock succession in the basin extends from: 1) the basal Hadrynian-Cambrian clastic sedimentary rocks (Windermere Supergroup), a synrift sequence formed by sediments shed from Hudsonian crystalline basement starting at around 760 Ma (Eisbacher, 1981); 2) Cambro-Ordovician carbonate rocks of the Rabbitkettle Formation; 3) basinal facies chert and shale of the Road River Group (Ordovician to Devonian); and 4) chert and autochthonous black shales of the Earn Group (Devonian to Mississippian) (Goodfellow, 2007 and references therein). Goodfellow et al. (1995) described alkalic rocks from three major episodes of

mafic volcanism during the Early Cambrian, Middle Ordovician, and Middle to Late Devonian. The volcanic rocks form discontinuous, lenticular belts that parallel rift-bounding faults or occur as isolated volcanic piles, and consist dominantly of mafic volcanic flows, dykes, and tuffs.

The Keno Hill district is well known for its Ag-Pb-Zn vein deposits hosted in the Carboniferous Keno Hill Quartzite, which is underlain by Devonian volcanic rocks of the Earn Group that have small VMS occurrences. In the Keno Hill district, the Earn Group underlies the Keno Hill Quartzite and consists of penetratively deformed carbonaceous phyllite, siliceous carbonaceous metasiltstone, rare calcareous greywacke, metaconglomerate and a felsic metavolcanic member (Roots, 1997). The felsic metavolcanic rocks that occur within the Lowe Schist Formation in the Mount Haldane and Keno Hill areas are defined by local concentrations of quartz and less commonly quartz and feldspar phenocrysts within the phyllite. Roots (1997) noted that embayments, reactions rims and beta-quartz morphology of quartz crystals indicate that they were phenocrysts, rather than detrital granules.

The Anvil district hosts large Zn-Pb (±Ag, ±Ba) SEDEX deposits (Faro, Vangorda, Swim, Grum, and Dy), some of which were previously mined, and several VMS showings (e.g. Rebel occurrence) (Carne and Cathro, 1982). These deposits have an estimated combined reserve of 120 million tonnes at a combined Pb + Zn grade of 9.3% (Jennings and Jilson, 1986). The SEDEX deposits are hosted within a 150 m thick stratigraphic interval straddling the contact between the metasedimentary lower Cambrian Mount Mye and Cambrian to Ordovician Vangorda formations. The Mount Mye Formation consists of brown, fine to medium-grained biotite-muscovite schist (Cobbett, 2013). The rocks of the Vangorda Formation are fine -grained calc-silicate schists and hornfels (Cobbett, 2013) that originated as regionally metamorphosed bedded carbonates (Pigage, 2004; Cobbett, 2013). The Silurian Menzie Creek Formation conformably overlies rocks of the Vangorda Formation and consists of mafic volcanic and intrusive rocks that host several VMS occurrences (such as the Rebel occurrence, formerly referred to as the KD showing).

The MacMillan Pass district contains Zn-Pb (±Ag, ±Ba) SEDEX deposits (i.e. Tom, Jason and Boundary Creek) that show a spatial relationship with the MacMillan Pass and Niddery Lake volcanic rocks. The deposits are hosted by clastic sedimentary rocks of the middle to upper Devonian Portrait Lake Formation, Earn Group. In this district, the Earn Group occurs in the MacMillan and Niddery Lake volcanic complexes that consist of discontinuous and interlayered volcanic flows, intrusive rocks and clastic sedimentary rocks (Abbott, 2013). The volcanic and intrusive rocks display orange weathering, and consist of carbonate-rich mafic to felsic flows, tuffs, volcaniclastic rocks, and minor coarse-grained gabbroic sills and dykes. Dominant volcanic rock types are amygdaloidal flows with flow -top auto breccia, volcaniclastic-hyaloclastic breccia, heterolithic lapilli tuff to tuff breccia, and ash-tuff (Goodfellow et al., 1995).

Analytical methods

A subset of the samples collected in 2016, together with a set of samples from the Misty Creek Embayment provided by Christopher Leslie and Jim Mortensen, comprising 142 samples in total were studied petrographically and analyzed for their whole rock geochemical composition. Polished thin sections were made at the Harquail School of Earth Sciences, Laurentian University. Whole rock geochemical analyses were performed at ALS Geochemistry, Vancouver, British Columbia. Whole rock samples were crushed and pulverized in a low Cr-Mo mild steel ring mill to 85% < 75 µm. Major elements (SiO_2, Al_2O_3, TiO_2, Fe_2O_3, MnO, MgO, CaO, Na_2O, K_2O, P_2O_5, Cr_2O_3, BaO and SrO) were determined by inductively coupled plasma atomic emission spectroscopy (ICP-AES) following lithium metaborate/lithium tetraborate ($LiBO_2/Li_2B_4O_7$) fusion. The resultant melt was digested in 4% HNO_3/2% HCl prior to introduction to the ICP-AES. Loss on ignition was determined by difference in weight after 1 g sample was heated at 1000°C for one hour. Trace elements, including rare earth elements, were determined by inductively coupled plasma mass spectrometry (ICP-MS) using the same digestion solutions as for the major elements. Total C analyses were performed on samples that were heated in a LECO induction furnace, with analysis of the generated CO_2 by infrared detection. Whole rock samples were also analyzed following a four-acid "total" digestion ($HClO_4$, HNO_3, HF and HCl; highly resistant phases such as chromite and zircon are not quantitatively digested). The resultant solution was analyzed by ICP-MS and ICP-AES for Ag, As, Be, Bi, Cd, Co, Cs, Cu, Ge, In, Li, Nb, Ni, Pb, S, Sb, Sc, Se, Sn, Ta, Te, Tl, and Zn. Lead isotopes were analyzed by ICP-MS on the four acid digestions using quadrupole ICP-MS. Certified reference materials (CRM) were analyzed as unknowns, with additional CRMs and blanks analyzed by ALS. In some cases, analytes were measured by more than one of the techniques above; however, only data from the most robust method are reported (e.g. Zr by fusion). With few exceptions, all analytes are within the target range for the CRMs (average RSD for major elements = 0.64%, for trace elements by fusion = 1.45% and for acid = 2.17%). Blank values are all below the target ranges.

Field relationships and petrography

Volcanism associated within the Keno Hill district (i.e. Earn Group) is the most difficult to characterize due to deformation and regional metamorphism to greenschist facies masking the protoliths. Some of the rocks preserve original depositional structures and textures making it possible to recognize a pyroclastic or volcaniclastic component without ascribing processes of volcanism. The Menzie Creek Formation volcanic rocks are characterized by interbedded pillow flow and pillow breccias, massive flows and flow breccias, and phreatomagmatic massive and bedded tuffs, indicative of a primarily (but not exclusively) subaqueous volcanic setting. The areas studied in the MacMillan Pass district are characterized by two distinct

volcanic complexes (i.e. MacMillan and Niddery Lake) and environments. Pyroclastic explosive magmatic and phreatomagmatic deposits and effusive deposits dominate most of the area, but the Niddery Lake area is characterized by deeper water subaqueous resedimented volcaniclastic turbidites, bedded cherts, and hyaloclastite breccias.

Keno Hill district

The contact between the Earn Group and the Keno Hill Quartzite appears conformable (Fig. 2a). The samples collected from the Keno Hill Quartzite are quartzites and phyllites. The quartzite is typically dark to medium grey and has a coarse granular texture, with a poorly developed foliation that is defined by chlorite, other phyllosilicate minerals, and pyrite. The quartzite beds are almost entirely of quartz, and have compositions > 85% weight % SiO_2. Quartz grains are equant with typically sutured grain boundaries. Trace amounts of biotite (commonly altered to chlorite) are present. Medium green-grey chlorite-quartz phyllite, interlayered with the quartzite, is foliated and crenulated (Fig. 2b).

The Earn Group in the Keno Hill district is characterized by medium green-grey quartz-sericite-chlorite phyllite to phyllitic schist displaying local crenulation cleavage (Fig. 2b), interbedded with more competent quartzite beds ranging in thickness from 1 to 60 cm, and carbonaceous slates. Metavolcanic rocks were distinguished in the field utilizing descriptions of Murphy and Roots (1996) and Hunt et al. (1996).

The metavolcanic rocks are light green to green-grey quartz -sericite-chlorite phyllite and schist, with varying amounts of sericite and chlorite, feldspar and quartz phenocrysts, relict lithic clasts, and rare disseminated pyrite. Chlorite commonly defines the foliation (Fig. 2c). The presence of volcanic quartz, possible lithic fragments, and ghosted (devitrified) volcanic glass shards in the matrix (Fig. 2d), along with lower SiO_2 contents in some samples suggests a felsic protolith, but this interpretation is speculative.

The volcanic and sedimentary rocks are cut by fine- to medium-grained, dark green-grey Triassic metadiorite to metagabbro dykes. Spatially, the dykes are commonly associated with mineralized Ag-Pb-Zn veins. The Triassic intrusive rocks (Fig. 2e–g) are medium to dark green-grey, aphanitic and massive, with disseminated pyrite and galena, and are commonly cut by quartz veins.

Anvil district

Fieldwork in 2016 within this district included five main traverses through the Menzie Creek Formation with additional targeted sampling of selected mafic intrusions. The sampling area is bisected by the Anvil Batholith, which trends northwestward across the Anvil district.

The volcanic rocks of the Menzie Creek Formation are alkali basalts that comprise amygdaloidal massive and pillow flows and pillow breccias. They are intruded by Ordovician to Silurian gabbro and pyroxenite sills and dykes. The volcanic rocks are massive to foliated, noncalcareous to slightly calcareous, with chlorite and epidote alteration, such that mafic phenocrysts and microlites are largely obscured. Unlike the Keno Hill district, here primary volcanic textures are commonly preserved (e.g. amygdaloidal pillow flows and vesicular flow-top breccias).

North of the Anvil Batholith, amygdaloidal massive and pillow basalts, monolithic matrix- and fragment-supported breccia, pillow flow breccia and tuff are exposed. Primary depositional textures are well preserved. The massive and pillow basalts are light brown-green, fine-grained, aphanitic to porphyritic with rare plagioclase phenocrysts.

Volcaniclastic rocks in the Menzie Creek Formation are interbedded with massive and pillowed flows and associated flow breccias. Volcaniclastic units range from bedded pyroclastic tuffs, lapilli tuffs and tuff breccias to autoclastic breccias. North of the Anvil Batholith we described a sequence of indistinctly bedded basaltic lapilli tuffs to tuff breccias with bedding defined in the field by flattening of larger bombs (Fig. 3a, b). The units are clast supported with a matrix of ash to lapilli sized fragments that are primarily 2 to 3 mm, but up to 0.5 cm across, and comprise massive basalt, and flattened scoriaceous fragments with fine microlites of plagioclase. Bubble wall and angular shards are observed in thin section. Larger lapilli and bombs are up to about 25 cm in long dimension, but mostly are under 10 cm, and are massive to scoriaceous. Clast shapes are wispy with ragged margins to blocky with partially wispy margins. Some fragments have thin (1–2 mm thick) fine-grained rims. These tuffs to tuff breccias are associated with a thinly bedded, dark-green grey to brown, fine-grained tuff and flows. The associated flows are primarily highly amygdaloidal and sheared in places. Chilled flow margins are 1 to 2 cm thick. The thicker flows have autobrecciated margins characterized by angular relict vitric fragments in a jigsaw puzzle arrangement and subhorizonal gas cavities similar to slabby pahoehoe flows. These characteristics are consistent with air fall and surge deposits from phreatomagmatic eruptions proximal to the vent area, in a subaqueous environment, which is further substantiated by the alteration pipe described below. This sequence is similar to phreatomagmatic monogenetic volcanic systems that have erupted both alkaline and subalkaline magmas (for example see the Auckland Volcanic Field; Needham et al., 2011).

From samples MC-25 to MC-35, we traversed through a sequence of pillow flows and breccias, including a malachite brecciated alteration pipe with associated alteration halo. Basalt proximal to the alteration pipe has disseminated sulphide. The mafic flows have variable contents of fine-grained plagioclase microlites, 3% small (< 1 mm in diameter) vesicles, common glomerophyric 1 to 2 mm plagioclase phenocrysts (3–6%), euhedral to subhedral phenocrysts of pyroxene up to 1.5 mm in diameter and altered to fresh olivine, and glomercrysts of olivine and pyroxene up to 0.5 mm in diameter. In one sample (MC-31) the pyroxene and olivine are in glomerophyric masses and both are unaltered (Fig. 3d).

Figure 2. Keno Hill district; a) The hammer head is on an apparently conformable contact between the Keno Hill Quartzite, and a possible lapilli tuff of the Earn Group; b) Quartz-chlorite phyllite of the Keno Hill Quartzite showing a well-developed crenulation cleavage (plain light (PL), field of view (FOV) is 3 mm wide; c) Keno Hill quartz-chlorite phyllite; d) Possible metatuff. It is compositionally distinct from the quartzites with 79.16 weight % SiO_2, on a volatile-free basis. Chlorite mantles more competent relict lithic fragments, some of which display shard-like morphologies, though this is also typical of the cuspate boundaries of metamorphic quartz. No volcanic feldspar was observed and the protolith is uncertain (sample EG-18, PL, FOV = 1.5 mm wide); e) The orange and grey exposure in the foreground is massive siderite and galena that is in contact with the dyke that forms the overlying resistant knob in the background; f) A large massive dyke in the Keno district; g) A sample from the dyke in the adjacent photo. This dyke is sheared and altered, obscuring many of the primary minerals, but the core of a large glomerocryst of olivine and clinopyroxene is preserved in the centre of the field of view. Other glomerocrysts and mafic phenocrysts also entirely altered to chlorite, and amphibole forming dark elliptical patches. The lighter coloured laths are relict plagioclase, now altered to sericite (sample Ti-04, crossed-polarized light (XP), FOV= 3 mm wide).

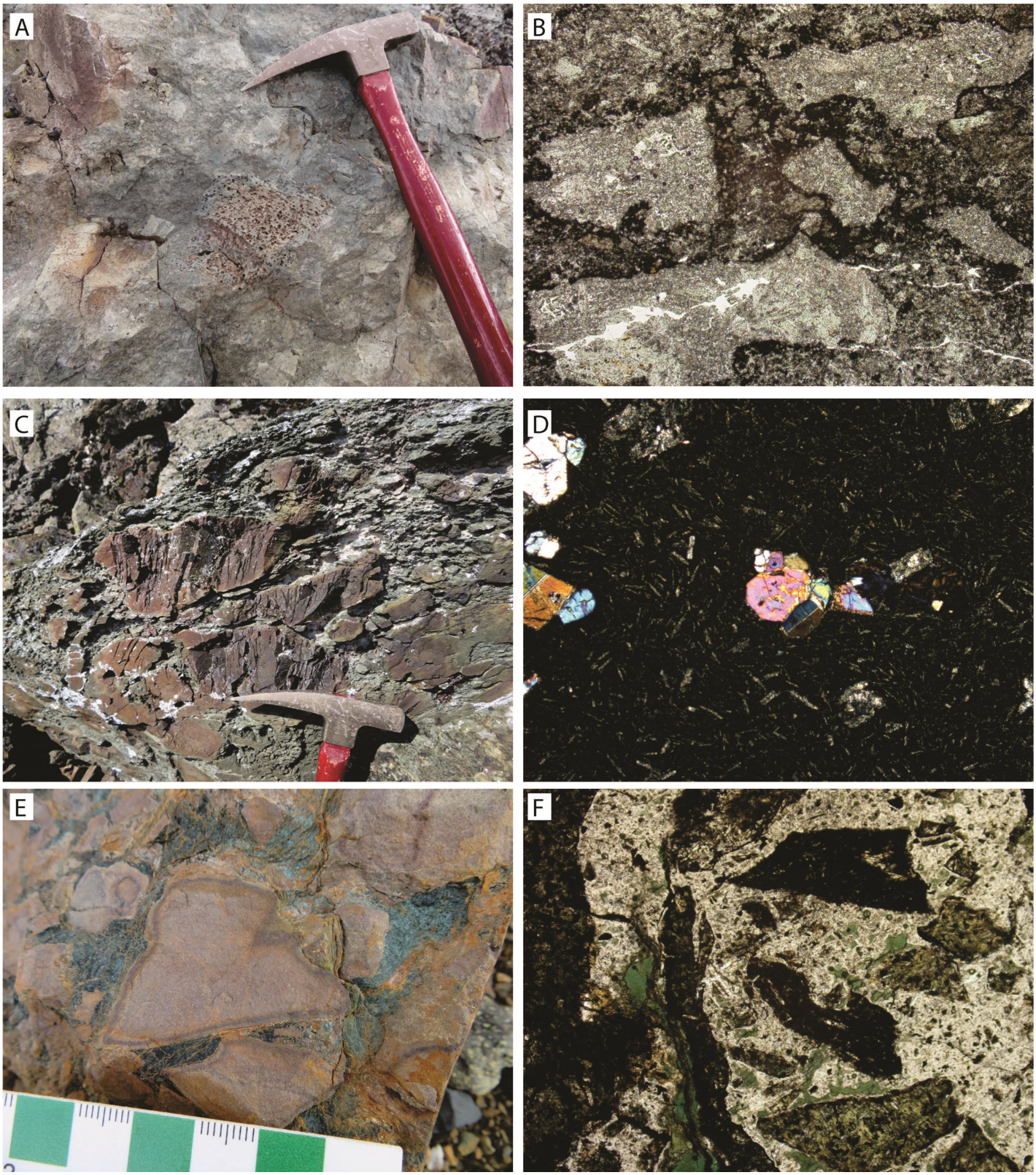

Figure 3. Anvil district extrusive sequences (caption continued opposite).

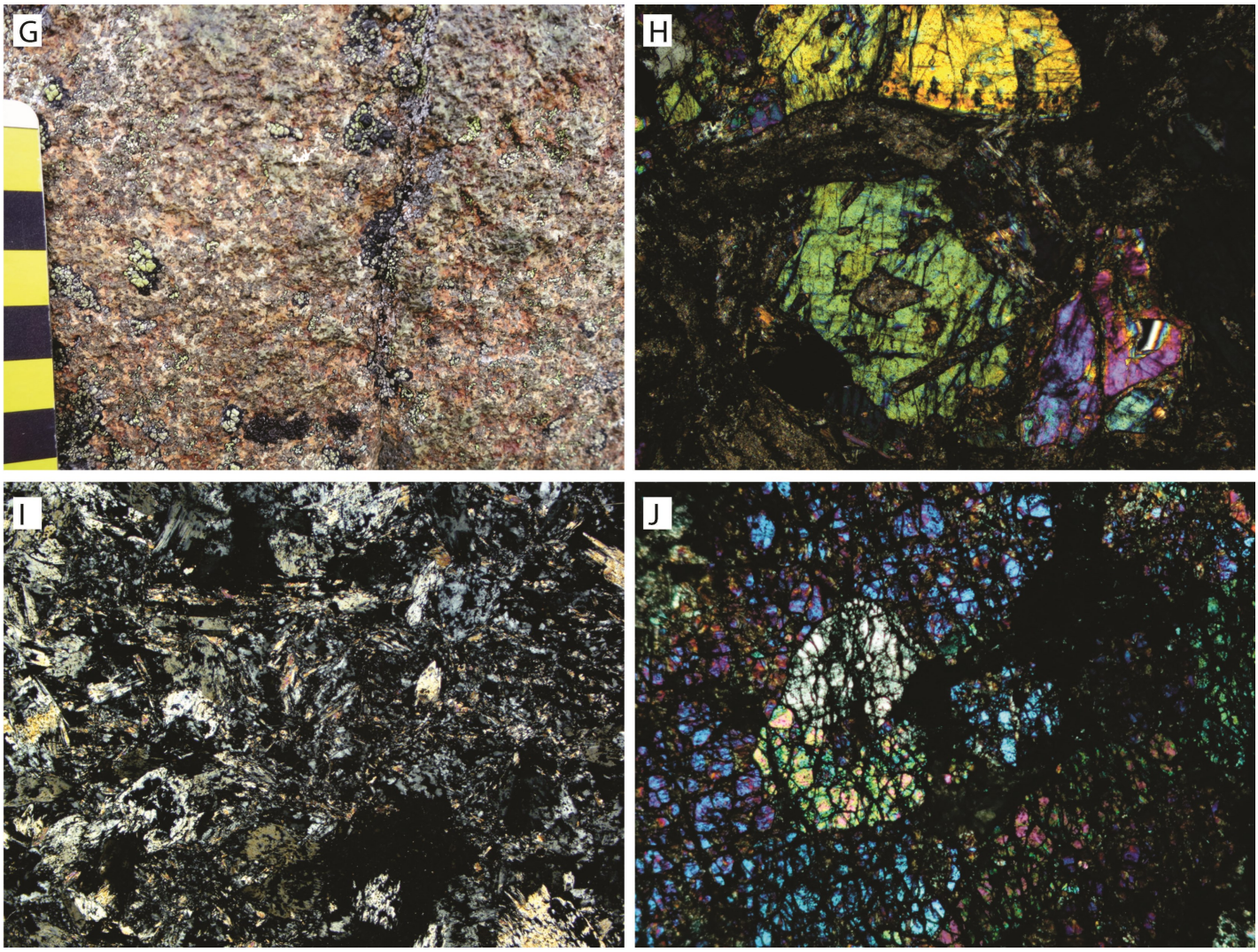

Figure 3. (Cont.) Anvil district extrusive sequences; a) Exposure from a phreatomagmatic volcanic deposit. The irregularly shaped scoriaceous fragment near the centre of the image represent the magmatic component of this ancient fallout deposit. The unit is indistinctly bedded, as evidenced by loss of coarser clasts, and monolithic composition, although it contains both magmatic scoriaceous lapilli and bombs with chilled margins and wispy shapes, and blocky cognate fragments with light-coloured reaction rims; b) Matrix of a unit similar to that shown in Figure 2a. Note the cuspate shape of the larger shards which is consistent in the finer ash-sized particles forming the matrix (PL, FOV = 3 mm wide); c) Slightly sheared pillow breccia; d) Compact flow of the pillow breccia; alkali basaltic composition, with a glomerocryst of olivine and twinned clinopyroxene in the centre of the field of view. The groundmass contains microlites of feldspar in an aphanitic felty matrix (XP, FOV = 3 mm wide); e) Outcrop photo (sample MC-33) of basalt breccia pipe comprising angular basalt fragments in a matrix of calcite, and malachite. Note the oxidized rims on the margins of the basalt clasts and along fractures; f) Sample MC-35 is from the alteration halo around a breccia pipe. The fragments are of variable size and primarily angular in shape, although some have been partially altered and have a more rounded shaped. Smaller fragments are completely replaced by malachite and other carbonate minerals (PL, FOV = 3 mm wide); g) Outcrop from peridotite north of the Anvil Batholith. The rock is mottled pink and green with a knobby texture due to variable alteration weathering of the minerals; h) Fresh olivine (note euhedral olivine near the center and a subhedral grain at the top of the image) and pyroxene (note the twinned grain at the lower right corner of the image within a variably calcite and chlorite altered matrix. These phenocrysts are internally altered to chlorite and calcite (sample MC-22, XP, FOV = 3 mm wide); i) Ophitic texture of the gabbro in (h). Although the primary minerals are highly altered, there are a few large crystals of pyroxene surrounding mostly altered smaller laths of plagioclase and scattered skeletal grains of olivine (sample MC-24, XP, FOV = 3 mm wide); j) Peridotite south of the Anvil pluton, showing primarily rounded grains of olivine with pyroxene in the centre of the field of view (sample MC-42, XP, FOV = 3 mm wide).

Samples MC-33 and MC-35 are from a breccia pipe cross cutting fine-grained basalt. The basalt is broken by in-situ brecciation into angular fragments that are 1 to 4 mm to several cm in size and oxidized. Carbonate and bright green malachite comprise the matrix to the fragments, forming veins up to about 0.5 cm thick (Fig. 3e, f).

Samples MC-19 and MC-20 were collected from an alteration pod about 50 m in diameter, crosscutting tuffs and flows. The unit is highly veined and fractured and is interpreted by us to be a possible hydrothermal vent within basalts and tuffaceous units, with epidote preceding quartz alteration. Sample MC-19 is amygdaloidal basalt with carbonate filling vesicles. Olivine has been altered to serpentine and chlorite.

The deformation is more pronounced south of the Anvil Batholith, masking some of the primary structures and textures. The fine tuff to lapilli tuff is finely bedded and occurs within fining-upward sequences.

We sampled gabbros and peridotites north and south of the Anvil Batholith, and the intrusions are distinct in the two areas. North of the Anvil Batholith we sampled a suite of proximal Menzie Creek Formation intrusions. A unit previously mapped as a pyroxenite (Fig. 3g: sample MC-22) is exposed near the top of a hill of mafic intrusions. In outcrop, the unit is mottled pink and contains phenocrysts of olivine and pyroxene (up to 80% of the unit) in apparently equal abundances (Fig. 3h) and may more correctly be classified as wehrlite or lherzolite. In contact with this unit is a coarse gabbro, followed by a finer-grained gabbro farther from the pyroxenite exposure (Fig. 3i). Although highly altered, this rock appears to have a relict ophitic texture. Sample MC-24 may be the margin of the intrusion as it is finer-grained.

Another lithology also previously mapped as a pyroxenite (sample MC-42) occurs south of the pluton and is also in contact with gabbros. The peridotite is comprised almost entirely of rounded crystals of olivine (Fig. 3j). Gabbros is in contact with the peridotites (Samples MC-40 and 41). Samples MC-40 and 41 are also gabbro and display an ophitic texture with large crystals of plagioclase (55% and 1–4 mm in length) surrounded by altered pyroxene.

The Devonian Earn Group in the Anvil district is dominated by a variety of volcanic and volcaniclastic flows, carbonaceous phyllite, shale, and chert with lesser quartzite and chert-pebble conglomerate (Pigage, 2004; Cobbett, 2016). The metatuff sequence consists of chlorite-rich and feldspar-rich fragments in a quartz-rich matrix, is on average 10 m thick, and is overlain by 1 to 10 m thick fine-grained fissile shale beds.

MacMillan Pass district

In most of the MacMillan Pass area original volcanic textures and structures are clear. Although the rocks have been altered, there is little tectonic deformation. A number of locations were sampled to give a sense of the nature of volcanism, but more work is required to understand the sequence or geometry of the volcanic edifices.

The volcanic rocks of the MacMillan Pass are generally highly vesicular, comprising primarily (but not exclusively) massive to thickly bedded lapilli tuffs and tuff breccias containing an abundance of highly scoriaceous magmatic fragments (Fig. 4a–d). The abundance of scoria and the size distribution, from larger clasts to ash-sized fragments, attests to the explosive nature of volcanism in this area. We observed few effusive flows. There appears to be both secondary and primary magmatic carbonate fragments, which is reflected in the bulk geochemical compositions, but due to the high degree of hydrothermal alteration, more detailed textural and mineralogical studies are required to determine the petrogenetic relationships of these rocks.

Samples MP-01 to MP-04 and MP-06 are a series of primarily non-welded, magmatic to phreatomagmatic, monolithic and heterolithic lapilli tuff to tuff breccias (Fig. 4a). Here the rocks are bedded up to about 35 cm thick, with the beds internally finely laminated, cross-bedded and graded, forming an alternating sequence of massive to graded and cross-laminated sets. Primary volcanic lapilli and bombs comprise from 5 to 85

Figure 4. (Opposite.) The MacMillan Pass district; a) Massive lapilli tuff to tuff breccia (samples MP-01 to MP-04 and MP-06) showing highly scoriaceous magmatic fragments giving the rock a knobby appearance. The yellow colour is due to the high content of carbonate in the rock; b) Magmatic lithic fragment in tuff breccia that contains a relict mineral of leucite, suggesting that this fragment is a phonolite. The crystal to the left and below the leucite are likely olivine, in a fine grained, aphanitic matrix. This fragment is rimmed by carbonate minerals and chalcedony. The lithochemical composition of this unit, as with many of these units, appears to be a hybrid (sample MP-06 PL, FOV = 1.5 mm wide); c) Carbonate veined scoriaceous magmatic fragments in a tuff breccia defining indistinct bedding; d) Matrix of tuff breccia in (c). The matrix is a crystal-lithic tuff. Every fragment is mantled by carbonate. The dark fragment in the centre of the field of view was a vitric fragment that now contains relict microspherulites. The more blocky black fragment in the upper left corner is actually the core of a larger fragment this is entirely carbonate in composition. The variable composition and morphology of these fragments reflects the complexity of the volcanism (Sample MP-23, PL, FOV = 3 mm wide); e) Outcrop photo of columnar joints in a mafic dyke (sample site MP-15); f) A single scoria fragment containing microlites of skeletal ‘lantern-shaped’ olivine (the largest of these is to the right of the large doubly line amygdule (sample MP-18, XP, FOV = 3 mm wide); g) Outcrop exposure at Niddery Lake of a peperitic breccia (right), intruded by a sediment dykelet of chert (sample MP-28); h). Peperitic breccia at Niddery Lake with angular to subangular fragments of basalt in a carbonate matrix (sample MP-30)).

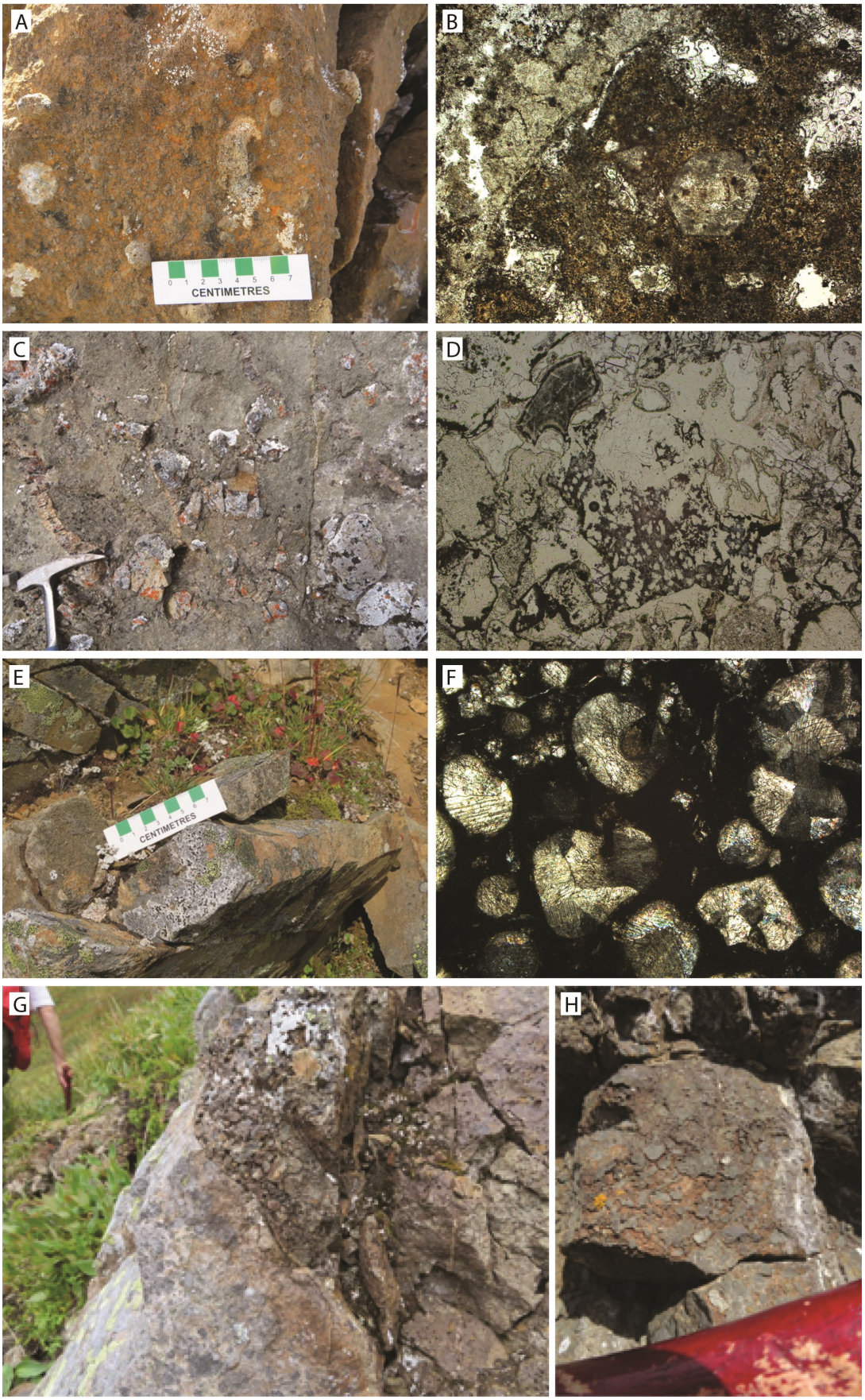
A
CENTIMETRES
B
C
D
E
CENTIMETRES
F
G
H

volume % of the beds and are scoriaceous with an abundance of small spherical vesicles (< 1 mm in diameter); delicate wispy margins attest to a phreatomagmatic or magmatic eruptive origin, and lack of reworking. Relict microspherulites, observed in thin section, are up to several millimetres in diameter, and replaced by radiating calcite, and/or chalcedony and chlorite. The matrix comprises ash-sized shards and smaller volcanic fragments of the same material (e.g. Fig. 4b). The massive beds are interpreted as fallout deposits, with the laminated and cross laminated sequences associated with surge deposits, indicating at least two eruptive pulses. Most of the primary minerals in these rocks are altered to carbonate minerals, with lesser amounts of chlorite and epidote.

More typically, thick units are massive or vaguely graded. For example, samples MP-07 and MP-08 are from a unit several metres thick that grades to the south from a heterolithic lapilli tuff with cored volcanic fragments (Fig. 4d) to a lapilli tuff by loss of accidental lithic fragments, representing a single explosive volcanic pulse (Fig. 4c).

Sample MP-05 differs in being a heterolithic felsic lapilli tuff with 0.5 to 2 cm, angular to subrounded xenoliths of chert, rhyolite and basalt xenocrysts of metamorphic and igneous quartz, cuspate and platy altered volcanic glass shards, and 3 to 5 % relict vesicular vitric fragments at the interstices of xenoliths and mantling some fragments. The matrix is microcrystalline quartz. This unit is interpreted to be a silicified conglomerate, consistent with its high silica content, but the texture suggests the possibility that it resulted from a phreatic eruption. This unit is less common than the tuffs.

The intrusions sampled in the MacMillan Pass – Niddery Lake area are coarse-grained gabbro (Fig. 4e) with phenocrysts of altered plagioclase, olivine and pyroxene. These intrusive rocks are much less alkalic than the volcanic rocks. No feeder dykes were observed.

These descriptions typify the nature of volcanic units observed the MacMillan Pass district, with the exception of the Niddery Lake region. The areas sampled in the Niddery Lake region are characterized by a sequence of deeper water turbidites with reworked volcanogenic sediments and bedded chert, and hyaloclastite/chert to silty radiolarian chert sequences (Fig. 4g). The turbidites comprise repeating sequences of graded polymictic detritus that fine upward (to the south) by loss of coarser clasts from a pebble conglomerate to a sandstone, overlain by finer laminated and cross laminated beds. Coarse graded beds are 1.5 to 2 m, and finer beds are less than 0.5 m thick. Hyaloclastite and peperitic breccias (Fig. 4h) comprise up to 85% angular mafic fragments from 0.5 to 3 mm in a matrix of smaller volcanic fragments, or chert.

Lithogeochemistry

For the purposes of this paper, the samples have been subdivided into 6 groups: 1) Menzie Creek Formation, Anvil district; 2) Earn Group, Anvil district; 3) Earn Group, Keno Hill district; 4) Triassic dykes, Keno Hill district; 5) MacMillan Pass district; and 6) Misty Creek Embayment. Volcanic rocks from the Misty Creek Embayment in NWT, an Early Paleozoic rifted basin on the northeastern margin of the Selwyn Basin, were also analyzed and are plotted here for comparison. All the analyses have been recalculated to 100% on a volatile-free basis. For some samples, especially those from the MacMillan Pass district, the results show high CaO contents (and likely MgO for some samples) owing to the extensive carbonate alteration overprint, and, therefore, SiO_2 contents are anomalously low as a result due to the closure problem. However, the trace element systematics are still dominated by the volcanic rock components of these samples. Future analyses of these rocks are planned to account for this alteration by extracting volcanic rock fragments from the breccias and analyzing these separately. However, Goodfellow et al. (1995) also noted that the parental magmas would have been volatile-rich, raising the possibility that at least some of the high carbonate contents may be primary rather than the result of hydrothermal alteration. Many of the volcanic rocks from the Keno Hill, and to a lesser extent, MacMillan Pass, area have undergone intense silicification; samples with > 90% weight % SiO_2 on a volatile-free basis have not been plotted. The extent of alteration of the samples is evident in the alteration box-plot of Large et al. (2001a) (Fig. 5a).

Samples analyzed in this study fall into broad groups in terms of chemical affinity (Fig. 5b. Rocks from the Keno Hill district are subalkalic (i.e. $Nb/Y < 0.67$) and range in composition from basalt to dacite/rhyodacite; the Triassic dykes are all mafic subalkalic rocks. Menzie Creek Formation rocks are dominantly alkali basalts, with one sample plotting as a subalkalic andesite. The single Earn Group sample from the Anvil district is subalkalic basalt in composition (Fig. 5b). The majority of the MacMillan Pass and the rocks from the Misty Creek Embayment are more alkalic than the other areas, straddling the boundary between alkali basalt and basanite/nephelinite (Fig. 5b). More evolved rocks from the MacMillan Pass distract are less alkalic and range from trachyandesite to subalkalic andesite (three samples; Fig. 5b).

Major elements

Owing to the pervasive hydrothermal alteration for Paleozoic rocks from the Keno Hill and MacMillan Pass districts, only a small number of major elements are presented to show the range in compositions (Fig. 6). Least altered volcanic rock samples of the Menzie Creek Formation volcanic rocks (massive flows and pillow flows) have SiO_2 values between 44 and 58 weight % (Fig. 6a). Two alkali basalts from the Menzie Creek Formation have lower SiO_2 contents (37.35 and 39.30 weight %) owing to carbonate alteration. The pyroxenites, gabbros and one high MgO flow have low SiO_2 (42.10–45.69 weight %; Fig. 6a) and moderate to elevated MgO (7.94–34.34 weight %; Fig. 6d) contents. The generally mafic character of most of the samples is evidenced by a positive trend between TiO_2 and Zr (Fig. 6b), as well as generally high $Fe_2O_3^T$, Cr and Ni contents (Fig. 6c, e, f). The ultramafic rocks from the Men-

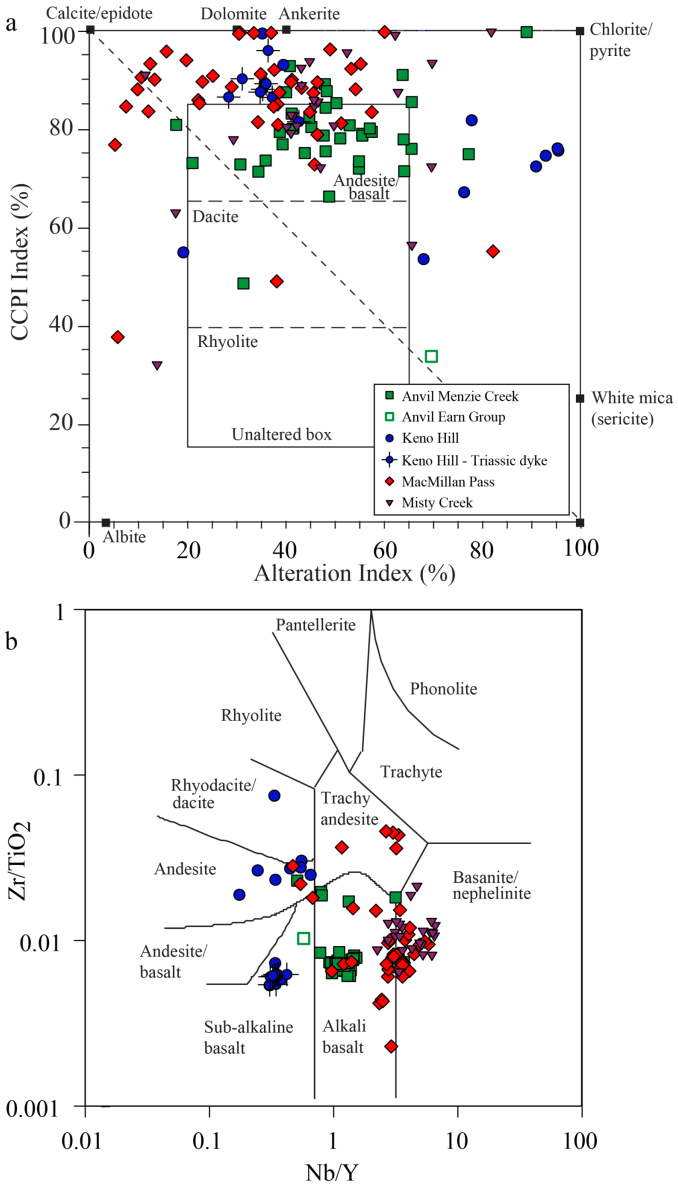

Figure 5. a) Chlorite–carbonate–pyrite index (CCPI) versus alteration index (AI) plot (after Large et al., 2001a) showing the extent of alteration for many of the samples in this study, with a trend towards carbonate-dominated alteration. CCPI = 100(MgO+ FeO)/(MgO + FeO + Na_2O + K_2O); AI = 100(K_2O + MgO)/(K_2O + MgO + Na_2O + CaO); b) Zr/TiO_2 versus Nb/Y classification diagram of Winchester and Floyd (1977).

zie Creek Formation have the highest Cr and Ni, up to 2265 and 1856 ppm, respectively.

Trace elements

One of the defining characteristics of the alkalic rocks from the Selwyn Basin is their high Ba contents (up to 40 100 ppm). Exceptions include Triassic dykes and Earn Group rocks from the Keno Hill district and ultramafic rocks from the Menzie Creek Formation, with Ba contents less than 100 ppm (Fig. 7a). Volcaniclastic rocks in the Menzie Creek Formation are interbedded with massive and pillowed flows and associated flow breccias. These units are lithologically variable, ranging from pyroclastic, bedded, tuffs, lapilli tuffs and tuff breccias, to autoclastic breccias. Most of the samples show a strong positive relationship between Zr and other high field strength elements (HFSE), including Nb, Th and Y (Fig. 7b–d). Some samples from the MacMillan Pass district and Misty Creek Embayment also have anomalously elevated HFSE and P compared to Zr (Fig. 7b–e). In terms of base metals and metalloids, Cu and Sb generally decrease with increasing Zr (Fig. 7f, j), whereas Pb, Zn and Mo display only subtle positive changes with Zr (Fig. 7g–i).

Rare earth elements

Rocks from the MacMillan Pass district and Misty Creek Embayment are strongly light rare earth element (REE)-enriched compared to those from the Menzie Creek Formation or Keno Hill district (Fig. 8a-d). Those from the Misty Creek Embayment show a greater flattening of the heavy REE than those from MacMillan Pass (Fig. 8c, d). All samples from the Menzie Creek Formation are less enriched in the REE and are less strongly light REE-enriched (Fig. 8b) than those of the MacMillan Pass and Misty Creek Embayment areas. The Triassic dykes and some flows from the Keno Hill district have much flatter chondrite-normalized REE patterns than the other areas, consistent with the subalkalic composition (Fig. 8a). Compared to primitive mantle, most samples show large ion lithophile (LILE) and (HFSE) enrichment, with the exception of the Triassic dykes from the Keno Hill area (Fig. 9). Most samples show large positive anomalies for Ba, Mo, Sb, Ti and Li (Fig. 9). Although many of the rocks are ultrapotassic, K_2O is generally depleted compared to adjacent elements on the primitive mantle-normalized diagrams (Fig. 9).

Pb isotopes

The data for the volcanic rocks from the four areas in this study (i.e. Keno Hill, Anvil, MacMillan Pass, Misty Creek Embayment) form linear trends for $^{206}Pb/^{204}Pb$ vs. $^{207}Pb/^{204}Pb$ and $^{206}Pb/^{204}Pb$ vs $^{208}Pb/^{204}Pb$ (Fig. 10a, b). Most samples plot on an array that extends to Pb isotope values for mineralization within the Selwyn Basin (Godwin and Sinclair, 1982; Hantelmann, 2013). Samples with the least-radiogenic Pb isotopic composition also have high Pb and Sb contents (Fig. 10c, d). Some samples from all four areas reported here extend to less radiogenic Pb isotopic compositions than SEDEX galena.

Discussion

Petrogenesis

A full treatment of the petrogenesis of the rocks in this study is outside the scope of this paper. However, some comments pertaining to the understanding of potential genetic links with SEDEX deposit formation, are warranted. Composition and petrogenesis for the MacMillan Pass district and Misty

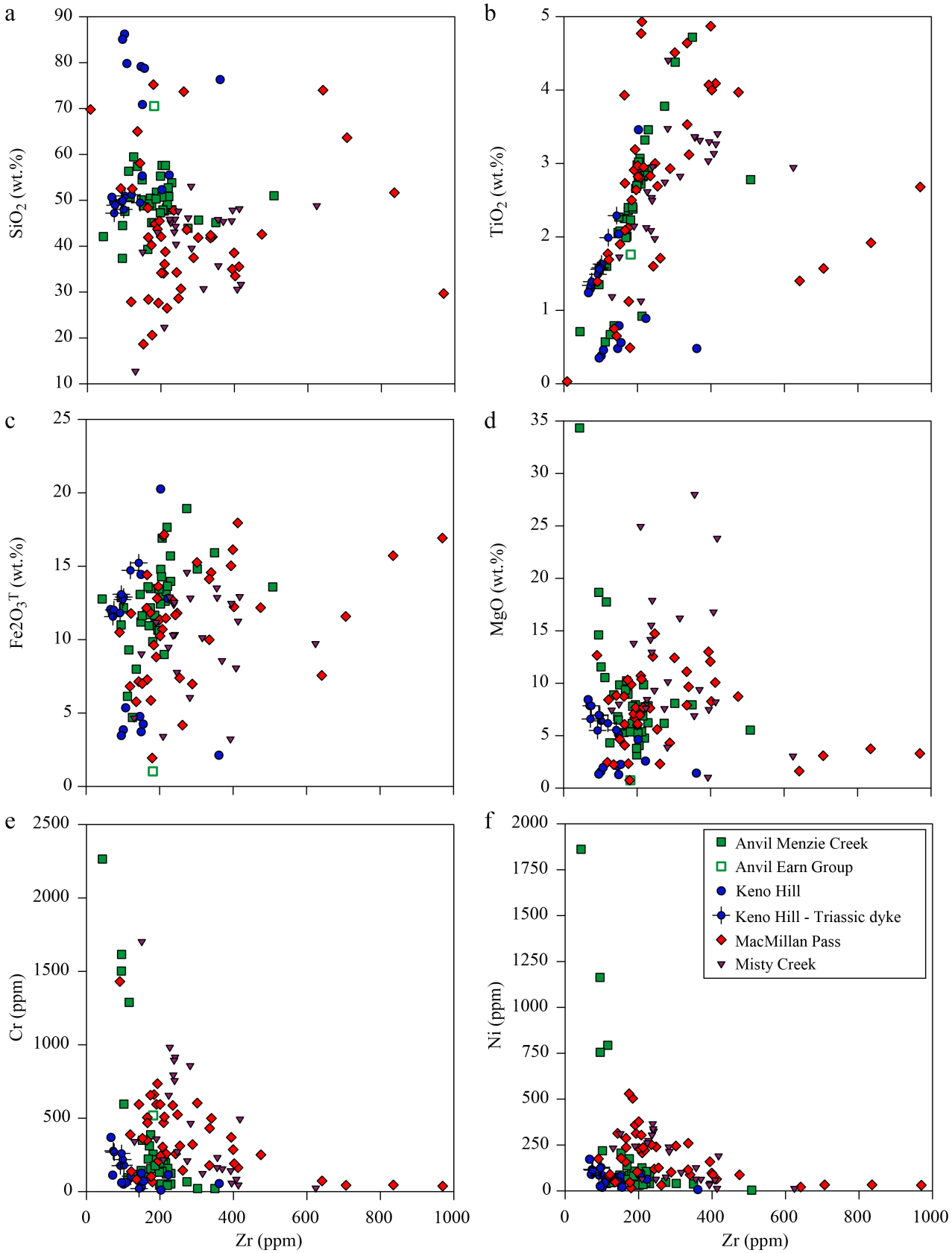

Figure 6. Plots of Zr versus selected major and minor element contents for Selwyn Basin volcanic rocks. a) SiO_2 vs. Zr; b) TiO_2 vs. Zr; c) $Fe_2O_3^T$ vs. Zr; d) MgO vs. Zr; e) Cr vs. Zr; f) Ni vs. Zr.

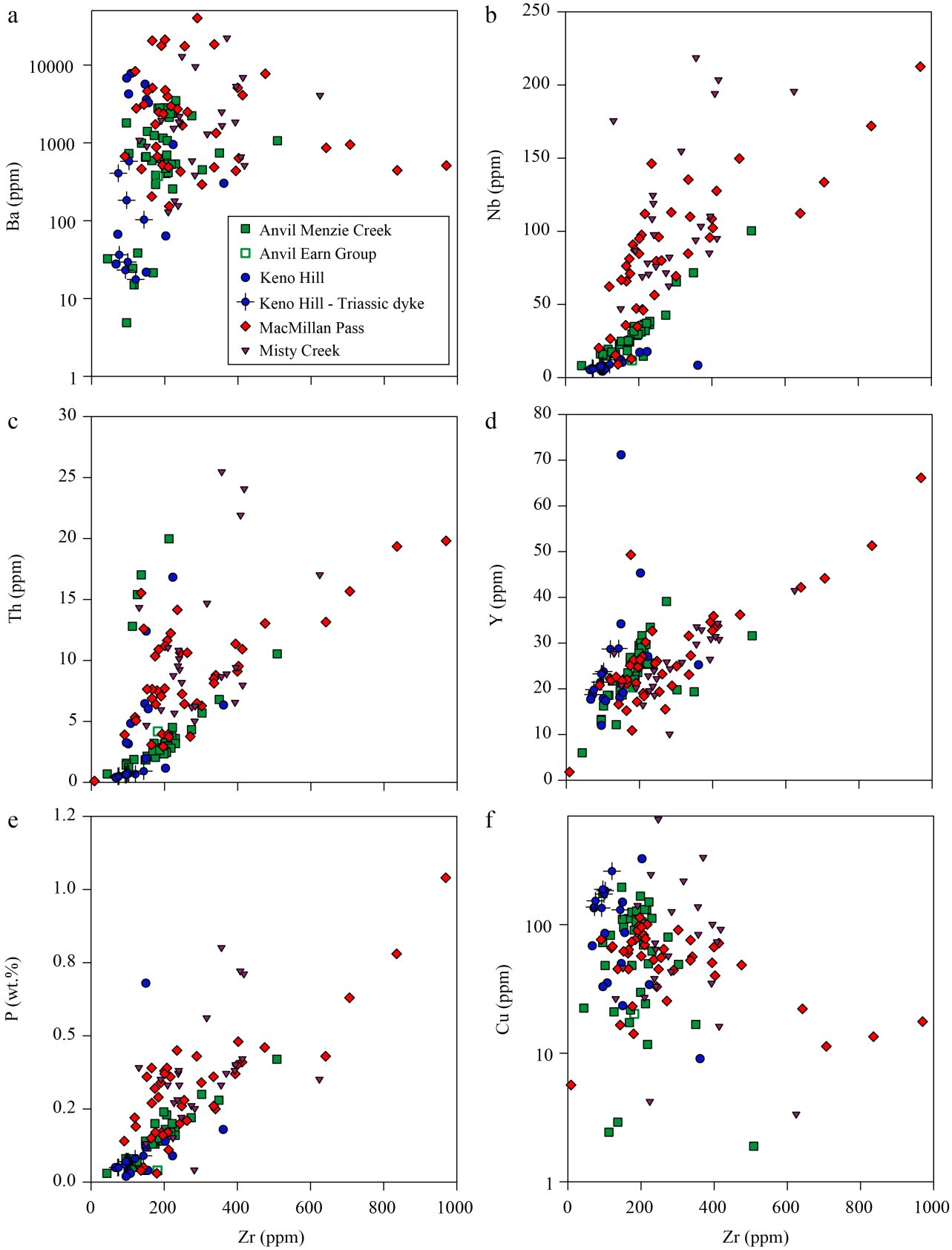

Figure 7. Plots of Zr versus selected trace elements for Selwyn Basin volcanic rocks. a) Ba vs Zr; b) Nb vs. Zr; c) Th vs. Zr; d) Y vs. Zr; e) P vs. Zr; f) Cu vs. Zr.

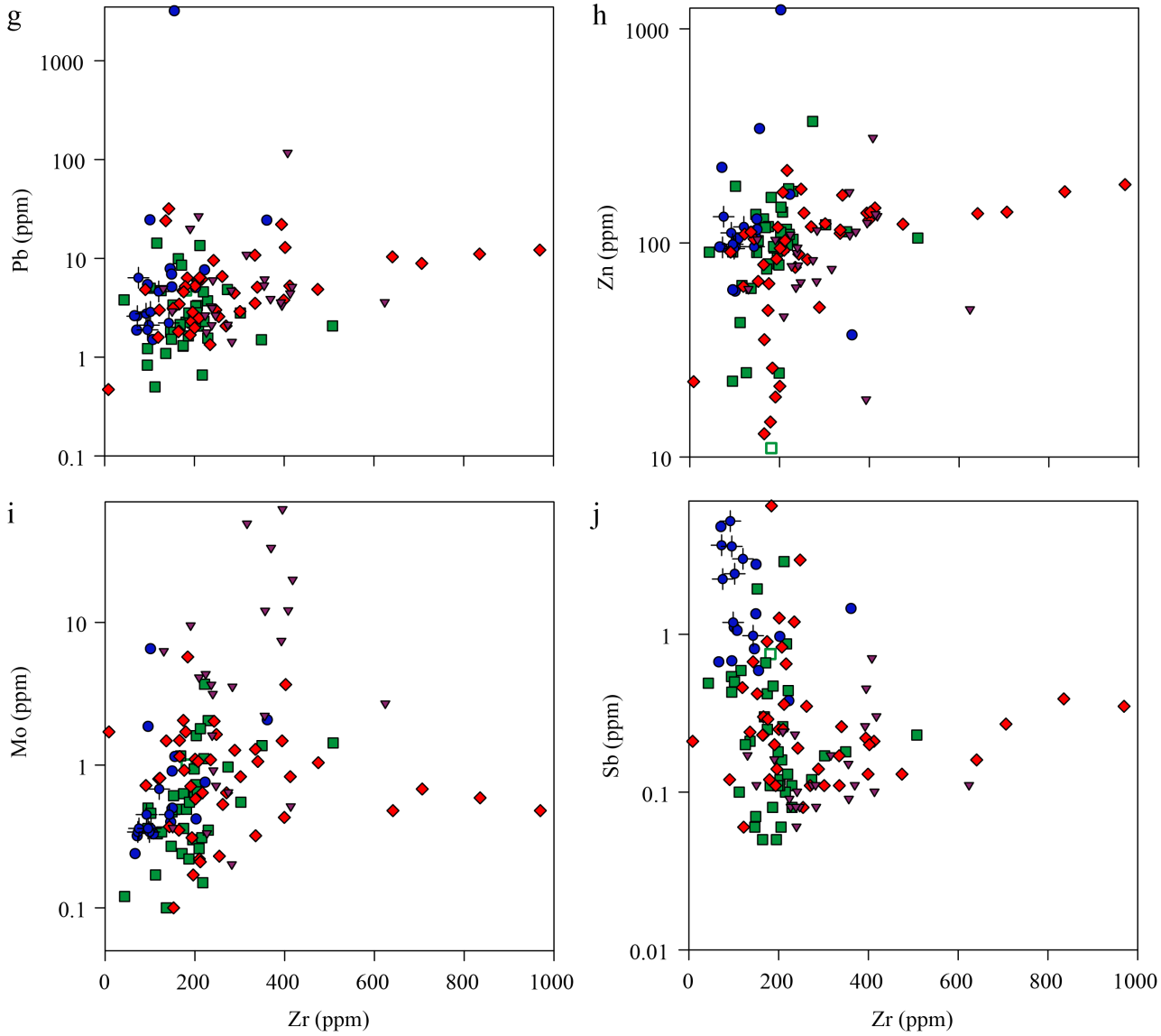

Figure 7. (Cont.) Plots of Zr versus selected trace elements for Selwyn Basin volcanic rocks. g) Pb vs. Zr; h) Zn vs. Zr; i) Mo vs. Zr; j) Sb vs. Zr.

Creek Embayment from this study concur with previous studies (e.g. Goodfellow et al., 1995). Volcanic rocks are dominantly mafic, highly alkalic to ultrapotassic, enriched in HFSE (e.g. Nb, Th, LREE) and LILE (e.g. Ba, Cs, Rb) and are present within the within-plate alkali basalt fields on tectonic discrimination plots (Fig. 11a, b). In addition, our new data extends interpretations to the Anvil and Keno Hill districts; areas not previously presented by Goodfellow et al. (1995). Rocks from the Menzie Creek Formation are less alkalic than those from the MacMillan Pass district or Misty Creek Embayment, but also plot in the within-plate alkali fields (Fig. 11a, b). These rocks are also characterized by moderate to high Ba contents, steep REE patterns (Fig. 8b) and fall along the mantle array (Fig. 12a), similar to other alkalic rocks. The Keno Hill district is geochemically and petrogenetically distinct from the other areas (Fig. 9, 11, 12). The Triassic dykes of the Keno Hill district are subalkalic and younger than other mafic rocks in the Selwyn Basin and depleted in Ba relative to Rb and Th (Fig. 9). These dykes plot as enriched (P-type) mid-ocean ridge basalt (Fig. 11, 12) and have primitive mantle-normalized Nb/La values (> 1; Fig. 12). Conversely, Earn Group mafic to felsic rocks in the Keno Hill area are subalkalic and are more volcanic arc-like in their geochemical signature (Fig. 11), with primitive mantle-normalized Nb/La values (< 1), and a calc-alkalic signature (Fig. 12). These rocks have been interpreted to be Devonian to Mississippian (Murphy and Roots, 1996) and may have formed during a period of greater extension towards the end of the development of the Selwyn Basin, allowing subduction-modified asthenospheric partial melt emplacement.

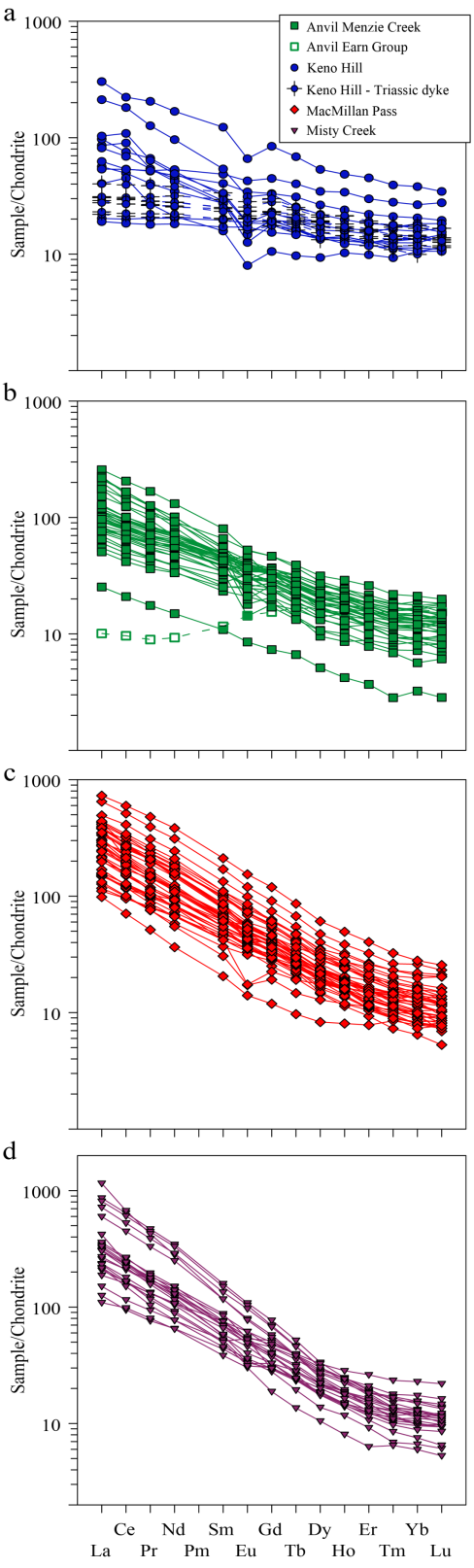

Figure 8. Chondrite-normalized REE plots for volcanic rocks from: a) Keno Hill district; b) Anvil district; c) MacMillan Pass district; d) Misty Creek Embayment. Normalizing data from McDonough and Sun (1995).

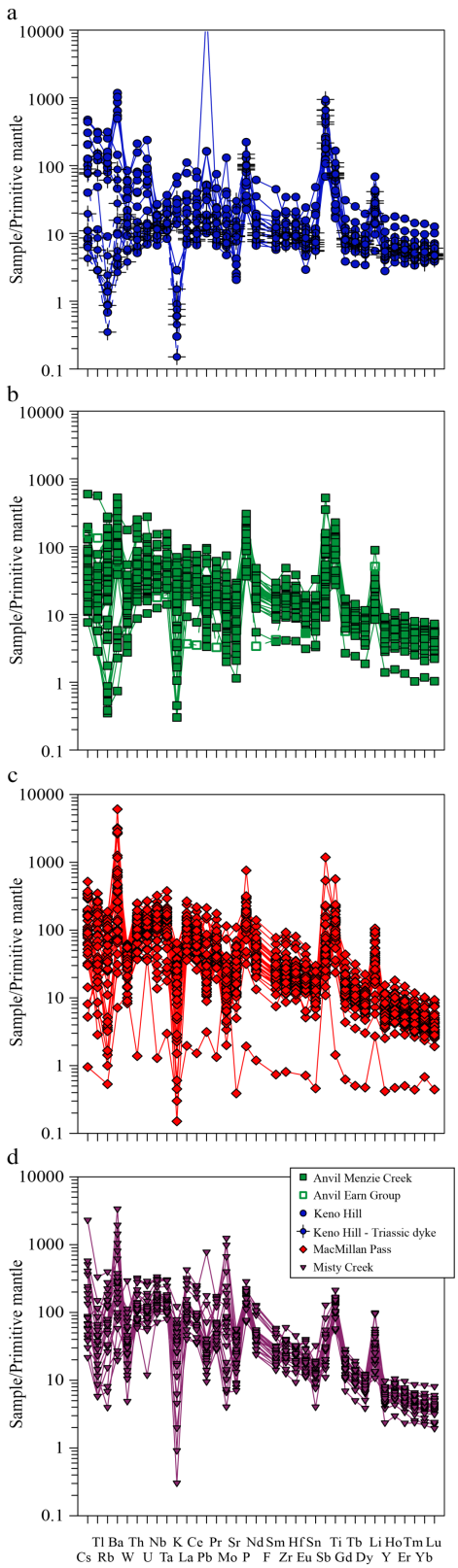

Figure 9. Primitive mantle-normalized extended element (spider) plots for volcanic rocks from: a) Keno Hill district; b) Anvil district; c) MacMillan Pass district; d) Misty Creek Embayment. Normalizing data from McDonough and Sun (1995).

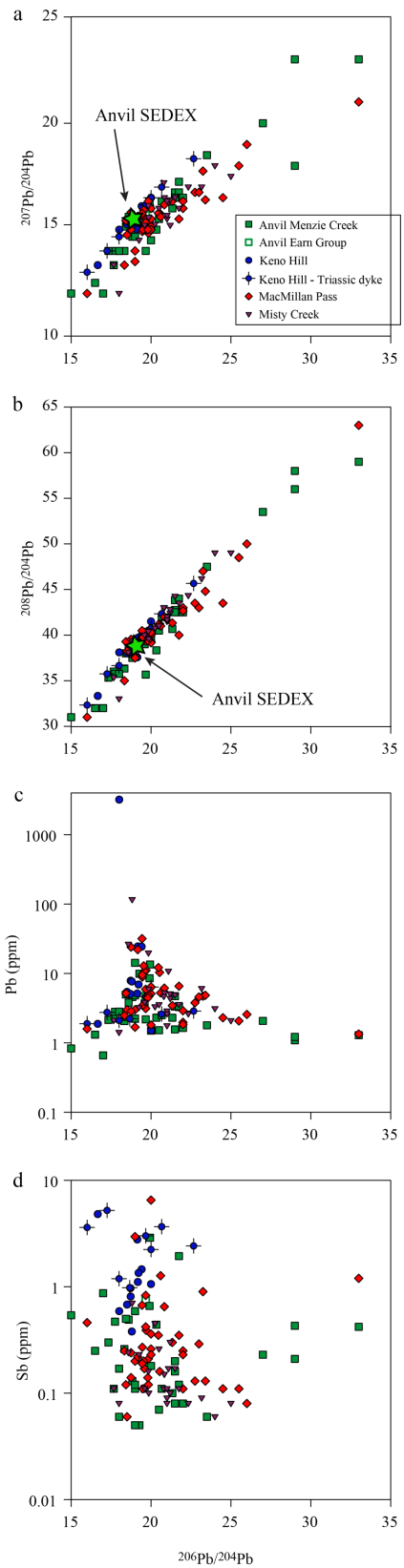

Figure 10. Plots of the Pb isotopic composition of the Selwyn Basin rocks. a) $^{206}Pb/^{204}Pb$ vs. $^{207}Pb/^{204}Pb$; b) $^{206}Pb/^{204}Pb$ vs. $^{208}Pb/^{204}Pb$; c) $^{206}Pb/^{204}Pb$ vs. Pb; d) $^{206}Pb/^{204}Pb$ vs. Sb.

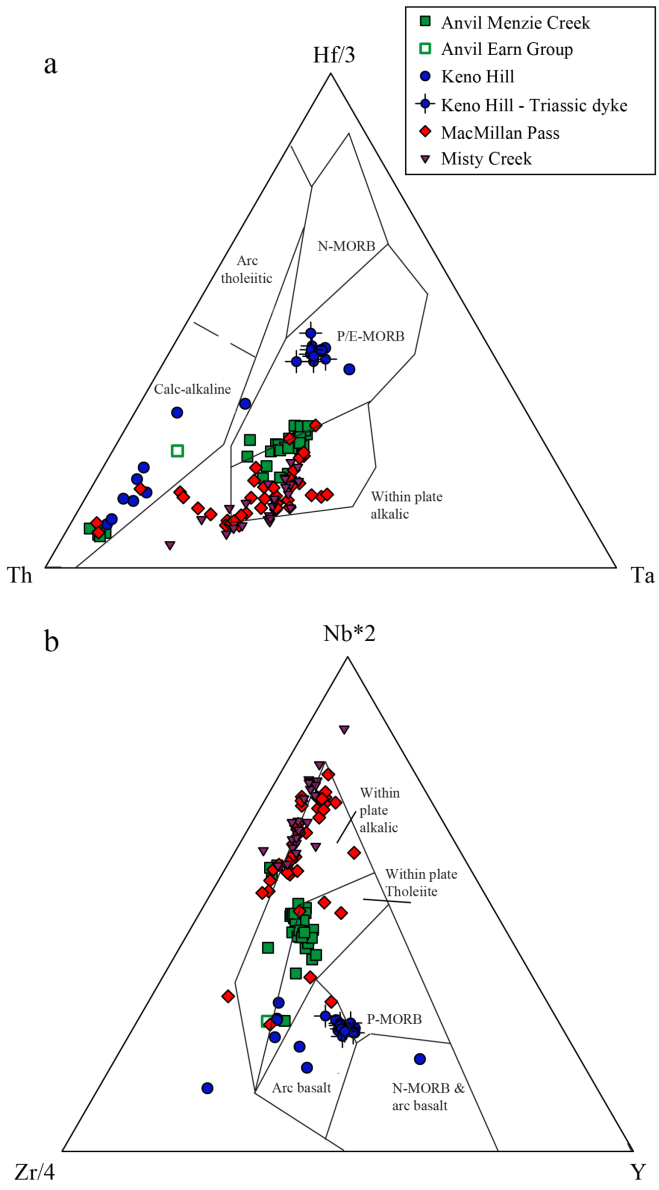

Figure 11. Plots of Selwyn Basin rocks: a) Th–Hf/3–Ta and b) Zr/4–Nb*2–Y, after Wood (1980) and Meschede (1986), respectively.

Relationship of magmatism to SEDEX and VMS mineralization

A main objective of this research is investigating if there are direct links between magmatism and SEDEX formation in the Selwyn Basin. Published genetic models for SEDEX deposits do not require a direct link, even as a heat source, but there has been increased recognition over the last couple of decades that magmatism may more directly influence the formation of some sediment-hosted Pb-Zn deposits, including the giant SEDEX Sullivan deposit in the Belt-Purcell basin of British Columbia (Anderson and Goodfellow, 2000) and some of the Irish-type deposits in Ireland (McCusker and Reed, 2013; Davidheiser-Kroll et al., 2014).

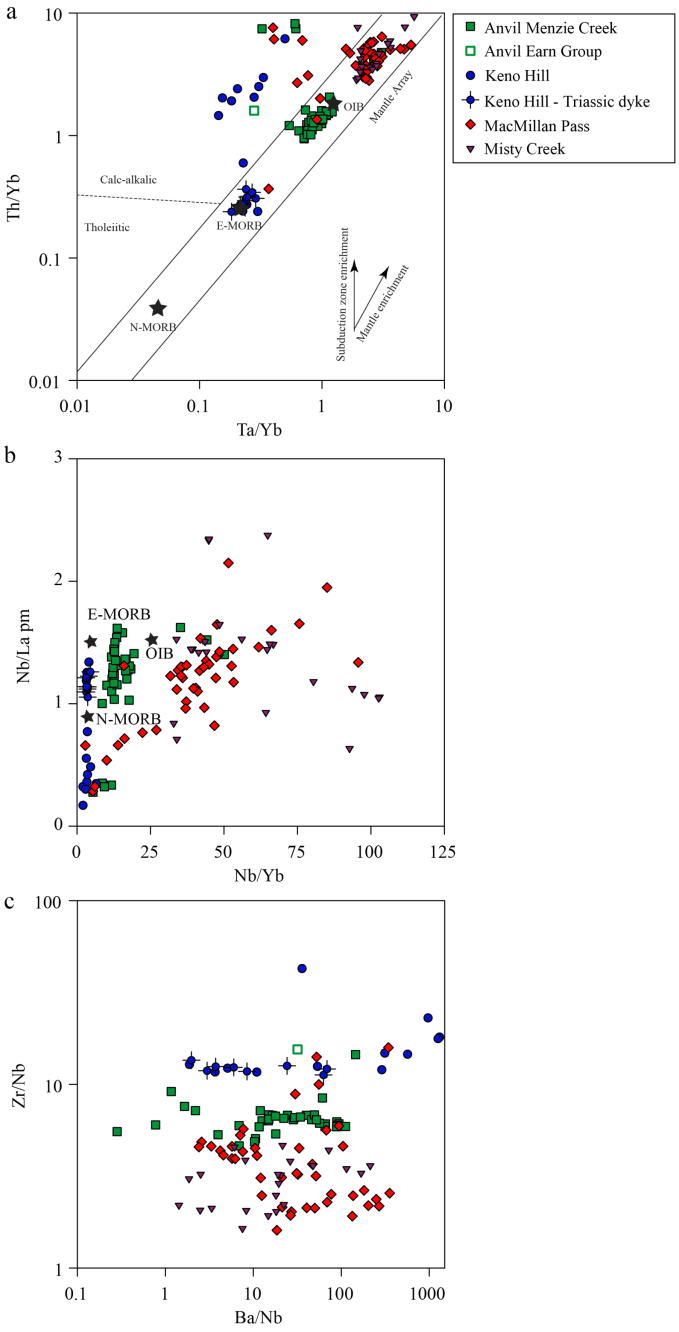

Figure 12. Plots of: a) Th/Yb vs. Ta/Yb, after Pearce (1983); b) Primitive mantle-normalized Nb/La vs. Nb/Yb; c) Zr/Nb vs. Ba/Nb.

Goodfellow et al. (1995) noted the apparent relationship between rate of magma production, depth of melting, melt composition and involvement of subcontinental lithosphere versus asthenosphere in the production of continental rift zone magmas. The alkalic volcanic rocks of the Selwyn Basin are similar to those in low volcanicity continental rift zones, such as the western arm of the East Africa Rift, which is characterized by highly alkalic to ultrapotassic rocks and typically low volume production from low degrees of partial melting of metasomatized subcontinental lithospheric mantle. Goodfellow et al. (1995) suggested that the generally lower geothermal gradients in low volcanicity rifts compared to those in high volcanicity rifts could account for the relatively low temperatures of the SEDEX-forming hydrothermal fluids in the Selwyn Basin (e.g. around 180°C at the Howards Pass deposit to 260°C at the Jason deposit). The alkalic rocks of the Selwyn Basin erupted along deep faults during basin extension throughout the Paleozoic (Goodfellow et al., 1995).

The challenge to ascribing a genetic link between volcanism and SEDEX deposit formation is determining which chemical parameters can be used to support or refute such a link. One approach is to focus on magmatic volatiles (e.g. $^{3}He/^{4}He$; de Ronde et al., 2011; Davidheiser-Kroll et al., 2014) and metals and metalloids that are commonly enriched in epithermal systems in which the direct contributions to from degassing magmas is evident (e.g. As, Hg, Tl, Sb, Mo, Sn, W) (Richards, 2011). One of the important characteristics of the alkalic rocks from the Selwyn Basin is the trend to high Ba contents (Fig. 7a, 13a–d) as also noted by Goodfellow et al. (1995). These ultrapotassic rocks have higher Ba contents than is typically of ultrapotassic rocks in other settings, such as those in the western arm of the East Africa Rift (Rosenthal et al., 2009), Italy (Peccerillo, 1998), and China (Sun et al., 2014). For example, ultrapotassic rocks from China reported by Sun et al. (2014) have Ba contents up to 4000 ppm, but have Ba/La values less than 40 compared to the Selwyn Basin rocks in this study where Ba contents vary up to 40 100 ppm and Ba/La values up to 710.

SEDEX deposits in the Selwyn Basin, such as Howards Pass, are typically enriched in Ba (Fig. 13e; J.M. Peter, pers. comm., 2018). Rocks with the highest Ba contents in our study also contain barium silicates (i.e. hyalophane and celsian, which form a solid solution with K-feldspar), suggesting a genetic link between extensional tectonism, magmatism, hydrothermal activity, and the formation of the Zn-Pb (±Ag, ±Ba) SEDEX deposits in the Selwyn Basin (Goodfellow et al., 1995). There is a moderately strong positive relationship between Ba and Tl contents for the Selwyn Basin volcanic rocks, suggesting that they share a common source; these elements (and Rb, Cs; Fig. 13a, b, d) can originate in the rocks either by hydrothermal alteration or direct magmatic origin. In the latter case, anomalous Ba and Tl in the magmatic rocks and in the SEDEX deposits would suggest a common origin, consistent with direct magmatic contributions to hydrothermal fluids, including the ore-forming fluids. Host sedimentary rocks (shales) and mineralization from SEDEX deposits in the Howard's Pass district range to high Ba contents (> 50 000 ppm; although there is a lack of barite at this deposit) and generally show a positive relationship between Ba and Tl (Fig. 13e; J.M. Peter, pers. comm., 2018). Conversely, Fernandes et al. (2017) described barite-rich horizons from the Canol Formation that are not interpreted to have a hydrothermal origin, but are rather related to high biological productivity and low seawater sulphate during diagenesis. Sedimentary rock samples from the

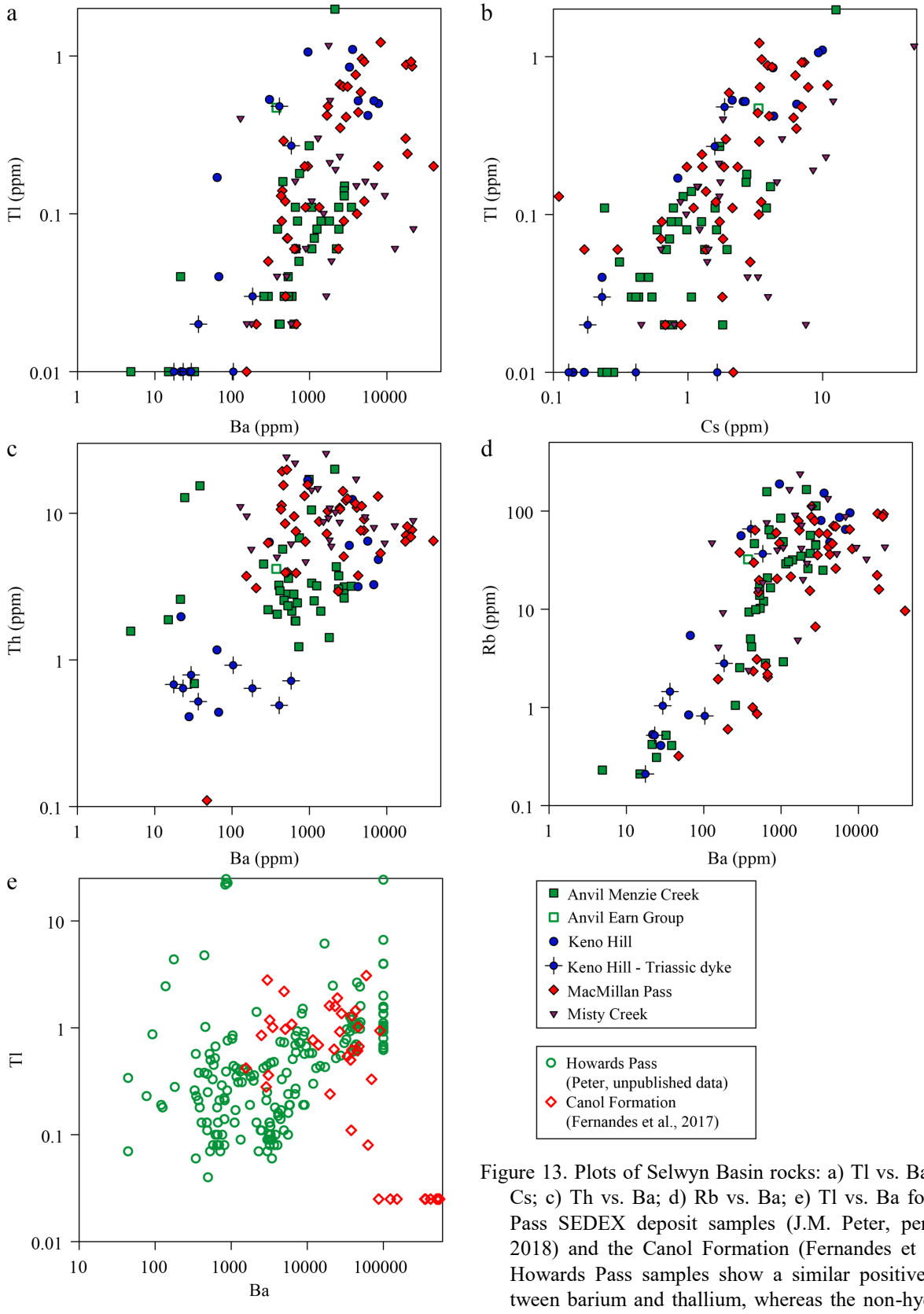

Figure 13. Plots of Selwyn Basin rocks: a) Tl vs. Ba; b) Tl vs. Cs; c) Th vs. Ba; d) Rb vs. Ba; e) Tl vs. Ba for Howards Pass SEDEX deposit samples (J.M. Peter, pers. comm., 2018) and the Canol Formation (Fernandes et al., 2017). Howards Pass samples show a similar positive trend between barium and thallium, whereas the non-hydrothermal barite beds of the Canol Formation show an inverse relationship.

Canol Formation show an inverse relationship between Ba and Tl (Fig. 13e); the positive correlation between Ba and Tl for the magmatic rocks and SEDEX deposits is thus unlikely to represent incorporation of sedimentary barium and thallium. Although thallium is volatile and may be redistributed outwards from the mineralization source (Large et al., 2001b; McGoldrick et al., 1979), we are impressed by the differences in the behaviour of barium and thallium between different Selwyn Basin reservoirs (magmatic and SEDEX versus sedimentary).

Barium and thallium enrichment process(es) for the alkalic volcanic rocks we have studied remain unresolved. The similar relationships (positive correlation) between Ba and Tl contents for our rocks and the Howards Pass SEDEX deposit suggests a genetic link between hydrothermal fluids and the magmatic rocks, rather than from diagenesis of a primary marine deposit, such as the Canol Formation. However, the Ba and Tl contents alone cannot be used to discriminate whether the metals and metalloids were contributed from the magmas (in addition to heat) to the mineralizing fluids, or if the volcanic rocks were altered by barium and metal-rich hydrothermal fluids subsequent to emplacement; indeed, there is not necessarily any requirement for a magmatic heat source to drive the ore-forming SEDEX fluids (e.g. Yang, 2006). Barium feldspars (celsian, hyalophane) can form from Ba-rich magmas, from hydrothermal alteration by Ba-rich fluids or diagenetically (see Essene et al., 2005; Azzone et al., 2009; Henry et al., 2015).

Recent studies at the Queen's Facility for Isotope Research has shown that significant thallium isotopic fractionation occurs during hydrothermal alteration and ore-formation, owing to the redox sensitive nature of thallium (Peter et al., 2018). Previous studies have documented the range in thallium isotopic fractionation in different geological reservoirs (Fig. 14; Peter et al., 2018). We will be performing Tl isotopic analyses on our volcanic rock samples, with the expectation of one of two outcomes: i) the samples will show little fractionation, with isotopic values similar to mantle-derived magmas, although there is not a simple range (Blusztajn et al., 2018; Nielsen et al., 2017); or ii) the large variation in Ba and Tl contents will correlate with fractionation of Tl isotopes as a function of variable hydrothermal alteration of the volcanic rocks (Coggon et al., 2014). The anomalous Ba contents of many of the rocks in this study is also shown by the variations in Ba/Nb values compared to Zr/Nb (Fig. 12c). Although the Zr/Nb values have a restricted range, they differ for the areas studied here, with lowest values for the most alkalic rocks, but overall there is a restricted range in Zr/Nb values. Conversely, within each area there is a large range in Ba/Nb values, suggesting addition of Ba, either during metasomatism of the subcontinental lithosphere (Goodfellow et al., 1995) or during hydrothermal alteration.

We also plan to measure the C, O and Sr isotopic composition of the carbonate alteration observed in many samples. Because these rocks are dominantly alkalic to ultrapotassic, it is possible that at least some of the carbonate represents elevated magmatic volatiles common to this style of volcanism. We expect that if there is a magmatic component to the carbonate minerals, this will be reflected in mantle $\delta^{13}C$ and $^{87}Sr/^{86}Sr$ values, and variation in $\delta^{18}O$ values of the carbonate minerals related to hydrothermal alteration, as is shown for carbonatite (e.g. Santos and Clayton, 1995; Oliveira et al., 2017).

Samples with the least-radiogenic Pb isotopic composition also have elevated Pb and Sb contents (Fig. 10c, d). If the metal contents of the volcanic rocks are genetically related to SEDEX mineralization, the Pb isotopic composition of the volcanic rocks, might be used as a vectoring tool. Some samples

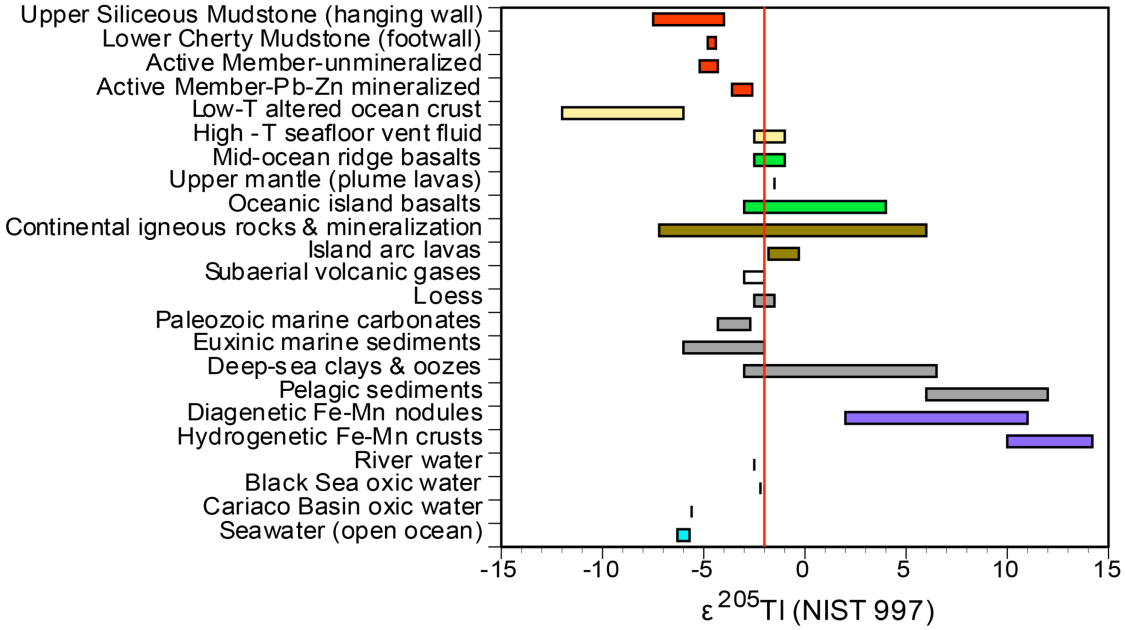

Figure 14. Range in isotopic fractionation for thallium, compiled by Peter et al. (2018).

are less radiogenic than galena from the Paleozoic Selwyn Basin SEDEX deposits (Fig. 10a, b) (Godwin and Sinclair, 1982; Hantelmann, 2013), consistent with a contribution of much older Pb, either from the subcontinental lithospheric mantle or older basement rocks.

Age dating

There are few reliable, precise age determinations for Selwyn Basin igneous rocks. Mineral liberation analysis (MLA -SEM) has documented zircon in polished sections. Eleven samples are undergoing zircon separation for U-Pb dating using a combination of laser ablation ICP-MS and chemical abrasion thermal ionization mass spectrometry. Sufficient zircons for dating have been documented for samples for the Keno Hill (Earn Group), Macmillan Pass (Earn Group of the MacMillan and Niddery volcanic complexes) and Anvil (Menzie Creek Formation) districts. These dates will help to better constrain the timing of magmatism and temporal relationships to SEDEX formation.

Next steps

Work in progress includes: 1) radiogenic isotopic analysis (Nd-Sm, Rb-Sr and U-Th-Pb) to further refine the petrogenesis and tectonic affinity of volcanic and intrusive rocks, the degree of crustal contamination, and source of metals; 2) mineralogy and mineral chemistry of primary and secondary phases using MLA-SEM, electron microprobe and in-situ trace element analysis and/or dating using LA-ICP-MS, along with additional imaging to better refine mechanisms and styles of volcanism, particularly related to the source, formation and transport of mineralizing fluids; 3) thallium isotopic analyses to determine the origin of thallium and barium in the volcanic rocks of the Selwyn Basin; 4) isotopic analyses (C, O, Sr) of carbonate minerals in these rocks to determine if there is a magmatic contribution, or if all of the carbonate originates from hydrothermal alteration; and 5) dating intrusive rocks to determine their potential as heat engines for hydrothermal systems.

Acknowledgments

This report is a contribution to the NRCan Targeted Geoscience Initiative Program (TGI). Support for this study was provided through the Volcanic- and Sedimentary-Hosted Base Metal Mineralization Project's 'Activity VS-2.2: Magmatism and Relationships to Sediment-Hosted Zn-Pb Deposits'.

The authors acknowledge Stephen Piercey (Memorial University) for his contributions to the research proposal and initial development of the project. This activity relies on the collaboration of the Yukon Geological Survey and Northwest Territories Geological Survey. In particular, Rosie Cobbett, Maurice Colpron, Lee Pigage and the late Charlie Roots provided invaluable geological information on the Faro and Keno Hill-Mayo districts. Jan Peter (GSC) and Neil Fernandes (Queen's University) are thanked for sharing Ba and Tl data from the Howards Pass deposit and Canol Formation, Selwyn Basin, respectively. Jim Mortensen (University of British Columbia) and Christopher Leslie (University of Tasmania) are thanked for providing Misty Creek Embayment samples. This report benefited from the review of Neil Rogers and Jan Peter.

References

Abbott, J.G., 2013. Bedrock geology of the Macmillan Pass area Yukon and adjacent Northwest Territories (NTS 105O/1,2 and parts of 105O/7,8 and 105P/4,5); Yukon Geological Survey Geoscience Map 2013-1, scale 1:50 000.

Anderson, H.E. and Goodfellow, W.D., 2000. Geochemistry and isotope chemistry of the Moyie Sills; implications for the early tectonic setting of the Mesoproterozoic Purcell Basin; Special Publication - Geological Association of Canada. Mineral Deposits Division 1, p. 302–321.

Azzone, R.G., Ruberti, E., Enrich, G.E.R., and Gomes, C.B., 2009. Zr- and Ba-rich minerals from the Ponte Nova alkaline mafic-ultramafic massif, southeastern Brazil: Indication of an enriched mantle source; The Canadian Mineralogist, v.47, p. 1087–1103.

Beaudoin, Y., Scott, S.D., Gorton, M.P., Zajacz, Z., and Halter, W., 2007. Effects of hydrothermal alteration on Pb in the active PACMANUS hydrothermal field, ODP Leg 193, Manus Basin, Papua New Guinea; A LA-ICP-MS study; Geochimica et Cosmochimica Acta, v. 71, p. 4256-4278.

Blusztajn, J., Nielsen, S.G., Marschall, H.R., Shu, Y., Ostrander, C.M., and Hanyu, T., 2018, Thallium isotope systematics in volcanic rocks from St. Helena – Constraints on the origin of the HIMU reservoir; Chemical Geology, v. 476, p. 292–301.

Carne, R.C. and Cathro, R.J., 1982. Sedimentary exhalative (SEDEX) zinc-lead deposits, northern Canadian Cordillera; Canadian Institute of Mining and Metallurgy Bulletin, v. 75, p. 66–78.

Cobbett, R., 2013. Preliminary observations on the geology of the Anvil Lake area (parts of NTS 105K/11 and 12), central Yukon; *in* Yukon Exploration and Geology 2013, (ed.) K.E. MacFarlane, M.G. Nordling and P.J. Sack; Yukon Geological Survey, p. 33–51.

Cobbett, R., 2016. Preliminary observations on the geology of Tay Mountain Area (parts of NTS 105K/12 and 13, 105L/09 and 16), central Yukon; *in* Yukon Exploration and Geology 2016, (ed.) K.E. MacFarlane and M.G. Nordling; Yukon Geological Survey, p. 79–98.

Coggon, R.M., Rehkämper, M., Atteck, C., Teagle, D.A.H., Alt, J.C., and Cooper, M.J., 2014. Controls on thallium uptake during hydrothermal alteration of the upper ocean crust; Geochimica et Cosmochimica Acta, v. 144, p. 25–42.

Davidheiser-Kroll, B., Stuart, F.M., and Boyce, A.J., 2014. Mantle heat drives hydrothermal fluids responsible for carbonate-hosted base metal deposits: evidence from $^{3}He/^{4}He$ of ore fluids in the Irish Pb-Zn ore district; Mineralium Deposita, v. 49, p. 547–553.

de Ronde, C.E.J., Massoth, G.J., Butterfield, D.A., Christenson, B.W., Ishibashi, J., Ditchburn, R.G., Hannington, M.D., Brathwaite, R.L., Lupton, J.E., Kamenetsky, V.S., Graham, I.J., Zellmer, G.F., Dziak, R.P., Embley, R.W., Dekov, V.M., Munnik, F., Lahr, J., Evans, L.J., and Takai, K., 2011. Submarine hydrothermal activity and gold-rich mineralization at Brothers Volcano, Kermadec arc, New Zealand; Mineralium Deposita, v. 46, p. 541–584.

Eckstrand, O.R. and Hulbert, L.J., 2007. Magmatic nickel-copper-platinum group element deposits; *in* Mineral Resources of Canada: A Synthesis of Major Deposit-types, District Metallogeny, the Evolution of Geological Provinces, and Exploration Methods, (ed.) W.D. Goodfellow; Geological Association of Canada, Mineral Deposits Division, Special Publication 5, p. 205–222.

Eisbacher, G.H., 1981. Sedimentary tectonic and glacial record in the Windermere Supergroup, Mackenzie Mountains, Northwestern Canada; Geological Survey of Canada, Paper 80-27, 40 p.

Essene, E.J., Claflin, C.L., Giorgetti, G., Mata, P.M., Peacor, D.R., Árkai, P., and Rathmell, M.A., 2005. Two-, three- and four-feldspar assemblages with hyalophane and celsian: implications for phase equilibria in $BaAl_2Si_2O_8$–$CaAl_2S_2O_8$–$NaAlSi_3O_8$–$KAlSi_3O_8$; European Journal of Mineralogy, v. 17, p. 515–535.

Fernandes, N.A., Gleeson, S.A., Magnall, J.M., Creaser, R.A., Martel, E., Fischer, B.J., and Sharp, R., 2017. The origin of Late Devonian (Frasnian) stratiform and stratabound mudstone-hosted barite in the Selwyn Basin, Northwest Territories, Canada; Marine and Petroleum Geology, v. 85, p. 1–15.

Godwin, C.I. and Sinclair, A.J., 1982. Average lead isotope growth curves for shale-hosted zinc-lead deposits, Canadian Cordillera; Economic Geology, v. 77, p. 675–690.

Goodfellow, W.D., 2007. Base metal metallogeny of the Selwyn Basin, Canada; *in* Mineral Resources of Canada: A Synthesis of Major Deposit-types, District Metallogeny, the Evolution of Geological Provinces, and Exploration Methods, (ed.) W.D. Goodfellow; Geological Association of Canada, Mineral Deposits Division, Special Publication 5, p. 553–580.

Goodfellow, W.D., Lydon, J.W., and Turner, R.J.W., 1993. Geology and genesis of stratiform sediment-hosted (SEDEX) zinc-lead-silver sulphide deposits; Geological Association of Canada Special Paper 40, p. 201–251.

Goodfellow, W.D., Cecile, M.P., and Leybourne, M.I., 1995. Geochemistry, petrogenesis, and tectonic setting of Lower Paleozoic alkalic and potassic volcanic rocks, Northern Canadian Cordilleran miogeocline; Canadian Journal of Earth Sciences, v. 32, p. 1236–1254.

Hantelmann, J.J., 2013. The paragenesis and geochemistry of the Bellekeno Ag-Pb-Zn vein, Keno Hill district, Yukon, Canada; M.Sc. thesis, University of Alberta, Edmonton, Alberta, 293 p.

Henry, D.J., Will, C.N., and Mueller, P.A., 2015. Ba-rich K-feldspar from mafic xenoliths within Mesoarchean granitic rocks, Beartooth Mountains, Montana, USA: Indicators for barium metasomatism; The Canadian Mineralogist, v. 53, p. 185–198.

Hunt, J.A., Murphy, D.C., Roots, C.F., and Poole, W.H., 1996. Geological map of the Mt. Haldane area, Yukon (105M/13); Exploration and Geological Services Division, Yukon, Indian and Northern Affairs Canada, Map 1996-4, scale 1:50 000.

Jennings, D.S. and Jilson, G.A., 1986. Geology and sulphide deposits of the Anvil Range, Yukon; *in* Mineral Deposits of Northern Cordillera, (ed.) J.A. Morin, J.A.; Canadian Institute Mining and Metallurgy, p. 339-361.

Large, R.R., Gemmell, J.B., Paulick, H., and Huston, D.L., 2001a. The alteration box plot: A simple approach to understanding the relationship between alteration mineralogy and lithogeochemistry associated with volcanic-hosted massive sulfide deposits; Economic Geology, v. 96, p. 957–971.

Large, R.R., Allen, R.L., Blake, M.D., and Herrmann, W., 2001b. Hydrothermal alteration and volatile element halos for the Rosebery K Lens volcanic-hosted massive sulfide deposit, Western Tasmania; Economic Geology, v. 96, p. 1055–1072.

Leybourne, M.I., Schwarz-Schampera, U., De Ronde, C.E.J., Baker, E.T., Faure, K., Walker, S.L., Butterfield, D.A., Resing, J.A., Lupton, J.E., Hannington, M.D., Gibson, H.L., Massoth, G.J., Embley, R.W., Chadwick, W.W., Jr., Clark, M.R., Timm, C., Graham, I.J., and Wright, I.C., 2012. Submarine magmatic-hydrothermal systems at the Monowai volcanic center, Kermadec Arc; Economic Geology, v. 107, p. 1669–1694.

Lydon, J.W., 1988. Volcanogenic Massive Sulfide Deposits Part 2: Genetic Models; Geoscience Canada, v. 15, p. 43–65.

Magnall, J.M., Gleeson, S.A., Blamey, N.J.F., Paradis, S., and Luo, Y., 2016. The thermal and chemical evolution of hydrothermal vent fluids in shale hosted massive sulphide (SHMS) systems from the MacMillan Pass district (Yukon, Canada); Geochimica et Cosmochimica Acta, v. 193, p. 251–273.

McCusker, J. and Reed, C., 2013. The role of intrusions in the formation of Irish-type mineralization; Mineralium Deposita, v. 48, p. 687–695.

McDonough, W.F. and Sun, S.S., 1995. The composition of the Earth; *in* Chemical evolution of the mantle, (ed.) W.F. McDonough, N.T. Arndt and S. Shirey; Elsevier, Amsterdam, Netherlands, p. 223–253.

McGoldrick, P.J., Keays, R.R., and Scott, B.B., 1979. Thallium: a sensitive indicator of rock/seawater interaction and of sulfur saturation of silicate melts; Geochimica et Cosmochimica Acta, v. 43, p. 1303–1311.

Meschede, M., 1986. A method of discriminating between different types of mid-ocean ridge basalts and continental tholeiites with the Nb-Zr-Y diagram; Chemical Geology, v. 56, p. 207–218.

Murphy, D.C. and Roots, C.F., 1996. Geological map of the Keno Hill area, Central Yukon (105M/14); Exploration and Geological Services Division, Indian and Northern Affairs Canada, Map 1996-5, scale 1:50 000.

Needham, A.J., Lindsay, J.M., Smith, I.E.M., Augustinus, P., and Shane, P.A., 2011. Sequential eruption of alkaline and sub-alkaline magmas from a small monogenetic volcano in the Auckland Volcanic Field, New Zealand; Journal of Volcanology and Geothermal Research, v. 201, p. 126–142.

Nielsen, S.G., Prytulak, J., Blusztajn, J., Shu, Y., Auro, M., Regelous, M., and Walker, J., 2017. Thallium isotopes as tracers of recycled materials in subduction zones: Review and new data for lavas from Tonga-Kermadec and Central America; Journal of Volcanology and Geothermal Research, v. 339, p. 23–40.

Nelson, J.L. and Colpron, M., 2007. Tectonics and metallogeny of the British Columbia, Yukon, and Alaskan Cordillera, 1.8 Ga to the present; *in* Mineral Resources of Canada: A Synthesis of Major Deposit-types, District Metallogeny, the Evolution of Geological Provinces, and Exploration Methods, (ed.) W.D. Goodfellow; Geological Association of Canada, Mineral Deposits Division, Special Publication 5, p. 755–792.

Oliveira, Í.L., Brod, J.A., Cordeiro, P.F.O., Dantas, E.L., and Mancini, L.H., 2017. Insights into the late-stage differentiation processes of the Catalão I carbonatite complex in Brazil: New Sr–Nd and C–O isotopic data in minerals from niobium ores; Lithos, v. 274-275, p. 214–224.

Pearce, J.A., 1983. Role of sub-continental lithosphere in magma genesis at destructive plate margins; *in* Continental Basalts and Mantle Xenoliths, (ed.) C.J. Hawkesworth and M.J. Norry; Shiva, Nantwich, p. 230–249.

Peccerillo, A., 1998. Relationships between ultrapotassic and carbonate-rich volcanic rocks in central Italy: Petrogenetic and geodynamic implications; Lithos, v. 43, p. 267–279.

Peter, J.M., Gadd, M.G., Layton-Matthews, D., and Voinot, A., 2018. Reconnaissance thallium isotope study of zinc-lead SEDEX mineralization and host rocks in the Howard's Pass district, Selwyn Basin, Yukon: Potential application to paleoredox determinations and fingerprinting of mineralization; *in* Targeted Geoscience Initiative: 2017 report of activities, volume 1, (ed.) N. Rogers; Geological Survey of Canada, Open File 8358, p. 179–191.

Pigage, L.C., 2004. Bedrock geology compilation of the Anvil District (parts of NTS 105K/2, 3, 5, 6, 7, and 11), central Yukon; Yukon Geological Survey Bulletin 15, 103 p.

Potra, A. and Moyers, A., 2017. Constraints on the sources of ore metals in Mississippi Valley-type deposits in central and east Tennessee, USA, using Pb isotopes; Ore Geology Reviews, v. 81, p. 201–210.

Richards, J.P., 2009. Postsubduction porphyry Cu-Au and epithermal Au deposits: Products of remelting of subduction-modified lithosphere; Geology, v. 37, p. 247–250.

Richards, J.P., 2011. Magmatic to hydrothermal metal fluxes in convergent and collided margins; Ore Geology Reviews, v. 40, p. 1-26.

Roots, C.L., 1997. Geology of the Mayo map area, Yukon Territory (105M), p. 82.

Rosenthal, A., Foley, S.F., Pearson, D.G., Nowell, G.M., and Tappe, S., 2009. Petrogenesis of strongly alkaline primitive volcanic rocks at the propagating tip of the western branch of the East African Rift; Earth and Planetary Science Letters, v. 284, p. 236–248.

Sangster, D.F., 1990. Mississippi Valley-type and SEDEX lead -zinc deposits: A comparative examination; Transactions of the Institution of Mining and Metallurgy, v. B99, p. 21–42.

Santos, R.V. and Clayton, R.N., 1995. Variations of oxygen and carbon isotopes in carbonatites: A study of Brazilian alkaline complexes; Geochimica et Cosmochimica Acta, v. 59, p. 1339–1352.

Simonov, V.A., Gaskov, I.V., and Kovyazin, S.V., 2010. Physico-chemical parameters from melt inclusions for the formation of the massive sulfide deposits in the Altai–Sayan Region, Central Asia; Australian Journal of Earth Sciences, v. 57, p. 737–754.

Sinclair, W.D., 2007. Porphyry deposits; *in* Mineral Resources of Canada: A Synthesis of Major Deposit-types, District Metallogeny, the Evolution of Geological Provinces, and Exploration Methods, (ed.) W.D. Goodfellow; Geological Association of Canada, Mineral Deposits Division, Special Publication 5, p. 223–243.

Sun, Y., Ying, J., Zhou, X., Shao, J.A., Chu, Z., and Su, B., 2014. Geochemistry of ultrapotassic volcanic rocks in Xiaogulihe NE China: Implications for the role of ancient subducted sediments; Lithos v. 208-209, p. 53–66.

Winchester, J.A. and Floyd, P.A., 1977. Geochemical discrimination of different magma series and their differentiation products using immobile elements; Chemical Geology, v. 20, p. 325–343.

Wood, D.A., 1980. The application of a Th-Hf-Ta diagram to problems of tectonomagmatic classification and to establishing the nature of crustal contamination of basaltic lavas of the British Tertiary volcanic province; Earth and Planetary Science Letters, v. 50, p. 11–30.

Yang, K.H. and Scott, S.D., 1996. Possible contribution of a metal-rich magmatic fluid to a sea-floor hydrothermal system; Nature, v. 383, p. 420–423.

Using basalt-hosted xenoliths as probes of the composition, structure and rheology of the sub-Cordilleran lithosphere in British Columbia

R.K. Kroner[1], J.B. Chapman[2] and J.K. Russell[1]

[1]*Department of Earth, Ocean, and Atmospheric Sciences, University of British Columbia, 2020–2207 Main Mall, Vancouver, British Columbia V6T 1Z4*

[2]*Geological Survey of Canada, 605 Robson Street, Vancouver, British Columbia, V6B 5J3*

Abstract

This study seeks to illuminate the chemistry, structure, and rheology of the crustal and mantle lithosphere beneath the Canadian Cordillera using crustal and mantle xenoliths entrained in Quaternary to early Paleogene mafic volcanics. Most of the xenolith-bearing units belong to the Chilcotin Group basalts in southern British Columbia and fall within the Quesnel and Stikine accreted terranes. The sampling locations of Summit Lake north of Prince George, Lightning Peak in the Okanagan region and Mt. Timothy east of Lac la Hache were selected for the diversity of entrained xenoliths. Ultramafic mantle xenoliths include multiple types of peridotite, with lherzolite the most abundant in all locations. Crustal xenoliths include gabbro, granitoid, granulite and quartzite.

Pressure and depths of equilibration for the samples will be determined by microprobe analyses of various minerals in the xenoliths. This will be the first step toward creating a comprehensive petrological cross section of the southern Cordilleran lithosphere .

Introduction

This study aims to investigate whether crustal- and mantle-derived xenolith populations entrained in alkali basalt flows can be used to interrogate physical and chemical properties of the sub-Cordilleran lithosphere of British Columbia. This will be accomplished by the application of several analytical methods to xenolith samples collected from multiple such volcanic centres throughout central and southern British Columbia. Thermobarometry based on the composition of the xenoliths will be used to bracket their depth of equilibration, and thus provide representative sections of the lithosphere that will be evaluated against previously formulated geophysical models for lithospheric structure beneath southern Canadian Cordillera.

Xenolith occurrences are well documented throughout the Canadian Cordillera (e.g. Littlejohn and Greenwood, 1974; Ghent et al., 2008). However, the majority of studies to date have focused on localities throughout northern British Columbia, Yukon and Alaska. This fieldwork focused on units in the Quesnel terrane in central and southern British Columbia (Fig. 1, 2). These xenolith-bearing volcanic rocks consist of basanite, nephelinite and alkaline olivine basalt that generally belong to the Chilcotin basalt. For this part of British Columbia, in addition to the Chilcotin basalt, there are several somewhat older, xenolith-rich volcanic exposures from north of Prince George (Peslier et al., 2002).

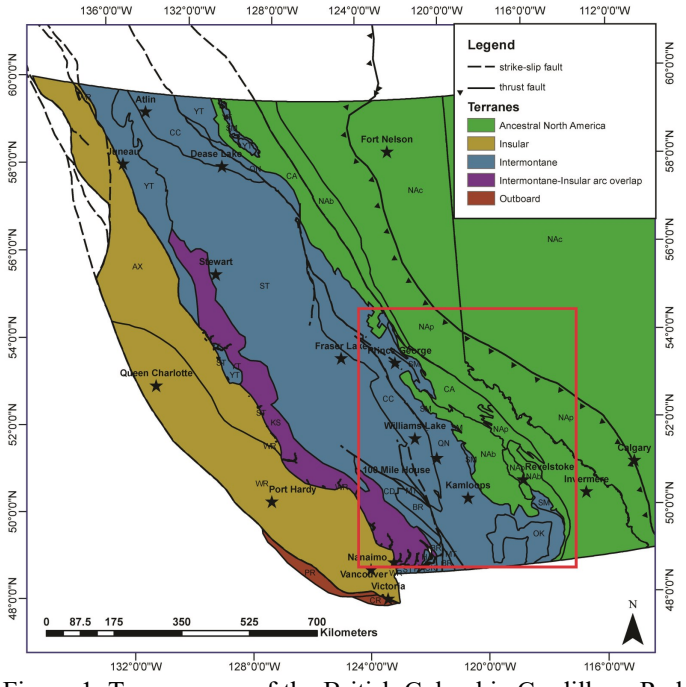

Figure 1. Terrane map of the British Columbia Cordillera. Red box indicates the region of interest for this study (see Figure 2). Modified after on Colpron and Nelson (2011).

Sampling localities from known xenolith-bearing volcanic units within the Quesnel terrane of south-central British Columbia (locations are highlighted in Figure 2) were selected based on: i) diversity of recorded xenolith types, especially with regard to less common crustal xenolith populations; ii) tectonic setting, with emphasis on collecting from a variety of

Corresponding author: Ryan Kroner (rkroner@eoas.ubc.ca)

Kroner, R.K, Chapman, J.B., and Russell, J.K., 2018. Using basalt-hosted xenoliths as probes of the composition, structure and rheology of the sub-Cordilleran lithosphere in British Columbia; *in* Targeted Geoscience Initiative: 2017 report of activities, volume 2, (ed.) N. Rogers; Geological Survey of Canada, Open File 8373, p. 93–100. https://doi.org/10.4095/306604

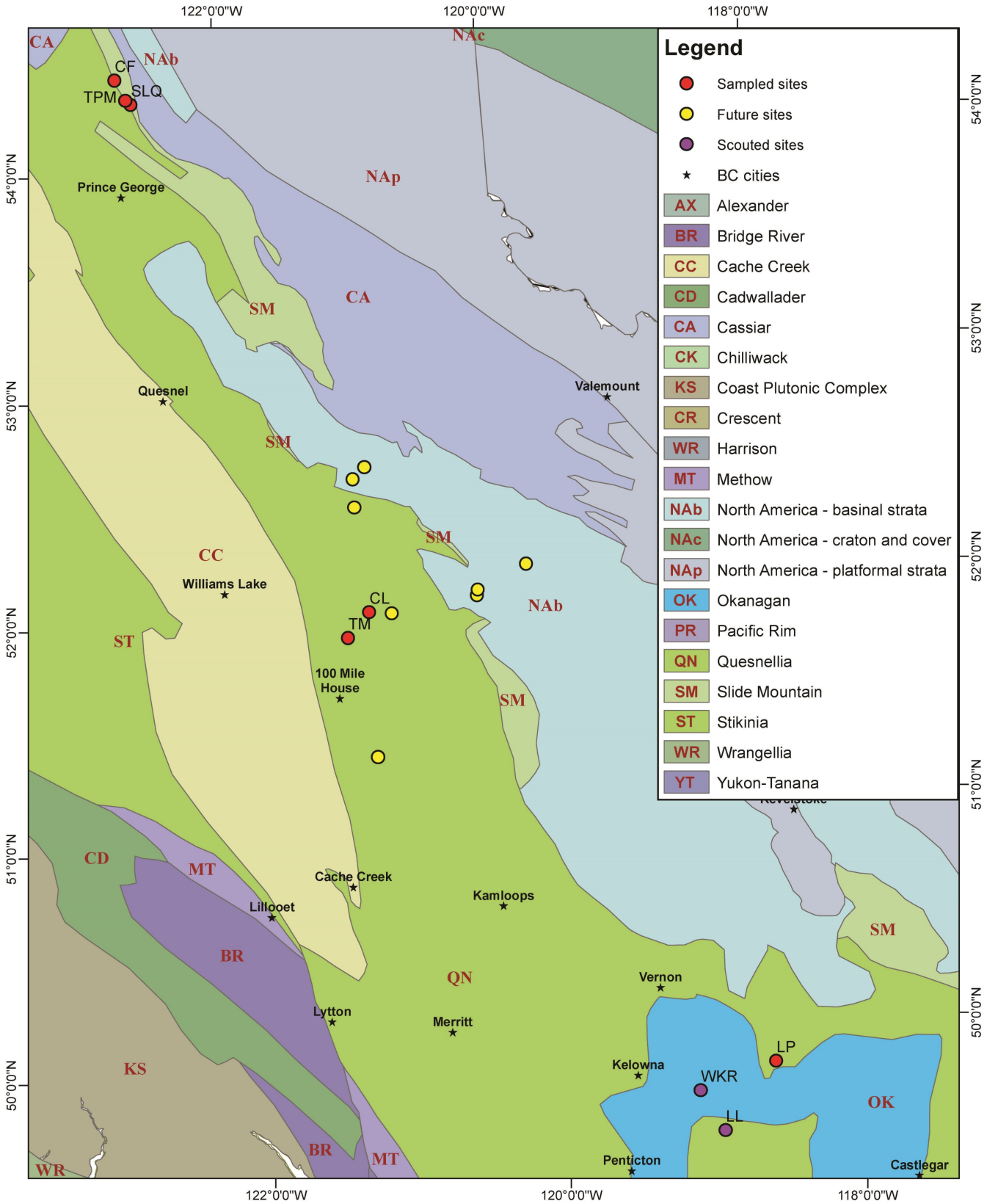

Figure 2. Terrane map of field sites from the south-central British Columbia region of interest. Sampled localities and potential future field areas are highlighted. CF = Coffeepot; SLQ = Summit Lake quarry; TPM = Teapot Mtn.; CL = Coffee Lake; TM = Mt. Timothy; LP = Lightning Peak; WKR = West Kettle River; LL = Lassie Lake. Modified after on Colpron and Nelson (2011) .

tectonic environments; and iii) areas that could be incorporated into future Cordilleran transects.

Summit Lake (54.307 N, 122.639 W)

The Summit Lake sequence, located north of Prince George, British Columbia (Fig. 2), was described in detail by Brearley et al. (1984) and was noted to contain a significant and diverse population of crustal xenoliths in addition to a wide variety of peridotite xenoliths, making it a priority target for sampling. This location consists of an abandoned quarry, with well-exposed columnar basalts up to roughly 25 m in height (Fig. 3a), and a smaller, sporadically active quarry on its southern periphery signposted as Talus Quarry (Fig. 3b). Peridotite xenolith geothermobarometry indicates that this sequence contains materials derived from deeper and hotter portions of the lithosphere than similar localities (Brearley et al., 1984). At ca. 26 Ma, it is also the oldest of the known xenolith-bearing outcrop of the Chilcotin basalt in south-central British Columbia by a significant margin (Bevier, 1983; Peslier et al., 2002). Additionally, it falls in a unique tectonic setting, right on the boundary between the Quesnel and North American basement terranes (Bevier, 1983; Colpron and Nelson, 2011; Peslier et al., 2002).

In total a 117 samples were collected from the Summit Lake sequence. This basalt, which contains 5 to 20% xenoliths by volume, yielded the greatest diversity of rock types of those sampled, four examples of which are pictured in Figure 4. Corroborating the descriptions given in Brearley et al. (1984), peridotites are the dominant xenolith type, including, in descending order of abundance, lherzolite, wehrlite, olivine websterite, websterite, dunite, and (rare) harzburgite. Black, augite-dominant pyroxenite is common, as are megacrystic augite inclusions. Megacrystic olivine and enstastite are also present, but less common. Xenoliths are largely subangular, and range in diameter from 1 cm to a maximum of about 15 cm with the majority from 1 to 5 cm.

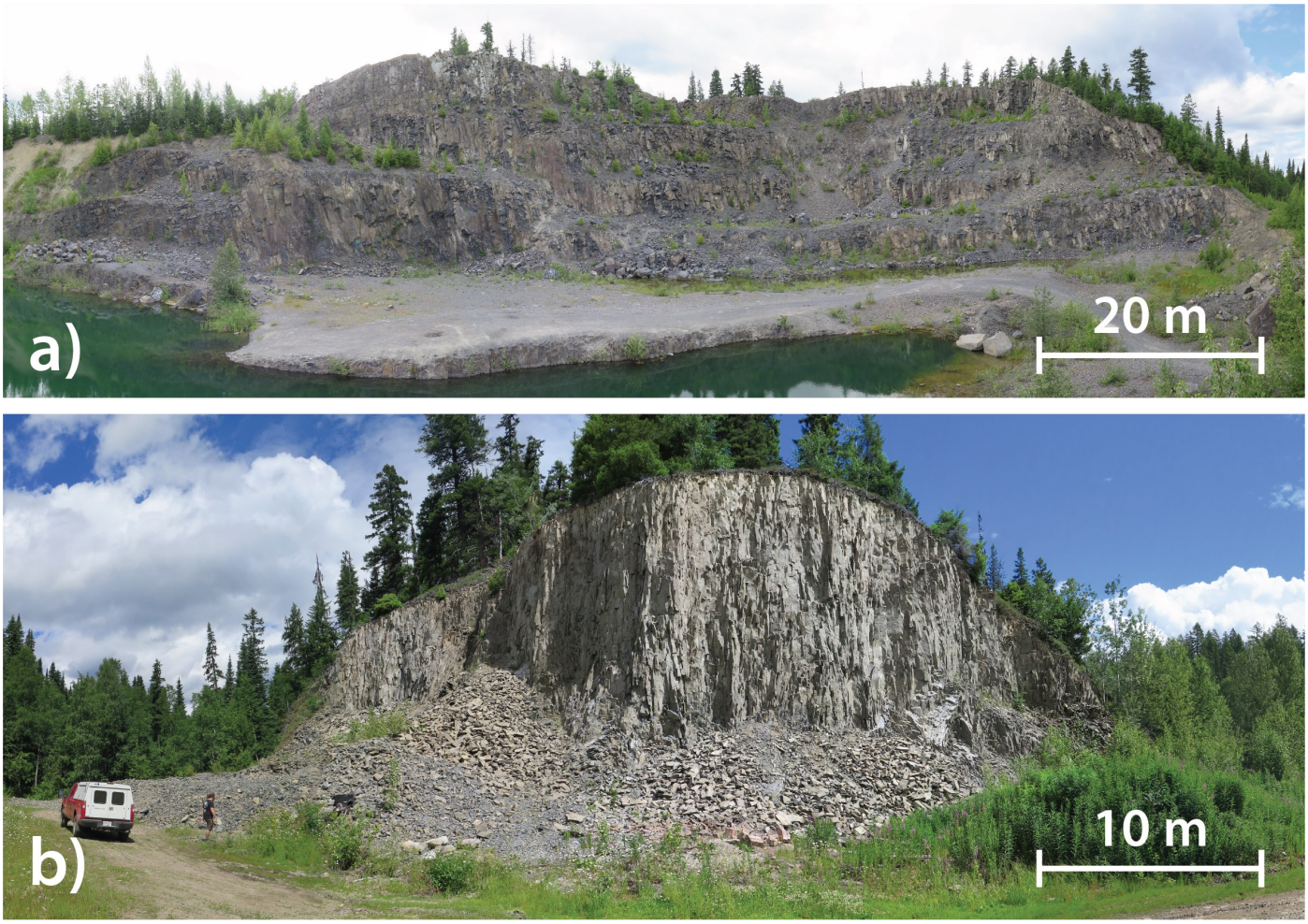

Figure 3. Neogene basalt flow outcrops in the Summit Lake area, central British Columbia. These two views are of quarry exposures within the same lobate edifice. Xenolith abundances and type proportions differ within different flows. a) Multiple flows and radial columnar jointing within the Summit Lake railroad ballast quarry; b) A single 10 to 15 m thick flow with vertical columnar jointing within the Tallus roadstone quarry.

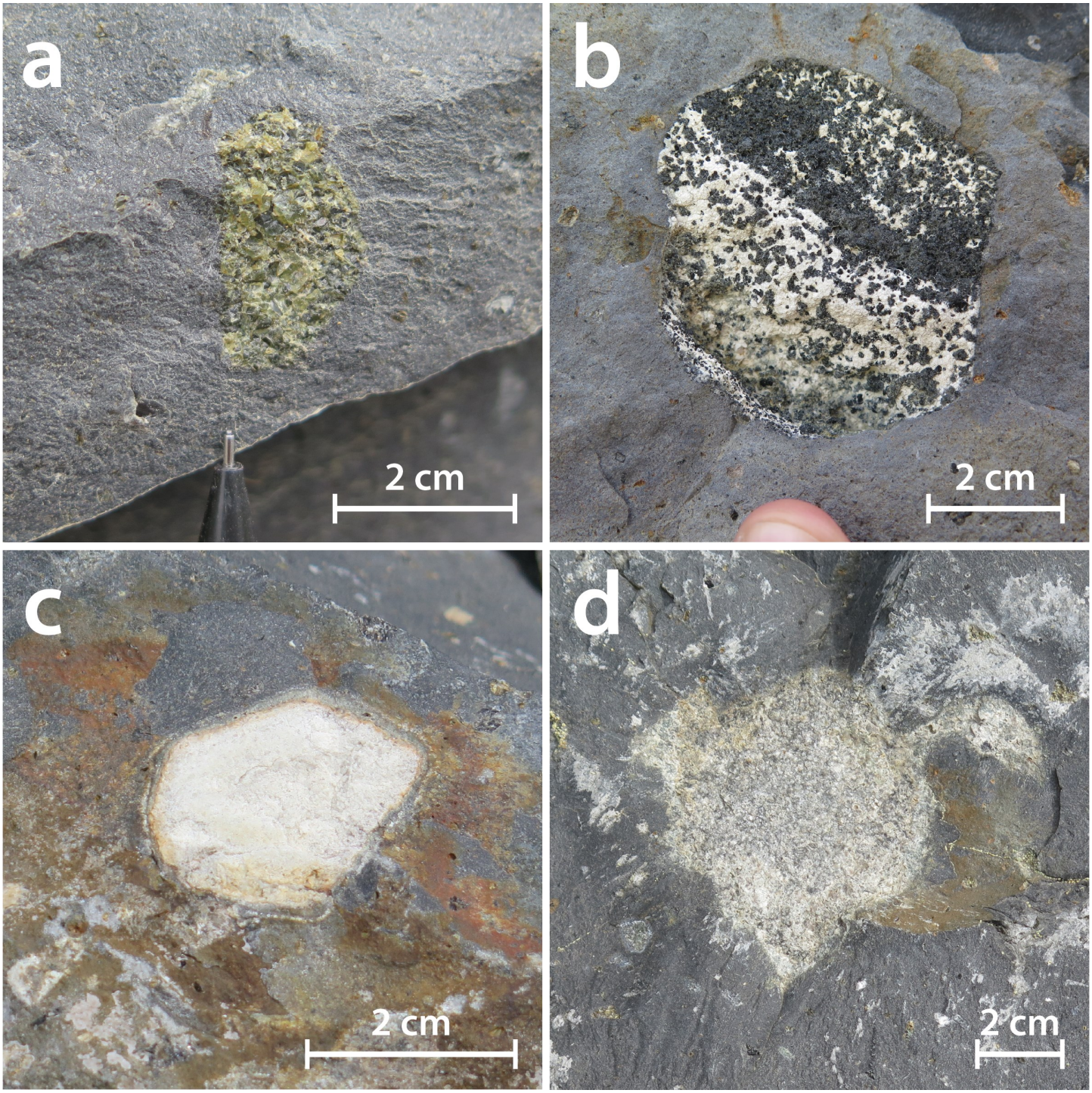

Figure 4. Representative images of xenoliths recovered from the Summit Lake quarry, describing full crustal thickness from mantle upward. Future thermobarometric analysis will be used to fingerprint the true depth of origin for these xenolith populations. a) Fresh, green, rounded to subrounded olivine-rich peridotite xenolith of presumed mantle origin; b) Layered gabbro xenolith, presumed lower crustal in origin, with characteristic subangular shape and sharp margins to host basalt; c) Strongly metamorphosed, sugary quartzite (presumed mid- to upper-crust) with distinct, 2 to 5 mm reaction rim between the xenolith and host basalt; d) Strongly metasomatized and partially digested leucogneiss (foliated granitoid?) xenolith, with lobate margins, presumed mid-crustal in origin .

The Summit Lake unit contains a significant population and wide variety of crustal xenoliths, comprising roughly 20% of the observed xenolith population. The primary crustal rock types sampled consisted of gabbro, quartzite and granitoid. The gabbroic xenoliths were a particular focus during sampling due to their frequently pronounced mineral fabrics, relative freshness, and mineralogical suitability to geothermometry and geobarometry (Ducea and Saleeby, 1996; McCarthy and Patiña Douce, 1998).

An additional eight samples were collected from the nearby Teapot Mountain, 3.5 km northwest of Summit Lake (Fig. 2). The host basalt here is similar to that of Summit Lake, albeit with a lower xenolith abundance, and occurs as a volcanic neck rising a few hundred meters from the surrounding landscape.

Three further samples were collected from another volcanic neck, called Coffeepot Mountain (Fig. 2), located approximately 11 km north of Teapot, and 10 samples from a series of unlabelled basalt bluffs 5 km south of Coffeepot (Fig. 2). Both displayed moderately developed columnar jointing. Coffeepot contained <1% by volume heavily altered crustal and peridotite xenoliths. The unlabelled basalt bluffs were similar in appearance, but with a slightly higher xenolith abundance (approximately 2% by volume).

Lightning Peak (49.879 N, 118.532 W)

The Lightning Peak xenolith-bearing unit, in the Okanagan region, occurs much further south than other Cordilleran xenolith localities. Pre-existing data on the xenolith population is scarce, described only briefly by Brearley and Scarfe (1984) in a paper that focuses entirely on a single amphibole-bearing lherzolite sample.

Lightning Peak is a small high point directly straddling the northwestern boundary of Granby Provincial Park, with a large talus slope with abundant fresh rocks on its northwest face. It consists of two basalt units, both of which form individual peaks. Thirty-five samples were taken from these units.

The first unit is a very coarse-grained, likely hypabyssal basalt with between 15 and 45% xenoliths by volume. The xenolith population (examples of which are pictured in Figure 5) is comprised of >95% ultramafic material. Some unusually large xenoliths (up to 30 cm in diameter) occur at this locality. As is the case with most xenolith-bearing suites, lherzolite is the most common rock type, with subordinate harzburgite, wehrlite, dunite, websterite, olivine websterite, orthopyroxenite, and clinopyroxenite. Peridotite xenoliths are typically less altered and coarser-grained than those at Summit Lake. An additional minor population of crustal xenoliths is also present, consisting mostly of quartzite and granitoid. Large (<3 cm) amphibole xenocrysts are also present, in addition to rare clots of megacrystic olivine and enstatite.

The second unit is a fine-grained columnar basalt with <5% xenoliths by volume, most of which are <3 cm white to grey crustal xenoliths. Well-preserved flow banding is occasionally present, with small plagioclase phenocrysts oriented with the banding.

Brief visits were also made to two other xenolith-bearing localities in the Okanagan region. The first of these, West Kettle River (Fig. 2), was described by Fujii and Scarfe (1982) and contains well-exposed, spectacularly preserved basalt columns with a significant population of peridotite xenoliths along with occasional crustal xenoliths. The second locality, adjacent to Lassie Lake, was reported by Ross (1983). This was significantly less xenolith-rich, and what material was present was far smaller and more weathered than at Kettle River or Lightning Peak.

Mt. Timothy (51.904 N, 121.265 W)

Similar to Lightning Peak, the Mt. Timothy sampling localities (Fig. 2), while having been reported to contain a rich xenolith suite, have not previously been subject to any significant published study or characterization (Schiarizza and Macauley, 2007; Schiarizza et al., 2008). A total of 34 samples were collected from the Mt. Timothy area, which consists of a series of xenolith-bearing volcanic units occurring as talus slopes, pyroclastic outcrops, lava flows, and scoria cones.

Mt. Timothy is primarily composed of Eocene-aged Kamloops group basaltic andesite (Schiarizza et al., 2013), with scattered outcrops of significantly younger (465 ± 12.6 ka) xenolith-bearing volcanics (unpublished K-Ar dates, 2008). The key outcrops for xenoliths are a southwest-facing talus slope and a pyroclastic unit on the mountain's south slope near its summit. South of the mountain, a large lava flow unit to the north of Lake Timothy is particularly rich in xenoliths (Fig. 2). This lava unit and the talus slope unit were similar in composition: both medium- to fine-grained dark basalt containing significant xenolith populations, >90% of which are peridotite. Peridotite xenoliths are mostly lherzolite with subordinant harzburgite, wehrlite, dunite, websterite, olivine websterite, orthopyroxenite, and clinopyroxenite. Non-mafic xenoliths are primarily granitoid and fine-grained quartzite.

The pyroclastic outcrop on Mt. Timothy's south slope was the only one of its type observed in this study. It contains sparse, yet striking and very well preserved, peridotite xenoliths that likely were emplaced as volcanic ejecta. These were, on average, coarser grained and much more fragile than samples from the other two field regions, and ranged from 2 to 6 cm in diameter.

A final volcanic unit surrounding Coffee Lake was visited, approximately 17 km northeast of Mt. Timothy (Fig. 2). This was a fine grained, medium to light grey basalt whose xenolith population contained a somewhat higher proportion of crustal material (20–30%) than most other localities. The xenoliths are mostly quartzite or granitoid with sparse granulite, and reach up to about 10 cm in diameter.

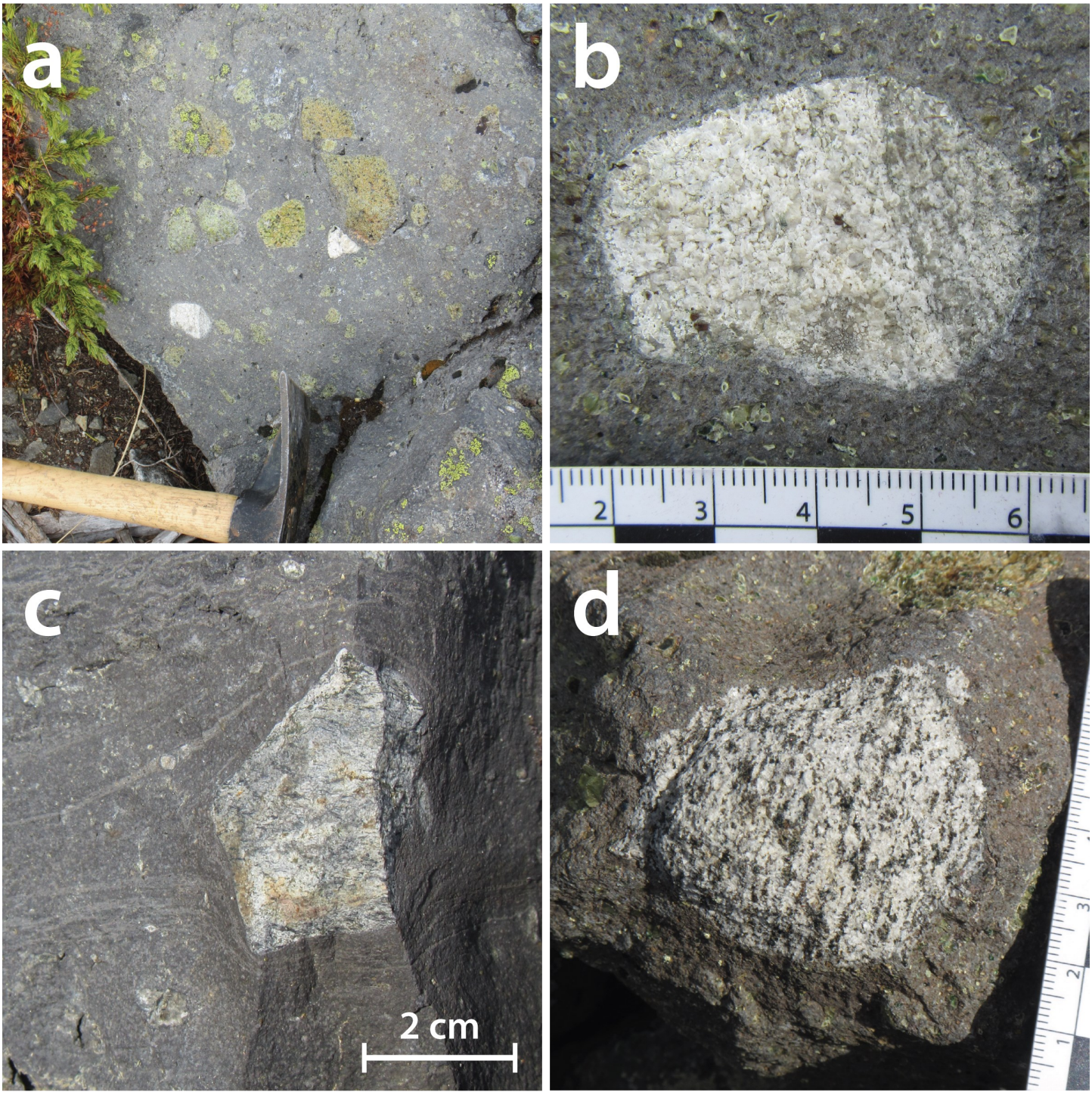

Figure 5. Representative images of xenoliths recovered from the Lightning Peak location, southeastern BC. a) A mixed mantle (green, rounded) and crustal (while to grey, subrounded to subangular) abundant (30–50% by volume) xenolith population hosted in coarse, olivine-phyric basalt; b) Subrounded and metasomatized leucogneiss, seen in lower-left of image (a), within coarse, olivine-phyric basalt; c) Wispy-foliated, medium-grained leucogabbro, subangular, within aphanitic to fine-grained, plag-phyric basalt, magmatic flow lines seen wrapping around xenolith; d) subrounded gneiss (granitoid protolith?) within coarse basalt unit.

Planned methodology

Approximately 200 samples have been collected to date. From these about 60 have been submitted for polished thin sections for analyses by optical petrography, electron microprobe, and laser ablation ICPMS. For samples of peridotite and gabbro, analyses will, when available, focus on orthopyroxene - clinopyroxene pairs. These mineral compositions will be used to calculate temperatures and depths of equilibration for the xenoliths based on available two-pyroxene geothermobarometers (Brey and Kohler, 1990; Greenfield et al., 2013).

Other analyses of xenolith samples will include electron backscatter diffraction analyses for quantification of mineral fabrics and ImageJ analyses of grain size distributions. Bulk geochemical composition will be measured when possible (dictated by sample sizes), and point counting will be used to assign more precise classifications to the different peridotite rock types (Larrea et al., 2014).

Future work

A number of additional areas are targeted for future sample collection (Fig. 2), including a series of xenolith-bearing units within the Wells Gray – Clearwater volcanic field (Canil and Scarfe, 1989) and a locality near Rayfield River (Canil et al., 1987). Also targeted for investigation are a series of xenolith-bearing flows and cones in the area around Quesnel Lake and Horsefly Lake (Friedman et al., 2016). These localities are noted as containing a diverse collection of both crustal and mantle xenoliths, and are married to a unique tectonic setting, lying well within North American cratonic basement rather than the accreted intermontane terranes with which most other such volcanic sequences are associated (Friedman et al., 2016). Originally, these series of outcrops were planned to be amongst the first sampled, however wildfires in the area required revision of these plans.

References

Bevier, M.L., 1983. Regional stratigraphy and age of Chilcotin Group basalts, south-central British Columbia; Canadian Journal of Earth Sciences, v. 20, p. 515–524.

Brearley, M. and Scarfe, C.M., 1984. Amphibole in a spinel lherzolite xenolith: Evidence for volatiles and partial melting in the upper mantle beneath southern British Columbia; Canadian Journal of Earth Sciences, v. 21, p. 1067–1072.

Brearley, M., Scarfe, C.M., and Fujii, T., 1984. The petrology of ultramafic xenoliths from Summit Lake, near Prince George, British Columbia; Contributions to Mineralogy and Petrology, v. 88, p. 53–63.

Brey, G.P. and Kohler, T., 1990. Geothermobarometry in four-phase lherzolites II: New thermobarometers, and practical assessment of existing thermobarometers; Journal of Petrology, v. 31, p. 1353–1378.

Canil, D. and Scarfe, C.M., 1989. Origin of phlogopite in mantle xenoliths from Kostal Lake, Wells Gray Park, British Columbia; Journal of Petrology, v. 30, p. 1159–1179

Canil, D., Brearley, M., and Scarfe, C.M., 1987. Petrology of ultramafic xenoliths from Rayfield River, south-central British Columbia; Canadian Journal of Earth Sciences, v. 24, p. 1679–1687.

Colpron, M. and Nelson, J.L., 2011. A digital atlas of terranes for the Northern Cordillera; Yukon Geological Survey, < http://www.geology.gov.yk.ca/pdf/terranes_readme.pdf > [accessed March 6, 2017].

Ducea, M.N. and Saleeby, J.B., 1996. Bouyancy sources for a large, unrooted mountain range, the Sierra Nevada, California: Evidence from xenolith thermobarometry; Journal of Geophysical Research, v. 101, p. 8229–8244.

Friedman, E., Polat, A., Thorkelson, D.J., and Frie, R., 2016. Lithospheric mantle xenoliths sampled by melts from upwelling asthenosphere: The Quaternary Tasse alkaline basalts of southeastern British Columbia, Canada; Gondwana Research, v. 33, p. 209–230.

Fujii, T. and Scarfe, C.M., 1982. Petrology of ultramafic nodules from West Kettle River, near Kelowna, southern British Columbia; Contributions to Mineralogy and Petrology, v. 80, p. 297–306.

Ghent, E.D., Edwards, B.R., Russell, J.K., and Mortensen, J., 2008. Granulite facies xenoliths from Prindle volcano, Alaska: Implications for the northern Cordilleran crustal lithosphere; Lithos, v. 101, p. 344–358.

Greenfield, A.M.R., Ghent, E.D., and Russell, J.K., 2013. Geothermobarometry of spinel peridotites from southern British Columbia: Implications for the thermal conditions in the upper mantle; Canadian Journal of Earth Sciences, v. 50, p. 1019–1032.

Larrea, M.L., Castro, S.M., and Bjerg, E.A., 2014. A software solution for point counting: petrographic thin section analysis as a case study; Arabian Journal of Geosciences, v. 7, p. 2981–2989.

Littlejohn, A.L. and Greenwood, H.J., 1974. Lherzolite nodules in basalts from British Columbia, Canada; Canadian Journal of Earth Sciences, v. 11, p. 1288–1308.

McCarthy, T.C. and Patiña Douce, A.E., 1998. Empirical calibration of the silica–Ca-tschermak's–anorthite (SCAn) geobarometer; Journal of Metamorphic Geology, v. 16, p. 675–686.

Peslier, A.H., Francis, D., and Ludden, J., 2002. The lithospheric mantle beneath continental margins: Melting and melt-rock reaction in Canadian Cordilleran xenoliths; Journal of Petrology, v. 43, p. 2013–2047.

Ross, J.V., 1983. The nature and rheology of the Cordilleran upper mantle of British Columbia: Inferences from peridotite xenoliths; Tectonophysics, v. 100, p. 321–357.

Schiarizza, P. and Macauley, J., 2007. Geology of the Hendrix Lake area (NTS 93A/02). BC Geological Survey, Open File 2007-3, scale 1:50 000.

Schiarizza, P., Bligh, J., and Tait, D., 2008. Geology of the Timothy Lake area (NTS 92P/14). BC Geological Survey, Open File 2008-5, scale 1:50 000.

Mineral markers of base metal mineralization: Progress report on the identification of indicator minerals in the fine heavy mineral fraction

H.D. Lougheed[1], M.B. McClenaghan[2] and D. Layton-Matthews[1]

[1]*Department of Geological Sciences and Engineering, Queen's University, Kingston, Ontario K7L 3N6*
[2]*Geological Survey of Canada, 601 Booth Street, Ottawa, Ontario K1A 0E8*

Abstract

Indicator minerals from heavy mineral concentrates have long been used in exploration for diamonds and gold, and more recently porphyry copper and volcanic massive sulphide deposits. This study is investigating the application of rapid automated mineralogy to identify and characterize indicator minerals in till and stream sediment samples. The fine (<0.250 mm) heavy mineral fraction is well suited to automated mineralogy as a large number of mineral grains can be analyzed from an individual sample. These small grains are difficult to visually recognize using traditional microscopic methods.

The initial phase of this study has assessed methods to process and analyze the <0.250 mm heavy mineral concentrate using archived samples from three test sites. Investigations focused on identifying key areas of loss and contamination during processing and workflow, and establishing mitigating protocols. Concentrates were split into four size fractions to better represent the large number of grains in a sample. Single-use sieves were developed to reduce potential for cross-contamination. Fractions were mounted into an epoxy plug, which were quartered and remounted to capture both basal and cross-sectional planes to compensate for any density settling, prior to rapid automated scanning by mineral liberation analysis.

Introduction

Indicator mineral methods are important exploration tools in glaciated terrain for diamonds (e.g. McClenaghan and Kjarsgaard, 2007) and gold (e.g. Averill and Zimmerman, 1986; Averill, 2001, 2013; McClenaghan and Cabri, 2011). More recently, their potential to aid porphyry copper (e.g. Kelley et al., 2011; Plouffe et al., 2016) and volcanic massive sulphide (VMS) exploration (e.g. McClenaghan et al., 2015a) has been demonstrated. The objective of this research activity is to further develop indicator mineral utility by examining the underutilized < 0.250 mm diameter grain portion of heavy mineral concentrates.

Large till or stream sediment samples (10–20 kg) are necessary to obtain detectable and meaningful numbers of indicator mineral grains in a single sample. Indicator minerals are recovered by a combination of sizing and density concentration methods to reduce the volume of material, prior to visual microscopy (McClenaghan, 2011). These methods focus on the recovery of the coarser (>0.250 mm, medium sand or larger) mineral fraction as they are relatively easy to recover and visually examine. Developments in rapid scanning electron microscope (SEM) scanning techniques, such as Mineral Liberation Analysis (MLA), in the past 10 years make it feasible to examine smaller (<0.025 mm) grains using automated technologies (e.g. Lehtonen et al., 2015). Mineral Liberation Analysis has the potential to characterize chemical variations that traditional visual examination of the coarser fraction may miss.

MLA-automated mineralogy uses high-resolution Backscatter Electron (BSE) images, image analysis, and elemental chemistry from Energy Dispersive X-ray Spectroscopy (EDS) to create a mosaic image of an epoxy grain mount. The MLA software collects a full X-ray spectrum (EDS) at the centre of each particle and compares it with an EDS mineral library to identify the mineral and create a false-colour mineral image, determine grain size, mineral associations (occurrence and interlocking), particle properties (roundness, area, shape), and mineral liberation (Layton-Matthews et al., 2017).

The challenges associated with using rapid automated methods are: the analyses are expensive to obtain, samples are costly to process and mount, ideal sample size has not been resolved (i.e. 1, 5 or 10 kg?), nor what grain size range or numbers of grains required to represent a single sample, and they rely on a well-developed EDS spectral library. Also, mineral grains are extremely small and thus the potential for sample loss and contamination is significantly greater than for coarser mineral fractions.

Till or stream sediment samples from several deposits types are being examined to develop protocols for sample processing, splitting, grain mounting and automated SEM analysis, as well as to determine indicator mineral suites present in this

Corresponding author: Don Lougheed (5hdl@queensu.ca)

Lougheed, H.D., McClenaghan, M.B., and Layton-Matthews, D., 2018. Mineral markers of base metal mineralization: Progress report on the identification of indicator minerals in the fine heavy mineral fraction; *in* Targeted Geoscience Initiative: 2017 report of activities, volume 2, (ed.) N. Rogers; Geological Survey of Canada, Open File 8373, p. 101–108. https://doi.org/10.4095/306605

smaller size fraction. Samples were selected for their well-characterized bedrock source, known glacial dispersal history and range of high to low metal contents. The initial phase of this study focused on identifying key areas of risk for contamination and loss in the sample processing and preparation workflow, and developing protocols to mitigate each.

Methods

Three test sites in glaciated terrain were chosen for the initial stage of this study:

- Izok Lake Cu-Zn-Pb-Ag VMS deposit, an amphibolite grade deposit in the Slave geological province, Nunavut (McClenaghan et al., 2015b);
- Sisson W-Mo deposit, a porphyry-style hydrothermal deposit hosted in Late Devonian granite intrusions in central New Brunswick (McClenaghan et al., 2017); and
- Triple B kimberlite in the Jurassic Lake Timiskaming field of northeastern Ontario (McClenaghan et al., 2004).

Samples were selected from each test site at varying distances up ice, overlying, and down ice of each deposit. The archived <0.250 mm heavy mineral concentrates (HMC) of each sample, previously prepared by tabling and heavy liquid separation, were used in this study. Once the methods and protocols are developed they will be applied to stream sediment samples recently collected from the unglaciated area around the Casino porphyry Cu-Mo-Au-Ag deposit, Yukon (McClenaghan et al., 2018).

The HMC of four till samples from the Izok Lake VMS deposit were tested first. Prior to the current study, each HMC sample was sieved into four size fractions (<0.250 mm; 0.25–0.5 mm; 0.5–1.0 mm; 1.0–2.0 mm) and the three coarsest fractions visually examined under a binocular microscope to identify and count the VMS indicator minerals present. The methods used to process the samples and the mineral grain count data are reported in McClenaghan et al. (2012) and Hicken et al. (2013). The <0.250 mm table pre-concentrate of each till sample was panned to document the number of gold and sulphide grains and the panned grains were then returned and the sample further processed using heavy liquids. A more detailed examination of the <0.250 mm fraction was not completed because of the prohibitive time and cost that would have been required. The mass of the original samples processed using tabling and heavy liquids and the mass of the resultant <0.250 mm fraction is reported in Table 1. For the Izok Lake till samples, the <0.250 mm fraction weighed between 16.9 and 29.7 g.

In the present study, the <0.250 mm HMC was sieved into four size fractions to characterize and compare the mineralogy and granulometric distribution of each size range (0.185–0.250 mm – 60+70 mesh, fine sand; 0.125–0.185 mm – -70+120 mesh, fine sand; 0.064–0.125 mm – -120+250 mesh, very fine sand; <0.064 mm – -250 mesh, silt+clay). This step was undertaken because: i) the total mass of <0.250 mm material in each sample was too great to be mounted into a mount; ii) the range in grain size was too great to examine in grain mounts without sieving; and iii) sieving the material allows for analysis of granulometric and mineralogical distributions between size fractions. These size ranges were chosen to conform to the Wentworth grain size scale, which typically corresponds with size fractions used in commercial labs.

Table 1. Mass data for: a) original sample processed by using tabling and heavy liquid methods (table feed); b) the four fractions sieved from the original <0.250 mm fraction; c) the entire <0.250 mm non-ferromagnetic <0.250 mm before and after sieving into the four size fractions, the amount of loss from sieving and the number of mounts required to mount all grains.

Sample	Location	< 2.0 mm Table Feed (kg)	Size Fraction (mm)	Mass (g)	Prepared mounts	Total Mass of 4 fractions (g)	Mass <0.25 mm prior to sieving (g)	Loss during sieving (g)	% Loss
09-MPB-060	1 km up-ice of mineralization	9.8	0.185-0.250	2.668	1	16.544	16.637	0.093	0.559
			0.125-0.185	5.145	1				
			0.064-0.125	6.624	1				
			<0.064	2.107	1				
09-MPB-058	0.5 km down-ice of mineralization	12	0.185-0.250	3.426	1	29.124	29.223	0.099	0.339
			0.125-0.185	7.060	1				
			0.064-0.125	12.064	2				
			<0.064	6.574	1				
09-MPB-075	2.5 km down-ice of mineralization	10.3	0.185-0.250	3.132	1	22.848	22.933	0.085	0.371
			0.125-0.185	5.959	1				
			0.064-0.125	9.584	2				
			<0.064	4.173	1				
12-MPB-902	8.0 km down-ice of mineralization	9.8	0.185-0.250	2.949	1	22.679	22.769	0.090	0.395
			0.125-0.185	4.814	1				
			0.064-0.125	9.716	2				
			<0.064	5.200	1				

Sieving

Commercial stainless-steel sieves were deemed to be significant risks for both contamination and sample loss. Cleaning of steel sieves between samples is time consuming and the risk of cross-contamination from inadequate sieve cleaning increases as grain size decreases and is unacceptable in a study such as this. The surface area of commercial sieves is much larger than that needed for the relatively small masses (<50 g) of sample being sieved. As a result, one-time use sieves were constructed for each of the four size fractions for each till sample using 2" diameter ABS tubing and nylon mesh (Fig. 1).

During the sieving procedure two factors that influenced sample loss were identified. The first of these are surface effects, including surface adherence inside containers or sieves because of static charge and material trapped on imperfect/rough surfaces. The other factor is aerosolization of fine material. Static charge was mitigated with the use of a static-removal gun. The tool bombards a surface with positive and negative ions, dispersing excess charge. The use of a static-removal gun prior to, and after, material transfer from storage pouches and sieves reduced the amount of material left on a surface.

Sieving tests were performed using the GSC in-house till standard Almonte Till (Plouffe et al., 2013). Test runs were performed to compare recovery between commercial stainless-steel sieves and prototypes of the disposable ABS sieves. Results indicated that there was 52% less loss of sample material when using the disposable sieves as compared to stainless steel sieves. The average loss using stainless steel sieves was 0.64% of original sample mass and the average loss using ABS sieves was 0.31% of original sample mass. Comparable sample loss was recorded during actual sample processing (see Table 1).

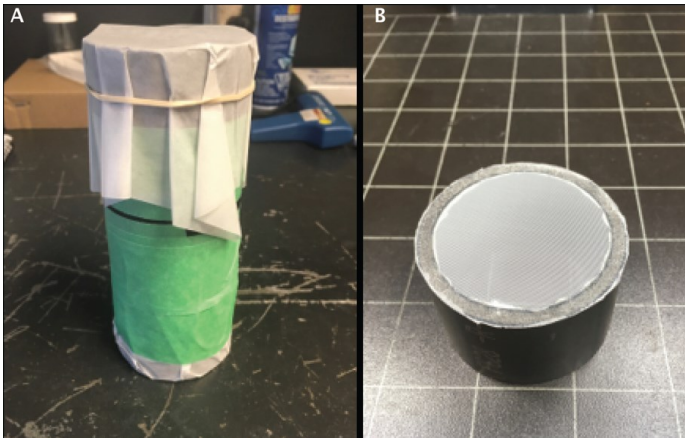

Figure 1. a) An assembled sieve tower, joined with painter's tape and capped at both ends with coated weigh paper. b) A single disposable ABS sieve section, displaying the super-glue bead attaching the nylon mesh to the ABS tube.

Grain mounting

To analyze each of the four size fractions using MLA, the grains were mounted in epoxy and the mounts polished. Given the potential for ppb concentrations of indicator minerals to be significant, it is important to know whether the exposed mineral grain surfaces analyzed by MLA are representative of the entire size fraction and total sample. Blaskovich (2013) described a mounting process using cut epoxy plugs, mounted to present a cross-sectional surface, and this project expands on that method. Each epoxy mount was cut into quarters, and arranged into a second mount as shown in Figure 2, so that it contained one top surface parallel quarter of the original mount and two vertical cross-sections. The fourth quarter was archived. This second mount was back-filled with epoxy, polished, carbon coated, and scanned. Vertical cross sections are presented in order to account for any differential settling that occurs within the epoxy due to density differences among grains. Lighter grains will have a lower settling velocity, and thus a density gradient may be present within the mount leading to different populations of grains represented on the vertical and basal layers. Quarters were used as cross-sectional sur-

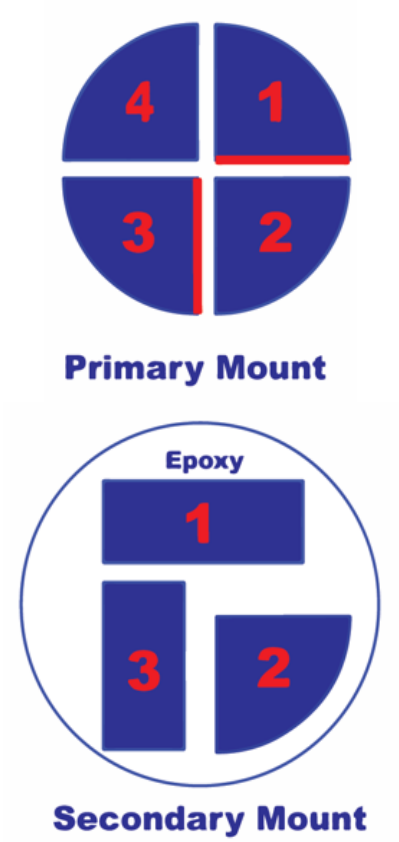

Figure 2. Schematic plan views showing the quartering of a primary epoxy mount, and the subsequent arrangement of quarters in the secondary mount. Red surfaces on the primary mount quarters represent the surface intersecting the polished face of the secondary mount.

faces so that two faces through the sample, oriented 90° to one another, would be analyzed. If too much HMC was contained in a primary mount, the quartered sections would not fit into a secondary mount. Testing using the Almonte Till material revealed that the maximum mass of HMC that can be incorporated into the primary mount is approximately 7 g. Sieved aliquots that were >7 g were split via cone-and-quartering and mounted as two separate mounts which were then cut and remounted to produce two secondary mounts. The masses of each size fraction from all Izok Lake till samples, and the number of mounts produced for each fraction, are listed in Table 1.

Discussion: Indicator mineral identification by mineral liberation analysis

To identify minerals using MLA, the spectral data provided by the EDS scan are compared to an existing library of known mineral spectra. This library is compiled by the user, and spectra can be pulled from standard reference libraries, libraries compiled by previous users, and manually inserted into the program via targeted spot analysis using an SEM. Thus, a comprehensive mineral reference library is a key component to the success of such a study.

Table 2 lists selected minerals identified in the basal quarter of each mount for each of the four size fractions of the Izok Lake till samples, measured in numbers of grains. Also listed in the table are normalized (10 kg of table feed) visual indicator mineral grain counts performed by Overburden Drilling Management (ODM) on the 0.25 to 0.5 mm heavy mineral fraction of each sample (from Hicken et al., 2013). Axinite abundance was not reported for the 0.25 to 0.5 mm fraction by ODM because axinite grains are difficult to visually identify in till HMC (Hicken, 2012) due to their optical similarity to grey pyroxene and pale almandine, both common minerals in Izok Lake area till. Ore minerals identified in this study include galena, sphalerite and chalcopyrite, along with VMS alteration associated minerals such as gahnite, staurolite and axinite.

Sulphide minerals are softer than silicate indicator minerals and thus liable to physical abrasion during glacial transport and reduction of grain size over relatively short transport distances. Sulphide minerals are also susceptible to chemical weathering in oxidizing environments. The typical reduced grain size following glacial comminution increases the relative surface area available for oxidation, leading to poor preservation in till deposited down-ice of deposits. Sulphide indicator minerals were most abundant in the coarsest size fraction studied (0.185–0.250 mm), found in highest abundance in sample 09-MPB-058 (0.5 km down ice of mineralization), and in decreasing abundance in the 0.185 to 0.250 mm size fraction of samples 09-MPB-075 and 12-MPB-902 (2.5 and 8 km down-ice of mineralization, respectively).

Indicator minerals such as gahnite (H=8), staurolite (H=7–7.5), and axinite (H=6–7.5) are more chemically and physically robust than sulphide minerals, and thus better equipped to survive glacial erosion, transport and deposition at greater distances down-ice than sulphide minerals. Gahnite abundance is highest in till sample 09-MPB-058, 500 m down-ice of the de-

Table 2. Number of grains of common ore and alteration indicator minerals within each size fraction of till samples studied. Includes the total number of grains present on each scanned surface, and grain count data from the 0.250 to 0.500 mm size fraction reported by McClenaghan et al. (2012).

Sample	Location relative to mineralization	Size fraction (mm)	Chalcopyrite	Galena	Pyrite	Sphalerite	Staurolite	Axinite	Gahnite	Total Grains
09-MPB-060	1 km up ice	0.185-0.250	0	1	0	0	165	4	0	12963
		0.125-0.185	0	0	0	0	285	2	2	24831
		0.064-0.125	0	0	0	0	416	18	1	32673
		<0.064	1	0	0	0	677	26	5	48399
		0.25-0.5 *	0	0	0	0	3061	ND	0	ND
09-MPB-058	0.5 km down ice	0.185-0.250	4	4	22	81	128	4	24	10060
		0.125-0.185	1	12	6	23	237	7	15	24097
		0.064-0.125	5	2	1	45	476	13	15	34078
		<0.064	3	0	1	24	688	16	50	41983
		0.25-0.5 *	9	0	339	1271	2542	ND	77	ND
09-MPB-075	2.5 km down ice	0.185-0.250	1	6	3	0	123	17	19	19230
		0.125-0.185	0	0	0	0	117	11	17	19397
		0.064-0.125B	0	3	0	0	278	23	35	32482
		<0.064	2	0	0	0	433	72	54	47786
		0.25-0.5 *	0	0	0	0	971	ND	64	ND
12-MPB-902	8 km down ice	0.185-0.250	2	5	2	0	109	16	7	20791
		0.125-0.185	1	0	0	2	149	23	23	25251
		0.064-0.125	2	1	0	0	274	25	21	37375
		<0.064	1	0	0	1	239	7	26	30427
		0.25-0.5 *	0	0	0	0	1634	ND	24	ND

* data from Hicken, 2012
ND= not determined

posit. The highest abundance of gahnite in every sample is found in the finest fraction (<0.064 mm). In the samples down-ice of the deposit, gahnite abundance decreases in the coarsest and finest fractions, while increasing slightly in the 0.125 to 0.185 and 0.064 to 0.125 mm fractions. The presence of gahnite was documented in the 0.25 to 0.5 mm heavy mineral fraction of till at Izok Lake (McClenaghan et al., 2012); 77 grains in sample 09-MPB-058, 0.5 km down-ice of mineralization, decreasing to 24 grains in sample 12-MPB-902 (8.0 km down-ice of mineralization) (see Table 2).

Axinite is a boron-bearing calc-silicate commonly found in hydrothermally altered calcareous sedimentary and mafic igneous rocks that have been calcite altered prior to metamorphism (Deer et al., 1992). Axinite was previously identified in bedrock from the Izok Lake deposit by Hicken et al. (2013), but not in any till samples. However, in this study axinite was identified in all till samples. Axinite was most abundant in the finest fraction (<0.064 mm) for 09-MPB-060, 09-MPB-058 and 09-MPB-075, whereas in the most distal sample (12-MPB-902, 8 km down-ice of the deposit) axinite is most abundant in the coarsest size fraction (0.185–0.250 mm).

Staurolite abundance is greatest in till samples 09-MPB-060 and 09-MPB-058, which are the most proximal up- and down-ice sites to mineralization, respectively. Generally, values decrease westward in till samples that are down-ice of the deposit. The most significant decrease in abundance is found in the finest fraction (<0.064 mm), with the finest fraction at 12-MPB-902 containing approximately 30% as many grains as sites 09-MPB-060 and 09-MPB-058. Staurolite was noted in the 0.25 to 0.5 mm heavy mineral fraction of tills at Izok Lake (McClenaghan et al., 2012, 2015b). The abundance in the 0.25 to 0.5 mm heavy mineral fraction decreased from 3061 grains at site 09-MPB-060 to 971 grains at site 09-MPB-075, before increasing to 1634 grains at site 12-MPB-902. Staurolite is a common alteration mineral in metamorphic terranes, and is likely to be present as background in highly metamorphosed country rocks in the Izok Lake region (Hicken et al., 2013). This widespread occurrence in local bedrock may be the source of the relatively consistent abundance in most size fractions observed in this study, but the increase in the finest fraction in the immediate vicinity of the deposit may indicate that the mineralization-associated staurolite is finer grained.

Celsian ($BaAl_2Si_2O_8$) is a barium-rich feldspar commonly associated with exhalative hydrothermal zones and low- and medium-grade metamorphic rocks (Moro et al., 2001) and was identified in the four size fractions of till in this study. It is present as an alteration mineral associated with oxide grains (ilmenite, rutile, titanite and hematite). Figure 3 displays celsian in X-ray maps, and the observed textures in backscatter imaging. The grains appear to be fractured and altered along fractures. Celsian is present in these altered fracture zones, possibly indicating that celsian was introduced by metasomatizing hydrothermal fluids. Because celsian rarely constituted an entire grain, the grain numbers were considered to be an inaccurate way of representing its abundance. Thus, Table 3 reports the occurrence of celsian as area percentage of polished grain surface.

Conclusions

This study represents the first systematic reporting and quantification of sample loss while sieving the <0.250 mm HMC of till samples. The average loss during testing using stainless-steel sieves was 0.64%. Although a small percentage

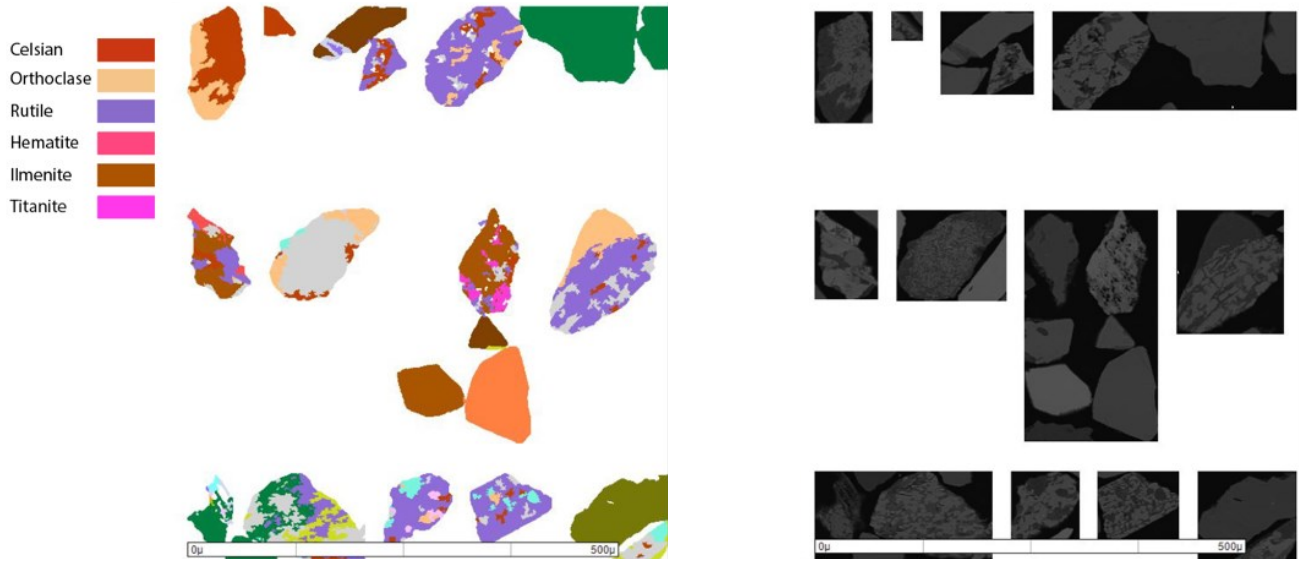

Figure 3. MLA image from the 0.064 to 0.125 mm size fraction of sample 09-MPB-075. The left frame displays X-ray maps of several grains displaying celsian alteration. The right frame displays the same grains as SEM backscatter images, showing their alteration texture.

Table 3. Celsian abundance, as area percentage of mapped grains, for each size fraction of till samples studied.

Sample	09-MPB-060	09-MPB-058	09-MPB-075	12-MPB-902
Size Fraction (mm)	Celsian (Area %)			
0.185-0.250	0.1	0.02	0.07	0.05
0.125-0.185	0.01	0.02	0.03	0.05
0.064-0.125	0.04	0.02	0.04	0.04
<0.064	0.04	0.06	0.08	0.05

of the total processed sample mass, given that 1 mg of <0.250 mm HMC typically contains between 10 000 and 100 000 grains, this represents a significant number of grains. Ensuring the loss is minimized is important, as several potentially important indicator mineral populations consist of so few grains that their presence could be completely missed by a loss of this magnitude. Use of the disposable sieves described above yielded an average sample loss of 0.31%: a significant improvement.

This study also constitutes the first reporting on the utility of disposable sieves when sieving <0.250 mm material. For grains this small, contamination is not always visible, warranting increased vigilance. The <0.250 mm fraction contains 'dust -sized' material, which is susceptible to suspension in air during sieving and handling, with decreasing grain size corresponding to lower settling velocities. Disposable sieves remove the necessity for time-consuming and potentially ineffective sieve cleaning, and with appropriate handling and packaging users can ensure that unused sieves are not exposed to contaminating environments.

Table 2 compares the indicator mineral abundance within each size fraction analyzed during this study with the grain counts produced by ODM from the coarser, visually examined 0.250 to 0.500 mm HMC for the same samples. In every sample where indicator mineral grains have been identified by ODM in the 0.250 to 0.500 mm fraction, MLA analysis of the <0.250 mm identified the same minerals in at least one of the size fractions examined. In sample 09-MPB-060, 8 gahnite grains were detected using MLA, where none had been found by ODM in the >0.25 mm fraction. As sample 09-MPB-060 is located 1 km up-ice of mineralization, the gahnite identified in the <0.250 mm HMC may indicate there is a wider gahnite alteration footprint to the deposit than previously known.

Sulphide grains were found in highest abundance in the coarsest fraction studied. The increasing surface area available for oxidation with decreasing grain size will increase the weathering rate of sulphide grains in progressively finer fractions. This could explain the lack of sulphide grains in the finest fractions studied, as well as the rapid decrease in grain abundance between samples down-ice of mineralization.

MLA analysis of <0.250 mm HMC of till samples detected axinite and celsian in all four size fractions the till samples. These two minerals were not identified in the >0.25mm fraction of the same till samples in previous studies. This discovery demonstrates the effectiveness of rapid-scanning automated mineralogy to routinely identify indicator minerals that do not meet the visual requirements for optical identification in coarser, commonly used fractions.

Figure 4 contains an MLA grain-map for all three remounted surfaces of the <0.064 mm size fraction of sample 12-MPB-902. The mineral reference library has been organized by specific gravity (SG), in descending order, and split into three equal groups (21 minerals in each). Each group was assigned a colour, red corresponding to the heaviest minerals, green to the intermediate ones, and teal to the lightest. The cut-offs are at SG 4.25 (red-green) and 3.24 (green-teal). When the colour ramp is applied to the grain-maps, a density gradient can be observed in the two vertical surfaces. On the remounted basal surface (XBSE), the red grains are evenly distributed throughout the grain-map. This image indicates that there is a density gradient to the settling of minerals within the epoxy mounts during curing, and suggests that the quartering and re-mounting of HMC material is a necessary step in the sample preparation process, mitigating bias towards overrepresentation of heavier minerals towards the bottom of mounts.

The visual identification of alteration rims/textures on individual grains is difficult when examining grains under a binocular microscope, but MLA is well suited to this task. The identification of celsian alteration is an example. The capabilities of MLA enable it to quantify the occurrence of minerals in several ways, and using area percentage is a more meaningful scale than grain counts when evaluating alteration minerals that are not necessarily present as discrete grains. The same methods could be applied to identify minerals present primarily as inclusions within other grains.

Future work

Statistical analysis of the Izok Lake data will be carried out to assess the similarities of the two vertical sections of each mount, as well as the similarities between the two vertical sections and the basal section. These data will also be compared to grain-picking work previously performed on the >0.250 mm fractions to assess whether any of the four splits of the <0.250 mm fractions are suitable for detecting indicator minerals in HMC. The identification of hydrothermal alteration rims and

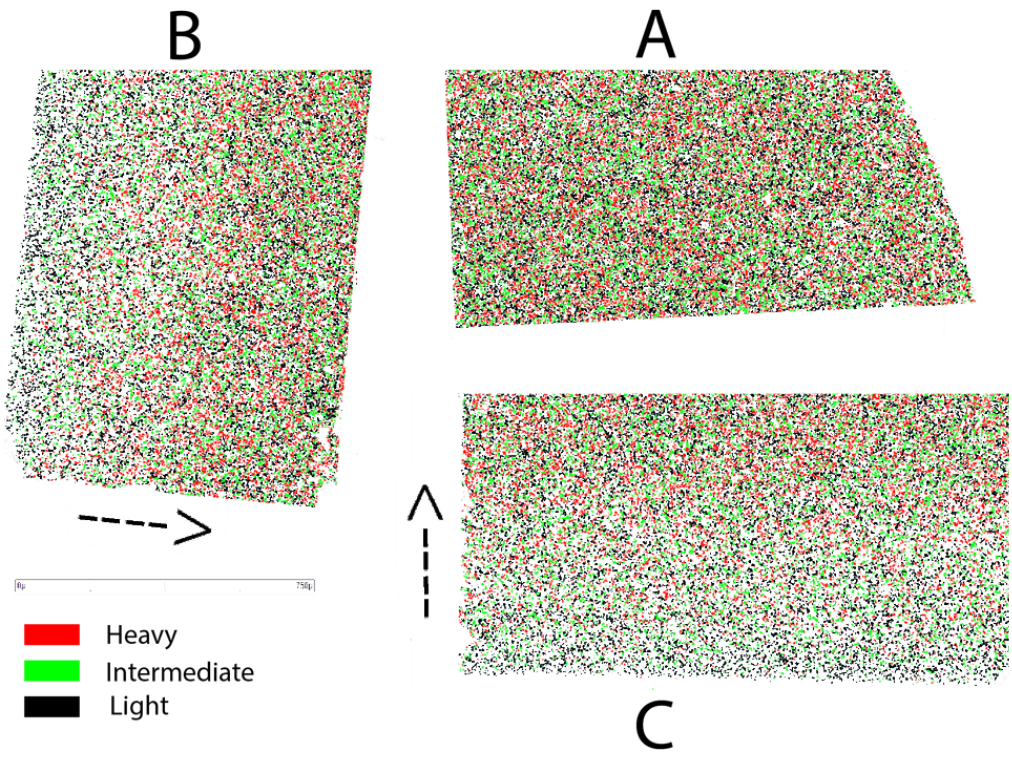

Figure 4. Plan view of the analyzed surface for the <0.064 mm fraction of till sample 12-MPB-902, with grain colours assigned based on specific gravity. A represents the basal surface, with a relatively uniform distribution of heavy (red) grains. B and C represent vertical slices, with dashed arrows representing the settling direction for each. Note the overrepresentation of heavy (red) grains towards the bottom of each vertical cross section.

textures will be investigated, beginning with further characterization of the celsian alteration present within the samples.

Samples selected from the Sisson porphyry-style W-Mo deposit and Triple B kimberlite are currently being mounted, following sieving using the new methods developed in this study. Once scanned, the samples will be processed using MLA to identify known and new indicator minerals associated with intrusion-hosted systems and kimberlites. The study will then proceed to investigate the Casino copper porphyry sample suite.

Acknowledgments

This report is a contribution to NRCan's Targeted Geoscience Initiative Program (TGI). Support for this study was provided through the Porphyry-style Mineral Systems Project's 'Activity P-3.3: Mineralogical controls on the fertility of porphyry-style systems' and the Volcanic- and Sedimentary-Hosted Base Metal Mineralization Project's 'Activity VS-2.4: Fingerprinting fluid source regions and pathways of volcanogenic massive sulphide deposits'.

Don Lougheed is conducting a TGI-supported M.Sc. project at Queen's University, Kingston, Ontario. The authors thank the team at Overburden Drilling Management Limited for their insights into the handling and processing of heavy mineral concentrate materials.

References

Averill, S.A., 2001. The application of heavy indicator minerals in mineral exploration with emphasis on base metal indicators in glaciated metamorphic and plutonic terrain; *in* Drift Exploration in Glaciated Terrain, (ed.) M.B. McClenaghan, P.T. Bobrowsky, G.E.M. Hall and S. Cook; Geological Society of London, Special Volume 185, p. 69–82.

Averill, S.A., 2013. Discovery and delineation of the Rainy River gold deposit using glacially dispersed gold grains sampled by deep overburden drilling; *in* New Frontiers for Exploration in Glaciated Terrain, (ed.) R.C. Paulen and M.B. McClenaghan; Geological Survey of Canada, Open File 7374, p. 37–46.

Averill, S.A. and Zimmerman, J.R., 1986. The Riddle resolved: The discovery of the Partridge gold zone using sonic drilling in glacial overburden at Waddy Lake, Saskatchewan; Canadian Geology Journal of the Canadian Institute of Mining and Metallurgy, v. 1, p. 14–20.

Blaskovich, R.J., 2013. Characterizing waste rock using automated quantitative electron microscopy; M.Sc. thesis, University of British Columbia, Vancouver, British Columbia, 310 p.

Deer, W.A., Howie, R.A., and Zussman, J., 1992. An Introduction to the Rock Forming Minerals. 2nd edition; Prentice Hall, England, 687 p.

Hicken, A.K., 2012. Glacial dispersal of indicator minerals from the Izok Lake Zn-Cu-Pb-Ag VMS deposit, Nunavut, Canada; M.Sc. thesis, Queen's University, Kingston, Ontario, 645 p.

Hicken, A.K., McClenaghan, M.B., Paulen, R.C., Layton-Matthews, D., Averill, S.A., and Crabtree, D., 2013. Indicator mineral signatures of the Izok Lake Zn-Cu-Pb-Ag volcanogenic massive sulfide deposit, Nunavut: Part 2 till; Geological Survey of Canada, Open File 7343, 48 p.

Kelley, K.D., Eppinger, R.G., Lang, J., Smith, S.M., and Fey, D.L., 2011. Porphyry copper indicator minerals (PCIMs) in glacial till samples as an exploration tool: example from the giant Pebble porphyry Cu-Au-Mo deposit; Geochemistry: Exploration, Environment, Analysis, v. 11, p. 321–334.

Layton-Matthews, D., Hamilton, C., and McClenaghan, M.B., 2017. Mineral chemistry: Modern techniques and applications to exploration; *in* Application of indicator mineral methods to bedrock and sediments, (ed.) M.B. McClenaghan and D. Layton-Matthews; Geological Survey of Canada, Open File 8345.

Lehtonen, M.L., Lahaye, Y., O'Brien, H., Lukkari, S. Marmo, J.S., and Sarala, P., 2015. Novel technologies for indicator mineral-based exploration; Geological Survey of Finland, Special Paper 57, p. 23–62.

McClenaghan, M.B., 2011. Overview of common processing methods for recovery of indicator minerals from sediment and bedrock in mineral exploration; Geochemistry: Exploration, Environment, Analysis, v. 11, p. 265–278.

McClenaghan, M.B. and Cabri, L.J., 2011. Gold and Platinum Group Element indicator minerals in surficial sediments; Geochemistry: Exploration, Environment, Analysis, v. 11, p. 251–263.

McClenaghan, M.B., Kjarsgaard, I.M., and Kjarsgaard, B.A., 2004. Kimberlite indicator mineral chemistry and till geochemistry around the Seed and Triple B kimberlites, Lake Timiskaming, Ontario; Geological Survey of Canada, Open File 4822, 31 p.

McClenaghan, M.B. and Kjarsgaard, B.A., 2007. Indicator mineral and surficial geochemical exploration methods for kimberlite in glaciated terrain; Examples from Canada; *in* Mineral Deposits of Canada: A synthesis of major deposit-types, district metallogeny, the evolution of geological processes, and exploration methods, (ed.) W.D. Goodfellow; Geological Survey of Canada, Mineral Deposits Division, Special Publication No. 5, p. 983–1006.

McClenaghan, M.B., Hicken, A.K., Averill, S.A, Paulen, R.C., and Layton-Matthews, D., 2012. Indicator mineral abundance data for bedrock and till samples from the Izok Lake Zn-Cu-Pb-Ag volcanogenic massive sulphide deposit, Nunavut; Geological Survey of Canada, Open File 7075, 11 p.

McClenaghan, M.B., Peter, J.M., and Layton-Matthews, D., 2015a. Overview of VMS exploration in glaciated terrain using indicator minerals, till geochemistry, and boulder tracing: A Canadian perspective; *in* Targeted Geoscience Initiative 4 Contributions to the Understanding of Volcanogenic Massive Sulphide Genesis and Exploration Methods Development, (ed.) J.M. Peter and P. Mercier-Langevin; Geological Survey of Canada, Open File 7853, p. 81–100.

McClenaghan, M.B., Paulen, R.C., Layton-Matthews, D., Hicken, A.K., and Averill, S.A., 2015b. Glacial dispersal of gahnite from the Izok Lake Zn-Cu-Pb-Ag VMS deposit, northern Canada; Geochemistry: Exploration, Environment, Analysis, v. 15, p. 333–349.

McClenaghan, M.B., Parkhill, M.A., Pronk, A.G., Seaman, A.A., McCurdy, M., and Leybourne, M.I., 2017. Indicator mineral and geochemical signatures associated with the Sisson W-Mo deposit, New Brunswick, Canada; Geochemistry: Exploration, Environment, Analysis, v. 17, p. 297–313.

McClenaghan, M.B., Beckett-Brown, C.E., McCurdy, M.W., McDonald, A.M., Leybourne, M.I., Chapman, J.B., Plouffe, A., and Ferbey, T., 2018. Mineral markers of porphyry copper mineralization: Progress report on the evaluation of tourmaline as an indicator mineral; *in* Targeted Geoscience Initiative: 2017 report of activities, volume 1, (ed.) N. Rogers; Geological Survey of Canada, Open File 8358, p. 69–77.

Moro, M.C., Cembranos, M.L., and Fernandez, A., 2001. Celsian (Ba, K)-feldspar and cymrite from SEDEX barite deposits of Zamora, Spain; The Canadian Mineralogist, v. 39, p. 1039–1051.

Plouffe, A., McClenaghan, M.B., Paulen, R.C., McMartin, I., Campbell, J.E., and Spirito, W.A., 2013. Processing of unconsolidated glacial sediments for the recovery of indicator minerals protocols used at the Geological Survey of Canada; Geochemistry Exploration, Environment, Analysis, v. 13, p. 303–316.

Plouffe, A., Ferbey, T., Hashmi. S., and Ward. B.C., 2016. Till geochemistry and mineralogy: Vectoring towards Cu porphyry deposits in British Columbia, Canada; Geochemistry: Exploration, Environment, Analysis, v. 16, p. 213–232.